SOLID STATE CRYSTALLIZATION OF AMORPHOUS PHARMACEUTICALS IN AN AQUEOUS ENVIRONMENT: FACTORS IMPACTING CRYSTALLIZATION AND THE ROLE OF ADDITIVES

by

Andrew Stevens Parker

A Dissertation

Submitted to the Faculty of Purdue University

In Partial Fulfillment of the Requirements for the degree of

Doctor of Philosophy

Davidson School of Chemical Engineering

West Lafayette, Indiana

May 2021

THE PURDUE UNIVERSITY GRADUATE SCHOOL
STATEMENT OF COMMITTEE APPROVAL

Dr. Stephen P. Beaudoin, Co-Chair

Davidson School of Chemical Engineering

Dr. Lynne S. Taylor, Co-Chair

Department of Industrial and Physical Pharmacy

Dr. Zoltan K. Nagy

Davidson School of Chemical Engineering

Dr. Brett M. Savoie

Davidson School of Chemical Engineering

Approved by:

Dr. John A. Morgan

Dedicated to Rebekah

ACKNOWLEDGMENTS

I am deeply indebted to the support of many who have contributed to the completion of this work. I will forever be thankful for the guidance I received from my dissertation advisors, Stephen P. Beaudoin and Lynne S. Taylor. Likewise, I must thank my colleagues in the Beaudoin and Taylor research groups, whose knowledge and insight has helped mold the work I performed, and whose friendship has helped carry me through my time as a graduate student. My biggest supporters have always been my family, and my greatest thankfulness is for my parents, my brothers, and my wife Rebekah to whom this dissertation is dedicated.

TABLE OF CONTENTS

LIST OF FIGURES 8
LIST OF ABBREVIATIONS 12
LIST OF SYMBOLS 13
ABSTRACT 15
1. INTRODUCTION 16
1.1 Background 16
1.2 Broader Impact 18
1.3 Dissertation Overview 19
1.4 References 20
2. LITERATURE REVIEW AND THEORY 24
2.1 Characteristics of the Amorphous State 24
2.2 Pharmaceutical Applications of the Amorphous Phase 27
2.3 Stability of Amorphous Formulations 29
2.4 Liquid-Liquid Phase Separation 32
2.5 Materials 33
2.6 Methods 34
2.6.1 Atomic Force Microscopy 34
2.6.2 Monte Carlo Modeling 36
2.6.3 Relaxation of Sinusoidal Film 37
2.7 References 38
3. THE ROLE OF SURFACE ENERGY HETEROGENEITY ON CRYSTAL MORPHOLOGY DURING SOLID-STATE CRYSTALLIZATION AT THE AMORHPOUS ATAZANAVIR-WATER INTERFACE 52
3.1 Introduction 52
3.2 Methods 54
3.2.1 Materials 54
3.2.2 Preparation of Amorphous Films 55
3.2.3 Crystallization of Amorphous Samples 55
3.2.4 Characterization 55

3.2.5 Relative Surface Energy Distribution Determination 56
3.2.6 Monte Carlo Simulation 56
3.3 Results and Discussion 58
3.3.1 Characterization of Surface Morphology During Crystallization 58
3.3.2 Monte Carlo Simulation Parameter Sensitivity 62
3.3.3 Monte Carlo Simulation Modeling Crystallization 66
3.3.4 MC Simulations for Various Surface Energy Configurations 69
3.4 Conclusions 75
3.5 References 76
4. POLYMER AND SURFACTANT EFFECTS ON CRYSTALLIZATION AT THE AMORPHOUS ATAZANAVIR-WATER INTERFACE 82
4.1 Introduction 82
4.2 Methods and Materials 84
4.2.1 Materials 84
4.2.2 Crystallization of Amorphous ATZ 85
4.2.3 Sample Characterization 85
4.2.4 Monte Carlo Simulation 86
4.3 Results 86
4.3.1 Experimental Investigation of Additive Effects on Crystallization 86
4.3.2 Modeling of Polymer Effects 94
4.4 Discussion 101
4.5 Conclusions 107
4.6 References 107
5. EFFECT OF DISSOLVED ADDITIVES ON TRANSPORT PROPERTIES OF AMORPHOUS PHARMACEUTICAL SURFACES 115
5.1 Introduction 115
5.2 Methods and Materials 116
5.2.1 Materials 116
5.2.2 Sinusoidal Film Preparation 117
5.2.3 Surface Decay Measurements 117
5.3 Theory and Method Development 118

5.3.1 Mathematical Theory 118
5.3.2 Sample Preparation 119
5.3.3 Sample Analysis 120
5.3.4 Experimental Challenges 123
5.4 Results to Date and Future Direction 125
5.5 References 127
6. CONCLUSIONS 131
6.1 Overview of Results 131
6.2 Critique of the Work 131
6.3 Future Directions 132
APPENDIX A. DERIVATION OF FILM DECAY EQUATIONS 134
APPENDIX B. COMPUTER CODE FOR CHAPTER 3 SIMULATIONS 142
APPENDIX C. COMPUTER CODE FOR CHAPTER 4 SIMULATIONS 151
APPENDIX D. COMPUTER CODE FOR CHAPTER 5 DATA ANALYSIS 166
APPENDIX E. SUPPLEMENTAL INFORMATION FOR DATA AND FIGURES 172

LIST OF FIGURES

Figure 2.1. Plots depicting structural and relaxation features of crystalline, liquid, and amorphous phases. A) Radial distribution plot of hypothetical material in liquid, crystal, and amorphous states. B) Heat capacity vs temperature of a hypothetical material in liquid, crystal, and amorphous states. Subfigure A) is adapted from Wang et al. and Caffarena and Grigera and B) is adapted from Kauzmann. 25

Figure 2.2. Excess entropy versus temperature for a hypothetical material demonstrating the Kauzmann paradox and zero entropy catastrophe. Image adapted from Rao, Bhat, and Kumar. 26

Figure 2.3. Plots depicting the solubility (A) and dissolution rates (B) of amorphous and crystalline indomethacin. Data are reproduced from Babu and Nangia. 29

Figure 2.4. Schematic of an atomic force microscope. Adapted from Butt et al. 34

Figure 3.1. AFM topography images (5 μm× 5 μm) of ATZ surface obtained after (A) 0, (B) 6, (C) 14, (D) 16, (E) 20, and (F) 24 hours incubation in pH 6.8 phosphate buffer containing 25 μg/mL ATZ at 40°C. Scale of heat map in (A-C) is 150.0 nm and scale of heat map in (D-F) is 450.0 nm. Scale bar in all images is 1 μm. 59

Figure 3.2. AFM topography images of ATZ surface crystallized from the subcooled melt. Images were obtained after isothermal crystallization for 5 minutes at (A) 185°C, (B) 175°C, (C) 170°C, and (D) 165°C in ambient air. 60

Figure 3.3. SEM micrograph of (A) fresh ATZ film and (B) ATZ film incubated for 22 hours in pH 6.8 buffer containing 25 μg/mL ATZ at 40°C. Scale bar in both images is 1 μm. 62

Figure 3.4. MC simulation snapshots after 15 million trial MC steps for interfacial penalty ratios of 1.0, 1.5, 2.0, 2.5, 3.0, 4.2, 5.0, and 10.0. Dark pixels are underlying amorphous surface, and light pixels are overlaying crystal. Simulations employ a uniform surface energy, nucleation barrier of 13, lattice energy of -5, and interfacial ratio 4.2. 63

Figure 3.5. MC simulation snapshots at 50% conversion for various nucleation barriers of 0.1, 1.0, 4.0, 6.0, 8.0, 10.0, 13.0, and 15.0. Simulations employ a uniform surface energy, lattice energy of -5, and interfacial ratio 4.2. 64

Figure 3.6. MC simulation snapshots at 25% surface crystallization for lattice energies of 0, -2, -4, -6, -8, -10, -15, and -20. Simulation employs a uniform surface energy, nucleation barrier of 13, and interfacial ratio 4.2. 65

Figure 3.7. Plots depicting the effect of (A) penalty ratio, (B) nucleation barrier, and (C) lattice energy on the number of simulation steps required to achieve a given conversion for the systems presented in Figure 1 through Figure 3. (A) represents the number of trial steps to 25% conversion from amorphous to crystalline, (B) the number of steps to 50% conversion, and (C) the number of steps to 25% conversion. 66

Figure 3.8. MC simulation snapshots depicting crystallization progression after (A) 5 million, (B) 10 million, (C) 15 million, (D) 20 million, (E) 25 million, (F) 30 million, (G) 35 million, and (H)

40 million trial MC steps. Dark pixels are underlying amorphous surface, and light pixels are overlaying crystal. 67

Figure 3.9. Plot comparing extent of crystallization between experimental data (●) and scaled simulation data (■). Error bars represent one standard deviation based on 5 replicates for simulation points and 5 to 10 replicates for experimental points. 68

Figure 3.10. MC simulation employing a (A) uniform surface energy configuration and (B-I) accompanying simulation snapshots. 70

Figure 3.11. MC simulation employing a (A) large 2D Gaussian function surface energy configuration and (B-I) accompanying simulation snapshots. The region of influence of the high surface energy is circumscribed with a black circle that is superimposed on simulation results to serve as a visual guide. 71

Figure 3.12. MC simulation employing a (A) randomly distributed small 2D Gaussian function surface energy configuration and (B-H) accompanying simulation snapshots. The regions of influence of the high surface energy are circumscribed with black circles that are superimposed on simulation results to serve as a visual guide. 72

Figure 3.13. MC simulation employing a (A) long diagonal surface energy configuration and (B-I) accompanying simulation snapshots. The region of influence of the high surface energy is circumscribed with two black lines that are superimposed on simulation results to serve as a visual guide. 73

Figure 3.14. Relative adhesion force map (A) of amorphous film obtained by AFM (500 nm × 500 nm), corresponding calculated relative surface energy distribution (B) employed in MC simulation with (C-H) snapshots of simulation progression. 74

Figure 4.1. Chemical structures of (A) atazanavir, (B) HPMCAS, (C) PVAc, (D) PVP, and (E) SDS. 85

Figure 4.2. AFM micrographs depicting polymer interactions with amorphous ATZ films. Images were captured at room temperature after 1 hour incubation with buffer containing dissolved polymer. (A)-(E) are topographical plots and (F)-(J) are phase contrast plots. (A) and (F) are the reference system containing no dissolved polymer, (B) and (G) contain 10 μg/mL PVAc, (C) and (H) contain 10 μg/mL HPMCAS-HF, (D) and (I) contain 10 μg/mL HPMCAS-MF, and (E) and (J) contain 10 μg/mL PVP. 88

Figure 4.3. AFM micrographs depicting surface evolution of amorphous ATZ film exposed to buffer with no additives. (A) and (C) are the initial film before incubation, while (B) and (D) are the same film after 3 hours of incubation at elevated temperature. (A) and (B) are topographical maps while (C) and (D) are phase contrast plots. 89

Figure 4.4. AFM micrographs capturing surface evolution of amorphous ATZ film incubated in buffer containing 10 μg/mL HPMCAS-HF at 40°C. (A) and (D) are the initial film before incubation, (B) and (E) show 1 day of incubation time, and (C) and (F) show 6 days of incubation time . (A) - (C) are topographical maps while (D) - (F) are phase contrast plots. 90

Figure 4.5. AFM micrographs capturing surface evolution of amorphous ATZ film incubated in buffer containing 10 μg/mL HPMCAS-MF at 40°C. (A) and (D) are the initial film before

incubation, (B) and (E) show 1 day of incubation time, and (C) and (F) show 6 days of incubation time . (A) - (C) are topographical maps while (D) - (F) are phase contrast plots. 91

Figure 4.6. AFM micrographs capturing surface evolution of amorphous ATZ film incubated in buffer containing 100 μg/mL HPMCAS-MF at 40°C. (A) and (D) are the initial film before incubation, (B) and (E) show 1 day of incubation time, and (C) and (F) show 2 days of incubation time . (A) - (C) are topographical maps while (D) - (F) are phase contrast plots. 92

Figure 4.7. Picture and micrographs depicting final surface of amorphous ATZ film before and after incubation for 24 hours in buffer containing 6 μg/mL SDS at 40°C. (A) is a macroscopic picture of the entire fresh film, (B) is a macroscopic picture of the film after incubation, (C) is an optical micrograph of the fresh film, (D) is an optical micrograph post-incubation containing an opaque overlaying region as well as a darker underlying region, (E) and (G) are representative SEM micrographs of the overlaying region, and (F) and (H) are representative SEM micrographs of the underlying region 93

Figure 4.8. MC model results for systems employing polymer pre-equilibration but no dynamic interactions with growing crystals. Red pixels are amorphous sites, yellow pixels are crystalline sites, and black pixels are polymer sites. (A) is several snapshots of a control system containing no polymer, (B) is several snapshots of a system with 25 percent polymer surface coverage, and (C) is a scaling analysis depicting the number of trial MC steps required to achieve 50 percent conversion from amorphous to crystalline of available sites for various polymer surface coverage fractions. Each point represents n = 10 replicates, with error bars representing one standard deviation. 95

Figure 4.9. MC model predictions of fractional polymer coverage and fractional conversion for systems employing dynamic polymer interactions. (A) shows several snapshots of simulation progress for the uniform interaction strength system (symmetric) depicted by the red diamonds and (B) shows several snapshots of simulation progress for the biased interaction strength system (asymmetric) depicted by blue triangles. (C) plots both dynamic polymer coverage as well as extent of conversion versus number of trial MC steps for three systems. Filled points represent fractional conversion and open points represent fractional polymer surface coverage. Black squares depict the control system with no polymer, red diamonds depict a system with 20 percent equilibrium polymer coverage with equal interaction strength between high energy and low energy crystal interfaces, and blue triangles depict a system with 20 percent equilibrium polymer coverage with stronger polymer interactions with high energy crystal interfaces. 97

Figure 4.10. MC model predictions of fractional polymer coverage and fractional conversion for systems employing dynamic polymer interactions. (A) shows several snapshots of simulation progress for the lower coverage and slow equilibration system depicted by orange circles, (B) shows several snapshots of simulation progress for the lower coverage and fast equilibration system depicted by blue triangles, and (C) shows several snapshots of simulation progress for the higher coverage and fast equilibration system depicted by purple diamonds. (D) plots both dynamic polymer coverage as well as extent of conversion versus number of trial MC steps for four systems. Filled points represent fractional conversion and open points represent fractional polymer surface coverage. Black squares depict the control system with no polymer, orange circles depict a system with 30 percent equilibrium polymer coverage with slow polymer equilibration, blue triangles depict a system with 30 percent equilibrium polymer coverage with

25 times faster polymer equilibration, and purple diamonds depict a system with 60 percent equilibrium polymer coverage with the faster polymer equilibration. 100

Figure 5.1. AFM micrographs of sinusoidal films prepared under different conditions. (A) depicts a film prepared with little down force and poor template wetting, preventing the transfer of template wave. (B) depicts a film subjected to force for twice the recommended imprint time, demonstrating film fracture which occurred when removing the template. (C) depicts a film prepared as described in Section 5.2.2. 120

Figure 5.2. Example of sinusoidal ATZ film. (A) is an AFM topographical plot, and (B) is the averaged cross-section. 121

Figure 5.3. Schematics outlining three surface analysis algorithms based on the averaged cross-section in Figure 5.2B. (A) shows the amplitude calculation based on an average of the tallest peaks and average of the lowest valleys with frequency determined by average peak-to-peak distance, (B) shows the amplitude spectrum based on an FFT and the fit of the dominant sine wave extracted from the FFT plot, and (C) depicts the fit from non-linear least squares regression using a sine wave as the objective function and the results of part (B) as the initial guess for amplitude and frequency. 122

Figure 5.4. AFM micrographs depicting aberrant behavior which confounded surface height measurements. (A) shows films which fracture and/or dissolve upon addition of buffer solution and (B) shows the tendency of film to uptake buffer and become plastic, preventing accurate tracking of surface topography by the AFM tip in contact mode. 124

Figure 5.5. Plot of surface height (blue x) and *in situ* sample temperature (red circles) as a function of time during a typical sinusoidal decay experiment. Time of zero indicates fluid addition and beginning of decay experiment, time before zero is during AFM setup and warm-up period. 125

Figure 5.6. Results from a typical surface decay experiment. (A) is an AFM micrograph time lapse of *in situ* topographical measurements obtained from the same location on a surface undergoing surface relaxation. (B) is a plot of sinusoidal surface height versus time, with the data fit to the exponential decay relation from Equation(2.2). 126

Figure 5.7. Scaling data for the additive free (control) system. Decay constant is extracted from the exponential term from fitting height versus time to Equation (2.2). Line of best fit is simple linear regression. 127

LIST OF ABBREVIATIONS

2D	Two dimensional
AFM	Atomic force microscopy
AIDS	Acquired immunodeficiency syndrome
API	Active pharmaceutical ingredient
ASD	Amorphous solid dispersion
ATZ	Atazanavir
ETD	Everhart-Thornley detecter
GLPS	Glass-liquid phase separation
HIV	Human immunodeficiency virus
HPMCAS	Hydroxypropyl methylcellulose acetate succinate
LLPS	Liquid-liquid phase separation
MC	Monte Carlo
PE	Polyethylene
PVAc	Polyvinyl acetate
PVP	Polyvinylpyrollidone
QNM	Quantitative nanomechanical mapping
SDS	Sodium dodecyl sulfate
SEM	Scanning electron microscopy

LIST OF SYMBOLS

A	Dissolution and deposition decay term
B	Surface diffusion decay term
C	Bulk diffusion decay term
c_0	Equilibrium concentration
D_b	Bulk self-diffusion coefficient
D_l	Diffusion coefficient of solute in solvent
D_s	Surface diffusion coefficient
E	Energy
$E_{Interface}$	Interfacial energy
$E_{lattice}$	Crystal lattice energy
E_{film}	Relative amorphous film energy
F	Viscous flow decay term
F_{ad}	Force of adhesion
G	Gibbs free energy
h	Height
k	Boltzmann's constant
K	Decay constant
P	Pressure
R	Radius of curvature
t	Time
T	Temperature
T_g	Glass transition temperature
T_k	Kauzmann temperature
T_m	Melting temperature
α	Amplitude
γ	Surface energy
γ_{film}	Surface energy of film
γ_{probe}	Surface energy of AFM probe tip
η	Viscosity

κ	Curvature
λ	Wavelength
μ	Chemical potential
ν	Area density
ρ	Density
φ	Probability of trial Monte Carlo move
ψ	Stream function
ω	Frequency
Ω	Molecular volume

ABSTRACT

Amorphous materials play an important role in pharmaceutical formulations due to their ability to generate supersaturation above the crystalline solubility, which is particularly advantageous for improving the bioavailability of poorly soluble drugs. Unfortunately, the high free energy of the amorphous state also means it has a propensity to crystallize, jeopardizing formulation performance. There is considerable interest in understanding the mechanisms of crystallization as well as means of mitigating this undesired phase transformation. Formulation additives such as polymers and surfactants are commonly used as stabilizers, though the ability to inhibit crystallization is specific to the drug and additive pair and the actual mechanisms of inhibition are not fully understood.

This dissertation outlines a project to study one particular trajectory of amorphous pharmaceutical formulations and the influence of additives on the fate of drug molecules. During dosing, it is possible for a sufficiently high supersaturation to occur such that the miscibility limit between water and drug is achieved and the supersaturated solution undergoes a liquid-liquid phase separation event. Liquid-liquid phase separation results in colloidal drug particles which are not intimately mixed with stabilizers and are prone to undergo solid-state crystallization. Thus, it is the intent of this project to study the solid-state phase transformation of amorphous drug surfaces exposed to aqueous media, as well as the impact of dissolved additives on surface evolution.

Experimental crystallization investigations employing the imaging techniques of atomic force microscopy and scanning electron microscopy paired with complementary lattice Monte Carlo models reveal the non-classic nucleation and growth mechanisms driving glass-to-crystal phase transformations. Evidence is also found of the previously uninvestigated role of the amorphous surface energy on the morphology of evolving surface crystals. Additive inhibitory effects are demonstrated to occur through competitive adsorption onto high surface energy sites, reducing surface mobility and blocking lattice integration, while crystallization promotion effects occur by additives partitioning at the drug-water interface and creating a more hydrophobic solution region which enhances molecular mobility. Finally, fundamental transport studies are described for quantitative determination of surface transport properties as well the regulatory effects of additives on surface transport.

1. INTRODUCTION

1.1 Background

Many of the challenges faced by humanity in the quest for disease treatment are understood through the evolution of drug discovery and development. Drug discovery and development are dynamic fields which have undergone various paradigm shifts since their inception. Pollen from medicinal flowers found in a Neanderthal gravesite has led to speculation that the use of natural products to treat disease may perhaps predate human history to as far back as 60,000 years ago[1]. Catalogs of pharmacologically active plant products date to ancient Mesopotamia between 3000 and 2000 BC, suggesting that humans have discovered and leveraged natural medicines for millennia[2]. However, it has not been until the past few centuries that advances in chemistry and biology have led to a modern conception of drug discovery which resembles the field today. Synthetic organic chemistry and its eventual application to the development of novel therapeutic compounds began almost by chance in 1856 when William Perkins synthesized the first artificial dye[3]. The ability to synthesize, isolate, purify, and characterize new compounds enabled the advent of the pharmaceutical industry[4]. However, just as Perkins' discovery was marked by serendipity, until very recently pharmaceutical science was likewise characterized largely by happenstance and fortuitous discoveries[5].

In the past few decades, a popular paradigm of drug discovery and development has been ushered in through combinatorial chemistry and high-throughput screening. Together, these techniques allow for the rapid synthesis and subsequent evaluation against markers for disease states of thousands of organic compounds, exponentially increasing the number of candidates for development into potential therapeutic agents[6]. While tremendously promising, this model for drug discovery has come with some unforeseen consequences. Among those of import for the work herein are challenges related to the dominant physiochemical properties of new molecular entities in the pharmaceutical pipeline. Unlike traditional empirical discovery methods which focused in detail on the few most promising leads, the ability to synthesize hundreds of thousands of novel compounds precludes such careful characterization. Rather than *in vitro* assays in thermodynamically equilibrated aqueous solutions, high throughput screening necessitates serial dilutions using organic solvents for rapid activity assessments[7]. Consequently,

this paradigm is biased towards lipophilic compounds which exhibit exceptionally poor aqueous solubility[8]. In fact, it is estimated that anywhere from 70 to 90 percent of candidate molecules in the pharmaceutical pipeline suffer from solubility limitations[9]. It is likely that the high attrition rate of molecules from the discovery pipeline, which contributes to the ever rising cost of pharmaceutical R&D, is heavily impacted by these solubility-limited candidate molecules[10,11].

Given the development challenge posed by solubility concerns, various formulation strategies have been employed to improve the apparent solubility of drug molecules. Popular strategies which have been successfully leveraged in commercial formulations can broadly be categorized by either modification of the active pharmaceutical ingredient (API) or the addition of solubilizing excipients. API modification techniques include co-crystals, nanocrystals, control of polymorphic or amorphous form and the conversion to a pharmaceutical salt, while performance enhancing excipients can include polymers, surfactants, cyclodextrins, co-solvents, and lipids[12,13]. Each of these have their own benefits and drawbacks, such that the optimum strategy depends on the structural and physiochemical features of the API, processing and manufacturing considerations for the given formulation, and safety and toxicity concerns for the given API application[14]. Solid dispersion, which involve both API modification by generation of the amorphous form as well as the incorporation of performance enhancing excipients including polymers and surfactants, is an increasingly popular solubilization technique[15]. Amorphous solid dispersions (ASDs) have been shown to increase both dissolution and absorption rates and can be prepared through various routes to accommodate different types of API compounds[16].

While there are clear advantages to ASD formulations, the use of the amorphous state is not without challenges. The free energy increase provided by the amorphous form relative to a crystalline state which provides the solubility advantage is also a double-edged sword, as this thermodynamic metastability is a driving force for crystallization and loss of solubility advantage[17]. The performance and phase behavior of ASDs have been extensively studied, with primary focus topics including physical stability during storage, dissolution behavior and supersaturation trajectories in various media environments, and various aspects of crystallization from the supersaturated solution[18–22]. A complex interplay of many factors influences these and other important phenomena which ultimately dictate ASD efficacy[23]. One important facet of ASD behavior which has not yet been fully explored involves crystallization of the amorphous API exposed to a dissolution environment with polymer and/or surfactant present. While an ASD

formulation is designed as a molecular level mixture of amorphous drug and polymer or surfactant, physical de-mixing, incongruent preferential release of polymer during dissolution, and glass-liquid phase separation (GLPS) when supersaturation exceeds the amorphous solubility can all result in amorphous API that is no longer intimately mixed with polymer during dosing[24,25]. Hence, understanding the fundamentals of this nuanced and complex system is important for guarding against crystallization and developing high performing ASD formulations.

1.2 Broader Impact

Solid-state phase behavior is of critical importance to industries beyond the pharmaceutical industry, ranging from food products to consumer products to even the defense industry. Some case studies highlight the necessity of controlling crystallinity as it relates to product performance. Of perhaps gravest consequence is the topic of energetic materials and the need for insensitive munitions. History has revealed many accidents and catastrophes resulting from premature detonation of munitions due to fires, impacts, blasts, and even high frequency periodic insults[26–28]. One strategy that has been developed to reduce the mechanical sensitivity of high explosives is utilizing energetic materials in an amorphous rather than crystalline form, where the polymeric binder which holds the formulation together also serves as a crystallization inhibitor[29]. On the complete opposite end of the spectrum is the food product industry. Anyone who enjoys sweets is familiar with some of the storage challenges with treats like chocolate chip cookies or cotton candy. Initially soft and chewy cookies become hard and crunchy after a few days on the shelf, and light and fluffy cotton candy becomes dense and granular if kept overnight. In both cases, the gradual crystallization of initially amorphous sugar causes product failure due to poor texture and palatability[30]. Solid phase characteristics also constitute major design criteria for the packaging industry. For example, the polymer that makes up many plastic packages (polyethylene or PE) can exhibit different physical properties as the crystallinity of the bulk material is tuned; high density, high crystallinity PE is suitable for hard plastic bottles while low density, low crystallinity PE is more pliable and is typically used in soft plastic bags[31]. In these examples and many others, identical molecules can behave quite differently when produced in different solid-state forms which can ultimately determine product success or failure. Therefore, understanding the amorphous form and maintaining phase control is essential for many of the products and technologies of the present and the future.

1.3 Dissertation Overview

As noted above, the primary aim of this work is to study solid-state crystallization at the amorphous drug-water interface and the impact of polymer and surfactant species on this phase transformation. It involves both qualitative, phenomenological observations of this phase change as well as quantitative, first-principles treatments to elucidate mechanistic insights. Furthermore, this body of work is composed of experimental findings, stochastic computation simulations of these systems, and closed-form theoretical modeling of fundamental transport processes.

Chapter 2 of this dissertation consists of a review of the relevant literature. It addresses in more detail the topics mentioned previously, including a rigorous discussion of the amorphous state and the other research conducted on factors influencing dissolution and crystallization of solid dispersions. Additionally, background is provided for the experimental and computational techniques utilized in these studies. This section is intended to provide all the pertinent knowledge to the reader to identify the current gaps in understanding and to fully appreciate the work presented herein.

Chapter 3 is an adaptation of a previously published article entitled “The role of surface energy heterogeneity on crystal morphology during solid-state crystallization at the amorphous atazanavir-water interface” by A.S. Parker, L.S. Taylor, and S.P. Beaudoin[32]. This study explores solid-state crystallization at the amorphous pharmaceutical/water interface, probed by experiments as well as computational modeling. This chapter also outlines the use of stochastic modeling to probe the role of the surface energy configuration of the underlying amorphous film on the morphology of the crystalline phase as it evolves. The findings highlight the non-classical crystallization that occurs during this interfacially driven crystallization phenomenon, as well as the important role played by the surface energy of the glass as well as the surface energy of the various crystal faces on crystal morphology.

Chapter 4 details the extension of the previous study into more complex systems containing polymer and surfactant species. Specifically, it details experimental observations of crystallization inhibition and activation via the inclusion of model additives and an extension of the stochastic model to interpret and explain these phenomenological observations. The results demonstrate competitive inhibition of crystal nucleation and growth by adsorbed polymer and activation of rapid solution-mediated crystallization by surfactant species.

Chapter 5 is the culminating study of this dissertation, which outlines a series of experiments to evaluate the transport phenomena facilitating rearrangement and crystallization of the amorphous surfaces in each of the systems from the previous chapters. Height measurements of decaying sinusoidal amorphous films are used in closed form solutions to the various transport equations to determine the dominant transport mechanism to connect the crystallization effects of additives to their control of the transport properties of amorphous drug molecules. A description of experimental methods and techniques for data interpretation are outlined, as well as promising preliminary data and a clear path forward for concluding this study. The experiments outlined in this chapter ultimately provide a fundamental, first principles understanding of the more qualitative results in chapters 3 and 4.

Chapter 6 provides some concluding thoughts and offers future directions of interest to the scientific community. A brief holistic and synthetic assessment of the contents of the dissertation in its entirety is provided, as are thoughts on completion of the study outlined in chapter 5. Some critiques of the work are offered, including strengths and limitations of the approach taken here. Finally, novel directions and interesting questions raised by this work are discussed to generate discussion towards avenues of fruitful research efforts.

1.4 References

(1) Solecki, R. S. Shanidar IV , a Neanderthal Flower Burial in Northern Iraq. *Science (80-.).* **1975**, *190* (4217), 880–881.

(2) Ji, H.-F.; Li, X.-J.; Zhang, H.-Y. Natural Products and Drug Discovery. *EMBO Rep.* **2009**, *10* (3), 194–200. https://doi.org/10.1007/978-1-59259-976-9_1.

(3) Sneader, W. *Drug Discovery: A History*; John Wiley & Sons: West Sussex, UK, 2005.

(4) Ban, T. A. Neuropsychopharmacology and the History of Pharmacotherapy in Psychiatry: A Review of Developments in the 20th Century. In *Reflections on Twentieth-Century Psychopharmacology*; Ban, T. A., Healy, D., Shorter, E., Eds.; Animula: Budapest, Hungary, 2004; pp 697–720.

(5) Ban, T. A. The Role of Serendipity in Drug Discovery. *Dialogues Clin. Neurosci.* **2006**, *8* (3), 335–344.

(6) Drews, J. Drug Discovery: A Historical Perspective. *Science (80-.).* **2000**, *287*, 1960–1964.

(7) Lipinski, C. A.; Lombardo, F.; Dominy, B. W.; Feeney, P. J. Experimental and Computational Approaches to Estimate Solubility and Permeability in Drug Discovery and Development Settings. *Adv. Drug Deliv. Rev.* **1997**, *23*, 3–25. https://doi.org/10.1016/j.addr.2012.09.019.

(8) Lipinski, C. A. Drug-like Properties and the Causes of Poor Solubility and Poor Permeability. *J. Pharmacol. Toxicol. Methods* **2000**, *44* (1), 235–249. https://doi.org/10.1016/S1056-8719(00)00107-6.

(9) Thayer, A. M. Finding Solutions. *Chem. Eng. News* **2010**, *88* (22), 13–18.

(10) Lipp, R. The Innovator Pipeline: Bioavailability Challenges and Advanced Oral Drug Delivery Opportunities. *Am. Pharm. Rev.* **2013**, *16* (3), 2–7.

(11) Amidon, G. L.; Lennernäs, H.; Shah, V. P.; Crison, J. R. A Theoretical Basis for a Biopharmaceutic Drug Classification: The Correlation of in Vitro Drug Product Dissolution and in Vivo Bioavailability. *Pharm. Res.* **1995**, *12* (3), 413–420. https://doi.org/10.1023/A:1016212804288.

(12) Leuner, C.; Dressman, J. Improving Drug Solubility for Oral Delivery Using Solid Dispersions. *Eur. J. Pharm. Biopharm.* **2000**, *50* (1), 47–60. https://doi.org/10.1016/S0939-6411(00)00076-X.

(13) Williams, H. D.; Trevaskis, N. L.; Charman, S. A.; Shanker, R. M.; Charman, W. N.; Pouton, C. W.; Porter, C. J. H. Strategies to Address Low Drug Solubility in Discovery and Development. *Pharmacol. Rev.* **2013**, *65*, 315–499. https://doi.org/10.1124/pr.112.005660.

(14) Jain, S.; Patel, N.; Lin, S. Solubility and Dissolution Enhancement Strategies: Current Understanding and Recent Trends. *Drug Dev. Ind. Pharm.* **2015**, *41* (6), 875–887. https://doi.org/10.3109/03639045.2014.971027.

(15) Kim, K. T.; Lee, J. Y.; Lee, M. Y.; Song, C. K.; Choi, J.; Kim, D.-D. Solid Dispersions as a Drug Delivery System. *J. Pharm. Investig.* **2011**, *41* (3), 125–142. https://doi.org/10.4333/KPS.2011.41.3.125.

(16) Chiou, W. L.; Riegelman, S. Pharmaceutical Applications of Solid Dispersion Systems. *J. Pharm. Sci.* **1971**, *60* (9), 1281–1302.

(17) Hancock, B. C.; Parks, M. What Is the True Solubility Advantage for Amorphous Pharmaceuticals? *Pharm. Res.* **2000**, *17* (4), 397–404. https://doi.org/10.1023/A:1007516718048.

(18) Alonzo, D. E.; Gao, Y.; Zhou, D.; Mo, H.; Zhang, G. G. Z. Z.; Taylor, L. S. Dissolution and Precipitation Behavior of Amorphous Solid Dispersions. *J. Pharm. Sci.* **2011**, *100* (8), 3316–3331. https://doi.org/10.1002/jps.22579.

(19) Alonzo, D. E.; Zhang, G. G. Z.; Zhou, D.; Gao, Y.; Taylor, L. S. Understanding the Behavior of Amorphous Pharmaceutical Systems during Dissolution. *Pharm. Res.* **2010**, *27* (4), 608–618. https://doi.org/10.1007/s11095-009-0021-1.

(20) Hilton, J. E.; Summers, M. P. The Effect of Wetting Agents on the Dissolution of Indomethacin Solid Dispersion Systems. *Int. J. Pharm.* **1986**, *31*, 157–164. https://doi.org/10.1016/0378-5173(86)90226-7.

(21) Lauer, M. E.; Siam, M.; Tardio, J.; Page, S.; Kindt, J. H.; Grassmann, O. Rapid Assessment of Homogeneity and Stability of Amorphous Solid Dispersions by Atomic Force Microscopy - from Bench to Batch. *Pharm. Res.* **2013**, *30*, 2010–2022. https://doi.org/10.1007/s11095-013-1045-0.

(22) Lauer, M. E.; Grassmann, O.; Siam, M.; Tardio, J.; Jacob, L.; Page, S.; Kindt, J. H.; Engel, A.; Alsenz, J. Atomic Force Microscopy-Based Screening of Drug-Excipient Miscibility and Stability of Solid Dispersions. *Pharm. Res.* **2011**, *28*, 572–584. https://doi.org/10.1007/s11095-010-0306-4.

(23) Kou, X.; Zhou, L. Stability of Amorphous Solid Dispersion. In *Amorphous Solid Dispersions*; 2014; pp 515–544. https://doi.org/10.1007/978-1-4939-1598-9_16.

(24) Mosquera-Giraldo, L. I.; Taylor, L. S. Glass-Liquid Phase Separation in Highly Supersaturated Aqueous Solutions of Telaprevir. *Mol. Pharm.* **2015**, *12* (2), 496–503. https://doi.org/10.1021/mp500573z.

(25) Indulkar, A. S.; Lou, X.; Zhang, G. G. Z.; Taylor, L. S. Insights into the Dissolution Mechanism of Ritonavir–Copovidone Amorphous Solid Dispersions: Importance of Congruent Release for Enhanced Performance. *Mol. Pharm.* **2019**, *16*, 1327–1339. https://doi.org/10.1021/acs.molpharmaceut.8b01261.

(26) Powell, I. J. Insensitive Munitions – Design Principles and Technology Developments. *Propellants, Explos. Pyrotech.* **2016**, *41* (3), 409–413. https://doi.org/10.1002/prep.201500341.

(27) Jean Isler. The Transition to Insensitive Munitions (IM). *Propellants, Explos. Pyrotech.* **1998**, *23*, 283–291.

(28) Mares, J. O.; Roberts, Z. A.; Emre Gunduz, I.; Parab, N. D.; Sun, T.; Fezzaa, K.; Chen, W. W.; Son, S. F.; Rhoads, J. F. In-Situ X-Ray Observations of Ultrasound-Induced Explosive Decomposition. *Appl. Mater. Today* **2019**, *15*, 286–294. https://doi.org/10.1016/j.apmt.2019.01.009.

(29) Stepanov, V.; Patel, R. B.; Paraskos, A. J.; Qiu, H. Method for Manufacture of Amorphous Energetics. US 9850180 B1, 2017.

(30) Labuza, T.; Roe, K.; Payne, C.; Panda, F.; Labuza, T. J.; Labuza, P. S.; Krusch, L. Storage Stability of Dry Food Systems: Influence of State Changes during Drying and Storage. In *Proceedings of the 14th International Drying Symposium*; 2004; pp 48–68.

(31) Riley, A. Basics of Polymer Chemistry for Packaging Materials. In *Packaging Technology: Fundamentals, Materials and Processes*; Woodhead Publishing Limited, 2012; pp 262–286. https://doi.org/10.1533/9780857095701.

(32) Parker, A. S.; Taylor, L. S.; Beaudoin, S. P. The Role of Surface Energy Heterogeneity on Crystal Morphology during Solid-State Crystallization at the Amorphous Atazanavir–Water Interface. *CrystEngComm* **2020**, *22*, 3179–3187. https://doi.org/10.1039/c9ce02007a.

2. LITERATURE REVIEW AND THEORY

2.1 Characteristics of the Amorphous State

Amorphous or glassy materials are studied through various lenses in a wide array of scientific disciplines. Conceptually, the amorphous phase is most intuitively understood by first considering a pure component liquid approaching its melting point T_m. Thermodynamics dictates that in most instances the liquid phase is stable above T_m while a solid phase is stable below T_m (though there are some exceptions where certain materials can undergo an inverse melting solid-to-liquid transition upon cooling through certain regions of phase space)[1]. However, an interesting rate-dependent hysteresis for the solid-to-liquid versus the liquid-to-solid pair can occur. Unlike the melting process, which occurs spontaneously upon crossing the coexistence curve, kinetic limitations can allow the liquid below T_m to persist in this subcooled state due to slower molecular motions at depressed temperatures[2]. Given enough time or with sufficiently slow cooling rates, the thermodynamically favorable crystalline state will eventually nucleate in the subcooled liquid[3]. If cooling is rapid, it is possible to bring the subcooled liquid to a temperature where the material is kinetically unable to undergo liquid-like molecular relaxations necessary for crystallization to occur over any meaningful timescale[4,5]. At this point, the subcooled liquid becomes a glass (also known as an amorphous solid). The transition temperature, known as the glass transition temperature T_g, is thought to mark a kinetic rather than thermodynamic phenomenon, as the amorphous phase is not strictly considered a thermodynamic state[6]. It should come as no surprise, then, that amorphous materials prove to be particularly challenging to characterize and understand, as they display features intermediate to the liquid and crystalline solid states[7].

The unexpected intermediary behavior of glasses can be understood by considering the molecular motions and packing of the various phases of matter. Some case studies depicting these features can be seen in Figure 2.1[7–9]. Figure 2.1 shows three radial distribution functions (Figure 2.1A), which describe local ordering and periodicity within a phase, as well as heat capacity as a function of temperature (Figure 2.1B), which captures molecular translocations, rotations, and vibrations[10,11]. Structurally, crystalline solids have local ordering as well as long range periodicity, resulting in sharp, distinct peaks in the radial density function (black dashed

line in Figure 2.1A). Liquids by contrast have no periodic lattice, and hence have much broader and smoother density functions (red dotted line in Figure 2.1A). Examining the density function for the amorphous material (blue solid line in Figure 2.1A), the packing retains short-range ordering but exhibits minimal long-range order. This reflects the molecular structure of glasses, which exhibit local order and interactions but no long-range lattice much like the liquid. By contrast, the molecular motions afforded each of the three phases (Figure 2.1B) reveal that amorphous materials cannot undergo the relaxations typical of the liquid phase and exhibit constrained motions like the crystalline solid despite the lack of lattice packing. As hinted to previously, this interesting intermediary behavior can be rationalized by understanding the amorphous state as a kinetically arrested liquid. Hence, glasses are ordered much like a liquid yet undergo motions like a solid. This type of behavior results in unexpected and often paradoxical features.

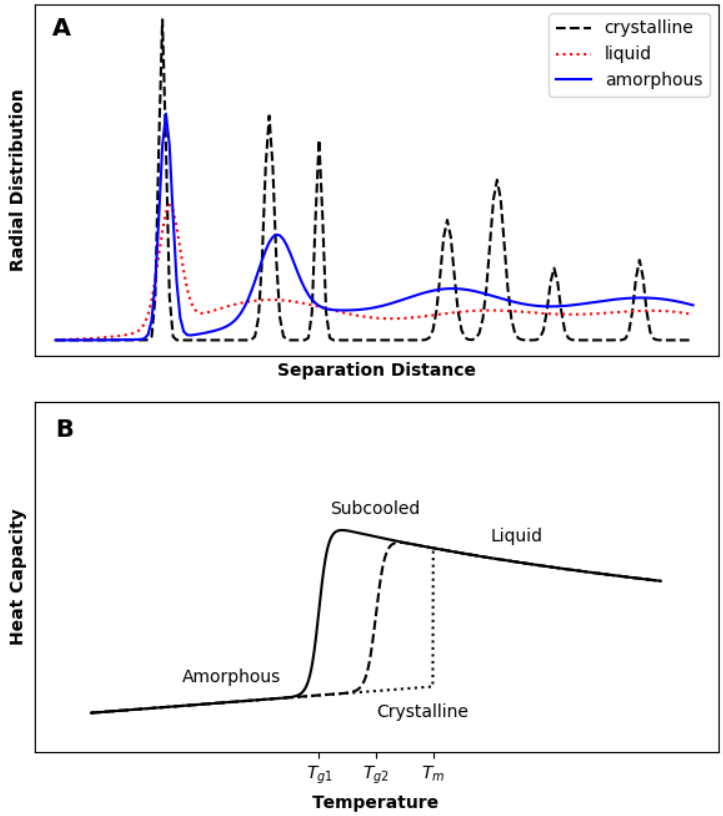

Figure 2.1. Plots depicting structural and relaxation features of crystalline, liquid, and amorphous phases. A) Radial distribution plot of hypothetical material in liquid, crystal, and amorphous states. B) Heat capacity vs temperature of a hypothetical material in liquid, crystal, and amorphous states. Subfigure A) is adapted from Wang et al.[8] and Caffarena and Grigera[9] and B) is adapted from Kauzmann[7].

One illustration highlighting the enigmatic nature of glassy materials and the glass transition is the infamous "Kauzmann's paradox," so named after an apparent entropic catastrophe first identified by Walter Kauzmann in 1947[7,12]. This paradox arises due to differences in the temperature dependence of the entropy of the crystalline solid and subcooled liquid, as well as the observation that T_g is not fixed but depends on the cooling rate. Namely, the entropy of the liquid decreases more rapidly upon cooling than that of the crystalline solid and the glass transition temperature is depressed as cooling is performed more slowly. Hence, if a subcooled liquid were to be cooled sufficiently slowly without crystallization occurring, extrapolating the entropy of this liquid suggests a finite temperature T_k where the subcooled liquid and crystalline solid curves would cross as well as a finite temperature where the entropy of the liquid would vanish, both of which violate the third law of thermodynamics[13]. These thermodynamic dilemmas are illustrated below in Figure 2.2. Various resolutions to this problem have been postulated, though the topic is still highly contentious in the field[14,15]. Such a challenging yet fundamental unanswered question underscores the complexity of amorphous materials and the difficulties faced by the community to deeply understand their characteristics and behavior.

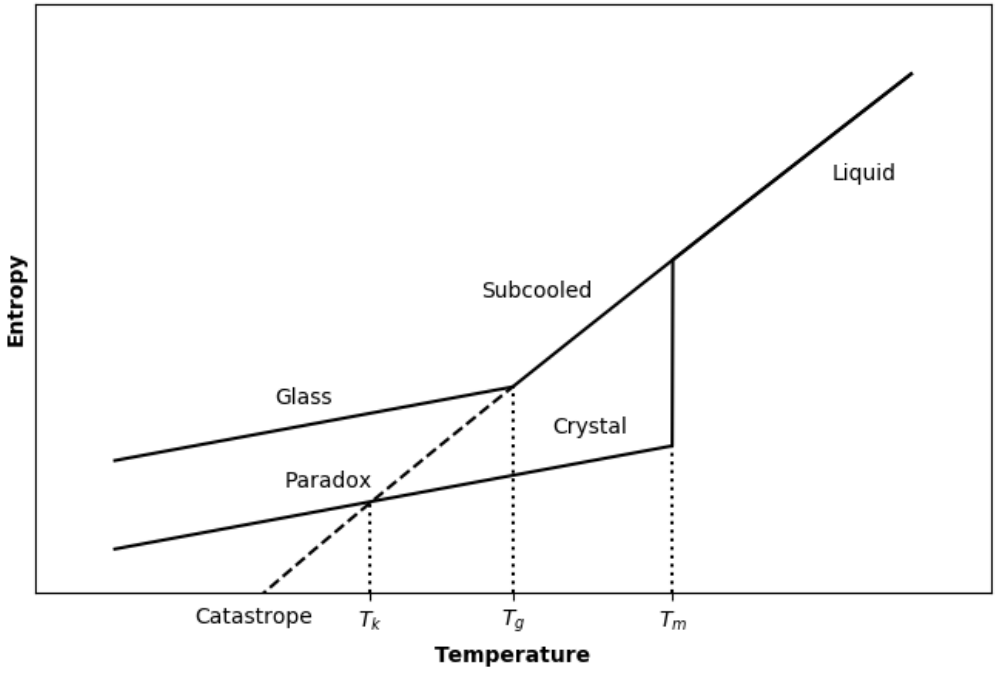

Figure 2.2. Excess entropy versus temperature for a hypothetical material demonstrating the Kauzmann paradox and zero entropy catastrophe. Image adapted from Rao, Bhat, and Kumar[16].

Another aspect of amorphous behavior which proves troublesome is the dependence on thermal/process history. Unlike a true thermodynamic state, the kinetic nature of glasses means that various properties which might impact physical or chemical utility such as density, heat capacity, glass transition temperature, and entropy, are path dependent (this can be seen, for instance, by the presence of multiple glass transitions in Figure 2.1B). Such path dependence is due to a functional loss of ergodicity, as a particular molecular configuration is kinetically frozen and the thermodynamically favorable state condition may not be accessible over relevant timescales[6]. Practically speaking, this implies that otherwise identical amorphous formulations prepared under different conditions can exhibit markedly different product performance[17,18].

In addition to the aforementioned difficulties with understanding the amorphous state, amorphous materials also possess some generalized mechanical differences from their crystalline counterparts which can often lead to processing problems. For instance, the powder morphology of an amorphous solid tends to be less regular than that of a crystalline solid, which is known to impact powder flowability[19]. Furthermore, compacts of amorphous drug material are also generally more brittle than crystalline compacts, increasing the likelihood of product fracture[20]. Investigations of non-pharmacologically active glasses have found that the amorphous phase exhibits a reduced modulus and hardness compared to the crystalline form, rationalized by differences in structural relaxation mechanisms under strain[21]. Another challenging aspect of the properties of glasses relates to what is termed “fragility”, which is a direct consequence of the aforementioned arrested molecular relaxations. This term describes the tendency of many organic glasses to display strong non-linear deviation from the extrapolated behavior of supercooled-liquids, leading to dramatic physical property changes near the glass transition[4,22]. These property differences together contribute to manufacturability limitations which must be considered if amorphous solids are to be effectively employed in a pharmaceutical setting.

2.2 Pharmaceutical Applications of the Amorphous Phase

In spite of the challenges associated with the characterization and processing of amorphous materials, the potential benefits can sometimes outweigh the difficulties, and as such amorphous solids have seen use in pharmaceutical formulations. Perhaps the most attractive features of amorphous materials with respect to drug development are the enhanced dissolution rate and ability to generate supersaturation[23]. For oral formulations of lipophilic drug molecules which

suffer from poor aqueous solubility in the stable crystalline form, bioavailability is limited both by slow dissolution kinetics as well as a weak thermodynamic driving force for absorption caused by low free drug concentration[24]. While many formulation strategies have been explored to mitigate these concerns, dispersing drug molecules in a carrier matrix to leverage an amorphous drug character (known as an amorphous solid dispersion, or ASD) has been advocated from as early as 1971[25–27]. Amorphous solids, which dissolve more rapidly than crystalline solids and generate solutions with a higher chemical potential than the saturated solutions from crystal dissolution, can leverage these physiochemical advantages synergistically for markedly improved oral bioavailability[28,29]. For instance, experimental solubility and dissolution studies of indomethacin have demonstrated a 5-fold increase in maximum solubility as well as a 2-fold increase in dissolution rate for the amorphous form compared to the stable crystalline form[30]. Graphically, these findings are depicted in Figure 2.3. Supersaturation generated during amorphous dissolution leads to enhanced absorption, as a well-documented linear relationship exists between degree of supersaturation and transport of drug into the bloodstream[28,31]. Other *in vivo* studies of amorphous pharmaceutical formulations likewise find 5 to 10-fold increases in oral bioavailability over crystalline drug formulations, explained primarily by the ability to maintain higher free drug concentration over time scales relevant for intestinal absorption[32]. Indeed, ASDs demonstrate sufficient utility such that at least 10 different formulations are commercially available, though far more have been developed and studied[33]. Theoretical calculations and *in vitro* dissolution experiments comparing amorphous and crystalline solubility are plentiful and demonstrate widely varying solubility enhancement from 1.1 to over 1500 fold, though it should be noted that theoretical predictions often greatly overestimate the experimental results[34]. Challenges with reconciling predictions and measurements are principally due to two underlying problems: difficulties with properly accounting for the activity of drug molecules in solution (thermodynamic) and crystallization during measurements preventing the "equilibration" of amorphous solids (kinetic)[35,36]. An example of crystallization preventing true "equilibration" of the amorphous form is illustrated in Figure 2.3A, where the solid circles representing amorphous indomethacin initially achieve high aqueous solubility (up to 5 times the crystalline solubility at 20 minutes) but over time de-supersaturate (down to 2 times the crystalline solubility by 80 minutes) as solution crystallization

takes place. While the first limitation is largely academic in nature, this second limitation poses a far more ubiquitous problem, which will be discussed at length in Section 2.3.

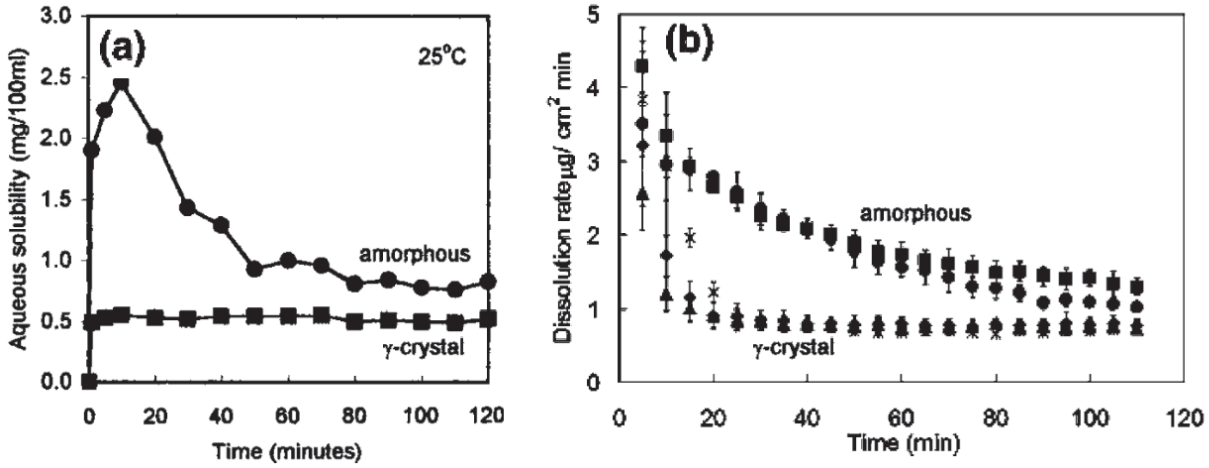

Figure 2.3. Plots depicting the solubility (A) and dissolution rates (B) of amorphous and crystalline indomethacin. Data are reproduced from Babu and Nangia[30].

2.3 Stability of Amorphous Formulations

Many potential failure mechanisms exist which can lead to underperformance of amorphous formulations. Solid-state homogeneity (that is, that the API exists entirely as amorphous or as an identical crystalline form) is critical to consistent performance; hence, unintended incorporation of crystals in an ASD or amorphous content in a crystalline formulation often spells disaster. For instance, process methods such as milling can introduce partial amorphous character into crystalline formulations, which can lead to a variety of issues in formulation, processing, manufacturing, and product performance[37,38]. On the other hand, processing methods can also leave residual crystallinity in an amorphous formulation, which reduces the theoretical solubility advantage of the ASD, speeds aging and solid-state crystallization during storage, and can even result in de-supersaturation due to seeded crystal growth from solution[18,39,40].

Chemical stability is always of great concern when considering materials of high free energy, and indeed chemical degradation limits the manufacturability of many potential formulations[41,42]. Both polymer and drug molecules risk undergoing thermal degradation during hot melt extrusion (one of the more popular manufacturing methods of solid dispersions),

requiring clever process and product design techniques to ensure product purity and performance[43]. Even solution-processed dispersions are not immune to chemical degradation, as solid-state reactions have been reported to take place between drug and polymer in spray dried ASDs, especially when exposed to elevated temperature or humidity during storage[44]. Temperature and humidity also accentuates physical stability issues, as both factors enhance molecular mobility, leading to more rapid reaction kinetics, phase separation and crystallization[45,46].

Physical stability limitations can affect ASDs throughout the entire lifecycle of the product, from manufacturing all the way through dosing. In general, when speaking of physical stability of ASDs the primarily instability in mind is crystallization of the API. Broadly speaking, crystallization of amorphous pharmaceutical formulations is understood to proceed via two routes; first, de-mixing and phase separation of the solid ASD during manufacturing and storage leads to unstabilized amorphous API which has a propensity to undergo solid-state crystallization and second, supersaturated solutions during dissolution can exhibit a solution-mediated nucleation and growth phenomenon[47,48]. Typically, it is assumed that the solid-state phase transition only occurs during storage (though, as will be discussed in section 2.4 this is not strictly true for highly supersaturating formulations), such that preventing phase separation before dosing is sufficient[49]. Phase separation between drug and polymer is governed by many factors, though it is primarily a miscibility problem; stability is contingent on molecular level mixing which requires thermodynamic miscibility[50,51]. Miscibility can be affected by parameters such as polymer selection, drug loading, temperature, and the introduction of moisture which can disrupt drug-polymer interactions[52–56]. Two thermodynamic features of import are configurational enthalpy and entropy, which capture the molecular thermodynamics related to orientation and the ability of the system to sample various configurations to achieve a minimized free energy[10]. Specifically, configuration entropy captures the entropic barrier to rearrangement necessary to achieve crystallization, which strongly correlates with the crystallization tendency of amorphous materials[57,58]. Evidence suggests intimate drug-polymer mixing can significantly enhance configurational entropy, though even when phase separation occurs this quantity can still be a deciding factor when determining if crystallization will procede[59]. In addition to thermodynamics, kinetic factors must be considered when assessing the timescale of phase separation and/or crystallization. In the solid state, kinetics are largely governed by the molecular

mobility, which describes the rate of relevant molecular motions required to undergo phase changes[60]. Given their similarities, it should come as no surprise that molecular mobility is intimately connected to configurational entropy[61]. Much like the thermodynamic quantities, crystallization tendency correlates to molecular mobility, and mobility is affected by environmental factors such as temperature and relative humidity[45,62–65]. Again, intimate mixing between drug and polymer decreases the molecular mobility of the amorphous phase and helps provide kinetic stabilization against any phase transformations even under thermodynamically unfavorable conditions[66].

Nucleation and growth from solution, the second primary physical instability, likewise has thermodynamic and kinetic factors to consider. Solution crystallization has long been leveraged for separation and purification in many fields including the pharmaceutical industry, and as such it has been widely studied[67]. Despite the prolific study, nucleation kinetics are still poorly understood with little experimentally or theoretically rigorous studies, such that most work in this area is computational in nature[68]. Crystal growth kinetics are dictated by the rate of the relevant steps: diffusion of a molecule through solution towards a crystal face and subsequent attachment to the face, diffusion along the surface to a high energy site (generally a kink or other defect), and incorporation into the lattice at that site[69,70]. Each of these can potentially be a bottleneck for crystal growth depending on the specific conditions of the system. The main thermodynamic feature driving nucleation and growth is supersaturation, or the extent to which the chemical potential of dissolved drug in solution is greater than thermodynamic equilibrium[71]. The relationship between supersaturation and crystal growth is sufficiently well understood that industrial processes can be designed to tune supersaturation in order to engineer crystal qualities of interest, such as shape or size[72,73]. Nucleation, on the other hand, is far more complex, though considerable insights have been made into fundamental understandings of nucleation theory in controlled environments[74–76]. However, a dosing environment is not controlled, and the aim is not crystal engineering but the complete inhibition of any crystal nucleation or growth. Moreover, little can be done from a macroscopic thermodynamic perspective, as the aim of generating high supersaturation for enhanced bioavailability runs directly contrary to the low supersaturation needed to mitigate crystallization out of solution. There is some evidence to suggest that delayed release formulations can maintain supersaturation by generating it more slowly, though even this turns out to be kinetic control more than thermodynamic[77]. Hence, the mostly widely accepted

means of preventing crystallization from solution is the use of crystallization inhibitors. Growth inhibition via surface poisoning by additives was identified accidentally as early as 1965 and has been studied for over three decades[78,79]. Many of the polymeric species used as carriers in ASD formulations can also act as nucleation or growth inhibitors by interacting with dissolved API molecules or small drug aggregates to prevent the formation of stable nuclei or by adsorbing onto crystal faces and sterically blocking crystal growth[80–83]. Mathematical determination of growth kinetics in the presence of additives is well developed, with good agreement between experiments and theory[84–86].

2.4 Liquid-Liquid Phase Separation

One important thermodynamic feature with significant implications when considering the phase behavior of amorphous drugs during dosing is liquid-liquid phase separation (LLPS) or glass-liquid phase separation (GLPS). Note that terms are functionally interchangeable, as the only distinction is the precise state of the second liquid-like phase and if this phase is above or below its glass transition and henceforth LLPS shall be used. LLPS is a phase separation event which occurs when a miscibility limit is reached of a solute in a solvent, resulting in a colloidally dispersed dense liquid-like phase (rich in solute) and a dilute phase (lean in solute)[87]. In the context of poorly soluble drugs, this miscibility limit is often termed the "amorphous solubility", as it represents the theoretical maximum concentration achievable if attempting to equilibrate the amorphous phase with dissolution media in the absence of crystallization[88]. Thus, highly supersaturating formulations of slowly crystallizing drugs or weakly basic compounds that undergo a significant solubility change upon exiting the stomach and entering the intestinal tract can achieve this amorphous solubility and undergo an LLPS event[89]. While research into the implication of LLPS is still ongoing, there is good evidence to suggest that it is beneficial to formulation performance by providing a reservoir of free drug at a high chemical potential to ensure maximum flux across cell membranes for uptake by the body[31,90]. However, one challenge raised by LLPS is the formation of high energy drug-rich amorphous interfaces exposed to dissolution media which are no longer intimately mixed with the polymer matrix from the ASD. As has been discussed at length in Section 2.3, intimate mixing between drug and polymer is important for inhibiting the solid-state crystallization, which is made all the more

likely by the plasticizing effect of water. Thus, drug-rich colloids pose a high risk of undergoing solid-state crystallization and subsequent loss of formulation performance.

2.5 Materials

The model pharmaceutical compound utilized throughout these studies was free-base atazanavir (ATZ), purchased from Attix Pharmaceuticals (Toronto, Canada). In a clinical setting, ATZ is an HIV-1 protease inhibitor indicated for the treatment of HIV/AIDS[91]. It is among those antiretroviral medications listed in the World Health Organization List of Essential Medicines, demonstrating its importance to the global medical community in the battle to end HIV and AIDS[92]. Commercial formulations utilize the sulfate or bisulfate salt form of ATZ, which exhibits slight aqueous solubility (4-5 mg/mL at pH 1.9)[93]. However, the free-base form studied here exhibits a crystalline solubility of only about 1 µg/mL, placing it in the category of molecules suffering from solubility limitations[89]. From a bench-top pharmaceutical research perspective, ATZ is a useful compound for crystallization studies as it is known to crystallize slowly, providing ample time to examine the amorphous to crystalline phase transformation[89]. Furthermore, given that ATZ is a weakly-basic drug (pK_a of the strongest base is 4.5), it is among those molecules expected to be soluble in the acidic gastric environment yet poorly soluble and rapidly supersaturated to the amorphous solubility limit upon entering the higher pH of the intestinal tract[89]. This in turn makes ATZ among those at-risk API molecules which can undergo an uncontrolled glass-liquid phase separation event, resulting in poorly stabilized drug-rich nanodroplets with a propensity to crystallize and deteriorate the formulation performance.

Various model additive species were considered in these studies with the intent of elucidating possible mechanisms of crystallization promotion and inhibition. Crystallization inhibition was studied through the incorporation of hydroxypropyl methylcellulose acetate succinate (HPMCAS), purchased from Shin Etsu Chemical (Tokyo, Japan) in both HF and MF grades. HPMCAS is a cellulose-derivative polymer often included in formulations which is known in many instances to inhibit crystallization, although its mechanism of action is still not entirely understood[94]. The grading of HPMCAS is due to the variability in substitutions of the acetate and succinate functional groups, where the HF grade contains a higher ratio of acetate to succinate, resulting in increased hydrophobicity as compared to the MF grade. While not employed in crystallization studies, reference measurements studying polymer interaction with

amorphous drug films also utilized two additional polymer species to explore a wider range of hydrophobicity. Polyvinylpyrollidone (PVP) purchased from Sigma-Aldrich (St. Louis, MO) and polyvinyl acetate (PVAc) purchased from Polysciences, Inc. (Warrington, PA) provided an experimental space with greater hydrophilicity and greater hydrophobicity than the cellulose-derived species[95]. Promotion of crystallization was probed via sodium dodecyl sulfate (SDS), purchased from Sigma-Aldrich (St. Louis, MO). SDS is a common surfactant which is occasionally included as an excipient in pharmaceutical formulations and which is known in some instances to hasten crystallization[96,97].

2.6 Methods

2.6.1 Atomic Force Microscopy

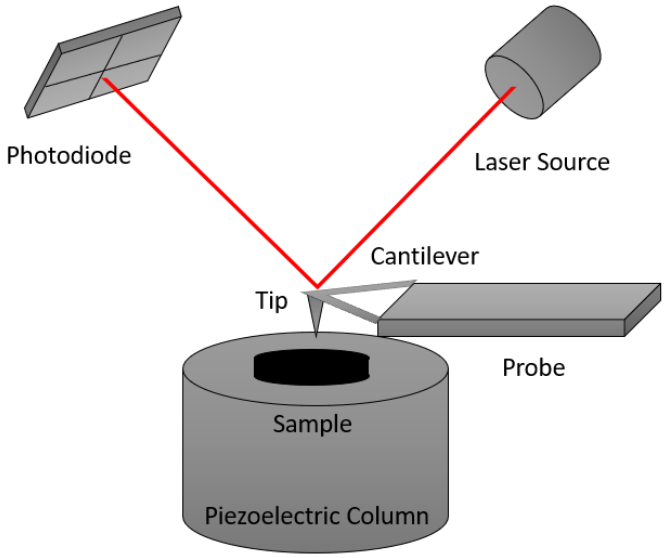

Figure 2.4. Schematic of an atomic force microscope. Adapted from Butt et al[98].

Atomic force microscopy (AFM) is a hybrid technique employing concepts of stylus profilometry and scanning tunneling microscopy first reported in 1986[99]. Since its inception, it has undergone various technological advances and successful implementation in a broad variety of applications. Generally speaking, AFM involves sensitive measurements of the interaction between a probe and sample to determine various topographical, mechanical, electrical, and/or

chemical properties of the sample surface. Modern AFM instrumentation consists of three main subsystems, depicted in Figure 2.4. A piezoelectric crystal acts as a scanner to control both the lateral position of the sample as well as probe/sample separation distance. Above the sample is the probe which consists of a flexible cantilever beam with a sharp tip protruding below the beam towards the sample. Various surface forces, such as electrostatic attraction/repulsion, capillary forces, and van der Waals forces cause the cantilever to deflect, which is measured via a laser reflecting off the end of the beam[100]. These deflections can be used to map the topographical features of a surface and measure various surface forces and interactions[101,102]. Even simple topographical measurements can often be sufficient to study complex phenomena; for instance, AFM topographical maps are sensitive to small differences in crystal step height characteristic of different polymorphs and have been used to studying polymorphic transitions in real time[103,104].

Advanced AFM operating modes facilitate the interrogation of nuanced facets of surface characteristics, which have been previously leveraged to study pharmaceutical systems. For instance, tapping or intermittent contact mode involves forced resonance of the AFM cantilever at a high frequency, generally several orders of magnitude faster than data acquisition rates. Interactions between cantilever and sample result in energy dissipation, manifested through a lag in the response of the cantilever compared to the driving frequency (known as a phase lag). This dissipation and corresponding phase lag are affected by the specific tip-surface interaction, such that this measurement contains information about the chemical and mechanical properties of the surface[105]. Previously, this technique has been used in applications including discrimination between polymer and API for studies on ASD homogeneity as well as studies of polymer interactions with drug-rich phases[95,106–108]. Despite its utility, one limitation of this technique is that researchers must typically interpret the data qualitatively; although cantilever dynamics have been studied at length, mathematical interpretation is extremely complex as the behavior depends on myriad factors, often confounding results[109–111].

Another powerful AFM mode with greater quantitative power is nanomechanical mapping of a surface. This technique leverages the intermittent contact mode discussed previously and simultaneously collects information about the interaction force between tip and surface. Data on the interaction force allows for quantitative calculations of surface mechanical properties such as modulus, while the high rate of data acquisition allows for material properties to be mapped with

nanometer resolution rather than simply determined at a single location[112,113]. While slower and more involved than traditional AMF, such information has been used to distinguish between crystalline and amorphous phases with high fidelity, to observe nucleation of new crystalline phases, and even to visualize molecular diffusion[38,114–116]. Furthering the analysis by applying contact mechanics fundamentals can extend the insight into chemical information like surface energy, an important quantity in the context of this work[117].

2.6.2 Monte Carlo Modeling

Monte Carlo (MC) models are a broad class of numerical simulation techniques employing stochastic events to predict the outcome of deterministic phenomena[118]. Historically, statistical techniques to study complex physical systems have been employed as far back as famous 18th and 19th century experiments, such as "Buffon's needle" where Georges Louis LeClerc, Comte de Buffon used probabilistic methods to determine the value of pi[119]. Modern MC techniques, and in fact the name itself, can be attributed to Nicholas Metropolis, Stan Ulam, and John von Neumann who utilized statistical techniques and electronic computing to model complex nuclear physics events during the Manhattan Project[120,121]. While Monte Carlo methods vary in application and formulation, a general pattern is to model the system in terms of probabilities, sample from the distribution of possible events, and track a metric of interest[118,119]. Within the context of this work, this straightforward method has been successfully applied to gain insight into the structural packing of molecular amorphous materials and into mechanisms of surface crystal growth[122–126]. Practically speaking, MC formulation involves identifying trial moves a system can undergo as well as designating a mathematical description of the probability of any such event occurring. In the context of molecular simulations, this is generally achieved by determining the energy of the system and assessing probability based on energetic changes[11]. Expressed mathematically:

$$\varphi(x) = \exp(-\Delta G(x)) \tag{2.1}$$

Here, x is some trial move for the system, $\varphi(x)$ is the probability of accepting or rejecting x and $\Delta G(x)$ is the energy change associated with performing x. The greatest challenge to implementing Equation (2.1) is determining the energy of the system, which will typically require various assumptions and simplifications. The specific assumptions in the MC models presented here are discussed in each chapter individually and can be found in Section 3.2.6 and

Section 4.2.4. Complete computer code for each MC model is also available in Appendices B Appendix C.

2.6.3 Relaxation of Sinusoidal Film

Mathematical determination of underlying transport phenomena can be performed in a number of ways, and one technique to analyze the transport of films is by surface relaxation. Surface tension has been understood as a driving force for the minimization of free surface area since 1805 when Thomas Young and Pierre-Simon Laplace made pinnacle insights into the physics governing interfaces, which later were combined into the Young-Laplace equation by Carl Gauss in 1830[127–129]. Within this paradigm, the chemical driving force for a film is related to the local shape and curvature. If a film is patterned with a well-defined shape with easily determined curvature (such as a sinusoidal wave), the chemical potential (or pressure gradient) across the interface is easily determined at any point along the surface. So long as the surface is nearly planar, that is, that the curvature at any point is sufficiently small that linearization of the governing equations can be performed, the transport equations predicting the rate of surface decay towards a flat film can be solved analytically. Such determinations have been done previously, and a rigorous derivation is provided in Appendix A[130,131]. What results is a series of scaling relationships between the intrinsic decay rate of the film and its wavelength based on Equation (2.2) and Equation (2.3)

$$h(t) = \alpha \exp(-Kt) \tag{2.2}$$

and

$$K = F\omega + (A + C)\omega^3 + B\omega^4 \tag{2.3}$$

where

$$\omega = \frac{2\pi}{\lambda} \qquad F = \frac{\gamma}{2\eta}$$

$$A = \frac{c_0 \gamma \Omega^2 D_l}{kT} \qquad C = \frac{D_b \gamma \Omega}{kT} \qquad B = \frac{\nu D_s \gamma \Omega^2}{kT}$$

Here, h is the surface height of the film, t is time, α is the amplitude of the sine wave, K is the decay constant, λ is the wavelength of the film, γ is the surface energy, η is the viscosity, c_0 is the solute concentration above the film, Ω is the molecular volume, m is the molecular mass, k is Boltzmann's constant, T is temperature, D_l is the diffusion coefficient of solute in solution, D_b is

the bulk diffusion coefficient, and D_s is the surface diffusion coefficient. The terms in Equation (2.3) correspond to viscous flow (*F*), dissolution and deposition (*A*), bulk diffusion (*C*) and surface diffusion (*B*). Practically speaking, if one performs a series of decay measurements for films of different wavelengths and extracts the decay constants by fitting the measured height data to Equation (2.2), a plot of the logarithm of the decay constant against the logarithm of the wavelength will yield a linear relationship, where the slope corresponds to the dominant decay mechanism[132]. Hence, a slope of 1 would indicate viscous flow dominates, a slope of 3 indicates bulk diffusion and/or dissolution and deposition, and a slope of 4 indicates surface diffusion.

2.7 References

(1) Stillinger, F. H.; Debenedetti, P. G. Phase Transitions, Kauzmann Curves, and Inverse Melting. *Biophys. Chem.* **2003**, *105* (2–3), 211–220. https://doi.org/10.1016/S0301-4622(03)00089-9.

(2) Gotze, W.; Sjogren, L. Relaxation Processes in Supercooled Liquids. *Reports Prog. Phys.* **1992**, *55*, 241–376.

(3) Jackson, K. A. Nucleation from the Melt. *Ind. Eng. Chem.* **1965**, *57* (12), 29–32.

(4) Angell, C. A. Formation of Glasses from Liquids and Biopolymers. *Science (80-.).* **1995**, *267*, 1924–1935. https://doi.org/10.1126/science.267.5206.1924.

(5) Bengtzelius, U.; Gotze, W.; Sjolander, A. Dynamics of Supercooled Liquids and the Glass Transition. *J. Phys. C Solid State Phys.* **1984**, *17*, 5915–5934.

(6) Ediger, M. D.; Angell, C. A.; Nagel, S. R. Supercooled Liquids and Glasses. *J. Phys. Chem.* **1996**, *100*, 13200–13212.

(7) Kauzmann, W. The Nature of the Glassy State and the Behavior of Liquids at Low Temperatures. *Chem. Rev.* **1948**, *43*, 219–256. https://doi.org/10.1021/cr60135a002.

(8) Wang, J.; Fang, F.; Zhang, X. Nanometric Cutting of Silicon with an Amorphous-Crystalline Layered Structure: A Molecular Dynamics Study. *Nanoscale Res. Lett.* **2017**, *12* (41). https://doi.org/10.1186/s11671-017-1829-y.

(9) Caffarena, E.; Grigera, J. R. Crystal, Melted and Glassy States of Glucose. A Molecular Dynamics Simulation. *J. Chem. Soc. - Faraday Trans.* **1996**, *92* (12), 2285–2289. https://doi.org/10.1039/ft9969202285.

(10) Tester, J. W.; Modell, M. *Thermodynamics and Its Applications*, 3rd ed.; Prentice Hall: Upper Saddle River, NJ, 1997.

(11) McQuarrie, D. A. *Statistical Mechanics*; 1976.

(12) Woodcock, L. V. Glass Transition in the Hard-Sphere Model and Kauzmann's Paradox. *Ann. N. Y. Acad. Sci.* **1981**, *371* (1), 274–298. https://doi.org/10.1111/j.1749-6632.1981.tb55667.x.

(13) Speedy, R. J. Kauzmann's Paradox and the Glass Transition. *Biophys. Chem.* **2003**, *105* (2–3), 411–420. https://doi.org/10.1016/S0301-4622(03)00105-4.

(14) Stillinger, F. H.; Debenedetti, P. G.; Truskett, T. M. The Kauzmann Paradox Revisited. *J. Phys. Chem. B* **2001**, *105* (47), 11809–11816. https://doi.org/10.1021/jp011840i.

(15) Beasley, M. S.; Bishop, C.; Kasting, B. J.; Ediger, M. D. Vapor-Deposited Ethylbenzene Glasses Approach "Ideal Glass" Density. *J. Phys. Chem. Lett.* **2019**, *10* (14), 4069–4075. https://doi.org/10.1021/acs.jpclett.9b01508.

(16) Rao, K. J.; Bhat, M. H.; Kumar, S. Fragility Thy Name Is Glass. *J. Indian Inst. Sci.* **2001**, *81* (1), 3–13.

(17) Karmwar, P.; Graeser, K.; Gordon, K. C.; Strachan, C. J.; Rades, T. Investigation of Properties and Recrystallisation Behaviour of Amorphous Indomethacin Samples Prepared by Different Methods. *Int. J. Pharm.* **2011**, *417* (1–2), 94–100. https://doi.org/10.1016/j.ijpharm.2010.12.019.

(18) Yang, Z.; Nollenberger, K.; Albers, J.; Moffat, J.; Craig, D.; Qi, S. The Effect of Processing on the Surface Physical Stability of Amorphous Solid Dispersions. *Eur. J. Pharm. Biopharm.* **2014**, *88*, 897–908. https://doi.org/10.1016/j.ejpb.2014.07.013.

(19) Hou, H.; Sun, C. C. Quantifying Effects of Particulate Properties on Powder Flow Properties Using a Ring Shear Tester. *J. Pharm. Sci.* **2008**, *97* (9), 4030–4039. https://doi.org/10.1002/jps.21288.

(20) Hancock, B. C.; Carlson, G. T.; Ladipo, D. D.; Langdon, B. A.; Mullarney, M. P. Comparison of the Mechanical Properties of the Crystalline and Amorphous Forms of a Drug Substance. *Int. J. Pharm.* **2002**, *241* (1), 73–85. https://doi.org/10.1016/S0378-5173(02)00133-3.

(21) Kulikovsky, V.; Vorlíček, V.; Boháč, P.; Stranyánek, M.; Čtvrtlík, R.; Kurdyumov, A. Mechanical Properties of Amorphous and Microcrystalline Silicon Films. *Thin Solid Films* **2008**, *516* (16), 5368–5375. https://doi.org/10.1016/j.tsf.2007.07.047.

(22) Angell, C. A. Relaxation in Liquids, Polymers and Plastic Crystals - Strong/Fragile Patterns and Problems. *J. Non. Cryst. Solids* **1991**, *131–133*, 13–31.

(23) Craig, D. Q. M.; Royall, P. G.; Kett, V. L.; Hopton, M. L. The Relevance of the Amorphous State to Pharmaceutical Dosage Forms: Glassy Drugs and Freeze Dried Systems. *Int. J. Pharm.* **1999**, *179*, 179–207. https://doi.org/10.1016/S0378-5173(98)00338-X.

(24) Dahan, A. S.; Amidon, G. L. Gastrointestinal Dissolution and Absorption of Class II Drugs. In *Drug Bioavailability: Estimation of Solubility, Permeability, Absorption and Bioavailability*; Han van des Waterbeemd, Bernard Testa, Eds.; 2009; pp 33–51. https://doi.org/10.1002/9783527623860.ch3.

(25) Chiou, W. L.; Riegelman, S. Pharmaceutical Applications of Solid Dispersion Systems. *J. Pharm. Sci.* **1971**, *60* (9), 1281–1302.

(26) Leuner, C.; Dressman, J. Improving Drug Solubility for Oral Delivery Using Solid Dispersions. *Eur. J. Pharm. Biopharm.* **2000**, *50* (1), 47–60. https://doi.org/10.1016/S0939-6411(00)00076-X.

(27) Williams, H. D.; Trevaskis, N. L.; Charman, S. A.; Shanker, R. M.; Charman, W. N.; Pouton, C. W.; Porter, C. J. H. Strategies to Address Low Drug Solubility in Discovery and Development. *Pharmacol. Rev.* **2013**, *65*, 315–499. https://doi.org/10.1124/pr.112.005660.

(28) Davis, A. F.; Hadgraft, J. Effect of Supersaturation on Membrane Transport: 1. Hydrocortisone Acetate. *Int. J. Pharm.* **1991**, *76*, 1–8. https://doi.org/10.1016/0378-5173(91)90337-N.

(29) Takano, R.; Takata, N.; Saito, R.; Furumoto, K.; Higo, S.; Hayashi, Y.; Machida, M.; Aso, Y.; Yamashita, S. Quantitative Analysis of the Effect of Supersaturation on in Vivo Drug Absorption. *Mol. Pharm.* **2010**, *7* (5), 1431–1440. https://doi.org/10.1021/mp100109a.

(30) Babu, N. J.; Nangia, A. Solubility Advantage of Amorphous Drugs and Pharmaceutical Cocrystals. *Cryst. Growth Des.* **2011**, *11*, 2662–2679. https://doi.org/10.1021/cg200492w.

(31) Taylor, L. S.; Zhang, G. G. Z. Physical Chemistry of Supersaturated Solutions and Implications for Oral Absorption. *Adv. Drug Deliv. Rev.* **2016**, *101*, 122–142. https://doi.org/10.1016/j.addr.2016.03.006.

(32) Gao, P.; Guyton, M. E.; Huang, T.; Bauer, J. M.; Stefanski, K. J.; Lu, Q. Enhanced Oral Bioavailability of a Poorly Water Soluble Drug PNU-91325 by Supersaturatable Formulations. *Drug Dev. Ind. Pharm.* **2004**, *30* (2), 221–229. https://doi.org/10.1081/DDC-120028718.

(33) Van Den Mooter, G. The Use of Amorphous Solid Dispersions: A Formulation Strategy to Overcome Poor Solubility and Dissolution Rate. *Drug Discov. Today Technol.* **2012**, *9* (2), e79–e85. https://doi.org/10.1016/j.ddtec.2011.10.002.

(34) Hancock, B. C.; Parks, M. What Is the True Solubility Advantage for Amorphous Pharmaceuticals? *Pharm. Res.* **2000**, *17* (4), 397–404. https://doi.org/10.1023/A:1007516718048.

(35) Murdande, S. B.; Pikal, M. J.; Shanker, R. M.; Bogner, R. H. Solubility Advantage of Amorphous Pharmaceuticals: I. a Thermodynamic Analysis. *J. Pharm. Sci.* **2010**, *99* (3), 1254–1264. https://doi.org/10.1002/jps.21903.

(36) Paus, R.; Ji, Y.; Vahle, L.; Sadowski, G. Predicting the Solubility Advantage of Amorphous Pharmaceuticals: A Novel Thermodynamic Approach. *Mol. Pharm.* **2015**, *12*, 2823–2833. https://doi.org/10.1021/mp500824d.

(37) Ward, G. H.; Schultz, R. K. Process-Induced Crystallinity Changes in Albuterol Sulfate and Its Effect on Powder Physical Stability. *Pharmaceutical Research: An Official Journal of the American Association of Pharmaceutical Scientists*. 1995, pp 773–779. https://doi.org/10.1023/A:1016232230638.

(38) Tejedor, M. B.; Nordgren, N.; Schuleit, M.; Pazesh, S.; Alderborn, G.; Millqvist-Fureby, A.; Rutland, M. W. Determination of Interfacial Amorphicity in Functional Powders. *Langmuir* **2017**, *33*, 920–926. https://doi.org/10.1021/acs.langmuir.6b03969.

(39) Moseson, D. E.; Parker, A. S.; Beaudoin, S. P.; Taylor, L. S. Amorphous Solid Dispersions Containing Residual Crystallinity: Influence of Seed Properties and Polymer Adsorption on Dissolution Performance. *Eur. J. Pharm. Sci.* **2020**, *146* (February), 105276. https://doi.org/10.1016/j.ejps.2020.105276.

(40) Moseson, D. E.; Mugheirbi, N. A.; Stewart, A. A.; Taylor, L. S. Nanometer-Scale Residual Crystals in a Hot Melt Extruded Amorphous Solid Dispersion: Characterization by Transmission Electron Microscopy. *Cryst. Growth Des.* **2018**, *18* (12), 7633–7640. https://doi.org/10.1021/acs.cgd.8b01435.

(41) Pandi, P.; Bulusu, R.; Kommineni, N.; Khan, W.; Singh, M. Amorphous Solid Dispersions: An Update for Preparation, Characterization, Mechanism on Bioavailability, Stability, Regulatory Considerations and Marketed Products. *Int. J. Pharm.* **2020**, *586* (June), 119560. https://doi.org/10.1016/j.ijpharm.2020.119560.

(42) Liu, X.; Lu, M.; Guo, Z.; Huang, L.; Feng, X.; Wu, C. Improving the Chemical Stability of Amorphous Solid Dispersion with Cocrystal Technique by Hot Melt Extrusion. *Pharm. Res.* **2012**, *29* (3), 806–817. https://doi.org/10.1007/s11095-011-0605-4.

(43) Lakshman, J. P.; Cao, Y.; Kowalski, J.; Serajuddin, A. T. M. Application of Melt Extrusion in the Development of a Physically and Chemically Stable High-Energy Amorphous Solid Dispersion of a Poorly Water-Soluble Drug. *Mol. Pharm.* **2008**, *5* (6), 994–1002. https://doi.org/10.1021/mp8001073.

(44) Peng, T.; She, Y.; Zhu, C.; Shi, Y.; Huang, Y.; Niu, B.; Bai, X.; Pan, X.; Wu, C. Influence of Polymers on the Physical and Chemical Stability of Spray-Dried Amorphous Solid Dispersion: Dipyridamole Degradation Induced by Enteric Polymers. *AAPS PharmSciTech* **2018**, *19* (6), 2620–2628. https://doi.org/10.1208/s12249-018-1082-4.

(45) Andronis, V.; Zografi, G. The Molecular Mobility of Supercooled Amorphous Indomethacin as a Function of Temperature and Relative Humidity. *Pharm. Res.* **1998**, *15* (6), 835–842.

(46) Crowley, K. J.; Zografi, G. Water Vapor Absorption into Amorphous Hydrophobic Drug/Poly(Vinylpyrrolidone) Dispersions. *J. Pharm. Sci.* **2002**, *91* (10), 2150–2165.

(47) Kou, X.; Zhou, L. Stability of Amorphous Solid Dispersion. In *Amorphous Solid Dispersions*; 2014; pp 515–544. https://doi.org/10.1007/978-1-4939-1598-9_16.

(48) Hughey, J. R. Dissolution of Stabilized Amorphous Drug Formulations. In *Poorly Soluble Drugs: Dissolution and Drug Release*; Gregory K. Webster, J. Derek Jackson, Robert G. Bell, Eds.; 2017; pp 393–418.

(49) Edueng, K.; Mahlin, D.; Larsson, P.; Bergström, C. A. S. Mechanism-Based Selection of Stabilization Strategy for Amorphous Formulations: Insights into Crystallization Pathways. *J. Control. Release* **2017**, *256*, 193–202. https://doi.org/10.1016/j.jconrel.2017.04.015.

(50) Rumondor, A. C. F.; Ivanisevic, I.; Bates, S.; Alonzo, D. E.; Taylor, L. S. Evaluation of Drug-Polymer Miscibility in Amorphous Solid Dispersion Systems. *Pharm. Res.* **2009**, *26* (11), 2523–2534. https://doi.org/10.1007/s11095-009-9970-7.

(51) Qian, F.; Huang, J.; Hussain, M. A. Drug-Polymer Solubility and Miscibility: Stability Consideration and Practical Challenges in Amorphous Solid Dispersion Development. *J. Pharm. Sci.* **2010**, *99* (7), 2941–2947. https://doi.org/10.1002/jps.22074.

(52) Chen, Y.; Liu, C.; Chen, Z.; Su, C.; Hageman, M.; Hussain, M.; Haskell, R.; Stefanski, K.; Qian, F. Drug-Polymer-Water Interaction and Its Implication for the Dissolution Performance of Amorphous Solid Dispersions. *Mol. Pharm.* **2015**, *12*, 576–589. https://doi.org/10.1021/mp500660m.

(53) Rumondor, A. C. F.; Stanford, L. A.; Taylor, L. S. Effects of Polymer Type and Storage Relative Humidity on the Kinetics of Felodipine Crystallization from Amorphous Solid Dispersions. *Pharm. Res.* **2009**, *26* (12), 2599–2606. https://doi.org/10.1007/s11095-009-9974-3.

(54) Aucamp, M.; Milne, M.; Liebenberg, W. Amorphous Sulfadoxine: A Physical Stability and Crystallization Kinetics Study. *AAPS PharmSciTech* **2016**, *17* (5), 1100–1109. https://doi.org/10.1208/s12249-015-0436-4.

(55) Li, N.; Gilpin, C. J.; Taylor, L. S. Understanding the Impact of Water on the Miscibility and Microstructure of Amorphous Solid Dispersions: An AFM–LCR and TEM–EDX Study. *Mol. Pharm.* **2017**, *14*, 1691–1705. https://doi.org/10.1021/acs.molpharmaceut.6b01151.

(56) Li, N.; Taylor, L. S. Nanoscale Infrared, Thermal, and Mechanical Characterization of Telaprevir-Polymer Miscibility in Amorphous Solid Dispersions Prepared by Solvent Evaporation. *Mol. Pharm.* **2016**, *13*, 1123–1136. https://doi.org/10.1021/acs.molpharmaceut.5b00925.

(57) Zhou, D.; Zhang, G. G. Z.; Law, D.; Grant, D. J. W.; Schmitt, E. A. Physical Stability of Amorphous Pharmaceuticals: Importance of Configurational Thermodynamic Quantities and Molecular Mobility. *J. Pharm. Sci.* **2002**, *91* (8), 1863–1872. https://doi.org/10.1002/jps.10169.

(58) Graeser, K. A.; Patterson, J. E.; Zeitler, J. A.; Rades, T. The Role of Configurational Entropy in Amorphous Systems. *Pharmaceutics* **2010**, *2* (2), 224–244. https://doi.org/10.3390/pharmaceutics2020224.

(59) Baird, J. A.; Taylor, L. S. Evaluation of Amorphous Solid Dispersion Properties Using Thermal Analysis Techniques. *Adv. Drug Deliv. Rev.* **2012**, *64* (5), 396–421. https://doi.org/10.1016/j.addr.2011.07.009.

(60) Hancock, B. C.; Shamblin, S. L.; Zografi, G. Molecular Mobility of Amorphous Pharmaceutical Solids below Their Glass Transition Temperatures. *Pharm. Res.* **1995**, *12* (6), 799–806. https://doi.org/10.1023/A:1016292416526.

(61) Shamblin, S. L.; Tang, X.; Chang, L.; Hancock, B. C.; Pikal, M. J. Characterization of the Time Scales of Molecular Motion in Pharmaceutically Important Glasses. *J. Phys. Chem. B* **1999**, *103* (20), 4113–4121. https://doi.org/10.1021/jp983964+.

(62) Knapik, J.; Wojnarowska, Z.; Grzybowska, K.; Hawelek, L.; Sawicki, W.; Wlodarski, K.; Markowski, J.; Paluch, M. Physical Stability of the Amorphous Anticholesterol Agent (Ezetimibe): The Role of Molecular Mobility. *Mol. Pharm.* **2014**, *11*, 4280–4290. https://doi.org/10.1021/mp500498e.

(63) Zhou, D.; Zhang, G. G. Z.; Law, D.; Grant, D. J. W.; Schmitt, E. A. Thermodynamics, Molecular Mobility and Crystallization Kinetics of Amorphous Griseofulvin. *Mol. Pharm.* **2008**, *5* (6), 927–936. https://doi.org/10.1021/mp800169g.

(64) Mehta, M.; Kothari, K.; Ragoonanan, V.; Suryanarayanan, R. Effect of Water on Molecular Mobility and Physical Stability of Amorphous Pharmaceuticals. *Mol. Pharm.* **2016**, *13* (4), 1339–1346. https://doi.org/10.1021/acs.molpharmaceut.5b00950.

(65) Bhugra, C.; Pikal, M. J. Role of Thermodynamic, Molecular, and Kinetic Factors in Crystallization from the Amorphous State. *J. Pharm. Sci.* **2008**, *97* (4), 1329–1349. https://doi.org/10.1002/jps.21138.

(66) Miyazaki, T.; Yoshioka, S.; Aso, Y.; Kojima, S. Ability of Polyvinylpyrrolidone and Polyacrylic Acid to Inhibit the Crystallization of Amorphous Acetaminophen. *J. Pharm. Sci.* **2004**, *93* (11), 2710–2717. https://doi.org/10.1002/jps.20182.

(67) Mohan, R.; Myerson, A. S. Growth Kinetics: A Thermodynamic Approach. *Chem. Eng. Sci.* **2002**, *57*, 4277–4285. https://doi.org/10.1016/S0009-2509(02)00344-5.

(68) Kashchiev, D.; Vekilov, P. G.; Kolomeisky, A. B. Kinetics of Two-Step Nucleation of Crystals. *J. Chem. Phys.* **2005**, *122*, 244706:1-6. https://doi.org/10.1063/1.1943389.

(69) Olafson, K. N.; Ketchum, M. A.; Rimer, J. D.; Vekilov, P. G. Molecular Mechanisms of Hematin Crystallization from Organic Solvent. *Cryst. Growth Des.* **2015**, *15*, 553–5542. https://doi.org/10.1021/acs.cgd.5b01157.

(70) Vekilov, P. G. What Determines the Rate of Growth of Crystals from Solution? *Cryst. Growth Des.* **2007**, *7* (12), 2796–2810. https://doi.org/10.1021/cg070427i.

(71) Mullin, J. W.; Sohnel, O. Expressions of Supersaturation in Crystallization Studies. *Chem. Eng. Sci.* **1977**, *32*, 683–686. https://doi.org/10.1016/0009-2509(77)80114-0.

(72) Nagy, Z. K.; Braatz, R. D. Advances and New Directions in Crystallization Control. *Annu. Rev. Chem. Biomol. Eng.* **2012**, *3* (1), 55–75. https://doi.org/10.1146/annurev-chembioeng-062011-081043.

(73) Nagy, Z. K. Crystallization Control Approaches and Models. In *Engineering Crystallography: From Molecule to Crystal to Functional Form*; 2017; pp 289–300. https://doi.org/10.1007/978-94-024-1117-1.

(74) De Yoreo, J. J.; Vekilov, P. G. Principles of Crystal Nucleation and Growth. *Rev. Mineral. Geochemistry* **2003**, *54* (1), 57–93.

(75) Vekilov, P. G. Nucleation. *Cryst. Growth Des.* **2010**, *10*, 5007–5019. https://doi.org/10.1021/cg1011633.

(76) Vekilov, P. G. Nucleation of Crystals in Solution. *AIP Conf. Proc.* **2010**, *1270*, 60–77. https://doi.org/10.1063/1.3476239.

(77) Sun, D. D.; Lee, P. I. Evolution of Supersaturation of Amorphous Pharmaceuticals: The Effect of Rate of Supersaturation Generation. *Mol. Pharm.* **2013**, *10*, 4330–4346. https://doi.org/10.1021/mp400439q.

(78) Holder, G. A.; Winkler, J. Crystal-Growth Poisoning of n-Paraffin Wax By Polymeric Additives and Its Relevance to Polymer Crystallization Mechanisms. *Nature* **1965**, *207* (4998), 719–721. https://doi.org/10.1038/207719a0.

(79) Black, S. N.; Davey, R. J.; Halcrow, M. The Kinetics of Crystal Growth in the Presence of Tailor-Made Additives. *J. Cryst. Growth* **1986**, *79*, 765–774. https://doi.org/10.1016/0022-0248(86)90552-X.

(80) Schram, C. J.; Beaudoin, S. P.; Taylor, L. S. Impact of Polymer Conformation on the Crystal Growth Inhibition of a Poorly Water-Soluble Drug in Aqueous Solution. *Langmuir* **2015**, *31*, 171–179. https://doi.org/10.1021/la503644m.

(81) Schram, C. J.; Beaudoin, S. P.; Taylor, L. S. Polymer Inhibition of Crystal Growth by Surface Poisoning. *Cryst. Growth Des.* **2016**, *16*, 2094–2103. https://doi.org/10.1021/acs.cgd.5b01779.

(82) Mosquera-Giraldo, L. I.; Borca, C. H.; Parker, A. S.; Dong, Y.; Edgar, K. J.; Beaudoin, S. P.; Slipchenko, L. V.; Taylor, L. S. Crystallization Inhibition Properties of Cellulose Esters and Ethers for a Group of Chemically Diverse Drugs: Experimental and Computational Insight. *Biomacromolecules* **2018**, *19* (12), 4593–4606. https://doi.org/10.1021/acs.biomac.8b01280.

(83) Ilevbare, G. A.; Liu, H.; Edgar, K. J.; Taylor, L. S. Inhibition of Solution Crystal Growth of Ritonavir by Cellulose Polymers – Factors Influencing Polymer Effectiveness. *CrystEngComm* **2012**, *14*, 6503–6514. https://doi.org/10.1039/c2ce25515d.

(84) Kubota, N.; Mullin, J. W. A Kinetic Model for Crystal Growth from Aqueous Solution in the Presence of Impurity. *J. Cryst. Growth* **1995**, *152*, 203–208.

(85) Kubota, N.; Yokota, M.; Mullin, J. W. Combined Influence of Supersaturation and Impurity Concentration on Crystal Growth. *J. Cryst. Growth* **2000**, *212*, 480–488. https://doi.org/10.1016/S0022-0248(00)00339-0.

(86) Kubota, N. Effect of Impurities on the Growth Kinetics of Crystals. *Cryst. Res. Technol.* **2001**, *36* (8–10), 749–769. https://doi.org/10.1002/1521-4079(200110)36:8/10<749::AID-CRAT749>3.0.CO;2-#.

(87) Alberti, S.; Gladfelter, A.; Mittag, T. Considerations and Challenges in Studying Liquid-Liquid Phase Separation and Biomolecular Condensates. *Cell* **2019**, *176* (3), 419–434. https://doi.org/10.1016/j.cell.2018.12.035.

(88) Ilevbare, G. A.; Taylor, L. S. Liquid-Liquid Phase Separation in Highly Supersaturated Aqueous Solutions of Poorly Water-Soluble Drugs: Implications for Solubility Enhancing Formulations. *Cryst. Growth Des.* **2013**, *13*, 1497–1509. https://doi.org/10.1021/cg301679h.

(89) Indulkar, A. S.; Box, K. J.; Taylor, R.; Ruiz, R.; Taylor, L. S. PH-Dependent Liquid-Liquid Phase Separation of Highly Supersaturated Solutions of Weakly Basic Drugs. *Mol. Pharm.* **2015**, *12* (7), 2365–2377. https://doi.org/10.1021/acs.molpharmaceut.5b00056.

(90) Indulkar, A. S.; Gao, Y.; Raina, S. A.; Zhang, G. G. Z.; Taylor, L. S. Exploiting the Phenomenon of Liquid-Liquid Phase Separation for Enhanced and Sustained Membrane Transport of a Poorly Water-Soluble Drug. *Mol. Pharm.* **2016**, *13* (6), 2059–2069. https://doi.org/10.1021/acs.molpharmaceut.6b00202.

(91) Fan, X.; Song, Y.; Long, Y. An Efficient and Practical Synthesis of the HIV Protease Inhibitor Atazanavir via a Highly Diastereoselective Reduction Approach. *Org. Process Res. Dev.* **2008**, *12*, 69–75.

(92) Organization, W. H. *World Health Organization Model List of Essential Medicines, 21st List*; Geneva, 2019.

(93) Squibb, B.-M. Reyataz ® (Atazanavir) Capsules [Package Insert]. 2016, pp 1–85.

(94) Curatolo, W.; Nightingale, J. A.; Herbig, S. M. Utility of Hydroxypropylmethylcellulose Acetate Succinate (HPMCAS) for Initiation and Maintenance of Drug Supersaturation in the GI Milieu. *Pharm. Res.* **2009**, *26* (6), 1419–1431. https://doi.org/10.1007/s11095-009-9852-z.

(95) Schram, C. J.; Taylor, L. S.; Beaudoin, S. P. Influence of Polymers on the Crystal Growth Rate of Felodipine: Correlating Adsorbed Polymer Surface Coverage to Solution Crystal Growth Inhibition. *Langmuir* **2015**, *31*, 11279–11287. https://doi.org/10.1021/acs.langmuir.5b02486.

(96) Chen, J.; Ormes, J. D.; Higgins, J. D.; Taylor, L. S. Impact of Surfactants on the Crystallization of Aqueous Suspensions of Celecoxib Amorphous Solid Dispersion Spray Dried Particles. *Mol. Pharm.* **2015**, *12* (2), 533–541. https://doi.org/10.1021/mp5006245.

(97) Schram, C. J. Impact of Polymers on the Solution Crystal Growth Rate of a Poorly Water-Soluble Active Pharmaceutical Ingredient, Purdue University, 2016.

(98) Butt, H.-J.; Cappella, B.; Kappl, M. Force Measurements with the Atomic Force Microscope: Technique, Interpretation and Applications. *Surf. Sci. Rep.* **2005**, *59* (1–6), 1–152. https://doi.org/10.1016/j.surfrep.2005.08.003.

(99) Binnig, G.; Quate, C. F.; Gerber, C. H. Atomic Force Microscope. *Phys. Rev. Lett.* **1986**, *56* (9), 930–933.

(100) Cappella, B.; Dietler, G. Force-Distance Curves by Atomic Force Microscopy. *Surf. Sci. Rep.* **1999**, *34*, 1–104. https://doi.org/10.1016/S0167-5729(99)00003-5.

(101) Ducker, W. A.; Senden, T. J.; Pashley, R. M. Direct Measurement of Colloidal Forces Using an Atomic Force Microscope. *Nature* **1991**, *353*, 239–241. https://doi.org/10.1038/353239a0.

(102) Gan, Y. Atomic and Subnanometer Resolution in Ambient Conditions by Atomic Force Microscopy. *Surf. Sci. Rep.* **2009**, *64*, 99–121. https://doi.org/10.1016/j.surfrep.2008.12.001.

(103) Thakuria, R.; Eddleston, M. D.; Chow, E. H. H.; Lloyd, G. O.; Aldous, B. J.; Krzyzaniak, J. F.; Bond, A. D.; Jones, W. Use of in Situ Atomic Force Microscopy to Follow Phase Changes at Crystal Surfaces in Real Time. *Angew. Chemie - Int. Ed.* **2013**, *52*, 10541–10544. https://doi.org/10.1002/anie.201302532.

(104) Thakuria, R.; Eddleston, M. D.; Chow, E. H. H.; Taylor, L. J.; Aldous, B. J.; Krzyzaniak, J. F.; Jones, W. Comparison of Surface Techniques for the Discrimination of Polymorphs. *CrystEngComm* **2016**, *18*, 5296–5301. https://doi.org/10.1039/c6ce01096b.

(105) Babcock, K. L.; Prater, C. B. Phase Imaging: Beyond Topography. *Veeco Instruments, Inc.* 2004. https://doi.org/10.1017/CBO9781107415324.004.

(106) Lauer, M. E.; Siam, M.; Tardio, J.; Page, S.; Kindt, J. H.; Grassmann, O. Rapid Assessment of Homogeneity and Stability of Amorphous Solid Dispersions by Atomic Force Microscopy - from Bench to Batch. *Pharm. Res.* **2013**, *30*, 2010–2022. https://doi.org/10.1007/s11095-013-1045-0.

(107) Wyttenbach, N.; Janas, C.; Siam, M.; Lauer, M. E.; Jacob, L.; Scheubel, E.; Page, S. Miniaturized Screening of Polymers for Amorphous Drug Stabilization (SPADS): Rapid Assessment of Solid Dispersion Systems. *Eur. J. Pharm. Biopharm.* **2013**, *84*, 583–598. https://doi.org/10.1016/j.ejpb.2013.01.009.

(108) Lauer, M. E.; Grassmann, O.; Siam, M.; Tardio, J.; Jacob, L.; Page, S.; Kindt, J. H.; Engel, A.; Alsenz, J. Atomic Force Microscopy-Based Screening of Drug-Excipient Miscibility and Stability of Solid Dispersions. *Pharm. Res.* **2011**, *28*, 572–584. https://doi.org/10.1007/s11095-010-0306-4.

(109) Song, Y.; Bhushan, B. Modeling of Tip-Cantilever Dynamics in Atomic Force Microscopy. In *Aplied Scanning Probe Methods V*; Bhushan, B., Kawata, S., Fuchs, H., Eds.; Springer: Berlin, 2007; pp 149–223.

(110) Raman, A.; Melcher, J.; Tung, R. Cantilever Dynamics in Atomic Force Microscopy. *Nano Today* **2008**, *3* (1–2), 20–27. https://doi.org/10.1016/S1748-0132(08)70012-4.

(111) De Beer, S.; Van Den Ende, D.; Mugele, F. Atomic Force Microscopy Cantilever Dynamics in Liquid in the Presence of Tip Sample Interaction. *Appl. Phys. Lett.* **2008**, *93* (25), 1–4. https://doi.org/10.1063/1.3050532.

(112) Young, T. J.; Monclus, M. A.; Burnett, T. L.; Broughton, W. R.; Ogin, S. L.; Smith, P. A. The Use of the PeakForceTM Quantitative Nanomechanical Mapping AFM-Based Method for High-Resolution Young's Modulus Measurement of Polymers. *Meas. Sci. Technol.* **2011**, *22* (12). https://doi.org/10.1088/0957-0233/22/12/125703.

(113) Poloni, L. N.; Zhong, X.; Ward, M. D.; Mandal, T. Best Practices for Real-Time in Situ Atomic Force and Chemical Force Microscopy of Crystals. *Chem. Mater.* **2017**, *29*, 331–345. https://doi.org/10.1021/acs.chemmater.6b03082.

(114) Wang, D.; Russell, T. P.; Nishi, T.; Nakajima, K. Atomic Force Microscopy Nanomechanics Visualizes Molecular Diffusion and Microstructure at an Interface. *ACS Macro Lett.* **2013**, *2*, 757–760. https://doi.org/10.1021/mz400281f.

(115) Warzecha, M.; Bhardwaj, R. M.; Reutzel-Edens, S.; Lamprou, D.; Florence; Alastair. Atomic Force Microscopy Studies on Two-Step Nucleation and Epitaxial Growth. In *46th BACG Annual Conference*; 2015.

(116) Egami, K.; Higashi, K.; Yamamoto, K.; Moribe, K. Crystallization of Probucol in Nanoparticles Revealed by AFM Analysis in Aqueous Solution. *Mol. Pharm.* **2015**, *12*, 2972–2980. https://doi.org/10.1021/acs.molpharmaceut.5b00236.

(117) Zhang, J.; Ebbens, S.; Chen, X.; Jin, Z.; Luk, S.; Madden, C.; Patel, N.; Roberts, C. J. Determination of the Surface Free Energy of Crystalline and Amorphous Lactose by Atomic Force Microscopy Adhesion Measurement. *Pharm. Res.* **2006**, *23* (2), 401–407. https://doi.org/10.1007/s11095-005-9144-1.

(118) Gentle, J. E. Computational Statistics. In *International Encyclopedia of Education*; 2010; pp 93–97. https://doi.org/10.1142/9789813148963_0013.

(119) Harrison, R. L. Introduction to Monte Carlo Simulation. *AIP Conf. Proc.* **2010**, *1204*, 17–21. https://doi.org/10.1063/1.3295638.

(120) Metropolis, N.; Ulam, S. The Monte Carlo Method. *J. Am. Stat. Assoc.* **1949**, *44* (247), 335–341.

(121) Eckhardt, R. Stan Ulam, John von Deumann, and the Monte Carlo Method. *Los Alamos Sci.* **1987**, 131–141. https://doi.org/10.1201/9781315365473-3.

(122) Guo, W.; Kundin, J.; Bickermann, M.; Emmerich, H. A Study of the Step-Flow Growth of the PVT-Grown AlN Crystals by a Multi-Scale Modeling Method. *CrystEngComm* **2014**, *16* (29), 6564–6577. https://doi.org/10.1039/c4ce00175c.

(123) Jackson, K. A. The Interface Kinetics of Crystal Growth Processes. *Interface Sci.* **2002**, *10* (2–3), 159–169. https://doi.org/10.1023/A:1015824230008.

(124) Rechtin, M. D.; Renninger, A. L.; Averbach, B. L. Monte-Carlo Models of Amorphous Materials. *J. Non. Cryst. Solids* **1974**, *15* (1), 74–82. https://doi.org/10.1016/0022-3093(74)90112-4.

(125) Eckert, M.; Neyts, E.; Bogaerts, A. Modeling Adatom Surface Processes during Crystal Growth: A New Implementation of the Metropolis Monte Carlo Algorithm. *CrystEngComm* **2009**, *11* (8), 1597–1608. https://doi.org/10.1039/b822973m.

(126) Beatty, K. M.; Jackson, K. A. Monte Carlo Modeling of Silicon Crystal Growth. *J. Cryst. Growth* **2000**, *211* (1), 13–17. https://doi.org/10.1016/S0022-0248(99)00836-2.

(127) Young, T. An Essay on the Cohesion of Fluids. *Philos. Trans. R. Soc. London* **1805**, *95*, 65–87.

(128) Laplace, P. S. *Traité de Mécanique Céleste*; Courcier: Paris, France, 1805.

(129) Gauss, C. F. *Principia Generalia Theoriae Figurae Fluidorum in Statu Aequilibrii*; Dieterichs: Gottingen, Germany, 1830.

(130) Mullins, W. W. Theory of Thermal Grooving. *J. Appl. Phys.* **1957**, *28* (3), 333–339. https://doi.org/10.1063/1.1722742.

(131) Mullins, W. W. Flattening of a Nearly Plane Solid Surface Due to Capillarity. *J. Appl. Phys.* **1959**, *30* (1), 77–83. https://doi.org/10.1063/1.1734979.

(132) Zhu, L.; Brian, C. W.; Swallen, S. F.; Straus, P. T.; Ediger, M. D.; Yu, L. Surface Self-Diffusion of an Organic Glass. *Phys. Rev. Lett.* **2011**, *106*, 256103. https://doi.org/10.1103/PhysRevLett.106.256103.

3. THE ROLE OF SURFACE ENERGY HETEROGENEITY ON CRYSTAL MORPHOLOGY DURING SOLID-STATE CRYSTALLIZATION AT THE AMORHPOUS ATAZANAVIR-WATER INTERFACE

This chapter is an adaptation of a manuscript published under the same title in *CrystEngComm*[1] and reproduced with permission from the Royal Society of Chemistry. Compared to the published article, this chapter has been rearranged with expanded results and discussion. As the journal article was published in a journal under the Royal Society of Chemistry, the British English spelling of some words was adjusted to the American English spelling.

3.1 Introduction

Poor aqueous solubility is a significant challenge in pharmaceutical development; the vast majority of candidate drug molecules are plagued by solubility concerns[2,3]. Various formulation strategies have been developed and successfully implemented to circumvent these limitations, each with their own advantages and drawbacks[4,5]. One strategy of interest is the use of the amorphous state of the active pharmaceutical ingredient (API), achieved through an amorphous solid dispersion (ASD) of pharmaceutical compound in a polymeric matrix[6,7]. ASD formulations can be preferred to other formulation strategies in that they result in thermodynamically metastable supersaturated solutions as opposed to enhancing the thermodynamic solubility of the drug compound[8]. As a result, the high activity solute molecules possess a higher driving force for membrane transport than is achieved from other formulation strategies[9,10]. A classic example of a commercial ASD formulation is itraconazole dispersed in hydroxypropyl methyl cellulose (Sporanox®)[11]. Formulating itraconazole in this ASD was reported to enhance its apparent solubility by about an order of magnitude compared to the practically insoluble crystalline form[12]. In addition to increasing the maximum achievable concentration, dispersion formulations are also reported to improve kinetic dissolution profiles in many instances[13–15].

The importance of dispersing the API in a polymer matrix compared to pure amorphous API alone is highlighted in the issue of physical stability, both in storage as well as during dissolution *in vivo*. During storage, a glass-to-crystal phase transformation is thermodynamically favorable. Fundamentally, environmental factors such as temperature and ambient moisture along with material specific properties such as molecular structure and hydrogen bonding propensity largely govern crystallization tendency, as these parameters control molecular

mobility and configurational entropy which ultimately determine the timescale of crystallization[16–18]. Dissolution studies on neat amorphous API compounds report that while initial dissolution rates are large and supersaturation can often be achieved, crystallization out of solution quickly occurs, resulting in equilibration at the crystalline solubility[19]. Hence, amorphous pharmaceutical systems include a stabilizing polymer matrix which has been shown in many instances to inhibit crystallization during storage as well as from solution[20,21].

While stabilization against crystallization out of solution and during storage have been studied at some length, considerably less is known about preventing the solid-state phase transition during dissolution. Often, it is assumed that the polymeric matrix is adequate to stabilize the amorphous material during dissolution and that crystallization out of solution is the only relevant phase transformation *in vivo*. However, unstabilized drug-rich phases can arise during dissolution through two primary routes. First, demixing between polymer and drug (or amorphous-amorphous phase separation) can result in incongruent release and the formation of amorphous drug-rich interfaces[22]. Second, ideal congruent release can result in drug supersaturation above the "amorphous solubility" (corresponding to the thermodynamic binodal curve) which results in a liquid-liquid or glass-liquid phase separation[23,24]. This phase transition will result in colloidal amorphous drug-rich domains. In either case, a polymer-poor amorphous drug interface can crystallize through a solid-to-solid transition, ultimately reducing drug concentration in solution and deteriorating formulation performance. Therefore, it is imperative to study this solid-state phase transition in the presence of dissolution media to understand mechanisms governing crystallization as well as factors affecting the arising crystalline phase.

While few detailed studies into solid-state crystallization in the presence of media have been conducted, there is some related research that informs the direction and interpretation of the investigation herein. Morphological observations of crystals grown from amorphous films reveal a treasure trove of insights into crystallization mechanisms, including the observation of non-classical lateral growth out of the plane of the film, rapid growth at the free glass interface compared to growth in the bulk, and multiple polymorphs coexisting[25,26]. Experimentally, atomic force microscopy and electron microscopy have successfully leveraged the out-of-plane growth as well as differences in mechanical properties to discriminate between the different solid state forms[27–29]. On the modeling front, predictions of crystal morphology during growth have demonstrated that surface energy due to surface chemistry variability and specific interactions

between the solid and any solvent or additives species on each crystallographic face are key parameters[30–32]. Some multi-scale models have been developed, though they have in general been relegated to straightforward systems such as crystal growth from the vapor[33,34]. Simulations of polymorphic transitions, another solid state phase change, reveal that this transition is mediated by collective molecular relaxations[35]. This perhaps lends further insight into the observation that crystallization from the glass is reported to occur at the interface where molecular mobility is elevated and collective relaxations could be facilitated by this enhanced mobility. However, at present, there remains the need to investigate and model the transition from glass to crystal in a more dosing-relevant environment.

The aim of this study was to observe solid-state phase behavior of an initially amorphous pharmaceutical surface in the presence of dissolution media. Amorphous pharmaceutical films were crystallized in the presence of buffer solution and topographical measurements were taken systematically over the course of crystallization using atomic force microscopy (AFM) and scanning electron microscopy (SEM). 2D-lattice Monte Carlo (MC) simulations were performed over a range of surface energy configurations to probe the role of surface energy on surface evolution. Results indicate non-classical solid-state crystallization likely facilitated by surface diffusion even in the presence of a dissolution medium. MC simulations demonstrate the importance of amorphous film surface energy on the ultimate morphology of the crystalline phase.

3.2 Methods

3.2.1 Materials

The pharmaceutical used in this study was free-base atazanavir (ATZ), purchased from Attix Pharmaceuticals (Toronto, Canada). Sodium phosphate dibasic anhydrous and sodium phosphate monobasic monohydrate were purchased from ThermoFisher Scientific (Fair Lawn, NJ), sodium chloride was purchased from Mallinckrodt Chemicals (Phillipsburg, NJ), and methanol was purchased from Avantor Macron Fine Chemicals (Radnor, PA).

3.2.2 Preparation of Amorphous Films

Amorphous films were prepared by melting 50 mg of ATZ onto 15 mm steel AFM sample pucks at 240°C. While molten, a 20 mm square glass cover slip was gently pressed onto the melt. Samples were then removed from heat and cooled to ambient temperature. Upon cooling, the cover slip was removed to leave a nominally flat and smooth amorphous surface.

3.2.3 Crystallization of Amorphous Samples

Crystallization was performed in an aqueous environment at elevated temperature. Phosphate buffer (50 mM, pH 6.8) was prepared by dissolving 0.690 g of sodium phosphate dibasic anhydrous, 0.709 g of sodium phosphate monobasic monohydrate, and 0.659 g of sodium chloride in 200 mL of deionized water. The solution was stirred for 24 hours to allow for complete dissolution. To minimize dissolution of the samples, a concentrated ATZ stock solution was prepared by dissolving 0.075 g of ATZ in 3 mL of methanol to achieve a concentration of 25 mg/mL. A 5 μL aliquot of ATZ stock solution was added to 5 mL of buffer while rapidly stirring the buffer solution to yield a final concentration of 25 μg/mL. ATZ samples were placed in this solution and were incubated at 40°C using an Isotemp 202 water bath (Fisher Scientific, Fair Lawn, NJ). At pH 6.8, ATZ is expected to exist almost entire as the free-base rather than as a salt form (pK_a of the strongest base is reported as 4.52)[36].

3.2.4 Characterization

Surface morphology was investigated by AFM and SEM. AFM was performed using a MultiMode 8 (Bruker Corporation, Technology Forest, TX) operated in tapping mode with an NPG probe, cantilever C (Bruker Corporation, Technology Forest, TX). Analysis was performed in a fluid cell to examine samples in the presence of crystallization media. At each time point, the sample surface was evaluated at 10 random locations and a representative image was selected.

Adhesion force heterogeneity of amorphous films was obtained using the same MultiMode 8 AFM operated in quantitative nanomechanical mapping (QNM) mode with a SCANASYST-AIR cantilever (Bruker Corporation, Technology Forest, TX). All reference samples were Bruker standards for QNM calibration. Calibrations for deflection sensitivity were obtained by performing force measurements on a hard, non-deformable sapphire sample. Cantilever spring

constants were determined using the thermal tune method. Cantilever tip curvature radii were determined by reverse imaging the tip onto a standard titanium roughness surface with regularly spaced, ultra-sharp spikes. All AFM data analysis was performed using Nanoscope Analysis v1.9 software (Bruker Corporation, Technology Forest, TX).

For SEM analysis, samples were dried, fixed onto SEM stubs, and sputter-coated with platinum at 40mA for 60 seconds. SEM was performed using a Teneo SEM/VolumeScope (FEI Company, Hillsboro, OR) operated at 5 kV accelerating voltage and 10 mm working distance. Secondary electrons were captured using an Everhart-Thornley detector (ETD).

3.2.5 Relative Surface Energy Distribution Determination

Relative surface energy configurations were determined by the adhesion force measurements obtained via AFM through the contact mechanics method described by Jhang *et al*[37]. For a surface assumed to be flat interacting with a cantilever tip assumed to be spherical at its apex, surface energy is related to adhesion (pull-off) force from an AFM measurement by the following relationship:

$$\gamma_{film} = \left(\frac{F_{ad}}{3\pi R}\right)^2 \frac{1}{\gamma_{probe}} \tag{3.1}$$

Here, F_{ad} is the adhesion force measured by AFM, R is the radius of the AFM probe determined by reverse imaging the tip onto the titanium calibration surface, γ_{probe} is the surface energy of the AFM probe, and γ_{film} is the desired unknown surface energy of the amorphous film. The surface energy of the probe material silicon nitride (Si_3N_4) is reported as 51.2 mJ/m^2 based on contact angle measurements[38].The cantilever radius varies probe to probe, but for the data presented in Figure 3.14 it was found to be approximately 80 nm.

3.2.6 Monte Carlo Simulation

Two-dimensional lattice Monte Carlo (MC) simulations were performed to model surface crystallization. Lattice sites were set to initially be amorphous, with allowed trial moves of converting a site chosen at random from amorphous to crystalline. The probability of accepting a trial move was determined by the balance between energy penalties from forming new amorphous/crystalline interfaces and energy benefits from the lattice energy of converting to the

crystalline phase. Only nearest neighbor interactions were considered. Mathematically, the probability of conversion is represented by:

$$\varphi(x) = \exp\left[-\left(\Delta E_{Interface} + \Delta E_{lattice} + \Delta E_{film}\right)\right] \quad (3.2)$$

Here, $\Delta E_{interface}$ is the increase in energy from forming a new horizontal or vertical interface, $\Delta E_{lattice}$ is the lattice energy benefit from incorporating a new unit into an existing lattice, and ΔE_{film} is the energy difference between the high energy amorphous site and the lower energy crystalline site. This film energy is related to the surface energy configuration of the film, where some sites are at a higher energy than others and hence have a higher crystallization tendency. Lastly, the total barrier to nucleation is the sum of four new interface penalties, two vertical and two horizontal interfaces. Sensitivity to input parameters (nucleation barrier, ratio of interfacial penalties, and lattice energy) was evaluated by systematically varying each parameter over a wide range. Sensitivity simulations were replicated 10 times for each set of conditions. Additionally, ΔE_{film} was adjusted by assigning a distribution of base energies to the initially amorphous surface to reflect heterogeneities in the surface energy for real amorphous films. Simulations were replicated 5 times for each surface energy configuration. When probing the role of initial film surface energy, a ratio of interfacial penalties of 4.2:1 was chosen to generate the desired anisotropy in forming crystals, with growth in the horizontal direction preferred over vertical growth. This ratio was determined by systematically varying the penalty ratio and qualitatively comparing the aspect ratio of the simulation crystalline domains to the crystals observed experimentally (available in supplemental material). The total energy penalty was adjusted to give a nucleation probability of 2×10^{-6} to control the relative timescale of the simulations. The probability of rotating a unit before addition was chosen to be 0.25 to incorporate branching. Computer code was written in Python and made use of NumPy[39] and Matplotlib[40] libraries for mathematical operations and simulation visualization, respectively (original code is available in Appendix B).

3.3 Results and Discussion

3.3.1 Characterization of Surface Morphology During Crystallization

Initially amorphous ATZ films were crystallized over various periods of time and monitored to observe the evolution of topographical features of these films. Representative AFM images of films obtained at zero, six, fourteen, sixteen, twenty, and twenty-four hours are provided in Figure 3.1. Figure 3.1A confirms that the freshly prepared films are relatively flat and smooth, with root-mean-squared roughness determined to be 4.1 nm ± 1.2 nm. Early stages of crystallization, represented in Figure 3.1B and Figure 3.1C, are characterized by highly anisotropic needle-shaped crystals which, despite undergoing nearly two-dimensional lateral growth, extend above the plane of the amorphous film rather than along or into the bulk. These crystals arise primarily as disparate needles or originate from centralized crystalline domains, seen in the upper left quadrant of Figure 3.1B. As crystal development continues, crystalline domains begin to exhibit branching, as observed in Figure 3.1C. Figure 3.1D depicts crystallization which has sufficiently progressed to develop a complex mesh-like network atop the surface. It should be noted that examination of the topographical maps reveals that the height of developing needle-like crystals does not change significantly, with typical crystals about 60 nm tall in Figure 3.1B and only growing to about 100 nm tall in Figure 3.1C and Figure 3.1D. However, once the complex crystalline networks begin to mature and coalesce into larger crystalline features (such as those in the bottom half of Figure 3.1D), substantial growth can occur. From this point, the crystalline surface undergoes significant surface rearrangement and annealing, as the surface progresses from a complex network (Figure 3.1D) to a polycrystalline patchwork (Figure 3.1E) to an ultimately mature polycrystalline solid (Figure 3.1F).

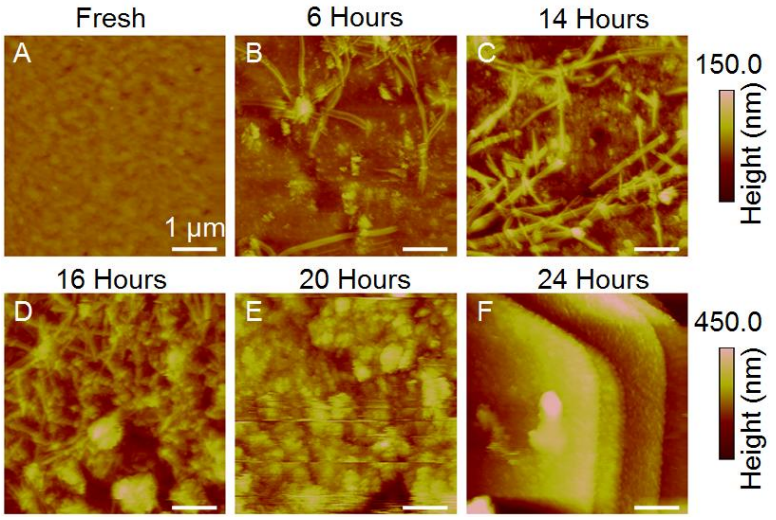

Figure 3.1. AFM topography images (5 µm× 5 µm) of ATZ surface obtained after (A) 0, (B) 6, (C) 14, (D) 16, (E) 20, and (F) 24 hours incubation in pH 6.8 phosphate buffer containing 25 µg/mL ATZ at 40°C. Scale of heat map in (A-C) is 150.0 nm and scale of heat map in (D-F) is 450.0 nm. Scale bar in all images is 1 µm.

Assessing the experimental results, a pressing question to be addressed is the origin of the crystalline features on the surface. While one might speculate that these crystals arise from solution, the buffer solution remains optically clear even after twenty-four hours, suggesting little if any crystal presence in solution. Furthermore, these crystalline domains display strikingly similar morphology to images reported in the literature for the crystallization of indomethacin from the amorphous state under ambient conditions[25]. Under these conditions, where solid-state crystallization is principally the only route for phase transformation, similar anisotropic needle-like crystals growing upward out of the underlying film are observed, which suggests a similar phase transformation mechanism. In order to provide a comparison to a system with known route of crystallization, ATZ crystals were grown isothermally at various temperatures from the subcooled melt in the absence of media, shown in Figure 3.2. Figure 3.2A depicts a system before the onset of nucleation due to the elevated temperature and short incubation time, providing a reference image for comparison. Figure 3.2B captures the early stages of crystallization. Here, the nucleation barrier is only crossed in areas of high energy like defects or regions of high local curvature such as the hemispherical concavities caused by air bubbles. Thus, virtually all the crystals nucleate and grow along the rim of these voids. Figure 3.2C and Figure 3.2D are at sufficiently low temperatures to drive more ubiquitous nucleation and growth, such that small crystalline nuclei as well as needle-like crystals can be observed along the surfaces,

particularly in Figure 3.2D. Here, the same archetypal surface evolution and crystal morphology as Figure 3.1 can be seen, further strengthening the argument that a solid-state phase transformation mechanism underlies the results in Figure 3.1.

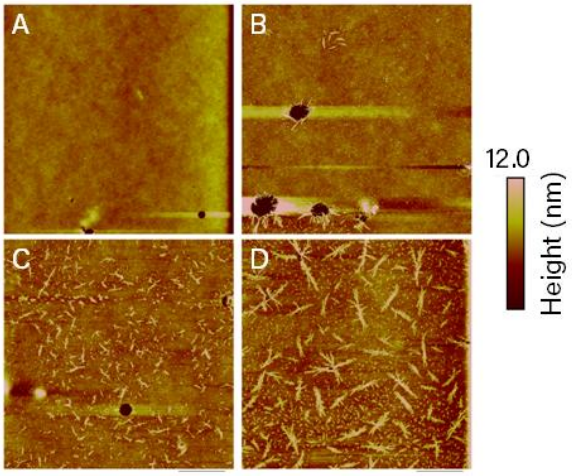

Figure 3.2. AFM topography images of ATZ surface crystallized from the subcooled melt. Images were obtained after isothermal crystallization for 5 minutes at (A) 185°C, (B) 175°C, (C) 170°C, and (D) 165°C in ambient air.

In addition to observational evidence, this conjecture of solid-state crystallization can be rationalized from nucleation theory. For solution-mediated crystallization from a dissolution medium relatively free from foreign particles, nucleation will proceed via primary homogeneous nucleation, which possesses the largest free energy barrier of all forms of nucleation[41]. Furthermore, for a poorly soluble compound, the solute will be quite dilute and in this instance a two-step nucleation mechanism would be a more appropriate description of this system[42,43]. Within this paradigm, nucleation requires fluctuations in both configuration as well as density, resulting in significantly delayed nucleation onset compared to classical nucleation theory (and in better agreement with experimental findings)[42,44]. Contrasted with the slow two-step homogeneous nucleation predicted to occur in solution, crystal nucleation in the glass experiences a very different mechanism. Nucleation from the glass is more akin to primary heterogeneous nucleation, as the existing amorphous solid interface is anticipated to provide a lower surface energy than the crystal-solution interface[45,46]. Furthermore, the chemical similarity between the amorphous and crystalline phases is expected to result in an even lower surface energy than an arbitrary solid surface[47]. Finally, experimental studies on the solid-state crystallization transition have found that for crystallization occurring at an interface (as opposed

to in the bulk of the amorphous phase), local stresses can result in increased molecular mobility at the interface which enhances solid-state crystallization kinetics[25,47,48]. These conceptual arguments along with experimental findings and comparison to related work in the literature strongly suggest a solid-state crystallization mechanism facilitated by surface diffusion; confirmation of this could be achieved by experimental determination of the transport mechanism facilitating surface rearrangement as described elsewhere[49,50], which is proposed as a future direction for study.

To further probe the dramatic and rapid transition from Figure 3.1D to Figure 3.1F, a sample surface after 22 hours of incubation was examined using SEM, with micrographs seen in Figure 3.3. First, excellent agreement is observed between the reference surfaces from Figure 3.1A and Figure 3.3A. Aside from the various pits in the surface, which can most likely be attributed to small air bubbles present during sample preparation, Figure 3.3A confirms the initial surface to be relatively flat, smooth, and homogeneous. Compared to this reference image, Figure 3.3B depicts a heterogeneous surface at various stages of crystallization, underscoring the heterogeneity that is likewise observed with AFM. For example, the large domain on the far right of Figure 3.3B resembles Figure 3.1F while the region in the center of Figure 3.3B more closely resembles Figure 3.1E. These data illustrate the highly stochastic and heterogeneous phenomena believed to be underlying this surface crystallization, namely surface diffusion and nucleation. Furthermore, Figure 3.3 underscores the challenge of systematically studying surface evolution, as even a few micrometers difference in surface location yields appreciably different topography. Ultimately, the data presented in Figure 3.1 and Figure 3.3 demonstrate a stochastic and non-classical solid-state crystallization mechanism, proposed to proceed through surface diffusion. Additionally, this insight underscores the importance of stabilizing the amorphous phase against crystallization by inhibiting this crystallization mechanism.

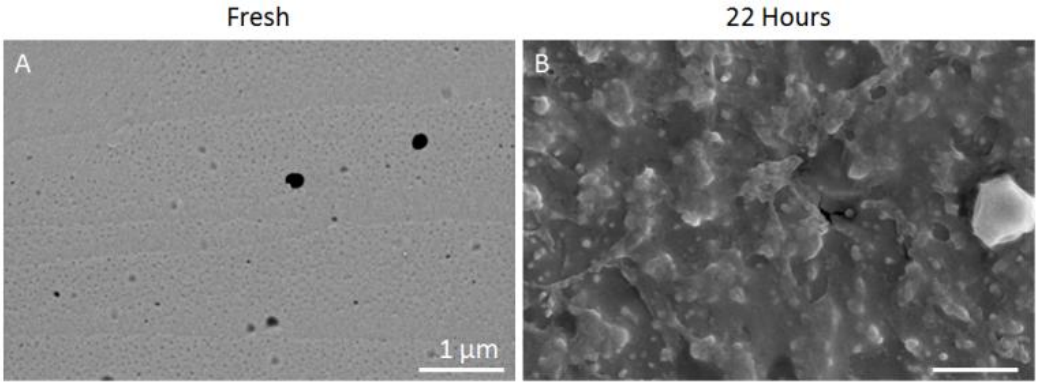

Figure 3.3. SEM micrograph of (A) fresh ATZ film and (B) ATZ film incubated for 22 hours in pH 6.8 buffer containing 25 µg/mL ATZ at 40°C. Scale bar in both images is 1 µm.

3.3.2 Monte Carlo Simulation Parameter Sensitivity

Two-dimensional lattice MC simulations were performed to explore the role of heterogeneities in the surface energy configuration of the initially amorphous film on the morphology of the arising crystals. Given the stochastic nature of surface crystallization and rearrangement, a stochastic simulation technique was anticipated to be a useful tool for analyzing surface crystallization. Furthermore, a similar modeling approach has been shown to be helpful for interpreting crystal dissolution as well as highlighting the role of defects and surface energy variability on the dissolution mechanism[51]. Before performing simulations to examine the role of input surface energy configurations, the sensitivity of the model to the other input parameters was evaluated.

The sensitivity of the simulation to the ratio of interfacial penalties is seen in Figure 3.4. As one might expect, identical vertical and horizontal interface penalties results in isotropic growth and spherulitic crystals. As one interface becomes increasingly thermodynamically favorable relative to the other, growth becomes biased to preferentially grow the favorable faces, leading to anisotropic needles. Recall that branching was incorporated by allowing for units to add in a rotated configuration (*i.e.* swapping the horizontal and vertical interfaces). This rotation accounts for anisotropic needles growing vertically rather than horizontally. The aspect ratio of the emerging crystals is approximately equal to twice the penalty ratio as new interfaces are formed in pairs. It can be noted that there does appear to be some effect on rate of simulation progression as the penalty ratio is increased, given that each subfigure in Figure 3.4 is taken after

15 million MC steps and extent of conversion from amorphous to crystalline decreases as the ratio increases. This observation is explored in greater depth below in Figure 3.7.

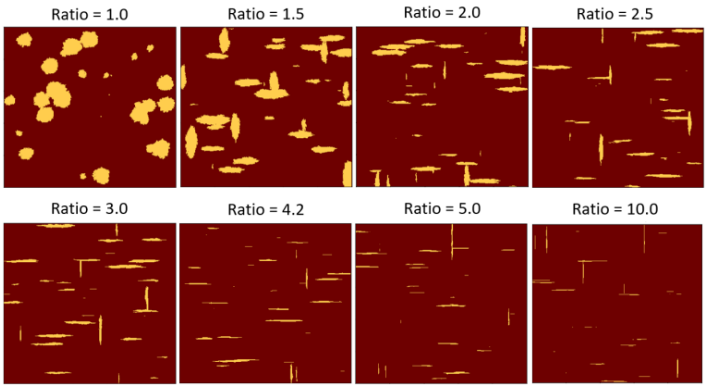

Figure 3.4. MC simulation snapshots after 15 million trial MC steps for interfacial penalty ratios of 1.0, 1.5, 2.0, 2.5, 3.0, 4.2, 5.0, and 10.0. Dark pixels are underlying amorphous surface, and light pixels are overlaying crystal. Simulations employ a uniform surface energy, nucleation barrier of 13, lattice energy of -5, and interfacial ratio 4.2.

A particularly interesting sensitivity analysis is the effect of nucleation barrier presented in Figure 3.5. At very low nucleation barriers, the system approaches spinodal decomposition where the transition is marked by the absence of any activation energy, as evidenced by the absence of distinct phase boundaries and approximately homogeneous distribution and intercalation of the two phases. This phenomenon persists for low nucleation barriers until a sufficiently large nucleation barrier begins to prefer growth on existing crystals to novel nucleation events, in this case around a nucleation barrier of 6. At these intermediate nucleation barrier values, the crystalline domains remain small and exhibit a smaller aspect ratio. The small crystal size is due to the gradual transition from growth-limited to nucleation-limited crystallization as the nucleation barrier increases. The small aspect ratio can be attributed to the nucleation barrier being roughly comparable to the lattice energy, meaning that horizontal and vertical growths are almost equally preferable. Finally, as the nucleation barrier becomes large, the system becomes nucleation limited and the crystal aspect ratio approaches the limit predicted by the interfacial penalty ratio. The effect of nucleation barrier on simulation time is explored further below in Figure 3.7.

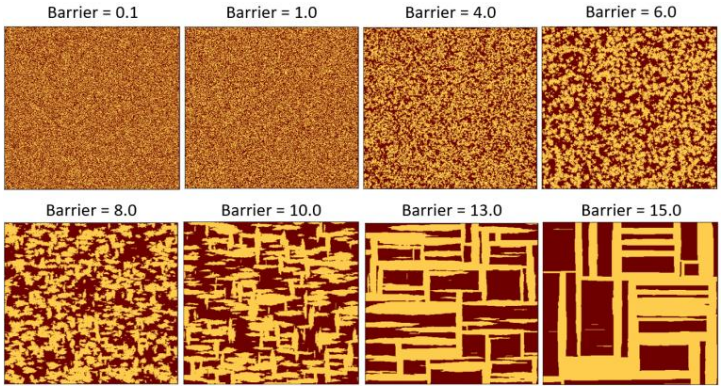

Figure 3.5. MC simulation snapshots at 50% conversion for various nucleation barriers of 0.1, 1.0, 4.0, 6.0, 8.0, 10.0, 13.0, and 15.0. Simulations employ a uniform surface energy, lattice energy of -5, and interfacial ratio 4.2.

The final input parameter for sensitivity assessment is the lattice energy, depicted in Figure 3.6. It can be noted that these sensitivity studies share many parallels to adjusting the interfacial penalty ratio from Figure 3.4. When the lattice energy is negligible, the only factor influencing nucleation and growth rates is the specific interfacial penalties, with no explicit energetic benefit to growth. Thus, crystallization is only about minimizing energy penalties and highly anisotropic needles form. This is not unlike the systems in Figure 3.4 with large interfacial penalty ratios, where only the least unfavorable growth events tend to occur. As the lattice energy approaches most intermediate values, a transition region occurs where the needles become more rounded and less dramatically sharp as a larger variety of possible growth events are possible. When the magnitude of the lattice energy becomes comparable to or larger than the nucleation barrier, the growth becomes nearly isotropic much like the systems in Figure 3.4 where the penalty ratio approaches unity. Much like those systems, when the lattice energy is sufficiently large, all growth events become almost equally likely as the benefit from adding an adjacent unit outweighs the penalty associated with the formation of new interfaces. Once this point is reached, this phenomenon will persist indefinitely. The effect of lattice energy on simulation time required to achieve a given degree of crystallization is discussed in Figure 3.7.

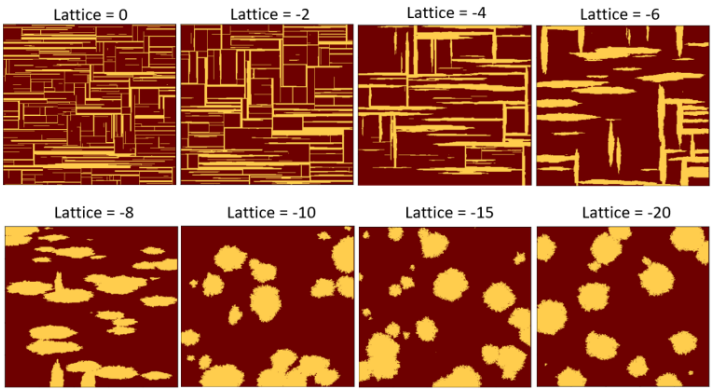

Figure 3.6. MC simulation snapshots at 25% surface crystallization for lattice energies of 0, -2, -4, -6, -8, -10, -15, and -20. Simulation employs a uniform surface energy, nucleation barrier of 13, and interfacial ratio 4.2.

A final quantitative consideration is the effect of input parameters on the rate of simulation progression, presented in Figure 3.7 where the natural logarithm of trial steps to achieve a particular percentage of conversion is plotted against the system parameter of interest. Each parameter has a distinct impact on the scaling of the simulation time, seen in the distinct trends in Figure 3.7A, Figure 3.7B, and Figure 3.7C. First, as noted previously, Figure 3.7A demonstrates a dependence of simulation time on the interfacial penalty ratio. Though this might at first seem counterintuitive (namely, since the lattice energy and total nucleation barrier are unchanging), this is most likely rationalized by the statistical likelihood of selecting a site with a higher propensity to convert. At a ratio near unity, any site adjacent to an existing crystalline unit is more favorable for conversion than a new nucleation event. Thus, growth is quite rapid as these systems are nucleation-limited. Furthermore, growth accelerates over time as the surface area of the crystalline domains increases. However, as the ratio between interface penalties becomes larger, the formation of the less favorable interfaces becomes the dominant penalty related to conversion from amorphous to crystalline. In this case, growing unfavorable interfaces becomes almost identical to a new nucleation event. Therefore, only growth on the end of the long needles is a statistically likely event. Because there are few sites at the end of the needle domains, the probability of selecting one such site at random is unlikely and does not improve significantly as the simulation progresses. Given that the nucleation penalty is fixed in these cases, a plateau is eventually reached at a sufficiently large interfacial penalty ratio as one would expect. It is worth mentioning that the scaling in Figure 3.7A is sub-exponential, consistent with the mathematics in Equation 2 where the penalty ratio is not explicitly present in the probability of conversion. The

dependence of simulation time on the nucleation barrier, as illustrated in Figure 3.7B, is straightforward to understand. The exponential dependence, made clear by the near linearity of the data on the logarithmic plot, flows naturally from the mathematics in Equation (3.2). Lastly, the dependence of simulation time on the lattice energy in Figure 3.7C shows an interesting bifurcation behavior. For lattice energies near 0, exponential dependence is observed as one might expect from the mathematics of Equation (3.2). This trend mirrors that of Figure 3.7B. However, as the magnitude of the lattice energy increases (*i.e.* as one moves further left on the x-axis), a threshold is reached where the lattice benefit outweighs the interfacial penalties. At this point, growth becomes rapid and no dependence on the lattice energy is observed, much like Figure 3.7A when the aspect ratio nears unity.

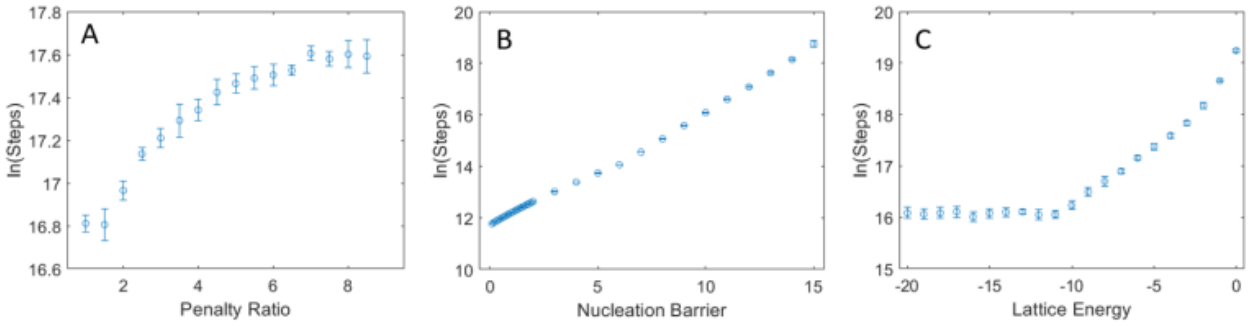

Figure 3.7. Plots depicting the effect of (A) penalty ratio, (B) nucleation barrier, and (C) lattice energy on the number of simulation steps required to achieve a given conversion for the systems presented in Figure 1 through Figure 3. (A) represents the number of trial steps to 25% conversion from amorphous to crystalline, (B) the number of steps to 50% conversion, and (C) the number of steps to 25% conversion.

3.3.3 Monte Carlo Simulation Modeling Crystallization

Simulation results for a random surface energy configuration are presented in Figure 3.8. Qualitatively, crystal domains initially emerge as high aspect ratio, needle-like features with preferred directionality and the presence of branching. Upon further growth and maturation, the later simulation point data from Figure 3.8G and Figure 3.8H begin to display interconnection and coalescence of the initially disparate needles into larger crystalline domains. These needle-like crystalline domains are consistent with the crystal habit for the one polymorph of ATZ available in the Cambridge Crystallographic Data Centre[52]. Thus, the model parameters and predictions can be compared to experimental observations of the solid-state crystallization of an initially amorphous ATZ sample, as shown in Section 3.3.1. Furthermore, the crystal surface

energy ratios used to generate anisotropy are similar to those reported in the literature for other anisotropic crystals[30,53], demonstrating that even the empirical tuning of model parameters can result in physically relevant results within a realistic parameter space.

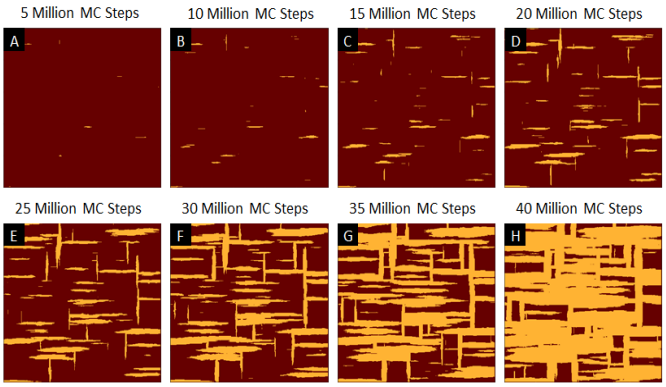

Figure 3.8. MC simulation snapshots depicting crystallization progression after (A) 5 million, (B) 10 million, (C) 15 million, (D) 20 million, (E) 25 million, (F) 30 million, (G) 35 million, and (H) 40 million trial MC steps. Dark pixels are underlying amorphous surface, and light pixels are overlaying crystal.

Beyond a qualitative analysis, a quantitative or semi-quantitative examination of the simulation was also desired. One metric of interest for comparison is the extent of crystallization. For this simulation, this was determined simply as the ratio of crystallized to total lattice sites. Such a measurement is more difficult for the experimental data; to a first approximation, the AFM topography plots were converted to binary with elevated locations on the surface indicative of crystallization. Upon conversion to binary, the ratio of light pixels to total pixels was used to approximate the extent of crystallization. A plot comparing these metrics for simulation and experimental data is shown in Figure 3.9. To plot the time-domain experimental data against the MC-domain simulation results, the simulation points were scaled to allow the end of the simulation to roughly align with the extensively crystallized surface (twenty four hours), which was taken to represent a fully crystallized surface.

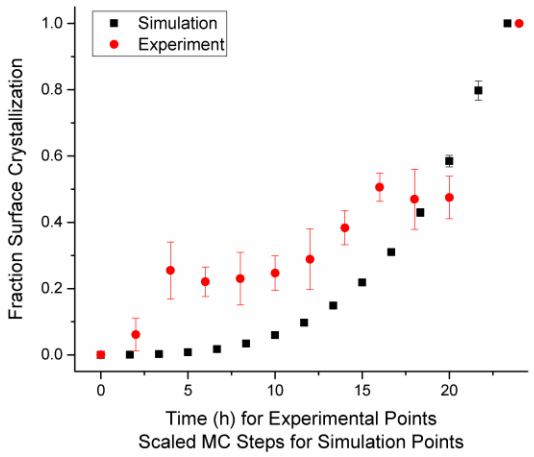

Figure 3.9. Plot comparing extent of crystallization between experimental data (●) and scaled simulation data (■). Error bars represent one standard deviation based on 5 replicates for simulation points and 5 to 10 replicates for experimental points.

From Figure 3.9, several important features should be noted. In general, the simulation results tend to underpredict the extent of crystallization observed experimentally, especially at early time points. Despite this discrepancy, the overall trend and shape of the data agree very well between theory and experiment, particularly for intermediate time points, such as those between 6 and 16 hours. The deviation in this trend for shorter and longer time point data can most likely be attributed to the limitations of using a binary topography plot as a measure of extent of crystallization. Such an approximation is only valid when variability in the topography of the surface is primarily attributed to the local solid-state character of the surface. For example, in Figure 3.1C virtually all the measured topography variation is a result of the formation of elevated, needle-like crystals. Hence, converting this image to binary accurately allows for discrimination between crystalline and amorphous regions. Conversely, Figure 3.1D or Figure 3.1E also exhibits large topography variability but this variability is no longer explicitly related to the amorphous or crystalline nature of the location. Similarly, the small topographical features in Figure 3.1A are simply the natural variability of the amorphous solid and do not reflect any crystalline features. Such physical rationalizations are consistent with the experimental data presented in Figure 3.9; the short time point data exhibit positive deviation while the long-time data exhibit negative deviation from the underlying trend. Thus, the perceived plateau in extent of crystallization between 16 and 20 hours for the experimental data in Figure 3.9 is primarily

due to the limitation of optical methods to evaluate extent of crystallization. Surface annealing of existing crystalline domains into larger, more mature crystals, which is observed in Figure 3.1E and Figure 3.1B, is not captured by simply assessing height variations and contributes towards this underestimation and apparent plateau. Given these limitations, the trend agreement for the intermediate time points in Figure 3.9 is very encouraging, suggesting that this simulation is a powerful interpretive tool to be paired with experimental observation for elucidation of the mechanism of phase transformation.

3.3.4 MC Simulations for Various Surface Energy Configurations

MC simulations for various idealized surface energy configurations of interest were performed, seen in Figure 3.10 through Figure 3.13. In real systems, local disorder, defects, and regions of local curvature can all result in heterogeneity across a surface[54]. This distribution of surface energies across a surface is generally difficult and time consuming to determine by experiments and is therefore often neglected in theoretical treatments of surface phenomena, with a single, average value used instead[55,56]. Given the resolving power of a lattice model, this simulation tool permits careful engineering of the surface energy configuration of the amorphous material to study the role played by the heterogeneity of the underlying film on the morphology of the arising crystalline domains. Figure 3.10 illustrates an idealized, uniform surface energy configuration (Figure 3.10A) with simulation snapshots taken every 5 million trial MC steps (Figure 3.10B through Figure 3.10I). Much like the simulation results in Figure 3.8, these data demonstrate patterns of highly anisotropic needles which exhibit branching and eventually form larger domains. Note that the average surface energy for Figure 3.8 and Figure 3.10 are nearly identical, although the simulation progresses more quickly for a randomly distributed surface energy (Figure 3.8) than for the uniform surface energy (Figure 3.10). This is explained primarily through the energy barrier for nucleation, which is seen to be the rate limiting step for crystallization. The high energy sites in Figure 3.8 can nucleate more quickly, such that the presence of this existing interface compensates for the energetic penalty of growing on low energy sites.

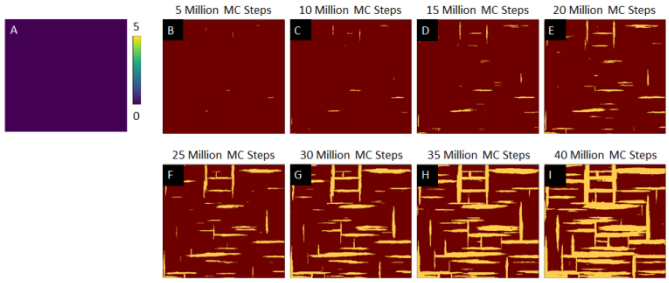

Figure 3.10. MC simulation employing a (A) uniform surface energy configuration and (B-I) accompanying simulation snapshots.

Turning towards a more relevant surface energy configuration, Figure 3.11A depicts a uniform distribution that contains a single 2D Gaussian hill in the center of the simulation. Accompanying snapshots of the simulation progress are given in Figure 3.11B through Figure 3.11I. This simulation was motivated by aspects of the experimental findings in Figure 3.1. Specifically, Figure 3.1B reveals a larger, centralized region of circular crystallization from which needle-like domains protrude (upper left quadrant of Figure 3.1B). As this crystal domain seems to have developed and matured incommensurate with the short incubation time, it is proposed that this crystal feature arose due to heterogeneities in the underlying amorphous surface. Thus, the surface energy configuration in Figure 3.11A was chosen as a possible explanation for the observed crystal morphology. The simulation results demonstrate that a substantial amount of crystallization in this system is driven by this high surface energy region of the underlying film. Furthermore, the arising topography of the central region (especially in Figure 3.11C through Figure 3.11F) underscores the significance of the underlying surface energy; the rapidly developed, somewhat circular crystal domain with emanating needle-like features mirrors the important topographical features Figure 3.1B.

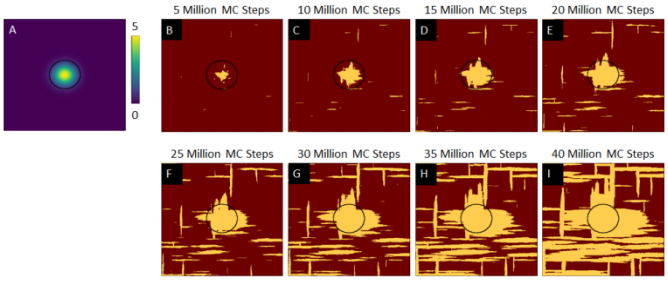

Figure 3.11. MC simulation employing a (A) large 2D Gaussian function surface energy configuration and (B-I) accompanying simulation snapshots. The region of influence of the high surface energy is circumscribed with a black circle that is superimposed on simulation results to serve as a visual guide.

Another surface energy configuration of import is shown in Figure 3.12A, which consists of many randomly placed high energy 2D Gaussian hills, reminiscent of random point defects in an underlying amorphous surface. Simulation snapshots given in Figure 3.12B through Figure 3.12H reflect the role played by these defect sites in promoting and directing crystallization. Without the visual aids provided in the form of the black circles, it would be difficult to detect differences between the simulation results in Figure 3.12 and those from Figure 3.8 or Figure 3.10. However, these visual aids, which serve to demonstrate regions on the surface where the high surface energy would affect crystallization, illuminate the subtle role played by the underlying surface. Almost all the crystal domains in Figure 3.12 originate from or interconnect with the high energy sites, an observation most clearly illustrated in Figure 3.12F. Here, 38 of the 40 defect regions exhibit crystallization and 28 of the 30 crystalline domains are connected to a high surface energy region. These data further highlight the importance of the surface energy of the amorphous film. While the general surface features that arise during crystallization can largely be reproduced without consideration for the surface energy of the underlying material, capturing the precise topography of the surface during evolution requires a nuanced understanding of the otherwise imperceptible amorphous surface energy configuration.

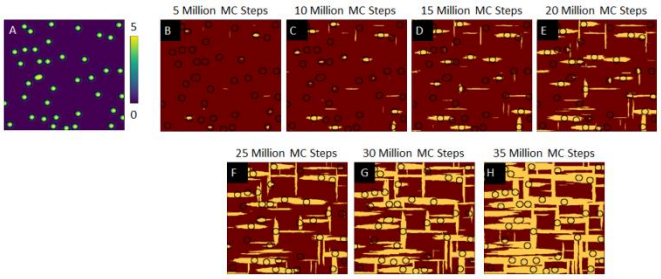

Figure 3.12. MC simulation employing a (A) randomly distributed small 2D Gaussian function surface energy configuration and (B-H) accompanying simulation snapshots. The regions of influence of the high surface energy are circumscribed with black circles that are superimposed on simulation results to serve as a visual guide.

The final idealized energetic configuration considered here is presented in Figure 3.13A, which is comprised of a long and narrow diagonal line of high surface energy. Such a system is intended to mimic the role played by a fracture in an amorphous film. While not the focus of these simulations, such a configuration could also reflect a grain boundary between two single-crystal domains. Simulation snapshots for this energy configuration are given in Figure 3.13B through Figure 3.13I. From the findings in Figure 3.13B through Figure 3.13E, nearly all the early crystallization is directed near the high energy region. Outside of the high energy region, the crystal domains are very similar to those seen in previous simulations, whereby crystals arise as anisotropic, high aspect ratio needles. However, crystals that have originated within the high energy region adopt a novel morphology which underscores two observations of interest. First, this central crystalline domain grows along this diagonal line despite the allowed trial moves consisting only of vertical or horizontal addition. Hence, this simulation demonstrates that the surface energy of the underlying film can overwhelm even the preferred growth directions favored by the energetics of the crystal. Second, although the high energy region is narrow, the influence it exerts on the morphology of the growing crystal extends far beyond the band itself (see Figure 3.13G through Figure 3.13I). These observations suggest that a high energy defect such as a fracture in an amorphous film could have a profound energetic impact on the evolution of the surface well beyond the spatial region near the defect site.

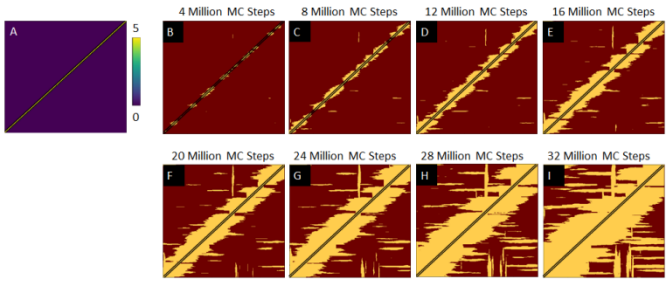

Figure 3.13. MC simulation employing a (A) long diagonal surface energy configuration and (B-I) accompanying simulation snapshots. The region of influence of the high surface energy is circumscribed with two black lines that are superimposed on simulation results to serve as a visual guide.

While the results in Figure 3.8 through Figure 3.13 are interesting and informative, it remains to be shown how simulation parameters are connected to real system properties. In order to provide a more physically motivated surface energy configuration, adhesion measurements on amorphous surfaces were performed and used to determine relative surface energy distributions, shown in Figure 3.14A and Figure 3.14B. The experimentally determined configuration was then used as an input for the 2D lattice MC model, with snapshots seen in Figure 3.14C through Figure 3.14H.

Despite the relatively flat topography of the amorphous films, it is well known that even nanoscale topography will influence adhesion measurements[57,58]. Furthermore, it was expected that molecules on both peaks and valleys (or any regions of high local curvature) would be at a higher chemical potential based on the Gibbs-Thomson effect and hence have a higher driving force to crystallize[59,60]. Thus, since the equation relating adhesion force to surface energy goes as force squared, the adhesion measurements were normalized based on the average (seen in Figure 3.14A) to accurately capture curvature effects as well as heterogeneities associated with interactions dependent on molecular orientation. Consequently, the relative surface energy for each pixel was calculated using Equation (3.1) and is seen in Figure 3.14B. This surface energy configuration exhibits a similar degree of variability as the idealized surface energy input from Figure 3.8, which suggests the model distributions are reasonable and provide useful, physically meaningful insight into the behavior of the real system.

Turning to snapshots of model outputs (Figure 3.14C-Figure 3.14H) based on this surface energy configuration, some comparisons to model predictions using the idealized surface energy can be made. An obvious difference between Figure 3.8 and Figure 3.14 is the length of the simulations; Figure 3.14 demonstrates a simulation which has progressed nearly to completion in

about 25% of the trial steps as Figure 3.8. This is quite easily rationalized due to differences in the simulation domains. Figure 3.14B is generated from AFM data collected with 256 x 256-pixel resolution, whereas the surface energy configuration in Figure 3.8 is 500 x 500 pixels. Hence, this configuration contains roughly 4 times more lattice sites and thus would be expected to require 4 times the simulation length, all else being equal. Therefore, the simulation durations are in good agreement when corrected for lattice size. Similarly, differences in the apparent size and aspect ratio of crystalline domains in Figure 3.14 are due to each pixel quadrupling in size due to the four-fold reduction in resolution.

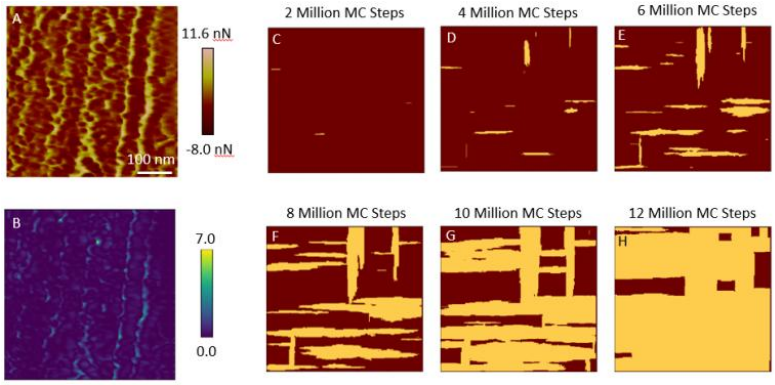

Figure 3.14. Relative adhesion force map (A) of amorphous film obtained by AFM (500 nm × 500 nm), corresponding calculated relative surface energy distribution (B) employed in MC simulation with (C-H) snapshots of simulation progression.

In assessing the validity of using amorphous film surface energy as a parameter determining crystallization tendency and crystal morphology, it is worth comparing the model to related reports in the literature. As hinted to previously, a similar lattice MC model was developed to study the effect of defects and high energy sites on crystal dissolution, which was shown to be very effective in validating the novel fragmentation driven dissolution mechanism[51]. Both experimental and computational studies into solution-mediated crystal growth where surface energy can be tuned via the introduction of surfactants have produced encouragingly similar findings[61]. Moreover, examples of controlling prenucleation clusters (which can be thought of much like a sort of dense, amorphous precursor) have shown that biasing the molecular orientation in this amorphous cluster, much like the sort of surface energy biasing simulated here, can dictate the polymorph which nucleates as well as the rate of nucleation[43].

Taken together, the data presented in Figure 3.8 and Figure 3.14 confirm the necessity of considering not only the surface energy of the arising crystal faces but also the surface energy of the underlying amorphous film if one is to rigorously understand and predict the morphology of a surface undergoing a solid-state crystallization transition. Therefore, it is proposed that amorphous phase surface energy can serve as a potential design parameter in selecting and optimizing strategies for controlling solid-state crystallization. Understanding the connection between surface energy and the propensity for a given crystallization inhibitor to interact with the amorphous phase could be used to design better inhibitor molecules for more effective supersaturating formulations. Furthermore, these findings highlight the value of even a rudimentary tool such as a simple 2D lattice MC model in elucidating important features and parameters in a complex phenomenon like surface crystallization in the presence of an aqueous medium. Such simulations allow for qualitative to semi-quantitative assessments of the role of surface energy on crystallization at minimal computational expense. In the future, it would be of great value to refine and extend this simple MC model into a more sophisticated scheme which incorporates molecular level information to make enhanced predictions regarding system properties such as surface energy and nucleation probability. This would allow for not only more predictive capabilities but would also facilitate the extension of this model to different API and solvent systems.

3.4 Conclusions

Systematic topographical measurements of the amorphous ATZ-water interface during crystallization have demonstrated highly anisotropic needle-like crystals, with growth occurring above the plane of the film. Furthermore, electron micrographs highlight the significant heterogeneity in surface morphology, indicative of the stochastic phenomena proposed to underlie interface-driven crystallization. A 2D lattice MC model suggests that the surface energy configuration of the amorphous film plays a key role in the nucleation and growth patterns observed for the emerging crystals. Considering the importance of amorphous surface energy, it is proposed that an important future direction of related work should involve examination of crystallization of amorphous films of different surface energy configurations (by, for example, casting films from different solvents). Additionally, it would be of great interest to the community to study the surface energy distribution and crystallization of amorphous

nanoparticles generated from glass-liquid phase separation given their relevance to the dosing behavior of amorphous pharmaceutical formations. Ultimately, these results provide fundamental insight into the solid-state transition which can occur at the amorphous-water interface, which is essential for understanding how amorphous drugs undergo phase transformations towards their more stable crystalline counterparts during dosing.

3.5 References

(1) Parker, A. S.; Taylor, L. S.; Beaudoin, S. P. The Role of Surface Energy Heterogeneity on Crystal Morphology during Solid-State Crystallization at the Amorphous Atazanavir–Water Interface. *CrystEngComm* **2020**, *22*, 3179–3187. https://doi.org/10.1039/c9ce02007a.

(2) Babu, N. J.; Nangia, A. Solubility Advantage of Amorphous Drugs and Pharmaceutical Cocrystals. *Cryst. Growth Des.* **2011**, *11*, 2662–2679. https://doi.org/10.1021/cg200492w.

(3) Thayer, A. M. Finding Solutions. *Chem. Eng. News* **2010**, *88* (22), 13–18.

(4) Williams, H. D.; Trevaskis, N. L.; Charman, S. A.; Shanker, R. M.; Charman, W. N.; Pouton, C. W.; Porter, C. J. H. Strategies to Address Low Drug Solubility in Discovery and Development. *Pharmacol. Rev.* **2013**, *65*, 315–499. https://doi.org/10.1124/pr.112.005660.

(5) Pouton, C. W. Formulation of Poorly Water-Soluble Drugs for Oral Administration: Physicochemical and Physiological Issues and the Lipid Formulation Classification System. *Eur. J. Pharm. Sci.* **2006**, *29*, 278–287. https://doi.org/10.1016/j.ejps.2006.04.016.

(6) Kim, K. T.; Lee, J. Y.; Lee, M. Y.; Song, C. K.; Choi, J.; Kim, D.-D. Solid Dispersions as a Drug Delivery System. *J. Pharm. Investig.* **2011**, *41* (3), 125–142. https://doi.org/10.4333/KPS.2011.41.3.125.

(7) Leuner, C.; Dressman, J. Improving Drug Solubility for Oral Delivery Using Solid Dispersions. *Eur. J. Pharm. Biopharm.* **2000**, *50* (1), 47–60. https://doi.org/10.1016/S0939-6411(00)00076-X.

(8) Liu, H.; Taylor, L. S.; Edgar, K. J. The Role of Polymers in Oral Bioavailability Enhancement; a Review. *Polymer (Guildf).* **2015**, *77*, 399–415. https://doi.org/10.1016/j.polymer.2015.09.026.

(9) Taylor, L. S.; Zhang, G. G. Z. Physical Chemistry of Supersaturated Solutions and Implications for Oral Absorption. *Adv. Drug Deliv. Rev.* **2016**, *101*, 122–142. https://doi.org/10.1016/j.addr.2016.03.006.

(10) Yalkowsky, S. H. Perspective on Improving Passive Human Intestinal Absorption. *J. Pharm. Sci.* **2012**, *101* (9), 3047–3050. https://doi.org/10.1002/jps.23093.

(11) Janssen Pharmaceuticals Inc. Sporanox® (Itraconazole) Capsules [Package Insert]. 2001.

(12) Namburi, R. R.; Kerr, J. E. Oral Itraconazole Formulations and Methods of Making the Same. US6663897B2, 2001.

(13) Ali, A. A.; Gorashi, A. S. Absorption and Dissolution of Nitrofurantoin from Different Experimental Formulations. *Int. J. Pharm.* **1984**, *19*, 297–306. https://doi.org/10.1016/0378-5173(84)90059-0.

(14) Chiou, W. L.; Riegelman, S. Pharmaceutical Applications of Solid Dispersion Systems. *J. Pharm. Sci.* **1971**, *60* (9), 1281–1302.

(15) Dalvi, P. B.; Gerange, A. B.; Ingale, P. R. Solid Dispersion: Strategy to Enhance Solubility. *J. Drug Deliv. Ther.* **2015**, *5* (2), 20–28.

(16) Craig, D. Q. M.; Royall, P. G.; Kett, V. L.; Hopton, M. L. The Relevance of the Amorphous State to Pharmaceutical Dosage Forms: Glassy Drugs and Freeze Dried Systems. *Int. J. Pharm.* **1999**, *179*, 179–207. https://doi.org/10.1016/S0378-5173(98)00338-X.

(17) Hancock, B. C.; Zografi, G. Characteristics and Significance of the Amorphous State in Pharmaceutical Systems. *J. Pharm. Sci.* **1997**, *86* (1), 1–12. https://doi.org/10.1021/js9601896.

(18) Zhou, D.; Zhang, G. G. Z.; Law, D.; Grant, D. J. W.; Schmitt, E. A. Physical Stability of Amorphous Pharmaceuticals: Importance of Configurational Thermodynamic Quantities and Molecular Mobility. *J. Pharm. Sci.* **2002**, *91* (8), 1863–1872. https://doi.org/10.1002/jps.10169.

(19) Hancock, B. C.; Parks, M. What Is the True Solubility Advantage for Amorphous Pharmaceuticals? *Pharm. Res.* **2000**, *17* (4), 397–404. https://doi.org/10.1023/A:1007516718048.

(20) Alonzo, D. E.; Zhang, G. G. Z.; Zhou, D.; Gao, Y.; Taylor, L. S. Understanding the Behavior of Amorphous Pharmaceutical Systems during Dissolution. *Pharm. Res.* **2010**, *27* (4), 608–618. https://doi.org/10.1007/s11095-009-0021-1.

(21) Theil, F.; Anantharaman, S.; Kyerematen, S. O.; Van Lishaut, H.; Dreis-Kühne, S. H.; Rosenberg, J.; Mägerlein, M.; Woehrle, G. H. Frozen in Time: Kinetically Stabilized Amorphous Solid Dispersions of Nifedipine Stable after a Quarter Century of Storage. *Mol. Pharm.* **2017**, *14* (1), 183–192. https://doi.org/10.1021/acs.molpharmaceut.6b00783.

(22) Indulkar, A. S.; Lou, X.; Zhang, G. G. Z.; Taylor, L. S. Insights into the Dissolution Mechanism of Ritonavir–Copovidone Amorphous Solid Dispersions: Importance of Congruent Release for Enhanced Performance. *Mol. Pharm.* **2019**, *16*, 1327–1339. https://doi.org/10.1021/acs.molpharmaceut.8b01261.

(23) Mosquera-Giraldo, L. I.; Taylor, L. S. Glass-Liquid Phase Separation in Highly Supersaturated Aqueous Solutions of Telaprevir. *Mol. Pharm.* **2015**, *12* (2), 496–503. https://doi.org/10.1021/mp500573z.

(24) Ilevbare, G. A.; Taylor, L. S. Liquid-Liquid Phase Separation in Highly Supersaturated Aqueous Solutions of Poorly Water-Soluble Drugs: Implications for Solubility Enhancing Formulations. *Cryst. Growth Des.* **2013**, *13*, 1497–1509. https://doi.org/10.1021/cg301679h.

(25) Sun, Y.; Zhu, L.; Kearns, K. L.; Ediger, M. D.; Yu, L. Glasses Crystallize Rapidly at Free Surfaces by Growing Crystals Upward. *Proc. Natl. Acad. Sci.* **2011**, *108* (15), 5990–5995. https://doi.org/10.1073/pnas.1017995108.

(26) Sun, Y.; Zhu, L.; Wu, T.; Cai, T.; Gunn, E. M.; Yu, L. Stability of Amorphous Pharmaceutical Solids: Crystal Growth Mechanisms and Effect of Polymer Additives. *AAPS J.* **2012**, *14* (3), 380–388. https://doi.org/10.1208/s12248-012-9345-6.

(27) Ji, Y.; Liu, J.; Xu, M.; Zeng, K.; Jiang, H.; Li, C.; Yang, L.; Chen, Y. Evolution of Crystal Growth in MgO-Al2O3-SiO2 Glass Ceramics. *CrystEngComm* **2019**, *21* (12), 1967–1973. https://doi.org/10.1039/c8ce02036a.

(28) Thakuria, R.; Eddleston, M. D.; Chow, E. H. H.; Lloyd, G. O.; Aldous, B. J.; Krzyzaniak, J. F.; Bond, A. D.; Jones, W. Use of in Situ Atomic Force Microscopy to Follow Phase Changes at Crystal Surfaces in Real Time. *Angew. Chemie - Int. Ed.* **2013**, *52*, 10541–10544. https://doi.org/10.1002/anie.201302532.

(29) Thakuria, R.; Eddleston, M. D.; Chow, E. H. H.; Taylor, L. J.; Aldous, B. J.; Krzyzaniak, J. F.; Jones, W. Comparison of Surface Techniques for the Discrimination of Polymorphs. *CrystEngComm* **2016**, *18*, 5296–5301. https://doi.org/10.1039/c6ce01096b.

(30) Khan, M. A. S.; Ganguly, B. Can Surface Energy Be a Parameter to Define Morphological Change of Rock-Salt Crystals with Additives? A First Principles Study. *CrystEngComm* **2013**, *15*, 2631–2639. https://doi.org/10.1039/c3ce26764d.

(31) Li, P.; Zhao, X.; Li, Y.; Sun, H.; Sun, L.; Cheng, X.; Hao, X.; Fan, W. Effects of Surface Chemistry on the Morphology Transformation of ZnWO 4 Nanocrystals: Investigated from Experiment and Theoretical Calculations. *CrystEngComm* **2012**, *14* (3), 920–928. https://doi.org/10.1039/c1ce06122d.

(32) Liu, Y.; Niu, S.; Lai, W.; Yu, T.; Ma, Y.; Gao, H.; Zhao, F.; Ge, Z. Crystal Morphology Prediction of Energetic Materials Grown from Solution: Insights into the Accurate Calculation of Attachment Energies. *CrystEngComm* **2019**, *21* (33), 4910–4917. https://doi.org/10.1039/c9ce00848a.

(33) Eckert, M.; Neyts, E.; Bogaerts, A. Modeling Adatom Surface Processes during Crystal Growth: A New Implementation of the Metropolis Monte Carlo Algorithm. *CrystEngComm* **2009**, *11* (8), 1597–1608. https://doi.org/10.1039/b822973m.

(34) Guo, W.; Kundin, J.; Bickermann, M.; Emmerich, H. A Study of the Step-Flow Growth of the PVT-Grown AlN Crystals by a Multi-Scale Modeling Method. *CrystEngComm* **2014**, *16* (29), 6564–6577. https://doi.org/10.1039/c4ce00175c.

(35) Van Den Ende, J. A.; Ensing, B.; Cuppen, H. M. Energy Barriers and Mechanisms in Solid-Solid Polymorphic Transitions Exhibiting Cooperative Motion. *CrystEngComm* **2016**, *18* (23), 4420–4430. https://doi.org/10.1039/c5ce02550h.

(36) Indulkar, A. S.; Box, K. J.; Taylor, R.; Ruiz, R.; Taylor, L. S. PH-Dependent Liquid-Liquid Phase Separation of Highly Supersaturated Solutions of Weakly Basic Drugs. *Mol. Pharm.* **2015**, *12* (7), 2365–2377. https://doi.org/10.1021/acs.molpharmaceut.5b00056.

(37) Zhang, J.; Ebbens, S.; Chen, X.; Jin, Z.; Luk, S.; Madden, C.; Patel, N.; Roberts, C. J. Determination of the Surface Free Energy of Crystalline and Amorphous Lactose by Atomic Force Microscopy Adhesion Measurement. *Pharm. Res.* **2006**, *23* (2), 401–407. https://doi.org/10.1007/s11095-005-9144-1.

(38) Pignataro, B.; Grasso, G.; Renna, L.; Marletta, G. Adhesion Properties on Nanometric Scale of Silicon Oxide and Silicon Nitride Surfaces Modified by 1-Octadecene. *Surf. Interface Anal.* **2002**, *33* (2), 54–58. https://doi.org/10.1002/sia.1161.

(39) Oliphant, T. E. *A Guide to NumPy*; Trelgol Publishing, 2006.

(40) Hunter, J. D. Matplotlib: A 2D Graphics Environment. *Comput. Sci. Eng.* **2007**, *9*, 90–95.

(41) Mullin, J. W. *Crystallization*, 4th ed.; Butterworth Heinemann: Oxford, 2001.

(42) Vekilov, P. G. The Two-Step Mechanism of Nucleation of Crystals in Solution. *Nanoscale* **2010**, *2*, 2346–2357. https://doi.org/10.1039/c0nr00628a.

(43) Vekilov, P. G. Dense Liquid Precursor for the Nucleation of Ordered Solid Phases from Solution. *Cryst. Growth Des.* **2004**, *4* (4), 671–685. https://doi.org/10.1021/cg049977w.

(44) Kashchiev, D.; Vekilov, P. G.; Kolomeisky, A. B. Kinetics of Two-Step Nucleation of Crystals. *J. Chem. Phys.* **2005**, *122*, 244706:1-6. https://doi.org/10.1063/1.1943389.

(45) Jackson, K. A. Nucleation from the Melt. *Ind. Eng. Chem.* **1965**, *57* (12), 29–32.

(46) De Yoreo, J. J.; Vekilov, P. G. Principles of Crystal Nucleation and Growth. *Rev. Mineral. Geochemistry* **2003**, *54* (1), 57–93.

(47) Descamps, M.; Dudognon, E. Crystallization from the Amorphous State: Nucleation-Growth Decoupling, Polymorphism Interplay, and the Role of Interfaces. *J. Pharm. Sci.* **2014**, *103*, 2615–2628. https://doi.org/10.1002/jps.24016.

(48) Chen, F.; Lam, C.-H.; Tsui, O. K. C. The Surface Mobility of Glasses. *Science (80-.).* **2014**, *343*, 975–976.

(49) Zhang, W.; Yu, L. Surface Diffusion of Polymer Glasses. *Macromolecules* **2016**, *49*, 731–735. https://doi.org/10.1021/acs.macromol.5b02294.

(50) Zhu, L.; Brian, C. W.; Swallen, S. F.; Straus, P. T.; Ediger, M. D.; Yu, L. Surface Self-Diffusion of an Organic Glass. *Phys. Rev. Lett.* **2011**, *106*, 256103. https://doi.org/10.1103/PhysRevLett.106.256103.

(51) Moseson, D. E.; Parker, A. S.; Gilpin, C. J.; Stewart, A. A.; Beaudoin, S. P.; Taylor, L. S. Dissolution of Indomethacin Crystals into a Polymer Melt: Role of Diffusion and Fragmentation. *Cryst. Growth Des.* **2019**, *19*, 3315–3328. https://doi.org/10.1021/acs.cgd.9b00200.

(52) Patel, M. A.; Luthra, S.; Shamblin, S. L.; Arora, K. K.; Krzyzaniak, J. F.; Taylor, L. S. *CCDC 1845134: Experimental Crystal Structure Determination*; 2018. https://doi.org/10.5517/ccdc.csd.cc1zy0gd.

(53) Lee, L.-H. Solid Surface Tensions of Amorphous and Crystalline Selenium. *J. Non. Cryst. Solids* **1971**, *6*, 213–220.

(54) Ho, R.; Wilson, D. A.; Heng, J. Y. Y. Crystal Habits and the Variation in Surface Energy Heterogeneity. *Cryst. Growth Des.* **2009**, *9* (11), 4907–4911. https://doi.org/10.1021/cg900696f.

(55) Tran, R.; Xu, Z.; Radhakrishnan, B.; Winston, D.; Sun, W.; Persson, Kristin, A.; Ong, S. P. Surface Energies of Elemental Crystals. *Sci. Data* **2016**, *3* (160080). https://doi.org/10.1038/cgt.2016.38.

(56) German, R. M. Thermodynamics of Sintering. In *Sintering of Advanced Materials*; Woodhead Publishing Limited, 2010; pp 3–32.

(57) Butt, H.-J.; Cappella, B.; Kappl, M. Force Measurements with the Atomic Force Microscope: Technique, Interpretation and Applications. *Surf. Sci. Rep.* **2005**, *59* (1–6), 1–152. https://doi.org/10.1016/j.surfrep.2005.08.003.

(58) Fronczak, S. G.; Browne, C. A.; Krenek, E. C.; Beaudoin, S. P.; Corti, D. S. Non-Contact AFM Measurement of the Hamaker Constants of Solids: Calibrating Cantilever Geometries. *J. Colloid Interface Sci.* **2018**, *517*, 213–220. https://doi.org/10.1016/j.jcis.2018.01.108.

(59) Almgren, F.; Wang, L. Mathematical Existence of Crystal Growth with Gibbs-Thomson Curvature Effects. *J. Geom. Anal.* **2000**, *10* (1), 20–99. https://doi.org/10.1007/BF02921806.

(60) Johnson, C. A. Generalization of the Gibbs-Thomson Equation. *Surf. Sci.* **1965**, *3* (5), 429–444. https://doi.org/10.1016/0039-6028(65)90024-5.

(61) Han, D.; Wang, Y.; Yang, Y.; Gong, T.; Chen, Y.; Gong, J. Revealing the Role of a Surfactant in the Nucleation and Crystal Growth of Thiamine Nitrate: Experiments and Simulation Studies. *CrystEngComm* **2019**, *21* (23), 3576–3585. https://doi.org/10.1039/c9ce00325h.

4. POLYMER AND SURFACTANT EFFECTS ON CRYSTALLIZATION AT THE AMORPHOUS ATAZANAVIR-WATER INTERFACE

4.1 Introduction

Aqueous solubility limitations are a significant challenge in the development of many candidate pharmaceutical products. It is well recognized that at any given time roughly three quarters of pipeline molecules suffer from bioavailability limitations due to low aqueous solubility[1,2]. Among the formulation strategies to mitigate this undesirable physical property is the use of an alternative solid-state form of the active pharmaceutical rather than the traditional stable form[3]. Of particular interest to the community is the amorphous or glassy state, which possesses a greater thermodynamic driving force for dissolution and generates a supersaturated solution at a higher chemical potential for superior absorption kinetics[4]. However, this theoretical solubility advantage proves a double-edged sword, as the high free energy which enhances dissolution also drives crystallization in both the solid state as well as from solution which can result in a loss of potential solubility enhancement[5]. In order to stabilize against this failure mechanism, amorphous pharmaceuticals are typically dispersed in a polymeric matrix, generating what is commonly known as an amorphous solid dispersion (ASD). Such dispersions have previously been employed to stabilized colloidal particles and improve wettability, and have proven to be effective at inhibiting crystallization and extending supersaturation, which are critical to amorphous product performance[6,7].

Understanding the physical stability of ASD formulations and the impact of formulation additives on crystallization tendency of the active pharmaceutical ingredient (API) is a key area of active research focus. Two areas where the greatest focus has typically been placed have been understanding and preventing phase separation and crystallization from the matrix in storage conditions as well as crystallization and de-supersaturation from solution during dosing[8–12]. While both of these failure mechanisms are important, an often overlooked formulation trajectory involves the solid-state amorphous-to-crystal transition in the dosing environment[13]. Traditionally, the rationale employed by formulation science argues that an ASD which is stable against the solid-state crystallization transition in storage will not undergo this phenomenon during dosing, such that the only kinetically relevant route of crystallization *in vivo* is from solution[14]. However, it has become increasingly clear that such an assumption is not necessarily

accurate. Specifically, the ability of solid dispersions to exhibit a liquid-liquid or glass-liquid phase separation (LLPS/GLPS) event in an aqueous medium, though largely beneficial for formulation performance, does raise questions regarding the stabilizing effect of formulation additives[15]. Such a phase separation event occurs when a highly supersaturating formulation releases API to such an extent that the miscibility limit between API and aqueous media is reached. At this point, two liquid phases form (or a glass and liquid phase, depending on the glass transition temperature of the API), with one aqueous-rich phase and a second collodial API-rich phase[16]. While the presence of these subcooled liquid or amorphous API droplets is beneficial for the formation performance by providing a reservoir of drug molecules to rapidly replace dissolved drug as it is absorbed by the body, these droplets also provide a high surface area of potentially unstabilized drug-water interfaces which can then undergo solid-state crystallization transformations[17–19].

Previous research efforts can lend some insight into important factors governing the amorphous-to-solid phase transformation in a dosing-relevant environment. For example, distinct parallels can be drawn between the colloidal amorphous systems produced by GLPS and the two-step nucleation models thought to describe the pathway of solution crystallization of large molecules such as proteins[20]. Within this paradigm, nucleation proceeds via two dimensions of variations in an energetic landscape: local concentration variations to create a dense liquid pre-nucleation cluster and structural variations to generate a molecular template of the crystal lattice[21]. If the drug rich colloids of LLPS are thought of much like dense liquid clusters, it is expected that the ability of API molecules in these drug rich domains to rearrange will be critically important to understanding the crystallization tendency. Indeed, studies demonstrate that molecular mobility is one of the key parameters dictating crystallization kinetics of glassy materials and that reducing the molecular mobility inhibits crystallization[22,23]. Furthermore, phase transformations of pharmaceutical glasses are reported to predominately occur at cracks, defects, and interfaces rather than in the bulk[23]. Of the various hypotheses rationalizing these findings, the data suggest that enhanced molecular mobility at free surfaces often underlies the more rapid crystallization kinetics[24]. A second complicating factor is the role played by water present in the system. Water vapor and moisture have a well-known deleterious effect on the physical stability of amorphous pharmaceuticals through a plasticization effect, whereby absorbed water enhances the molecular mobility and depresses the glass transition temperature of

both unary (neat amorphous API or polymer) and binary (API/polymer mixture) systems[25,26]. Furthermore, water vapor sorption can undermine API/polymer miscibility and result in phase separation and subsequent API crystallization both by enhancing the mobility and by disrupting favorable interactions between API and polymer[27]. These reports apply primarily to systems in ambient conditions with limited water available; the situation becomes increasingly complex in a dosing environment where bulk water exists. The complex interplay between API, polymer, and water molecules makes it quite difficult to predict dynamic phase trajectories and thus product performance[28,29].

The aim of these studies was to shed light onto the phase behavior of amorphous API exposed to aqueous media containing additives of relevance to pharmaceutical formulations. Specifically, these experiments aimed to lend insight into the mechanisms by which dissolved formulation additives might accelerate or inhibit the thermodynamically favorable solid-state phase transformation from amorphous to crystalline drug. Given the important role of surface molecular mobility on the surface crystallization of amorphous organic films in ambient environments, it was hypothesized that the impact of additives in solution during the crystallization of an amorphous API film could be rationalized by the anticipated effect these additives might have on the molecular transport of API molecules.

4.2 Methods and Materials

4.2.1 Materials

Free base atazanavir (ATZ) purchased from Attix Pharmaceuticals (Toronto, Canada) was used as the model compound for this study. Model additives purchased for these studies were hydroxypropyl methyl cellulose acetate succinate (HPMCAS), MF grade and HF grade, from Shin-Etsu Chemical Co. (Tokyo, Japan), polyvinyl acetate (PVAc) from Polysciences, Inc. (Warrington, PA), polyvinylpyrrolidone (PVP) from Sigma-Aldrich (St. Louis, MO), and sodium dodecyl sulfate (SDS) from ThermoFisher Scientific (Fair Lawn, NJ). Buffer was prepared using sodium phosphate dibasic anhydrous and sodium phosphate monobasic monohydrate purchased from ThermoFisher Scientific and sodium chloride purchased from Mallinckrodt Chemicals (Phillipsburg, NJ). Methanol was purchased from Avantor Macron Fine Chemicals (Radnor, PA). The chemical structures of the model materials are shown in Figure 4.1.

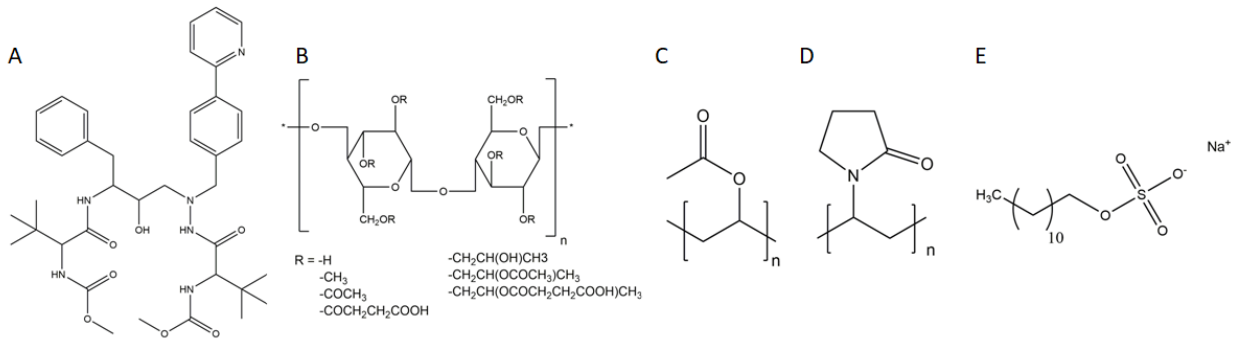

Figure 4.1. Chemical structures of (A) atazanavir, (B) HPMCAS, (C) PVAc, (D) PVP, and (E) SDS.

4.2.2 Crystallization of Amorphous ATZ

Amorphous ATZ samples, buffer solutions, and stock ATZ in methanol solutions were prepared as described previously in Section 3.2. Stock additive solutions were prepared by pre-dissolving polymer into buffer. Stock solutions were then diluted with fresh buffer to generate working solutions of 10 μg/mL HPMCAS, 100 μg/mL HPMCAS, 10 μg/mL PVAc, 10 μg/mL PVP, and 6 μg/mL SDS. Stock ATZ in methanol was added to these to create final crystallization solutions containing additive and 25 μg/mL ATZ in order to minimize surface dissolution (crystalline solubility is approximate 1 μg/mL and amorphous solubility is approximately 68 μg/mL at 37°C). Amorphous ATZ samples were placed into crystallization solutions and held at 40°C via a Fisher Scientific Isotemp 202 water bath.

4.2.3 Sample Characterization

Surface evolution and crystal growth were observed via atomic force microscopy (AFM) and scanning electron microscopy (SEM). AFM measurements were made with a Bruker MultiMode 8 (Technology Forest, TX) operated in Tapping Mode using an NPG probe, cantilever C. A fluid cell was utilized to analyze samples in the presence of incubation media. Samples analyzed with SEM were first fixed onto SEM stubs and sputter coated with platinum at 40mA for 60 seconds. Platinum coated samples were then imaged using a Teneo SEM/VolumeScope (FEI Company, Hillsboro, OR) operated at 5 kV accelerating voltage and 10 mm working distance, with secondary electrons captured using an Everhart-Thornley detector (ETD).

4.2.4 Monte Carlo Simulation

Two-dimensional lattice Monte Carlo (MC) simulations were performed to model the effects of additives on crystal growth. The basis of the model as well as parameter sensitivity studies are described in Section 3.2.6. Lattice sites were set as all initially amorphous pharmaceutical. When a site is selected at random, empty amorphous sites can either undergo a conversion from amorphous to crystalline or a polymer globule could adsorb onto surrounding lattice sites. If a site occupied by a polymer was selected, a trial move of polymer desorption is also possible. The probability of accepting a trial move is determined by the energetic penalties and/or benefits of the given trial move. For crystallization, these energetic changes consist of penalties associated with the formation of new interfaces and a lattice energy benefit to crystallizing adjacent to an existing crystal site. For polymer adsorption/desorption, polymer adsorption is favorable both onto the amorphous material itself as well any crystal faces. Mathematically, polymer driving force for adsorption was described by the Langmuir isotherm and the Gibbs energy for a reversible process. Within this framework, several simplifying assumptions were made to facilitate model formulation. First, only nearest neighbor interactions were considered for energetic calculations. Polymer globules were treated as non-interacting, and polymer adsorption did not affect the likelihood of another globule adsorbing nearby. When selecting polymer adsorption as a trial move, the randomly selected grid site was always chosen to be the upper left corner of the globule, and any overlap of trial polymer sites with existing polymer sites or crystalline sites would result in rejecting the trial move. Computer code for the model was written in Python utilizing Numpy and Matplotlib libraries for mathematical functions and visualization of simulation results (copy of code is available in Appendix C)[31,32].

4.3 Results

4.3.1 Experimental Investigation of Additive Effects on Crystallization

Before performing any crystallization experiments, ATZ films were incubated at room temperature with buffer solutions containing dissolved polymer to understand the manner in which polymer species might interact with the amorphous films. Data from these measurements are presented in Figure 4.2. Figure 4.2A and Figure 4.2F again present the control system in the absence of any additive species in solution. The polymer species in Figure 4.2 are then presented

in order of increasing hydrophilicity, with Figure 4.2B and Figure 4.2G being the most hydrophobic and Figure 4.2E and Figure 4.2J being the most hydrophilic. Beginning with PVAc, Figure 4.2B and Figure 4.2G demonstrate the largest and most distinct polymer globules, as seen by the largest topographical circular features in Figure 4.2B and the most significant contrast in the phase plot of Figure 4.2G. As the polymer chemistry changes to become more hydrophilic, the polymer globules become smaller and less distinct, as illustrated in Figure 4.2C, Figure 4.2D, Figure 4.2H, and Figure 4.2I. It should be noted that while the globules in Figure 4.2C are smaller than those in Figure 4.2B, the surface coverage of HPMCAS-HF is actually greater than the coverage of PVAc. As the hydrophilicity further increases transitioning from HPMCAS-HF to HPMCAS-MF, the number of globules significantly decreases, presumably as more polymer remains in solution or adsorbing as extended, undetectable chains rather than adsorbing onto the film as distinct globules. This can be seen by the sparsity of globular features in Figure 4.2D and the almost completely uniform phase plot in Figure 4.2I. An interesting observation is made in the most hydrophilic system of PVP in Figure 4.2E and Figure 4.2J. The largest surface features are seen in Figure 4.2E which do not appear to take the circular structure typical of polymer globule adsorption. Rather, these features are much sharper and display an almost prismatic habit, indicative of surface crystals rather than polymer. For further confirmation of this assessment, the phase plot in Figure 4.2J shows contrast along the edges of the raised features while the bulk of the features is largely identical to the underlying material. This is in contrast to Figure 4.2G and Figure 4.2H where adsorbed polymer globules show significant phase contrast compared to the amorphous ATZ film. Hence, the surface features present in the PVP system are likely crystalline ATZ rather than polymer.

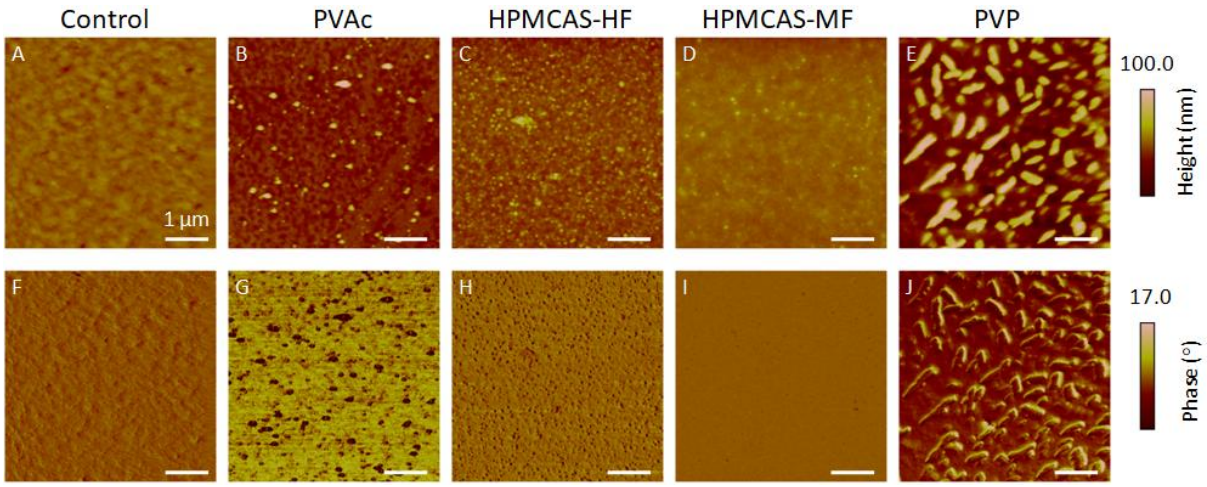

Figure 4.2. AFM micrographs depicting polymer interactions with amorphous ATZ films. Images were captured at room temperature after 1 hour incubation with buffer containing dissolved polymer. (A)-(E) are topographical plots and (F)-(J) are phase contrast plots. (A) and (F) are the reference system containing no dissolved polymer, (B) and (G) contain 10 µg/mL PVAc, (C) and (H) contain 10 µg/mL HPMCAS-HF, (D) and (I) contain 10 µg/mL HPMCAS-MF, and (E) and (J) contain 10 µg/mL PVP.

Initially amorphous ATZ was crystallized in the absence of any polymer or surfactant additives to serve as a control system, with surface evolution shown in Figure 4.3. The initial film in Figure 4.3A in shown to be quite smooth, with a root mean square roughness calculated to be about 3 nm. The phase contrast plot in Figure 4.3C likewise demonstrates very little variability, suggesting a uniform surface of homogenous amorphous state with minimal contamination. After the course of a few hours, the morphology of the surface changes quite significantly; Figure 4.3B and Figure 4.3D reveal the presence of surface crystals. Figure 4.3B depicts raised features with a highly anisotropic needle-like morphology, smaller dispersed nuclei, and larger central structures, representing the variety of expected structural features as well as reflecting the heterogeneity of surface crystallization. Branching off of the larger needles and the spherulitic features is also observed, resulting in an interconnected crystal network. Important features of this phase transformation have been examined at in Section 3.3.1, so the key points to recall for comparison with additive-containing systems are crystal morphology, crystal branching, and the overall timescale of phase transformation[30].

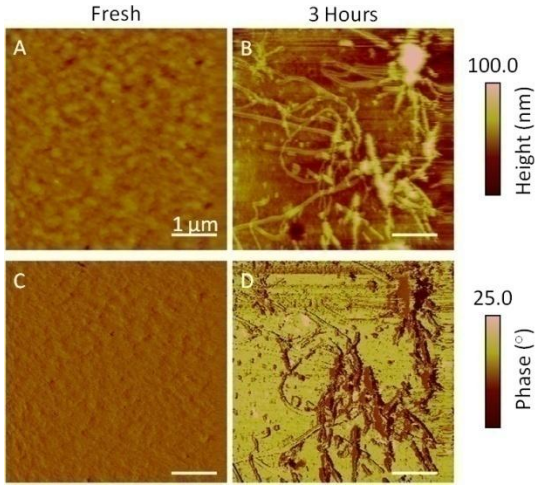

Figure 4.3. AFM micrographs depicting surface evolution of amorphous ATZ film exposed to buffer with no additives. (A) and (C) are the initial film before incubation, while (B) and (D) are the same film after 3 hours of incubation at elevated temperature. (A) and (B) are topographical maps while (C) and (D) are phase contrast plots.

With control experiments performed for reference, the cellulose-based systems from Figure 4.2 were explored more thoroughly via a series of crystallization experiments, with the data presented below in Figure 4.4, Figure 4.5, and Figure 4.6. First, a system containing a dilute HPMCAS-HF solution is studied in Figure 4.4. Much like the reference images in Figure 4.2C, Figure 4.2H, Figure 4.4A and Figure 4.4D show extensive coverage of polymer globules onto the neat amorphous surface, as indicated by raised hemispheres on the topographical plot as well as distinct shifts in phase from the phase contrast plot. After incubation at 40°C for one day (Figure 4.4B and Figure 4.4E), no evidence of crystallization is observed. While the topographical variation does become more pronounced than in the freshly prepared film, the topographical features remain globular. Furthermore, the phase contrast plot in Figure 4.4E is quite consistent with the reference, where dark circular features characteristic of polymer globules can be observed. Even after six days of incubation (Figure 4.4C and Figure 4.4F), both the topographical and phase contrast plots confirm polymer adsorption and do not provide any indication of surface crystals. Hence, these data suggest that the extensive HPMCAS-HF coverage is able to effectively inhibit surface crystallization by shutting down all nucleation.

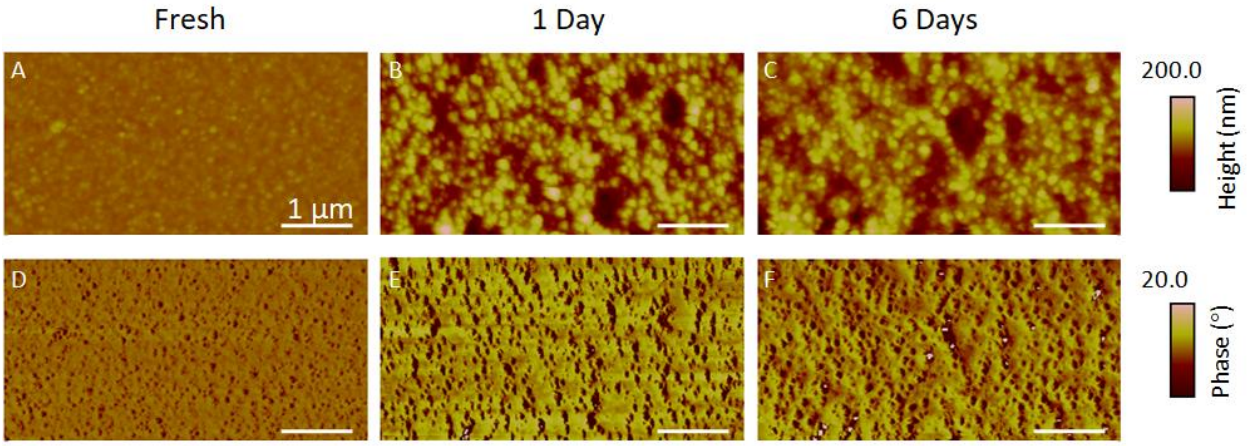

Figure 4.4. AFM micrographs capturing surface evolution of amorphous ATZ film incubated in buffer containing 10 µg/mL HPMCAS-HF at 40°C. (A) and (D) are the initial film before incubation, (B) and (E) show 1 day of incubation time, and (C) and (F) show 6 days of incubation time . (A) - (C) are topographical maps while (D) - (F) are phase contrast plots.

Next, a system containing a dilute HPMCAS-MF solution was studied, with findings presented in Figure 4.5. Given the much less pronounced evidence of polymer interaction as compared to the HPMCAS-HF system (compare Figure 4.2C and Figure 4.2H to Figure 4.2D and Figure 4.2I), it was anticipated that HPMCAS-MF would provide less inhibitory power than the more strongly interacting HPMCAS-HF. Indeed, assessing the system after one day of incubation reveals some subtle differences in topography and phase contrast which suggest evidence of surface crystal nucleation. Examining first the topographical plot (Figure 4.5B), more significant topographical variation can be observed as compared to the reference (Figure 4.5A). Furthermore, the topographical features are largely smooth and rounded, at least at the scale observable when mapping the height. However, the phase contrast plot tells a slightly different story. Unlike the polymer globules in Figure 4.4, the features in Figure 4.5E only show contrast along the edges of the features, which indicates both that these are not smooth or rounded and that they are chemically identical to the film. Additionally, careful observation of Figure 4.5E reveals that these new features exhibit a distinct tabular habit. Hence, there is a strong argument that these surface features are crystalline nuclei rather than adsorbed polymer. Further extending the incubation time to six days results in the growth of these nuclei into needle like crystals, as seen in Figure 4.5C and Figure 4.5F. Morphologically, these crystals are remarkably similar to those from the control system in Figure 4.3 with one important difference; these crystalline domains exhibit significantly less branching. Therefore, dilute HPMCAS-MF is

able to delay, though not prevent, the onset of nucleation and can inhibit branching of the needle-like crystals.

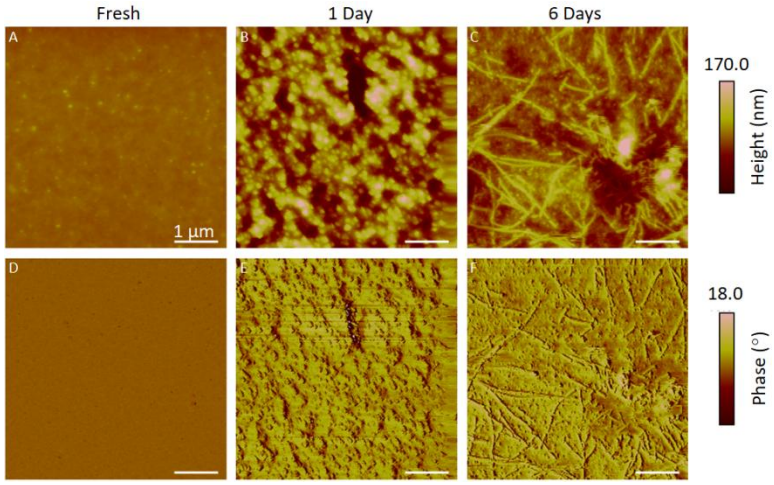

Figure 4.5. AFM micrographs capturing surface evolution of amorphous ATZ film incubated in buffer containing 10 µg/mL HPMCAS-MF at 40°C. (A) and (D) are the initial film before incubation, (B) and (E) show 1 day of incubation time, and (C) and (F) show 6 days of incubation time . (A) - (C) are topographical maps while (D) - (F) are phase contrast plots.

The last polymer system studied, presented in Figure 4.6, contained a more concentrated HPMCAS-MF solution with an order of magnitude increase in polymer concentration. The reference plots in Figure 4.6A and Figure 4.6D show a relatively flat surface, though the presence of globular structures does suggest more extensive polymer adsorption in contrast to the dilute HPMCAS-MF system. This is consistent with the one day incubation time point in Figure 4.6B and Figure 4.6E, which demonstrates evidence of polymer adsorption and no evidence of crystal formation. Thus, the order of magnitude increase in polymer concentration has effectively inhibited crystallization onset relative to the dilute polymer system, which itself inhibited crystallization onset relative to the control system. By two days of incubation (Figure 4.6C and Figure 4.6F), nucleation has occurred as evidenced by the presence of dispersed features displaying a tabular habit. These dispersed nuclei are morphologically similar to those observed after one day of incubation in the more dilute HPMCAS-MF system (Figure 4.5B and Figure 4.5E); the apparent difference in size is merely due to a difference in scale. However, unlike the dilute system, the concentrated HPMCAS-MF system does not exhibit crystal growth and the formation of anisotropic needles. Here, not only has adsorbed polymer delayed the onset of

nucleation and inhibited branching, but polymer also seems to effectively inhibit all crystal growth such that only dispersed crystalline nuclei arise.

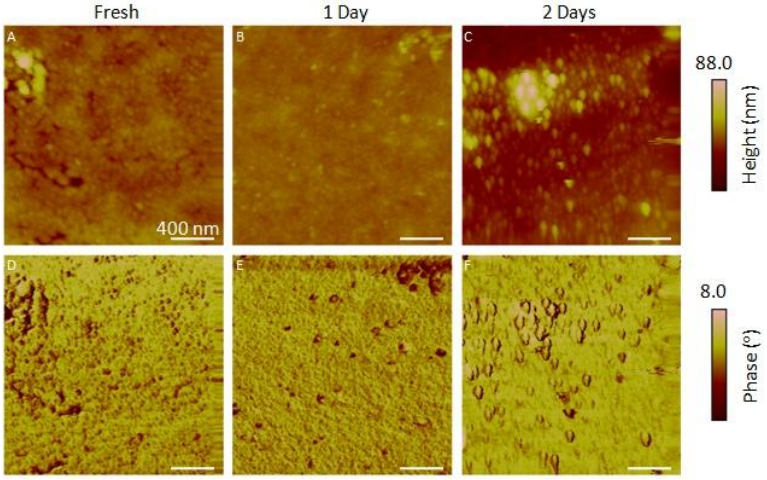

Figure 4.6. AFM micrographs capturing surface evolution of amorphous ATZ film incubated in buffer containing 100 μg/mL HPMCAS-MF at 40°C. (A) and (D) are the initial film before incubation, (B) and (E) show 1 day of incubation time, and (C) and (F) show 2 days of incubation time . (A) - (C) are topographical maps while (D) - (F) are phase contrast plots.

The final system considered in this study contained a surfactant (SDS) rather than a strictly polymer molecule. Data for ATZ crystallization in this system are presented in Figure 4.7. Due to the dramatic nature of the changes in the surface, analysis of this system necessitated more macroscopic imaging techniques. Figure 4.7A and Figure 4.7B compare the entirety of the ATZ sample before and after 24 hours of incubation. Even with the low resolution photograph, there is clear evidence of significant surface evolution, as the surface goes from colorless and translucent to white and opaque. This is a clear indication of crystallization and far more extensive than what occurs in the control or polymer containing systems. Optical microscopy data, shown in Figure 4.7C and Figure 4.7D, further support the assertion of crystallization. Here, an initially translucent glassy material is replaced with a dark and moderately opaque underlying film (see the red circle labeled F, H) along with white and opaque spherulitic features (see the red circle labeled E, G). More detailed assessments of each of these characteristic domains is shown in the SEM micrographs Figure 4.7E through Figure 4.7H.

Turning first to the overlaying white region captured in Figure 4.7E and Figure 4.7G, large crystals are easily observed. Unlike the dendritic or fibrous habit of the needles seen in Figure

4.3 and Figure 4.5, the needle-like crystals seen in Figure 4.7E and Figure 4.7G exhibit a more columnar habit as they become wider and flatter. Moreover, the size of these crystals as well as the interconnected crystalline domains is substantially larger, suggesting significant enhancement of crystal growth. It should also be noted that these crystalline domains are clearly not directly connected to initially amorphous film, unlike all the crystals observed in Figure 4.3, Figure 4.5, and Figure 4.6. Turning now to the remnants of the underlying film shown in Figure 4.7F and Figure 4.7H, it can be seen that most of the film has been cannibalized to grow the extensive crystalline structures, leaving behind a highly porous and intricate amorphous network. Given that the crystals in Figure 4.7E and Figure 4.7G are disconnected from the film, the disintegration of the surface is likely dissolution driven rather than arising from surface diffusion. A particularly interesting insight can be made by examining the higher magnification image in Figure 4.7H. Evidence of a patchwork of thin needle-like crystals quite similar to Figure 4.3 and Figure 4.5 can be seen covering the remainder of the amorphous film, suggesting crystallization at the amorphous surface still occurs via a similar mechanism. However, the new pathway which has generated the much larger crystals in Figure 4.7E and Figure 4.7G has activated crystal growth to occur much more rapidly.

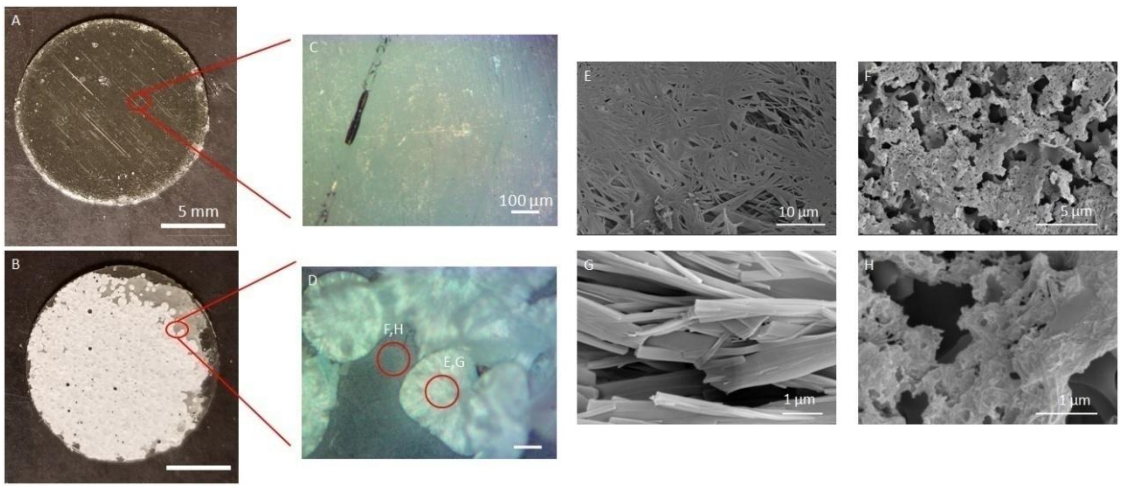

Figure 4.7. Picture and micrographs depicting final surface of amorphous ATZ film before and after incubation for 24 hours in buffer containing 6 µg/mL SDS at 40°C. (A) is a macroscopic picture of the entire fresh film, (B) is a macroscopic picture of the film after incubation, (C) is an optical micrograph of the fresh film, (D) is an optical micrograph post-incubation containing an opaque overlaying region as well as a darker underlying region, (E) and (G) are representative SEM micrographs of the overlaying region, and (F) and (H) are representative SEM micrographs of the underlying region

4.3.2 Modeling of Polymer Effects

Lattice MC simulations exploring the effects of adsorbed polymer on rate of conversion from amorphous to crystalline were performed, with results shown in Figure 4.8, Figure 4.9, and Figure 4.10. The first and simplest system considered, given in Figure 4.8, was crystal growth where polymer pre-equilibrates before the simulation begins to run. During the course of the simulation, adsorbed polymer does not interact with the growing crystals except to restrict sites available to convert. The red pixels represent amorphous sites, yellow pixels represent crystalline sites, and black pixels represent adsorbed polymer. For reference, Figure 4.8A shows simulation snapshots of a control system containing no adsorbed polymer. Important details to note are the morphology of emerging anistropic, interconnected crystalline domains (with great similarity to the needle-like crystals observed experimentally in Figure 4.3) as well as the relative "time scale" of simulation progression and crystal development. It is important to note here that this is not a kinetic MC simulation, as no experimentally determined parameters are being used to govern kinetics, though the relative rate of simulation progression is still a useful semi-quantitative surrogate for rates of crystal growth under different conditions. Figure 4.8B then details a system under identical conditions except for the pre-equilibration of adsorbed polymer up to 25 percent surface coverage. Comparing Figure 4.8A to Figure 4.8B through the lens of morphology and time scale, it can be seen that the shape of emerging crystals in Figure 4.8B is very similar to the control system, albeit with somewhat stunted growth and more exaggerated anisotropy. Similarly, the time scale of conversion is fairly similar, with the polymer system not surprisingly progressing somewhat more slowly. Assessing the rate of simulation progression more quantitatively in Figure 4.8C, there is a very clear trend of increasing polymer coverage resulting in delayed simulation progression. However, this trend is a fairly weak quadratic dependence, as 25 percent polymer surface coverage increases the simulation steps required to convert 50 percent of available sites from amorphous to crystalline by about 30 percent (from 45 million steps to 60 million steps), while 50 percent polymer surface coverage only increases simulation length by about 50 percent (from 45 million steps to 95 million steps).

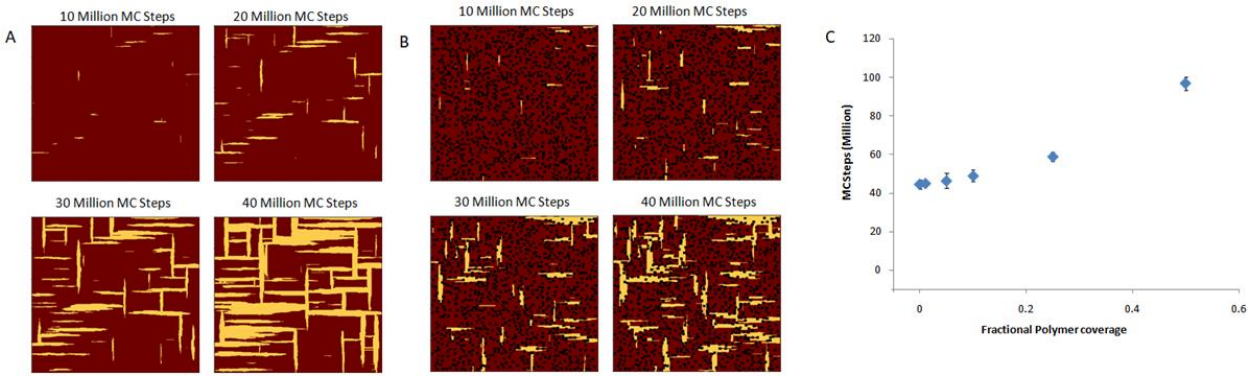

Figure 4.8. MC model results for systems employing polymer pre-equilibration but no dynamic interactions with growing crystals. Red pixels are amorphous sites, yellow pixels are crystalline sites, and black pixels are polymer sites. (A) is several snapshots of a control system containing no polymer, (B) is several snapshots of a system with 25 percent polymer surface coverage, and (C) is a scaling analysis depicting the number of trial MC steps required to achieve 50 percent conversion from amorphous to crystalline of available sites for various polymer surface coverage fractions. Each point represents n = 10 replicates, with error bars representing one standard deviation.

The next version of the MC model, involving more nuance and complexity, is given in Figure 4.9. Now, polymer adsorption/desorption is dynamic and occurs as the simulation progresses. Moreover, this version of the simulation incorporates an energetic benefit for polymers adsorbing onto growing crystals. The aspect of the system explored in Figure 4.9 is the preference of polymer interaction with the various crystal interfaces. Initially simplifying the model by assuming polymer globules have identical interaction strengths with all crystal interfaces, it can be seen in Figure 4.9A that incorporating any polymer interactions with growing crystals results in substantially more growth inhibition than just growth with pre-equilibrated polymers. Specifically comparing Figure 4.9A to Figure 4.8B which depict systems of comparable equilibrium polymer coverage, it is interesting to note that while the system in Figure 4.9A exhibits much lower initial coverage (roughly 5 percent by 5 million MC steps), the tendency of polymer to adsorb onto the growing crystals ultimately leads to much more effective growth inhibition than the pre-equilibrated system. Morphologically, the crystals in Figure 4.9A also exhibit a higher aspect ratio as the adsorbed polymers much more effectively prevent broadening of the crystalline domains. Narrower crystals likely also contribute to sluggish simulation progression, as fewer free interfaces are available for growth compared to the wider crystals in Figure 4.8B.

A more realistic model is visualized in Figure 4.9B, where polymer globules have a variable energetic preference for different crystal interfaces, linearly related to the surface energy

of the interfaces. At a first glance, both Figure 4.9A and Figure 4.9B are nearly identical, with similar rate of simulation progression, apparent polymer coverage and polymer location (namely, grouped along crystal interfaces), and crystal morphology. Figure 4.9C plots both polymer coverage and fractional surface conversion to crystal as a function of trial MC steps for both systems, with a polymer-free system for reference. While only subtle differences can be seen between the two systems, the implications are important for understanding which aspects of the physics need to be taken into account to properly model this phenomenon. Specifically, examining the fractional conversion data depicted by the filled red diamonds (corresponding to Figure 4.9A) and the filled blue triangles (corresponding to Figure 4.9B), it can be seen that enhancing polymer interactions with higher energy interfaces more effectively inhibits crystal growth than indiscriminate polymer interactions. Interestingly, the fractional polymer coverage data reveals that the system from Figure 4.9B (open blue triangles) actually exhibits a lower coverage than the system from Figure 4.9A (open red diamonds) despite superior crystal growth inhibition. This suggests that polymer adsorption and corresponding competitive inhibition at high energy sites is more important than simply achieving high surface coverage. This particular feature is dramatically demonstrated in Figure 4.10, which will be addressed below.

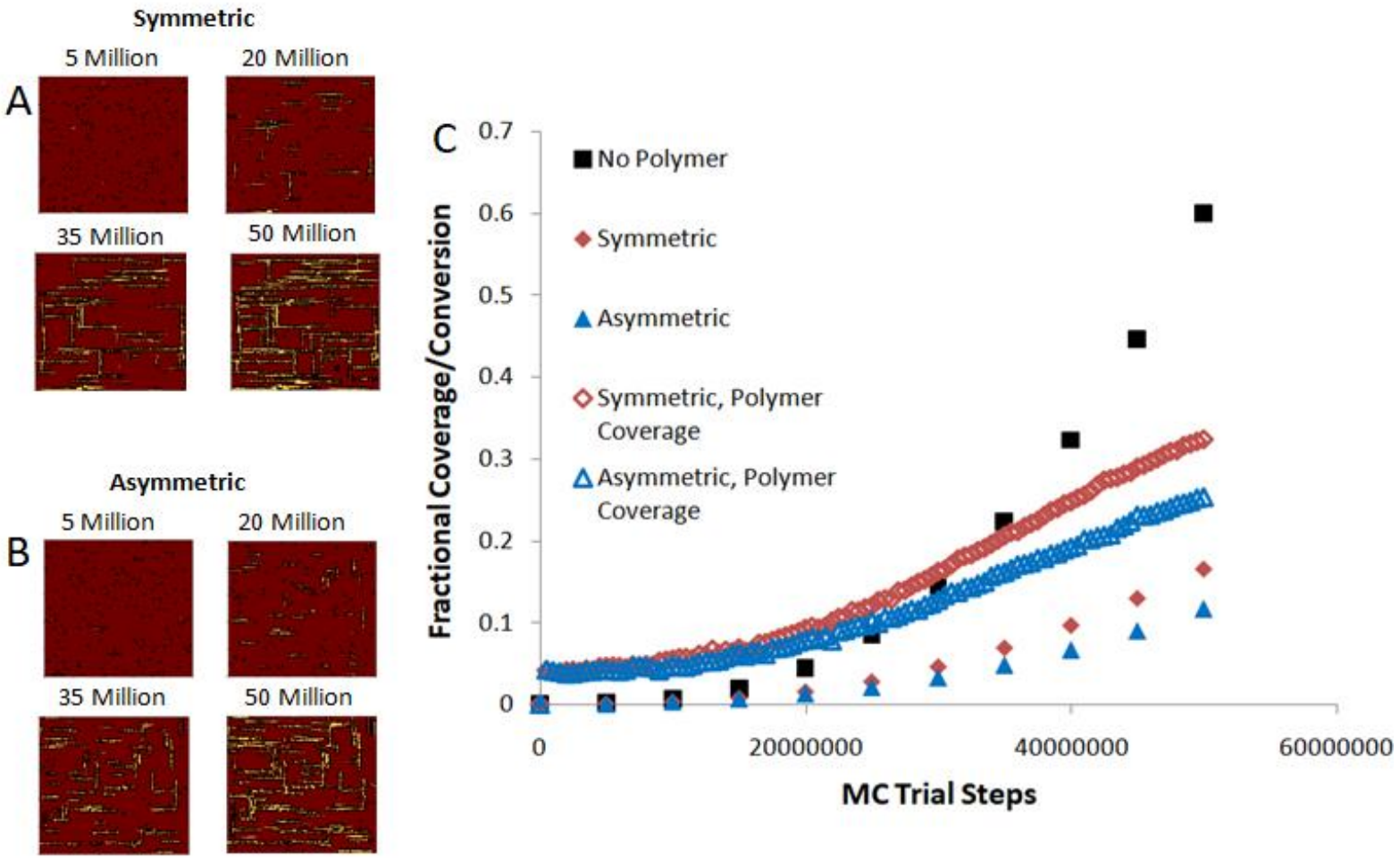

Figure 4.9. MC model predictions of fractional polymer coverage and fractional conversion for systems employing dynamic polymer interactions. (A) shows several snapshots of simulation progress for the uniform interaction strength system (symmetric) depicted by the red diamonds and (B) shows several snapshots of simulation progress for the biased interaction strength system (asymmetric) depicted by blue triangles. (C) plots both dynamic polymer coverage as well as extent of conversion versus number of trial MC steps for three systems. Filled points represent fractional conversion and open points represent fractional polymer surface coverage. Black squares depict the control system with no polymer, red diamonds depict a system with 20 percent equilibrium polymer coverage with equal interaction strength between high energy and low energy crystal interfaces, and blue triangles depict a system with 20 percent equilibrium polymer coverage with stronger polymer interactions with high energy crystal interfaces.

A final parameter examined in these computational studies was the rate of polymer equilibration. In terms of the simulation paradigm, when a vacant site is selected the trial moves available are either i) attempt to convert to crystalline, or ii) attempt to adsorb a polymer. Tuning the rate of polymer equilibration (which has no energetic barrier compared to the potentially high energetic barrier to conversion), is easily achieved by tuning the probability of attempting either of the two trial moves.

Slow polymer equilibration, which is utilized by the systems in Figure 4.9 and Figure 4.10A, corresponds to a 1 percent chance of attempting polymer adsorption and a 99 percent chance of attempting crystallization. Fast polymer equilibration, utilized in the systems in Figure 4.10B and Figure 4.10C, increases the probability of attempting polymer adsorption to 25 percent. Figure 4.10A then is comparable to Figure 4.9B, with similar equilibrium polymer coverage and identical rate of polymer equilibration. Unsurprisingly, the time lapse images for both systems are likewise quite similar with regards to crystal morphology and extent of surface conversion. Accelerating polymer equilibration then has profound effects on surface evolution. Comparing the 10 million step snapshots of Figure 4.10A and Figure 4.10B show dramatically different surfaces with fast equilibration resulting in over twice the polymer surface coverage with similar surface conversion at this early stage of simulation progress. One important difference between the two systems is the apparent morphology of the emerging crystalline domains; there is some evidence of needle-like crystals beginning to form in Figure 4.10A which would be expected to mature as the simulation progresses, while Figure 4.10B shows no high aspect ratio features, only a few small dispersed crystal nuclei. This distinction becomes only more exaggerated after 30 and 50 million trial moves, as the slow equilibration system demonstrates many branching needle like crystals of considerable length whereas the fast equilibration system looks quite uniform across all time lapse snapshots. Doubling the equilibrium polymer coverage as depicted in Figure 4.10C is remarkably similar to Figure 4.10B at all stages of time lapse images, with the only exception being the much darker surface due to more substantial polymer coverage. With regards to crystal conversion and the morphology of emerging crystalline domains, these two systems are largely identical despite the marked difference in polymer coverage. This suggests that rapid equilibration plays a more important role in inhibiting crystallization than high surface coverage. Quantitative treatments of each system are provided in Figure 4.10D which provides more authoritative insights into the state of

each system as the simulations progress. Again offering the polymer-free control system for comparison, the polymer coverage and fractional conversion versus trial steps are plotted (much like Figure 4.9C). Visualized in this manner, quantitative validation is provided for the qualitative observations based on the simulation snap shots. As expected, the 30 percent coverage slow equilibrating system shows an identical trend to the systems in Figure 4.9, with polymer coverage (open orange circles) fitting a sigmoidal trend and crystalline conversion (filled orange circles) following a weak quadratic trend. Rapid equilibration, on the other hand, results in almost instantaneous equilibrium polymer coverage (open blue triangles), with a slight upward linear trend due to polymer adsorbing onto any new crystalline sites. Consequently, crystal growth is almost completely shut down as evidenced by the flat fractional conversion (filled blue triangles). Lastly, the high polymer coverage system rapidly achieves a consistent surface coverage roughly twice the lower coverage system's (open purple diamonds), yet the surface conversion data (filled purple diamonds) is indistinguishable from the fast equilibration, lower coverage system. Even when adjusting the scale of the plot both systems track identically with a very weak quadratic trend.

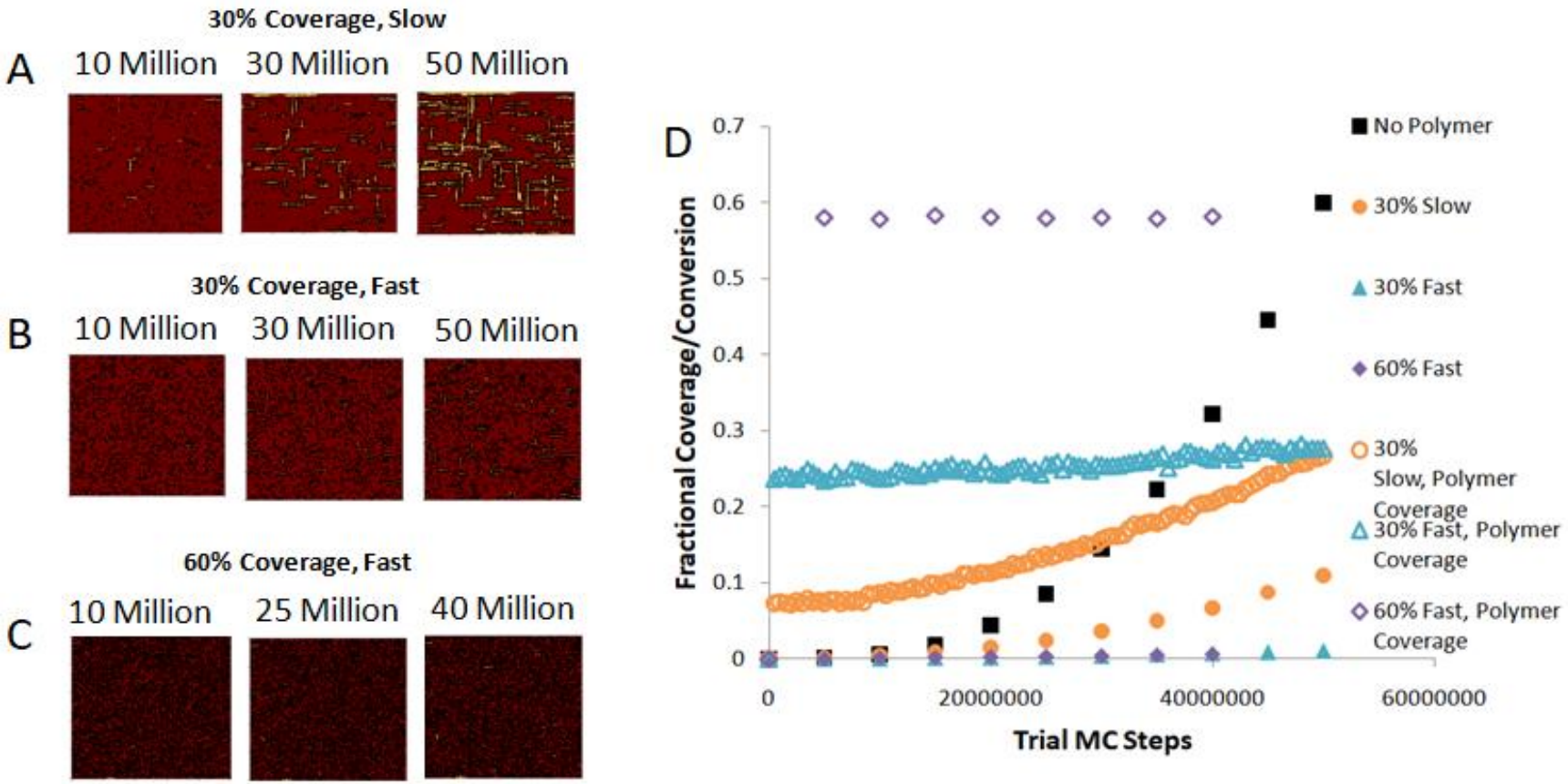

Figure 4.10. MC model predictions of fractional polymer coverage and fractional conversion for systems employing dynamic polymer interactions. (A) shows several snapshots of simulation progress for the lower coverage and slow equilibration system depicted by orange circles, (B) shows several snapshots of simulation progress for the lower coverage and fast equilibration system depicted by blue triangles, and (C) shows several snapshots of simulation progress for the higher coverage and fast equilibration system depicted by purple diamonds. (D) plots both dynamic polymer coverage as well as extent of conversion versus number of trial MC steps for four systems. Filled points represent fractional conversion and open points represent fractional polymer surface coverage. Black squares depict the control system with no polymer, orange circles depict a system with 30 percent equilibrium polymer coverage with slow polymer equilibration, blue triangles depict a system with 30 percent equilibrium polymer coverage with 25 times faster polymer equilibration, and purple diamonds depict a system with 60 percent equilibrium polymer coverage with the faster polymer equilibration.

4.4 Discussion

Many potential factors can influence interactions between species in this complex water-API-additive ternary system. One typical way to represent this interaction strength would be through a ternary Flory-Huggins model and corresponding Flory-Huggins interaction parameters[28,33]. However, this model requires that the ternary system be allowed to mix, which does not necessarily hold when LLPS has occurred and polymer species can interact with but not readily partition into the drug-rich phase[16,34]. Thus, more reliance on experimental insights is necessary in order to properly interpret these data. Previous investigations have revealed that the additive interactions at the drug-water interface are critical to inhibiting or promoting crystallization in systems involving LLPS[35]. Similarly, polymer adsorption tendency at the amorphous drug-water interface, which correlates well with interaction energy, has been shown to be a good predictor of nucleation inhibition from solution[36]. Therefore, a strong argument can be made that understanding the interactions of additives with amorphous drug-water interfaces is critical to predicting and rationalizing crystallization tendency. A clear trend between polymer surface coverage and polymer hydrophobicity can be seen in Figure 4.2, with low coverage for very hydrophobic or hydrophilic species and higher coverage for the intermediate species. The non-monotonic trend of adsorption against hydrophobicity is largely rationalized by considering the balance of polymer-water, polymer-drug, and drug-water interactions[37]. Specifically, given the hydrophobic nature of ATZ, very hydrophobic polymers will prefer to minimize any interactions with water, resulting in large polymer globules which will interact with the drug surface (confirmed by Figure 4.2B and Figure 4.2G). A very hydrophilic polymer, on the other hand, is likely to not interact with the hydrophobic drug and will likely remain in solution. This can have interesting implications, as evidenced by the presence of surface crystals in the system containing PVP (Figure 4.2E and Figure 4.2J). Crystallization promotion in this system will be revisited below in the discussion on the role of SDS. Intermediate interactions with water and drug maximizes the energetic preference for interacting with both species simultaneously, which leads to the most extensive surface coverage through more extended polymer confirmations and/or smaller globules with a larger surface area to volume ratio[38]. Similar findings to these trends are reported in an investigation of polymer inhibition of crystal growth for another hydrophobic API, which then ultimately found that polymer coverage strongly correlated with solution crystal growth inhibition effectiveness[39].

Given that crystallization inhibition in these systems is mediated through polymer interaction, the next important question to ask is mechanistic in nature. How, precisely, do polymer species serve to influence nucleation or growth? Growth inhibition by adsorbed species is explained by poisoning of growth sites and pinning of growth fronts, which has been well validated by theory and experiments[40–43]. This model of growth inhibition is relegated to crystal growth from solution, where adsorbed polymer has little influence on the transport of drug molecules to growth sites and simply physically blocks integration into growth fronts. Nucleation inhibition from solution is likewise thought to be driven by interactions between dissolved polymer and API molecules, physically preventing the association of drug molecules into a crystal lattice[44]. While these factors and mechanisms are also relevant for solid-state crystallization at the amorphous drug-water interface, adsorbed polymer onto amorphous drug surfaces is proposed to modulate film transport properties for an additional mode of nucleation and growth regulation. Models of crystallization from the melt (most similar to the solid-state amorphous to crystal transition) have revealed that nucleation and growth rates are controlled by the velocity of interfacial atoms even as atoms in the bulk liquid are unable to diffuse[45,46]. This is more consistent with the two-step nucleation model (generally more accurate for large and complex molecules) where fluctuations in both orientation and concentration are required to form stable nuclei, as compared to the classical model which only depends on variation in local ordering to form a stable lattice[13,47]. Viewed through this lens, adsorbed polymer species form intermolecular interactions with surface API molecules, hindering their ability to translocate. Drug molecules must break interactions with adsorbed polymers before they can self associate or diffuse across the surface, and many studies have found these interactions to be sufficiently favorable that they are nearly irreversible, leading to very effective inhibition of both transport of surface drug molecules as well as their rearrangement and self association into a crystal lattice[37,43,48–50]. For this reason, the ability of polymer to interact with as many surface molecules as possible will directly affect its ability to modulate surface transport. Hence, high surface coverage, large polymer molecules, and more extended confirmations of adsorbed species all result in greater transport suppression and hence depressed nucleation and growth rates[8,51].

Turning now to the crystallization results in Figure 4.4, Figure 4.5, and Figure 4.6, experimental observation of surface evolution can further refine the understanding of the mechanistic role of adsorbed polymer species. First, inhibition effectiveness is shown to be

directly related to adsorption affinity, clearly demonstrated by the complete nucleation inhibition in Figure 4.4 compared to the delayed nucleation onset in Figure 4.5. In the context of transport modulation, the nearly complete surface coverage of HPMCAS-HF means virtually all interfacial ATZ molecules are bound to polymer, preventing any diffusion or concerted rearrangement into a lattice. This is consistent with other findings that even a few nanometers (smaller than the size of the globules here) of polymer coating on amorphous drug surfaces completely inhibits crystal growth and reduces API mobility by orders of magnitude[8]. HPMCAS-MF exhibits far less extensive coverage, meaning many surface molecules are still able rearrange. It should be noted that there is still a significant delay in the onset of nucleation and much slower growth compared to the control system (Figure 4.3), which, too, can be understood in the framework of thermodynamic driving forces and transport kinetics. It is well established that amorphous surfaces have a distribution of surface energy sites, with local and global heterogeneities related to cracks, defects, and the relative orientation of surface molecules[52–55]. This surface energy heterogeneity has a two-fold effect on surface evolution; sites of high surface energy have a greater chemical potential, meaning they are preferred sites of nucleation, growth, and branching and they have a greater driving force for transport down the chemical potential gradient leading to a spatial distribution of mobility[56]. However, high surface energy sites also serve as preferential sites for additive adsorption due to the greatest decrease in free energy upon adsorbing[57]. Biased adsorption onto different crystallographic faces has already been known to influence crystal habit as high coverage faces are unable to grow even as surface energy of disparate faces in the absence of additive dictates the preferred crystal habit[58–61]. Hence, it is plausible for corresponding nucleation and growth modulation to be true in amorphous systems, which is explored by comparing Figure 4.3, Figure 4.5, and Figure 4.6. The delayed onset of nucleation in systems with a low concentration of HPMCAS-MF present is explained by competitive adsorption onto the highest energy sites where nucleation is most likely to occur. When nucleation does eventually occur, the next highest energy molecules will be those which undergo surface transport towards the nuclei to grow the crystal as well as towards the high energy crystal sites which are most prone to initiate branching (as this generally occurs at defects or dislocations)[62]. Slow crystal growth and the absence of branching in Figure 4.5 are then consistent with the notion that polymer adsorption onto the most mobile surface molecules prevents transport towards the growing surface while adsorption onto high energy crystal sites

(which promote branching) prevent branching from taking place. Increasing the dissolved polymer concentration by an order of magnitude (Figure 4.6) will lead to more extensive adsorption. There is evidence of this based on the presence of more globular features in the AFM micrographs and there are substantial experimental and theoretical studies validating this phenomenon[37]. Increasing the driving force for adsorption means lower energy sites will also become occupied by polymer globules, such that only slow nucleation is possible and crystal growth is not observed. Figure 4.6 is consistent with this argument, as disparate nuclei are observed by 48 hours of crystallization but no crystal growth is seen.

Orthogonal interrogation of crystallization inhibition is explored by Monte Carlo simulation, where Figure 4.8, Figure 4.9, and Figure 4.10 provide additional insight into the important features of polymer adsorption necessary to reproduce the physical systems. There are a few noteworthy limitations of this simplistic model which need to be addressed from the outset. Perhaps most importantly, this model is unable to fully capture the impact on molecular transport due to the nature of model formulation. Kinetic and transport impacts are merely inferred, though this does not undermine model utility. A similar model has already successfully been used to study the control system from Figure 4.3 and has been used to validate a novel model of dissolution in amorphous solid dispersion systems[30,63]. With this in mind, each figure allows for exploration of different hypothetical modes of polymer interaction with the film to aid in elucidation of the mechanism of polymer action. Figure 4.8 tests the model of polymer interaction solely with amorphous drug, essentially acting as a template for crystal growth by physically blocking sites but not interacting with the emerging crystalline domains. There is some argument to be made for this model, as the average surface energy of the amorphous film is expected to be significantly greater than that of the crystals[64]. However, such an assumption fails to account for the thermodynamic sink provided by a surface for growth to occur as nearby amorphous molecules can reduce their free energy by incorporation into a stable lattice. Observing Figure 4.8, it is evident that polymer pre-equilibration (or polymers interacting exclusively with the amorphous surface) is not an accurate model of the physical system. Comparing Figure 4.8A to Figure 4.8B, it is clear that even 25 percent surface coverage has minimal influence on the onset of nucleation, rate of simulation progression, or the morphology of crystalline domains, in stark contrast to the experimental data. The weak scaling presented in Figure 4.8C is not consistent with inhibition effectiveness correlations to surface coverage

demonstrated by both theory and experiment, further cementing the judgment that interactions with the emerging crystals are a critical feature of polymer action[39,65].

Next, Figure 4.9 explores the role of interaction preference with different crystal faces. Examining the literature, the data are fairly conclusive that additive adsorption is face specific, both due to specific interactions between additive and API as well as the general surface energy differences of each face[58,66]. By extension, it is expected that relating the probability of polymer adsorption to the surface energy of a given face will provide a more realistic model. Comparing Figure 4.9A to Figure 4.9B, only subtle differences can be seen in simulation progression. To accurately assess these systems, the quantitative data in Figure 4.9C provides more insight. As noted previously, this plot shows that despite exhibiting lower coverage as the simulation progresses, the adsorbed polymers in system in Figure 4.9B more effectively inhibit crystal growth, albeit the disparity is less significant than the general effect of allowing polymers to interact with the growing crystals. The only difference between the symmetric and asymmetric interaction systems in Figure 4.9 are the preference of interaction with high energy crystal faces, so any difference in simulation progression can be attributed to the effect of preferential inhibition at high energy sites. These data, particularly when interpreted in light of Figure 4.8C, highlight that the inhibition effectiveness through surface poisoning is not simply governed by surface coverage but by coverage onto the highest energy sites.

Figure 4.10 now explores the importance of the rate of polymer equilibration. Theory and experiments confirm that in the absence of a well mixed vessel, it is not known *a priori* if mass transport to the surface or adsorption/integration of polymer will be rate limiting which can make it difficult to presume the rate of polymer equilibration relative to the timescale of surface evolution[67]. However, looking at the experimental data in Figure 4.2, Figure 4.4, Figure 4.5, and Figure 4.6 there is strong evidence to suggest that in this system polymer equilibration will occur much more quickly than crystal growth. Furthermore, Figure 4.4A, Figure 4.4B, and Figure 4.4C demonstrate that while equilibration might take up to one day in this system, equilibrium coverage appears to have been achieved before any evidence of crystallization is seen. In light of these observations, Figure 4.10 demonstrates that rapid equilibration is critical to crystallization inhibition. Significantly delayed growth is seen in Figure 4.10B compared to Figure 4.10A where equilibrium coverage is identical but equilibration rate is approximate 25 times as large. Doubling the equilibrium coverage provides no further inhibitory effect, demonstrating that rapid

equilibrium is far more important than surface coverage for effective growth inhibition. This can largely be rationalized by understanding where these polymers will adsorb. In the slow equilibration system, crystal nuclei have sufficient time to grow into needle like crystals before being capped by polymers. When equilibration is rapid, polymers can adsorb onto the high energy faces which most promote growth, competitively inhibiting any crystal growth and effectively resulting in stunted nuclei not unlike the surface features seen in Figure 4.6C. If these sites are inhibited, any additional polymer will only serve to slightly delay nucleation in the simulation by removing viable sites but will do little to further inhibit crystal growth. Therefore, properly accounting for the rate of polymer equilibration and where on the surface polymer will equilibrate is key to understanding inhibition effectiveness.

The final phenomenon for consideration in these studies is crystallization promotion in the surfactant laden system. Crystallization promotion by SDS and some other surfactants is reported in the literature though the precise mechanism is not generally known[42,68]. In fact, there are several surfactant effects that one would expect to delay crystallization rather than promote it. For instance, surfactants will reduce the surface energy of any interface where they partition, which reduces the thermodynamic driving force for any phase change. Furthermore, surfactant assembling around API molecules could be expected to prevent integration into a crystal lattice much like polymer adsorption. Understanding the promotion effect requires returning to the earlier points of the balance of interactions in such a ternary system and the effect of these interactions on molecular transport. In this case, interactions between additive and water are much more favorable than in the cases of more hydrophobic polymer species while still maintaining favorable additive-drug interactions due to the hydrophobic SDS tail. Thus, surfactant will partition in such a manner near the interface so as to create a slightly more lipophilic environment just above the amorphous surface. Since interactions with the API will not be as strong as the additive becomes more hydrophilic, additive will be able to move somewhat more freely in this region of media. This can both enhance surface diffusion as well as activate a solution-mediated crystallization mechanism, both of which serve to enhance crystallization kinetics. Only the right additive properties will enable this effect to occur, with just the right balance between drug-additive and water-additive interaction thermodynamics. It is suggested that this same effect explains the behavior of the PVP system in Figure 4.2, as this polymer is quite hydrophilic and will thus predominantly remain in solution rather than

adsorbing onto the surface. However, ATZ molecules will still prefer to interact with the hydrophobic portions of PVP as compared to water, which means that PVP near the surface will serve to create this more lipophilic environment that is more favorable for ATZ transport. This also helps explain the morphology difference of the crystals observed in Figure 4.2E where the crystals appear wider than the high anisotropy needles in other systems. Rather, these crystals could be an earlier stage of the large crystals seen in Figure 4.7 given their morphological similarities. Thus, it is likely that crystallization promotion by additives is likely due to bridging the thermodynamic gap between water and drug to create an intermediate region where drug transport is rapid and crystals can readily nucleate and grow.

4.5 Conclusions

The ultimate aim of these studies was to provide more fundamental insight into the role of dissolved additive species on the crystallization tendency of drug-rich amorphous surfaces exposed to aqueous media, with the goal of motivating future work to elucidate mechanisms of action. Instances of both crystallization inhibition and promotion are observed, where the effect of additive is largely rationalized by interaction preferences between drug and polymer, drug and water, and polymer and water along with the corresponding impact on transport of drug molecules as these thermodynamics change. Favorable polymer-drug interactions are shown to inhibit crystallization through competitive adsorption onto high energy sites, physically blocking crystal growth and reducing the mobility of surface molecules. Favorable polymer-water interactions are proposed to create a lipophilic water environment which can activate solution mediated crystallization and enhance the mobility of surface molecules. Taken together, these data lend significant insight into the phase trajectory of drug rich amorphous drug interfaces during dosing and can provide guidance towards formulation design principles to maintain amorphous character to ensure product performance.

4.6 References

(1) Thayer, A. M. Finding Solutions. *Chem. Eng. News* **2010**, *88* (22), 13–18.

(2) Babu, N. J.; Nangia, A. Solubility Advantage of Amorphous Drugs and Pharmaceutical Cocrystals. *Cryst. Growth Des.* **2011**, *11*, 2662–2679. https://doi.org/10.1021/cg200492w.

(3) Williams, H. D.; Trevaskis, N. L.; Charman, S. A.; Shanker, R. M.; Charman, W. N.; Pouton, C. W.; Porter, C. J. H. Strategies to Address Low Drug Solubility in Discovery and Development. *Pharmacol. Rev.* **2013**, *65*, 315–499. https://doi.org/10.1124/pr.112.005660.

(4) Craig, D. Q. M.; Royall, P. G.; Kett, V. L.; Hopton, M. L. The Relevance of the Amorphous State to Pharmaceutical Dosage Forms: Glassy Drugs and Freeze Dried Systems. *Int. J. Pharm.* **1999**, *179*, 179–207. https://doi.org/10.1016/S0378-5173(98)00338-X.

(5) Hancock, B. C.; Parks, M. What Is the True Solubility Advantage for Amorphous Pharmaceuticals? *Pharm. Res.* **2000**, *17* (4), 397–404. https://doi.org/10.1023/A:1007516718048.

(6) Chiou, W. L.; Riegelman, S. Pharmaceutical Applications of Solid Dispersion Systems. *J. Pharm. Sci.* **1971**, *60* (9), 1281–1302.

(7) Kim, K. T.; Lee, J. Y.; Lee, M. Y.; Song, C. K.; Choi, J.; Kim, D.-D. Solid Dispersions as a Drug Delivery System. *J. Pharm. Investig.* **2011**, *41* (3), 125–142. https://doi.org/10.4333/KPS.2011.41.3.125.

(8) Sun, Y.; Zhu, L.; Wu, T.; Cai, T.; Gunn, E. M.; Yu, L. Stability of Amorphous Pharmaceutical Solids: Crystal Growth Mechanisms and Effect of Polymer Additives. *AAPS J.* **2012**, *14* (3), 380–388. https://doi.org/10.1208/s12248-012-9345-6.

(9) Knapik, J.; Wojnarowska, Z.; Grzybowska, K.; Hawelek, L.; Sawicki, W.; Wlodarski, K.; Markowski, J.; Paluch, M. Physical Stability of the Amorphous Anticholesterol Agent (Ezetimibe): The Role of Molecular Mobility. *Mol. Pharm.* **2014**, *11*, 4280–4290. https://doi.org/10.1021/mp500498e.

(10) Bhugra, C.; Pikal, M. J. Role of Thermodynamic, Molecular, and Kinetic Factors in Crystallization from the Amorphous State. *J. Pharm. Sci.* **2008**, *97* (4), 1329–1349. https://doi.org/10.1002/jps.21138.

(11) Alonzo, D. E.; Gao, Y.; Zhou, D.; Mo, H.; Zhang, G. G. Z. Z.; Taylor, L. S. Dissolution and Precipitation Behavior of Amorphous Solid Dispersions. *J. Pharm. Sci.* **2011**, *100* (8), 3316–3331. https://doi.org/10.1002/jps.22579.

(12) Alonzo, D. E.; Zhang, G. G. Z.; Zhou, D.; Gao, Y.; Taylor, L. S. Understanding the Behavior of Amorphous Pharmaceutical Systems during Dissolution. *Pharm. Res.* **2010**, *27* (4), 608–618. https://doi.org/10.1007/s11095-009-0021-1.

(13) Vekilov, P. G. Dense Liquid Precursor for the Nucleation of Ordered Solid Phases from Solution. *Cryst. Growth Des.* **2004**, *4* (4), 671–685. https://doi.org/10.1021/cg049977w.

(14) Edueng, K.; Mahlin, D.; Larsson, P.; Bergström, C. A. S. Mechanism-Based Selection of Stabilization Strategy for Amorphous Formulations: Insights into Crystallization Pathways. *J. Control. Release* **2017**, *256*, 193–202. https://doi.org/10.1016/j.jconrel.2017.04.015.

(15) Mosquera-Giraldo, L. I.; Taylor, L. S. Glass-Liquid Phase Separation in Highly Supersaturated Aqueous Solutions of Telaprevir. *Mol. Pharm.* **2015**, *12* (2), 496–503. https://doi.org/10.1021/mp500573z.

(16) Ilevbare, G. A.; Taylor, L. S. Liquid-Liquid Phase Separation in Highly Supersaturated Aqueous Solutions of Poorly Water-Soluble Drugs: Implications for Solubility Enhancing Formulations. *Cryst. Growth Des.* **2013**, *13*, 1497–1509. https://doi.org/10.1021/cg301679h.

(17) Indulkar, A. S.; Gao, Y.; Raina, S. A.; Zhang, G. G. Z.; Taylor, L. S. Exploiting the Phenomenon of Liquid-Liquid Phase Separation for Enhanced and Sustained Membrane Transport of a Poorly Water-Soluble Drug. *Mol. Pharm.* **2016**, *13* (6), 2059–2069. https://doi.org/10.1021/acs.molpharmaceut.6b00202.

(18) Indulkar, A. S.; Lou, X.; Zhang, G. G. Z.; Taylor, L. S. Insights into the Dissolution Mechanism of Ritonavir–Copovidone Amorphous Solid Dispersions: Importance of Congruent Release for Enhanced Performance. *Mol. Pharm.* **2019**, *16*, 1327–1339. https://doi.org/10.1021/acs.molpharmaceut.8b01261.

(19) Lee, S.; Teich, E. G.; Engel, M.; Glotzer, S. C. Entropic Colloidal Crystallization Pathways via Fluid–Fluid Transitions and Multidimensional Prenucleation Motifs. *Proc. Natl. Acad. Sci. U. S. A.* **2019**, *116* (30), 14843–14851. https://doi.org/10.1073/pnas.1905929116.

(20) Vekilov, P. G. The Two-Step Mechanism of Nucleation of Crystals in Solution. *Nanoscale* **2010**, *2*, 2346–2357. https://doi.org/10.1039/c0nr00628a.

(21) Vekilov, P. G. Nucleation of Crystals in Solution. *AIP Conf. Proc.* **2010**, *1270*, 60–77. https://doi.org/10.1063/1.3476239.

(22) Cai, T.; Zhu, L.; Yu, L. Crystallization of Organic Glasses: Effects of Polymer Additives on Bulk and Surface Crystal Growth in Amorphous Nifedipine. *Pharm. Res.* **2011**, *28*, 2458–2466. https://doi.org/10.1007/s11095-011-0472-z.

(23) Descamps, M.; Dudognon, E. Crystallization from the Amorphous State: Nucleation-Growth Decoupling, Polymorphism Interplay, and the Role of Interfaces. *J. Pharm. Sci.* **2014**, *103*, 2615–2628. https://doi.org/10.1002/jps.24016.

(24) Sun, Y.; Zhu, L.; Kearns, K. L.; Ediger, M. D.; Yu, L. Glasses Crystallize Rapidly at Free Surfaces by Growing Crystals Upward. *Proc. Natl. Acad. Sci.* **2011**, *108* (15), 5990–5995. https://doi.org/10.1073/pnas.1017995108.

(25) Mehta, M.; Kothari, K.; Ragoonanan, V.; Suryanarayanan, R. Effect of Water on Molecular Mobility and Physical Stability of Amorphous Pharmaceuticals. *Mol. Pharm.* **2016**, *13* (4), 1339–1346. https://doi.org/10.1021/acs.molpharmaceut.5b00950.

(26) Hancock, B. C.; Zografi, G. The Relationship between the Glass Transition Temperature and the Water Content of Amorphous Pharmaceutical Solids. *Pharm. Res.* **1994**, *11* (4), 471–477. https://doi.org/10.1023/A:1018941810744.

(27) Li, N.; Gilpin, C. J.; Taylor, L. S. Understanding the Impact of Water on the Miscibility and Microstructure of Amorphous Solid Dispersions: An AFM–LCR and TEM–EDX Study. *Mol. Pharm.* **2017**, *14*, 1691–1705. https://doi.org/10.1021/acs.molpharmaceut.6b01151.

(28) Chen, Y.; Liu, C.; Chen, Z.; Su, C.; Hageman, M.; Hussain, M.; Haskell, R.; Stefanski, K.; Qian, F. Drug-Polymer-Water Interaction and Its Implication for the Dissolution Performance of Amorphous Solid Dispersions. *Mol. Pharm.* **2015**, *12*, 576–589. https://doi.org/10.1021/mp500660m.

(29) Raina, S. A.; Alonzo, D. E.; Zhang, G. G. Z.; Gao, Y.; Taylor, L. S. Impact of Polymers on the Crystallization and Phase Transition Kinetics of Amorphous Nifedipine during Dissolution in Aqueous Media. *Mol. Pharm.* **2014**, *11*, 3565–3576. https://doi.org/10.1021/mp500333v.

(30) Parker, A. S.; Taylor, L. S.; Beaudoin, S. P. The Role of Surface Energy Heterogeneity on Crystal Morphology during Solid-State Crystallization at the Amorphous Atazanavir–Water Interface. *CrystEngComm* **2020**, *22*, 3179–3187. https://doi.org/10.1039/c9ce02007a.

(31) Oliphant, T. E. *A Guide to NumPy*; Trelgol Publishing, 2006.

(32) Hunter, J. D. Matplotlib: A 2D Graphics Environment. *Comput. Sci. Eng.* **2007**, *9*, 90–95.

(33) Rumondor, A. C. F.; Taylor, L. S. Effect of Polymer Hygroscopicity on the Phase Behavior of Amorphous Solid Dispersions in the Presence of Moisture. *Mol. Pharm.* **2010**, *7* (2), 477–490. https://doi.org/10.1021/mp9002283.

(34) Taylor, L. S.; Zhang, G. G. Z. Physical Chemistry of Supersaturated Solutions and Implications for Oral Absorption. *Adv. Drug Deliv. Rev.* **2016**, *101*, 122–142. https://doi.org/10.1016/j.addr.2016.03.006.

(35) Ilevbare, G. A.; Liu, H.; Pereira, J.; Edgar, K. J.; Taylor, L. S. Influence of Additives on the Properties of Nanodroplets Formed in Highly Supersaturated Aqueous Solutions of Ritonavir. *Mol. Pharm.* **2013**, *10* (9), 3392–3403. https://doi.org/10.1021/mp400228x.

(36) Mosquera-Giraldo, L. I.; Borca, C. H.; Parker, A. S.; Dong, Y.; Edgar, K. J.; Beaudoin, S. P.; Slipchenko, L. V.; Taylor, L. S. Crystallization Inhibition Properties of Cellulose Esters and Ethers for a Group of Chemically Diverse Drugs: Experimental and Computational Insight. *Biomacromolecules* **2018**, *19* (12), 4593–4606. https://doi.org/10.1021/acs.biomac.8b01280.

(37) Somasundaran, P.; Krishnakumar, S. Adsorption of Surfactants and Polymers at the Solid-Liquid Interface. *Colloids Surfaces A Physicochem. Eng. Asp.* **1997**, *123–124*, 491–513. https://doi.org/10.1016/S0927-7757(96)03829-0.

(38) Roiter, Y.; Minko, S. AFM Single Molecule Experiments at the Solid-Liquid Interface: In Situ Conformation of Adsorbed Flexible Polyelectrolyte Chains. *J. Am. Chem. Soc.* **2005**, *127*, 15688–15689. https://doi.org/10.1021/ja0558239.

(39) Schram, C. J.; Taylor, L. S.; Beaudoin, S. P. Influence of Polymers on the Crystal Growth Rate of Felodipine: Correlating Adsorbed Polymer Surface Coverage to Solution Crystal Growth Inhibition. *Langmuir* **2015**, *31*, 11279–11287. https://doi.org/10.1021/acs.langmuir.5b02486.

(40) Kubota, N. Effect of Impurities on the Growth Kinetics of Crystals. *Cryst. Res. Technol.* **2001**, *36* (8–10), 749–769. https://doi.org/10.1002/1521-4079(200110)36:8/10<749::AID-CRAT749>3.0.CO;2-#.

(41) Black, S. N.; Davey, R. J.; Halcrow, M. The Kinetics of Crystal Growth in the Presence of Tailor-Made Additives. *J. Cryst. Growth* **1986**, *79*, 765–774. https://doi.org/10.1016/0022-0248(86)90552-X.

(42) Schram, C. J.; Beaudoin, S. P.; Taylor, L. S. Polymer Inhibition of Crystal Growth by Surface Poisoning. *Cryst. Growth Des.* **2016**, *16*, 2094–2103. https://doi.org/10.1021/acs.cgd.5b01779.

(43) Ziller, K. H.; Rupprecht, H. Control of Crystal Growth in Drug Suspensions. *Drug Dev. Ind. Pharm.* **1988**, *14* (15–17), 2341–2370.

(44) Song, R. Q.; Cölfen, H. Additive Controlled Crystallization. *CrystEngComm* **2011**, *13* (5), 1249–1276. https://doi.org/10.1039/c0ce00419g.

(45) Jackson, K. A. Crystal Growth Kinetics. *Mater. Sci. Eng.* **1984**, *65* (1), 7–13. https://doi.org/10.1016/0025-5416(84)90194-0.

(46) Jackson, K. A. The Interface Kinetics of Crystal Growth Processes. *Interface Sci.* **2002**, *10* (2–3), 159–169. https://doi.org/10.1023/A:1015824230008.

(47) Vekilov, P. G. Nucleation. *Cryst. Growth Des.* **2010**, *10*, 5007–5019. https://doi.org/10.1021/cg1011633.

(48) Baird, J. A.; Taylor, L. S. Evaluation of Amorphous Solid Dispersion Properties Using Thermal Analysis Techniques. *Adv. Drug Deliv. Rev.* **2012**, *64* (5), 396–421. https://doi.org/10.1016/j.addr.2011.07.009.

(49) Holmber, K.; Jonsson, B.; Kronberg, B.; Lindman, B. *Surfactants and Polymers in Aqueous Solutions*, 2nd ed.; John Wiley & Sons: Wets Sussex, 2002. https://doi.org/10.1109/MEI.1998.714652.

(50) Hughey, J. R. Dissolution of Stabilized Amorphous Drug Formulations. In *Poorly Soluble Drugs: Dissolution and Drug Release*; Gregory K. Webster, J. Derek Jackson, Robert G. Bell, Eds.; 2017; pp 393–418.

(51) Etika, K. C.; Cox, M. A.; Grunlan, J. C. Tailored Dispersion of Carbon Nanotubes in Water with PH-Responsive Polymers. *Polymer (Guildf).* **2010**, *51*, 1761–1770. https://doi.org/10.1016/j.polymer.2010.02.024.

(52) Lee, L.-H. Solid Surface Tensions of Amorphous and Crystalline Selenium. *J. Non. Cryst. Solids* **1971**, *6*, 213–220.

(53) Tran, R.; Xu, Z.; Radhakrishnan, B.; Winston, D.; Sun, W.; Persson, Kristin, A.; Ong, S. P. Surface Energies of Elemental Crystals. *Sci. Data* **2016**, *3* (160080). https://doi.org/10.1038/cgt.2016.38.

(54) German, R. M. Thermodynamics of Sintering. In *Sintering of Advanced Materials*; Woodhead Publishing Limited, 2010; pp 3–32.

(55) Ho, R.; Wilson, D. A.; Heng, J. Y. Y. Crystal Habits and the Variation in Surface Energy Heterogeneity. *Cryst. Growth Des.* **2009**, *9* (11), 4907–4911. https://doi.org/10.1021/cg900696f.

(56) Berthier, L. Dynamic Heterogeneity in Amorphous Materials. *Physics (College. Park. Md).* **2011**, *4*, 42. https://doi.org/10.1103/physics.4.42.

(57) Khan, M. A. S.; Ganguly, B. Can Surface Energy Be a Parameter to Define Morphological Change of Rock-Salt Crystals with Additives? A First Principles Study. *CrystEngComm* **2013**, *15*, 2631–2639. https://doi.org/10.1039/c3ce26764d.

(58) You, H.; Liu, X.; Liu, H.; Fang, J. Theoretical Description of the Role of Amine Surfactant on the Anisotropic Growth of Gold Nanocrystals. *CrystEngComm* **2016**, *18* (21), 3934–3941. https://doi.org/10.1039/c6ce00550k.

(59) Liu, Y.; Niu, S.; Lai, W.; Yu, T.; Ma, Y.; Gao, H.; Zhao, F.; Ge, Z. Crystal Morphology Prediction of Energetic Materials Grown from Solution: Insights into the Accurate Calculation of Attachment Energies. *CrystEngComm* **2019**, *21* (33), 4910–4917. https://doi.org/10.1039/c9ce00848a.

(60) Zhou, D.; Jin, S.; Li, Y.; Qiu, F.; Deng, F.; Wang, J.; Jiang, Q. Effect of Stoichiometry on the Surface Energies of {100} and {111} and the Crystal Shape of TiCx and TiNx. *CrystEngComm* **2013**, *15* (4), 643–649. https://doi.org/10.1039/c2ce26419f.

(61) Han, D.; Wang, Y.; Yang, Y.; Gong, T.; Chen, Y.; Gong, J. Revealing the Role of a Surfactant in the Nucleation and Crystal Growth of Thiamine Nitrate: Experiments and Simulation Studies. *CrystEngComm* **2019**, *21* (23), 3576–3585. https://doi.org/10.1039/c9ce00325h.

(62) Mullin, J. W. *Crystallization*, 4th ed.; Butterworth Heinemann: Oxford, 2001.

(63) Moseson, D. E.; Parker, A. S.; Gilpin, C. J.; Stewart, A. A.; Beaudoin, S. P.; Taylor, L. S. Dissolution of Indomethacin Crystals into a Polymer Melt: Role of Diffusion and Fragmentation. *Cryst. Growth Des.* **2019**, *19*, 3315–3328. https://doi.org/10.1021/acs.cgd.9b00200.

(64) Zhang, J.; Ebbens, S.; Chen, X.; Jin, Z.; Luk, S.; Madden, C.; Patel, N.; Roberts, C. J. Determination of the Surface Free Energy of Crystalline and Amorphous Lactose by Atomic Force Microscopy Adhesion Measurement. *Pharm. Res.* **2006**, *23* (2), 401–407. https://doi.org/10.1007/s11095-005-9144-1.

(65) Kubota, N.; Mullin, J. W. A Kinetic Model for Crystal Growth from Aqueous Solution in the Presence of Impurity. *J. Cryst. Growth* **1995**, *152*, 203–208.

(66) Zimmermann, A.; Millqvist-Fureby, A.; Elema, M. R.; Hansen, T.; Mullertz, A.; Hovgaard, L. Adsorption of Pharmaceutical Excipients onto Microcrystals of Siramesine Hydrochloride: Effects on Physicochemical Properties. *Eur. J. Pharm. Biopharm.* **2009**, *71*, 109–116. https://doi.org/10.1016/j.ejpb.2008.06.014.

(67) Bourne, J. R.; Davey, R. J.; Gros, H.; Hungerbühler, K. The Rotating Disc Configuration in the Measurement of Crystal Growth Kinetics from Solution. *J. Cryst. Growth* **1976**, *34* (2), 221–229. https://doi.org/10.1016/0022-0248(76)90133-0.

(68) Chen, J.; Ormes, J. D.; Higgins, J. D.; Taylor, L. S. Impact of Surfactants on the Crystallization of Aqueous Suspensions of Celecoxib Amorphous Solid Dispersion Spray Dried Particles. *Mol. Pharm.* **2015**, *12* (2), 533–541. https://doi.org/10.1021/mp5006245.

5. EFFECT OF DISSOLVED ADDITIVES ON TRANSPORT PROPERTIES OF AMORPHOUS PHARMACEUTICAL SURFACES

5.1 Introduction

Amorphous materials continue to be increasingly relevant to pharmaceutical formulations, particularly as drug discovery paradigms identify lipophilic and poorly water soluble candidate molecules for development[1–3]. Many other formulation strategies, despite improving the solubilization of active pharmaceutical ingredients (API), often fail to improve intestinal absorption and bioavailability as these solubilizing techniques do not increase the activity of free drug molecules in solution[4,5]. Amorphous drug formulations can generate supersaturation with an enhanced chemical potential leading to superior formulation performance, supported by *in vivo* evidence of bioavailability enhancement[6]. Challenges to the development and implementation of amorphous formulations include unfavorable mechanical properties which undermine manufacturability as well as physical and chemical instabilities[7–11]. Among these difficulties is the double-edged sword of the chemical potential of the amorphous state; the same thermodynamic advantage which promotes supersaturation and absorption also provides a driving force for crystallization and loss of theoretical solubility advantage[12,13]. Another related double-edged sword of amorphous formulation behavior is liquid-liquid phase separation (LLPS). During dissolution, if sufficient supersaturation is achieved the solution concentration can exceed the miscibility limit of drug in water and induce a phase separation event, resulting in a colloidal drug-rich phase and aqueous phase[14–16]. It is generally accepted that the presence of LLPS nandroplets is favorable to formulation performance, as colloidal drug particles rapidly dissolve to maintain the solution at high supersaturation, providing a reservoir of drug and improving absorption during dosing[17,18]. However, these colloidal drug domains exhibit high curvature (and corresponding high surface energy) due to their size and they are not necessarily intimately mixed with stabilizing additives, meaning there is a propensity for crystallization to occur[19–21]. This phase transition must be properly understood and mitigated for highly supersaturating oral drug formulation strategies to flourish.

Previous investigations of this phase transformation phenomenon and the general dynamics of amorphous pharmaceutical systems have provided some key insights into important factors underlying crystallization as well as the means by which additive species can regulate

nucleation and growth. In these systems, crystal growth is shown to occur predominantly at the surface, with surface growth rates orders of magnitude faster than growth rates in the bulk[22]. Furthermore, these surface crystals tend to grow up out of the plane of the surface even as they grow laterally, in some cases growing hundreds of nanometers above the amorphous surface below[23]. Studies of crystallization in the absence of any nucleation- or growth-regulating additives have revealed the important role played by the surface energy of the film in dictating sites of probable nucleation, rates of crystal growth, and eventual crystal morphology[24]. Surface energy is also shown to be an important term describing the method of crystallization inhibition by adsorbed polymer species; polymers can competitively adsorb onto high energy sites to reduce surface molecular mobility and prevent nucleation and growth at the most preferred high energy sites. Crystallization promotion by polymer or additive species appears to occur by dissolved species assembling at the API-water interface and improving the thermodynamic favorability of API molecules moving through this solvated region, enhancing their mobility, as described in Chapter 4.

Together, these observations hint at additive species influencing surface crystallization by regulating the transport phenomena of API molecules. It is well supported in the literature that this solid-state crystallization is mediated by surface diffusion of interfacial API molecules driven by chemical potential gradients and interfacial energy[25,26]. Hence, it is hypothesized that additives will have a measurable and predictable impact on the transport of drug molecules based on their observed effect on crystallization behavior; crystallization inhibition is predicted to correlate to a reduction in the surface diffusion coefficient while crystallization promotion is predicted to correlate to the activation of the dissolution-deposition (or solution mediated) transport pathway. A method for determining the dominant transport mechanism facilitating surface rearrangement in similar systems is reported in the literature and suggested as an appropriate means by which to test this hypothesis[27,28].

5.2 Methods and Materials

5.2.1 Materials

Surface decay studies were performed with free base atazanavir (ATZ) purchased from Attix Pharmacuetical (Toronto, Canada) as the model compound. Additive species in this study

were MF grade hydroxypropyl methyl cellulose acetate succinate (HPMCAS), purchased from Shin Etsu Chemical Co. (Tokyo, Japan) and sodium dodecyl sulfate (SDS) purchased from ThermoFisher Scientific (Fair Lawn, NJ). Phosphate buffer was prepared from sodium chloride purchased from Mallinckrodt Chemicals (Phillipsburg, NJ) as well as sodium phosphate monobasic monohydrate and sodium phosphate dibasic anhydrous purchased from ThermoFisher Scientific. Methanol for preparing stock ATZ solutions was purchased from Avantor Macron Fine Chemicals (Radnor, PA).

5.2.2 Sinusoidal Film Preparation

Amorphous sinusoidal ATZ films were prepared by template imprinting and cooling the melt. First, 50 mg of ATZ powder were melted at 240°C onto a 15 mm steel puck and cooled to room temperature to leave an unpatterned amorphous sample. Sinusoidal patterns were imprinted using holographic diffraction gratings purchased from Edmunds Optics (Barrington, NJ). To imprint, ATZ samples were placed onto an MPress Heat Press (HeatPressNation, Fullerton, CA) held at 135°C. The template was then pressed onto the sample with a fixed down force for 60 seconds. The sample was then cooled and the template was removed to leave an amorphous sinusoidal ATZ film.

5.2.3 Surface Decay Measurements

Measurements of surface topography were performed *in situ* using a MultiMode 8 atomic force microscope (AFM) from Bruker (Technology Forest, TX) operated in contact mode using an NPG probe, cantilever C in a fluid cell. Samples were maintained at 30°C with a resistive heating element affixed to the AFM scanner. Surface decay took place in media composed of pH 6.8 phosphate buffer, 25 μg/mL ATZ, and 10 μg/mL HPMCAS-MF, 100 μg/mL HPMCAS-MF, or 6 μg/mL SDS, prepared as described in Section 4.2.2. Topographical images were processed using Nanoscope Analysis software, using a 6^{th} order flattening algorithm to remove non-sinusoidal surface variation and were cross-section averaged orthogonal to the direction of the sine wave. An original MATLAB script was used to analyze the averaged cross-sections and subsequent decay over time (full copy of code is available in Appendix D).

5.3 Theory and Method Development

5.3.1 Mathematical Theory

Under carefully controlled conditions, it is possible to model mathematically the evolution of liquid and solid surfaces driven by surface energy gradients. If a surface of interest can be patterned with a well-defined shape, one can solve the governing transport equations analytically and arrive at an exact expression for how a surface will rearrange depending on which transport mechanism is dominant. These expressions have been determined previously in the literature, and a thorough derivation is provided in Appendix A[29,30]. As discussed in Section 2.6.3 the relaxation of a nearly planar sinusoidal film is given by Equation (2.2) and Equation (2.3):

$$h(t) = \alpha \exp(-Kt) \tag{5.1}$$

and

$$K = F\omega + (A + C)\omega^3 + B\omega^4 \tag{5.2}$$

where

$$\omega = \frac{2\pi}{\lambda} \qquad F = \frac{\gamma}{2\eta}$$

$$A = \frac{c_0 \gamma \Omega^2 D_l}{kT} \qquad C = \frac{D_b \gamma \Omega}{kT} \qquad B = \frac{\nu D_s \gamma \Omega^2}{kT}$$

Here, h is the surface height of the film, t is time, α is amplitude of the sine wave, K is the decay constant, λ is the wavelength of the film, γ is the surface energy, η is the viscosity, c_0 is the solute concentration above the film, Ω is the molecular volume, m is the molecular mass, k is Boltzmann's constant, T is temperature, D_l is the diffusion coefficient of solute in solution, D_b is the bulk diffusion coefficient, and D_s is the surface diffusion coefficient. The terms in Equation (5.2) correspond to viscous flow (F), dissolution and deposition (A), bulk diffusion (C) and surface diffusion (B). Based on this knowledge, a method has been previously reported in the literature describing a systematic means of performing surface decay measurements to extract the transport properties of amorphous films under various conditions[31]. While this technique has thus far been successfully applied to glass and subcooled liquid systems studied in air, to date no reports of successful implementation in an aqueous environment are available. Furthermore, there are no studies utilizing these techniques to study a heterogeneous API-additive surface to measure the effect of additives on film transport properties. Additionally, the sample preparation technique is highly dependent on the precise API studied, with no previous related studies

utilizing ATZ. Thus, further development and extension of the method beyond what is available in the literature was necessary.

5.3.2 Sample Preparation

Sample preparation proved to be quite difficult to optimize, as imprinting a high fidelity sine wave onto the glass or subcooled liquid required systematic study of imprint temperature, force, and time. Some examples of films prepared under different conditions are shown in Figure 5.1.Generally speaking, if the sample was subjected to insufficient temperature, force, or printing time, the surface was unable to adequately wet the template and no usable sine wave was imparted, as seen in Figure 5.1A. Alternatively, excessive temperature, force, or print time resulted in complete wetting of the template and substantial interfacial adhesion such that attempting to remove the template resulted in cohesive internal failure within the film and subsequent film fracture and removal of sinusoidal surface, as seen in Figure 5.1B. Optimizing imprint temperature was the most straightforward, as imprinting occurs to the subcooled liquid so the operating temperature is bounded by the melting point and the glass transition temperature. The temperature in fact has a reduced upper bound due to solid state crystallization occurring in the subcooled liquid. As shown in Figure 3.2, solid state crystallization from the melt can occur on the time scale of surface preparation, so the true upper bound on operating temperature is set by the maximum temperature before crystals are observed on the timescale of sample preparation. Imprint force and time is optimized more empirically, though force is limited by the capabilities of the heated press used to imprint the film or the force transducer used to measure the printing force. In this case, print force was optimized to the point where the force would remain stable and the film would not relax via viscous flow under the pressure generated by the template on the film. Lastly, imprint time could be optimized by producing the highest quality film under the given temperature and force selection. A proper balance of all sample preparation parameters allows the film to adopt the shape of the template while still ensuring film integrity, such as the sample shown in Figure 5.1C.

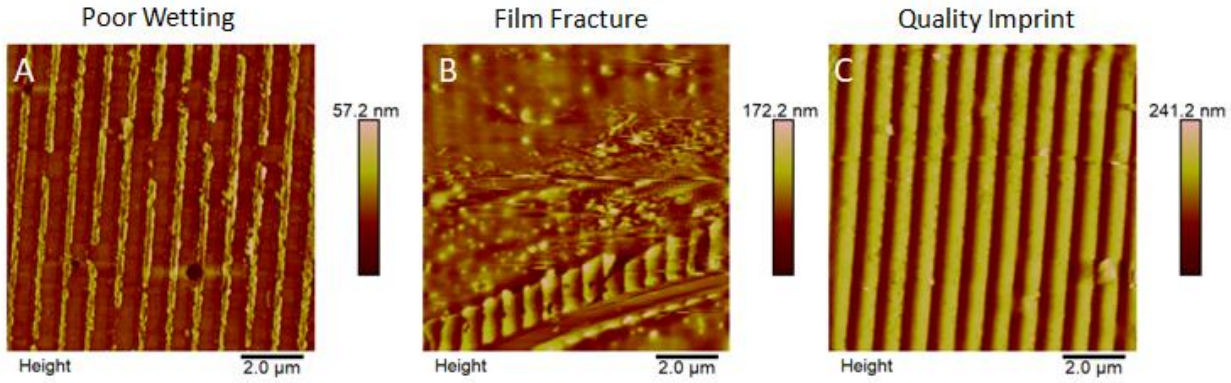

Figure 5.1. AFM micrographs of sinusoidal films prepared under different conditions. (A) depicts a film prepared with little down force and poor template wetting, preventing the transfer of template wave. (B) depicts a film subjected to force for twice the recommended imprint time, demonstrating film fracture which occurred when removing the template. (C) depicts a film prepared as described in Section 5.2.2.

5.3.3 Sample Analysis

One particular challenge which was not addressed in the literature is illustrated by a typical sample and averaged cross section shown in Figure 5.2. Considering Equation (2.2) and Equation (2.3), it is critical to accurately determine both the frequency as well as amplitude of the sine wave describing this surface. Quite obviously, the while Figure 5.2A does appear fairly regular, the surface function in Figure 5.2B is not a perfect sine wave. Thus, it is unclear what value should be used for the amplitude. While this surface could be modeled and reconstructed mathematically, the transport equations are only solved exactly in the base case of a single sine wave used to construct the surface.

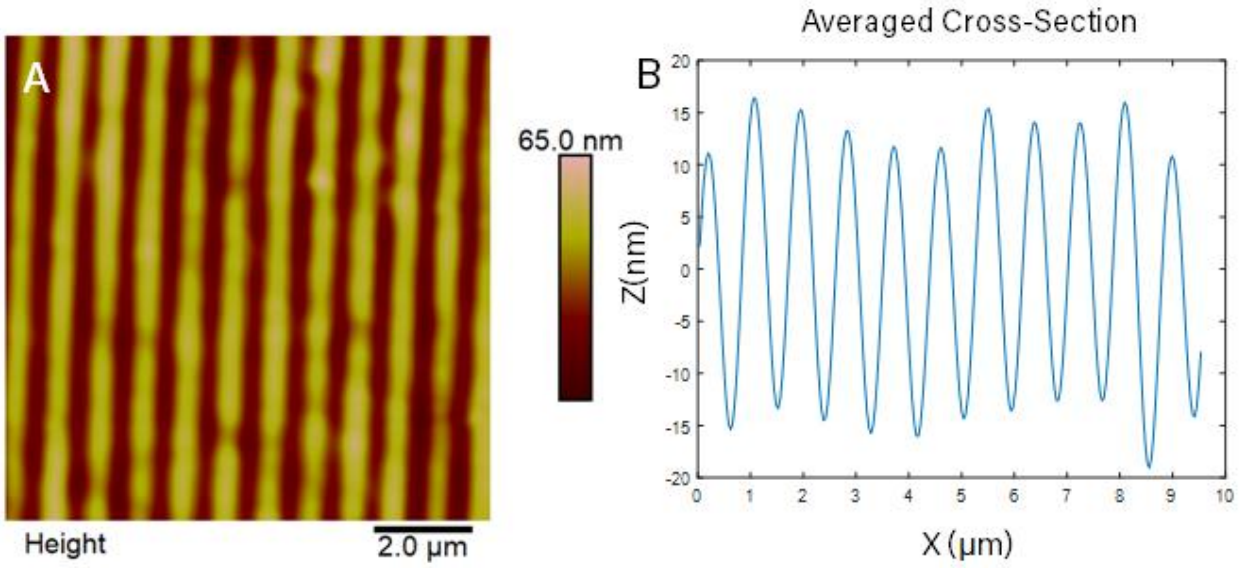

Figure 5.2. Example of sinusoidal ATZ film. (A) is an AFM topographical plot, and (B) is the averaged cross-section.

In light of this challenge, three feasible strategies were proposed to model a nearly sinusoidal surface as a single sine wave and extract the relevant parameters. Schematics depicting each method are given in Figure 5.3. First, Figure 5.3A depicts the simplest means of estimating the parameters of surface features. Here, amplitude is estimated by half the difference between the average of the five highest peaks and the average of the five lowest valleys. Frequency is determined by the average of peak-to-peak or valley-to-valley distance. These measures are intuitive and trivial to determine, though sensitive to any outlier data and of course they require a user's judgment to ensure the surface is sinusoidal in nature lest the interpretation be misleading. The next logical level of sophistication for describing the surface is performing a Finite Fourier Transform (FFT) of the surface, which effectively decomposes a surface function into the constitutive sine waves which, when combined, reproduce the surface. The amplitude spectrum (which plots the amplitude against the frequency of each constitutive sine wave) for the trial surface is shown in the top of Figure 5.3B. From the amplitude spectrum it is obvious that the FFT has identified one dominant sine wave (corresponding to the tallest peak around frequency 1.9 μm^{-1}), plotted along with the real surface in the bottom of Figure 5.3B. It can be seen that this single sine function from the FFT severely underestimates the actual size of peaks, though the frequency is quite similar to the true periodicity of the surface features. Failing to incorporate higher frequency noise means the FFT will always underestimate the true size of

surface features, which only becomes more pronounced the more the surface deviates from a perfect sine wave. The final technique involves the greatest mathematical complexity, which consists of non-linear least squares regression using a sine wave with variable frequency and amplitude as the trial function for regression. Non-linear regression is quite complex, in this case using built-in MATLAB fitting algorithms to determine the best amplitude and frequency to minimize error between the trial function and the surface height data. Convergence in non-linear regression is known to be quite fickle, such that generally a very good initial guess for the fitting parameters (in this case, particularly the frequency) is needed to ensure confidence in algorithmic convergence. Fortunately, the FFT from Figure 5.3 provides an excellent initial guess for the frequency, ensuring convergence as long as the surface continues to resemble a sine wave. A fit using this algorithm is provided in Figure 5.3C, showing excellent agreement between the fitted function and the cross-section data.

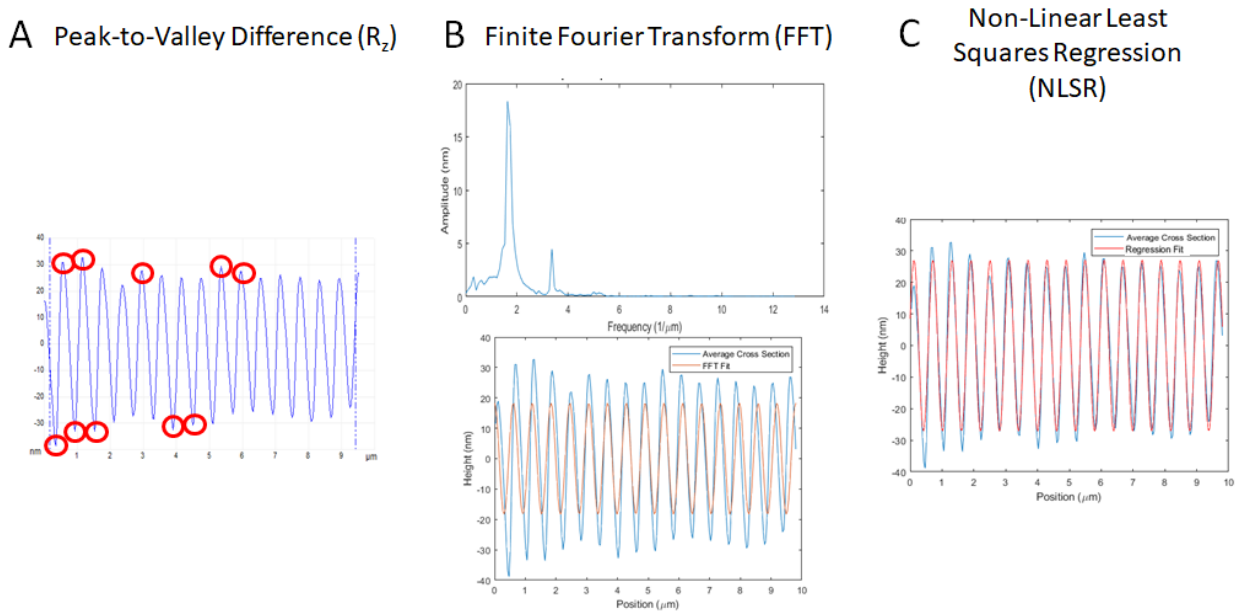

Figure 5.3. Schematics outlining three surface analysis algorithms based on the averaged cross-section in Figure 5.2B. (A) shows the amplitude calculation based on an average of the tallest peaks and average of the lowest valleys with frequency determined by average peak-to-peak distance, (B) shows the amplitude spectrum based on an FFT and the fit of the dominant sine wave extracted from the FFT plot, and (C) depicts the fit from non-linear least squares regression using a sine wave as the objective function and the results of part (B) as the initial guess for amplitude and frequency.

5.3.4 Experimental Challenges

Experimental observation of film topography in solution via AFM was fraught with difficulties, as illustrated in Figure 5.4. The experimental setup was intended to create a system where the only driving force for surface rearrangement was derived from curvature. However, due to the metastability of the film and the supersaturated solution, the film integrity could often be compromised upon addition of solution for measurements. Specifically, unless the solution is maintained at the amorphous solubility limit (which in practice is nearly impossible without precipitation inhibitors), there is a tendency for the film to dissolve somewhat in order to achieve equilibrium with the solution. Furthermore, large portions of the film could be removed from the surface either due to significant dissolution or film fracture and the high pressure gradients which can occur during rapid fluid addition. These sample failures are depicted in Figure 5.4A, which shows a film which undergoes sample fracture upon fluid addition and a film which exhibits surface dissolution upon fluid addition. Another measurement difficulty shown in Figure 5.4B relates to problems with the AFM cantilever tip accurately tracking the surface. Water sorption into the surface of the film can create an almost gel-like interface rather than a hard solid surface. As the surface becomes increasingly malleable, the AFM cantilever when in contact mode will tend to drag through the surface rather than tracing its features, as is seen in the time lapse of images in Figure 5.4B. One possible solution to this problem is operating the AFM in tapping or intermittent contact mode rather than contact mode, as this reduces the force imparted into the surface and is less destructive during imaging. However, it was found early on in these studies that contact and tapping mode did not produce quantitatively identical height measurements, such that operating in tapping mode risks introducing inaccuracy into height determination. While the effects in Figure 5.4 do not necessarily lead to measurement error, they do result in unusable data and the loss of many samples, significantly hindering progress of studies of these systems.

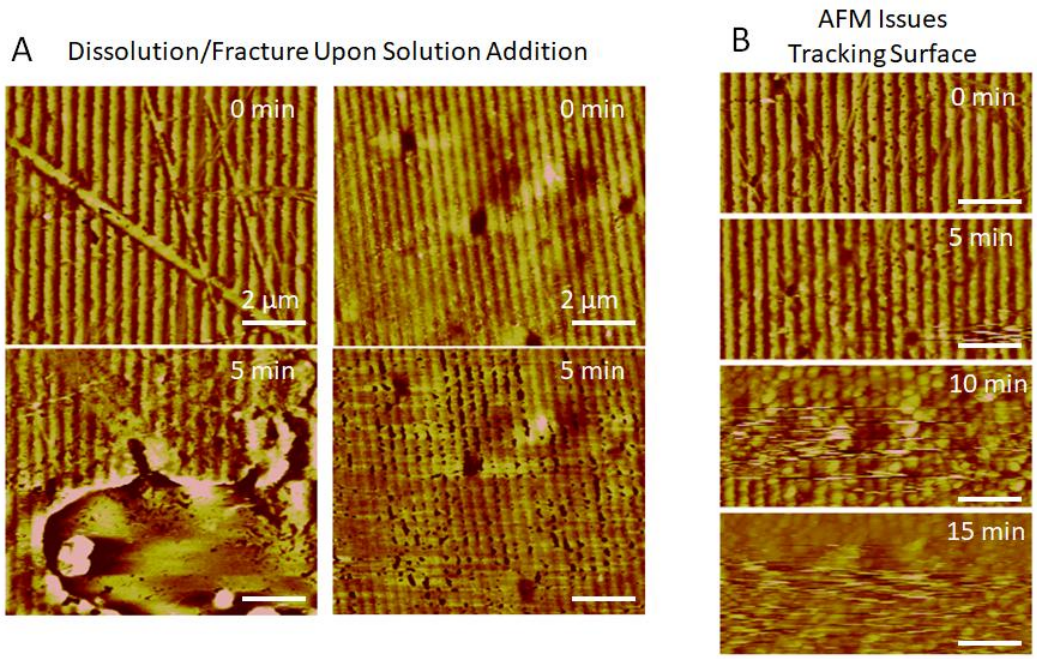

Figure 5.4. AFM micrographs depicting aberrant behavior which confounded surface height measurements. (A) shows films which fracture and/or dissolve upon addition of buffer solution and (B) shows the tendency of film to uptake buffer and become plastic, preventing accurate tracking of surface topography by the AFM tip in contact mode.

One subtle factor undermining reproducibility was temperature variability during the course of experiments. Initially, no forced temperature control was used and samples were regulated by ambient temperature. However, it was discovered that decay kinetics tended to depend on how long the AFM had been powered on and operated any given day, leading to systematic error in initial experiments. Thus, temperature measurements were made using a dual thermocouple/resistive heater which used the thermocouple for feedback control with a PID controller. Temperature and surface height for a trial experiment are shown in Figure 5.5. It can be seen that in the absence of any temperature control, the actual sample temperature can rise by almost 10 degrees by the time thermal equilibrium with the surroundings is achieved, even though ambient laboratory temperature is roughly 20°C. This is largely due to thermal inputs from the laser used to measure AFM cantilever deflection, along with the lack of convective heat transfer away from the sample. It is quite clear then that the true sample temperature can vary by several degrees over the course of a day. Given the strong temperature dependence of molecular relaxations, even a few degrees of temperature variability can dramatically change surface decay kinetics. In order to prevent variation, sample temperature was held at 30°C such that ambient

cooling would be sufficient to maintain a constant temperature. A second confounding factor evident in Figure 5.5 is a jump in the measured surface height after fluid addition. This is a consequence of surface swelling due to water sorption, much like the challenges with surface tracking in Figure 5.4B. The simplest means of accounting for this phenomenon is only using surface height measurements once solution is added.

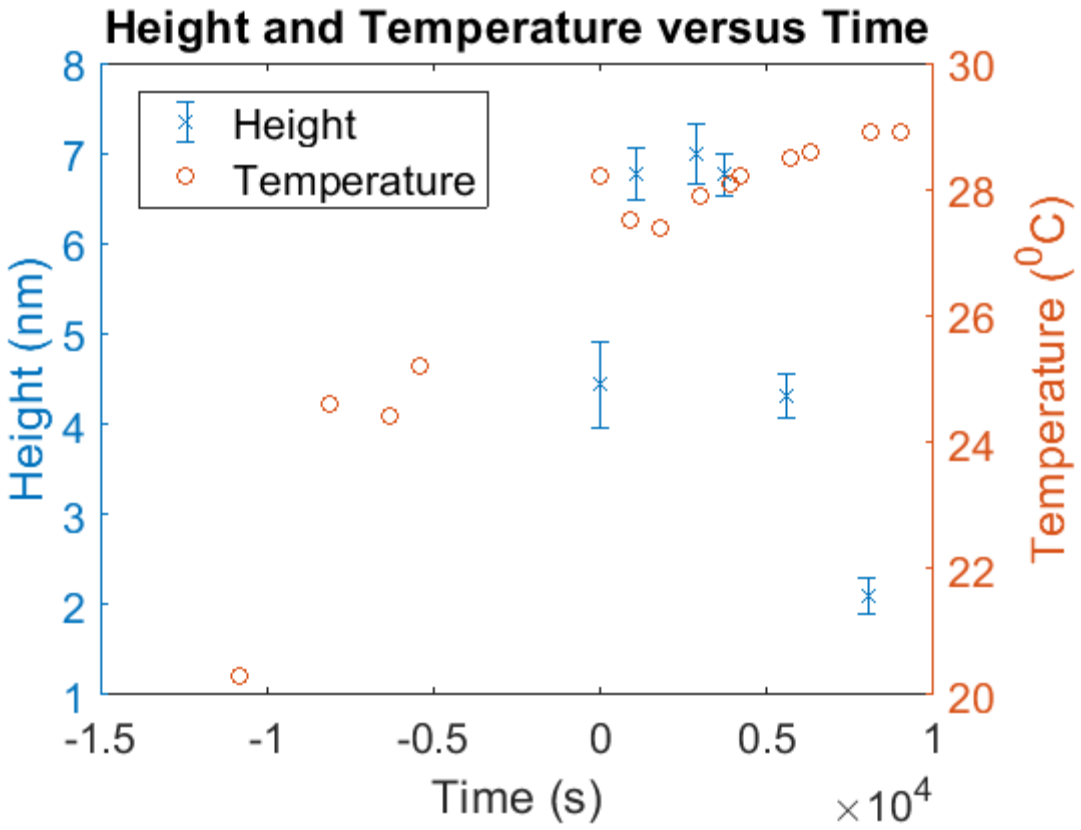

Figure 5.5. Plot of surface height (blue x) and *in situ* sample temperature (red circles) as a function of time during a typical sinusoidal decay experiment. Time of zero indicates fluid addition and beginning of decay experiment, time before zero is during AFM setup and warm-up period.

5.4 Results to Date and Future Direction

Despite the many experimental challenges raised in Section 5.3 there has been great success in generating some preliminary, proof of concept results demonstrating the potential for this approach. Figure 5.6 shows the results of a typical successful sinusoidal relaxation experiment. Figure 5.6A presents a time series of AFM topographical micrographs, which clearly depict decay over time as well as the maintenance of sinusoidal character of the film

throughout the course of the experiment. Surface height measurements were made, and the height of the sine wave describing the film is plotted as a function of time in Figure 5.6B. This data is then fit to the theoretical decay expression given in Equation (2.2), with the equation and r^2 value provided. It can be seen the the film height measurements almost perfectly follow the exponential decay predicted by theory, as indicated by the r^2 value very near unity. Together these suggest a reliable experimental method which successfully studies the surface rearrangement phenomenon of interest.

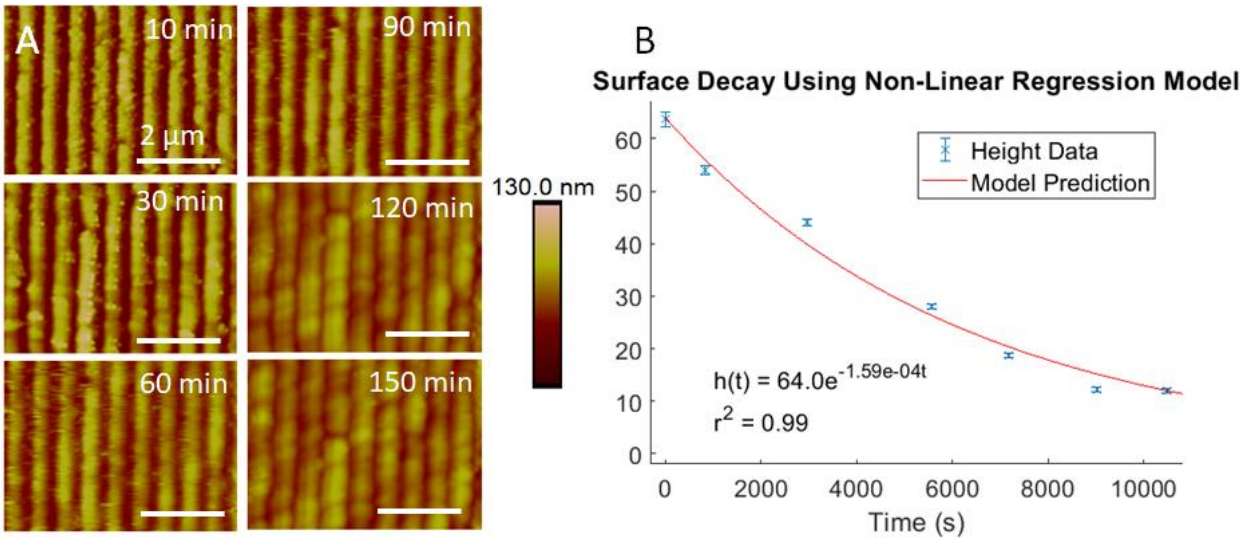

Figure 5.6. Results from a typical surface decay experiment. (A) is an AFM micrograph time lapse of *in situ* topographical measurements obtained from the same location on a surface undergoing surface relaxation. (B) is a plot of sinusoidal surface height versus time, with the data fit to the exponential decay relation from Equation(2.2).

Lastly, composite data from many decay experiments can be compiled and analyzed as shown in Figure 5.7. Here, the decay constant determined from the exponential decay fit is plotted against the wavelength of the film from the experiment. From the scaling relations in Equation (2.3), the slope of this line reveals the dominant transport mechanism and the intercept can then also be used to determine the magnitude of the relevant transport parameter. Thus, the slope of approximately -2.5 suggests either bulk diffusion (highly unlikely) or a solution mediated transport pathway. This is not expected, as the control system is expected to decay due to surface diffusion yielding a plot with a slope of approximately -4. However, as previously mentioned, it was quite challenging to minimize any surface dissolution caused by low solution concentration, which confounds these data. Further, more replicates and additional

measurements using films of longer wavelength are needed. Finally, the path forward with this study is to perform these experiments in buffer containing the additives from Chapter 4 to observe any change on surface transport due to the presence of dissolved polymer or surfactant.

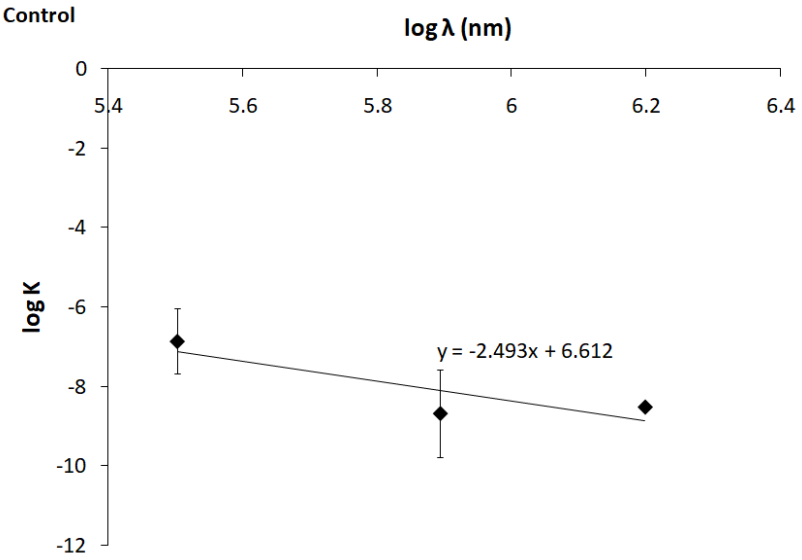

Figure 5.7. Scaling data for the additive free (control) system. Decay constant is extracted from the exponential term from fitting height versus time to Equation (2.2). Line of best fit is simple linear regression.

5.5 References

(1) Leuner, C.; Dressman, J. Improving Drug Solubility for Oral Delivery Using Solid Dispersions. *Eur. J. Pharm. Biopharm.* **2000**, *50* (1), 47–60. https://doi.org/10.1016/S0939-6411(00)00076-X.

(2) Kim, K. T.; Lee, J. Y.; Lee, M. Y.; Song, C. K.; Choi, J.; Kim, D.-D. Solid Dispersions as a Drug Delivery System. *J. Pharm. Investig.* **2011**, *41* (3), 125–142. https://doi.org/10.4333/KPS.2011.41.3.125.

(3) Pouton, C. W. Formulation of Poorly Water-Soluble Drugs for Oral Administration: Physicochemical and Physiological Issues and the Lipid Formulation Classification System. *Eur. J. Pharm. Sci.* **2006**, *29*, 278–287. https://doi.org/10.1016/j.ejps.2006.04.016.

(4) Williams, H. D.; Trevaskis, N. L.; Charman, S. A.; Shanker, R. M.; Charman, W. N.; Pouton, C. W.; Porter, C. J. H. Strategies to Address Low Drug Solubility in Discovery and Development. *Pharmacol. Rev.* **2013**, *65*, 315–499. https://doi.org/10.1124/pr.112.005660.

(5) Yalkowsky, S. H. Perspective on Improving Passive Human Intestinal Absorption. *J. Pharm. Sci.* **2012**, *101* (9), 3047–3050. https://doi.org/10.1002/jps.23093.

(6) Gao, P.; Guyton, M. E.; Huang, T.; Bauer, J. M.; Stefanski, K. J.; Lu, Q. Enhanced Oral Bioavailability of a Poorly Water Soluble Drug PNU-91325 by Supersaturatable Formulations. *Drug Dev. Ind. Pharm.* **2004**, *30* (2), 221–229. https://doi.org/10.1081/DDC-120028718.

(7) Kulikovsky, V.; Vorlíček, V.; Boháč, P.; Stranyánek, M.; Čtvrtlík, R.; Kurdyumov, A. Mechanical Properties of Amorphous and Microcrystalline Silicon Films. *Thin Solid Films* **2008**, *516* (16), 5368–5375. https://doi.org/10.1016/j.tsf.2007.07.047.

(8) Hancock, B. C.; Carlson, G. T.; Ladipo, D. D.; Langdon, B. A.; Mullarney, M. P. Comparison of the Mechanical Properties of the Crystalline and Amorphous Forms of a Drug Substance. *Int. J. Pharm.* **2002**, *241* (1), 73–85. https://doi.org/10.1016/S0378-5173(02)00133-3.

(9) Pandi, P.; Bulusu, R.; Kommineni, N.; Khan, W.; Singh, M. Amorphous Solid Dispersions: An Update for Preparation, Characterization, Mechanism on Bioavailability, Stability, Regulatory Considerations and Marketed Products. *Int. J. Pharm.* **2020**, *586* (June), 119560. https://doi.org/10.1016/j.ijpharm.2020.119560.

(10) Lakshman, J. P.; Cao, Y.; Kowalski, J.; Serajuddin, A. T. M. Application of Melt Extrusion in the Development of a Physically and Chemically Stable High-Energy Amorphous Solid Dispersion of a Poorly Water-Soluble Drug. *Mol. Pharm.* **2008**, *5* (6), 994–1002. https://doi.org/10.1021/mp8001073.

(11) Peng, T.; She, Y.; Zhu, C.; Shi, Y.; Huang, Y.; Niu, B.; Bai, X.; Pan, X.; Wu, C. Influence of Polymers on the Physical and Chemical Stability of Spray-Dried Amorphous Solid Dispersion: Dipyridamole Degradation Induced by Enteric Polymers. *AAPS PharmSciTech* **2018**, *19* (6), 2620–2628. https://doi.org/10.1208/s12249-018-1082-4.

(12) Hancock, B. C.; Parks, M. What Is the True Solubility Advantage for Amorphous Pharmaceuticals? *Pharm. Res.* **2000**, *17* (4), 397–404. https://doi.org/10.1023/A:1007516718048.

(13) Babu, N. J.; Nangia, A. Solubility Advantage of Amorphous Drugs and Pharmaceutical Cocrystals. *Cryst. Growth Des.* **2011**, *11*, 2662–2679. https://doi.org/10.1021/cg200492w.

(14) Ilevbare, G. A.; Taylor, L. S. Liquid-Liquid Phase Separation in Highly Supersaturated Aqueous Solutions of Poorly Water-Soluble Drugs: Implications for Solubility Enhancing Formulations. *Cryst. Growth Des.* **2013**, *13*, 1497–1509. https://doi.org/10.1021/cg301679h.

(15) Hsieh, Y. L.; Ilevbare, G. A.; Van Eerdenbrugh, B.; Box, K. J.; Sanchez-Felix, M. V.; Taylor, L. S. PH-Induced Precipitation Behavior of Weakly Basic Compounds: Determination of Extent and Duration of Supersaturation Using Potentiometric Titration and Correlation to Solid State Properties. *Pharm. Res.* **2012**, *29*, 2738–2753. https://doi.org/10.1007/s11095-012-0759-8.

(16) Indulkar, A. S.; Box, K. J.; Taylor, R.; Ruiz, R.; Taylor, L. S. PH-Dependent Liquid-Liquid Phase Separation of Highly Supersaturated Solutions of Weakly Basic Drugs. *Mol. Pharm.* **2015**, *12* (7), 2365–2377. https://doi.org/10.1021/acs.molpharmaceut.5b00056.

(17) Mosquera-Giraldo, L. I.; Taylor, L. S. Glass-Liquid Phase Separation in Highly Supersaturated Aqueous Solutions of Telaprevir. *Mol. Pharm.* **2015**, *12* (2), 496–503. https://doi.org/10.1021/mp500573z.

(18) Indulkar, A. S.; Gao, Y.; Raina, S. A.; Zhang, G. G. Z.; Taylor, L. S. Exploiting the Phenomenon of Liquid-Liquid Phase Separation for Enhanced and Sustained Membrane Transport of a Poorly Water-Soluble Drug. *Mol. Pharm.* **2016**, *13* (6), 2059–2069. https://doi.org/10.1021/acs.molpharmaceut.6b00202.

(19) Alberti, S.; Gladfelter, A.; Mittag, T. Considerations and Challenges in Studying Liquid-Liquid Phase Separation and Biomolecular Condensates. *Cell* **2019**, *176* (3), 419–434. https://doi.org/10.1016/j.cell.2018.12.035.

(20) Lee, S.; Teich, E. G.; Engel, M.; Glotzer, S. C. Entropic Colloidal Crystallization Pathways via Fluid–Fluid Transitions and Multidimensional Prenucleation Motifs. *Proc. Natl. Acad. Sci. U. S. A.* **2019**, *116* (30), 14843–14851. https://doi.org/10.1073/pnas.1905929116.

(21) Vekilov, P. G. Dense Liquid Precursor for the Nucleation of Ordered Solid Phases from Solution. *Cryst. Growth Des.* **2004**, *4* (4), 671–685. https://doi.org/10.1021/cg049977w.

(22) Cai, T.; Zhu, L.; Yu, L. Crystallization of Organic Glasses: Effects of Polymer Additives on Bulk and Surface Crystal Growth in Amorphous Nifedipine. *Pharm. Res.* **2011**, *28*, 2458–2466. https://doi.org/10.1007/s11095-011-0472-z.

(23) Sun, Y.; Zhu, L.; Kearns, K. L.; Ediger, M. D.; Yu, L. Glasses Crystallize Rapidly at Free Surfaces by Growing Crystals Upward. *Proc. Natl. Acad. Sci.* **2011**, *108* (15), 5990–5995. https://doi.org/10.1073/pnas.1017995108.

(24) Parker, A. S.; Taylor, L. S.; Beaudoin, S. P. The Role of Surface Energy Heterogeneity on Crystal Morphology during Solid-State Crystallization at the Amorphous Atazanavir–Water Interface. *CrystEngComm* **2020**, *22*, 3179–3187. https://doi.org/10.1039/c9ce02007a.

(25) Descamps, M.; Dudognon, E. Crystallization from the Amorphous State: Nucleation-Growth Decoupling, Polymorphism Interplay, and the Role of Interfaces. *J. Pharm. Sci.* **2014**, *103*, 2615–2628. https://doi.org/10.1002/jps.24016.

(26) Huang, C.; Ruan, S.; Cai, T.; Yu, L. Fast Surface Diffusion and Crystallization of Amorphous Griseofulvin. *J. Phys. Chem. B* **2017**, *121* (40), 9463–9468. https://doi.org/10.1021/acs.jpcb.7b07319.

(27) Zhu, L.; Brian, C. W.; Swallen, S. F.; Straus, P. T.; Ediger, M. D.; Yu, L. Surface Self-Diffusion of an Organic Glass. *Phys. Rev. Lett.* **2011**, *106*, 256103. https://doi.org/10.1103/PhysRevLett.106.256103.

(28) Zhang, W.; Yu, L. Surface Diffusion of Polymer Glasses. *Macromolecules* **2016**, *49*, 731–735. https://doi.org/10.1021/acs.macromol.5b02294.

(29) Mullins, W. W. Theory of Thermal Grooving. *J. Appl. Phys.* **1957**, *28* (3), 333–339. https://doi.org/10.1063/1.1722742.

(30) Mullins, W. W. Flattening of a Nearly Plane Solid Surface Due to Capillarity. *J. Appl. Phys.* **1959**, *30* (1), 77–83. https://doi.org/10.1063/1.1734979.

(31) Zhang, W.; Brian, C. W.; Yu, L. Fast Surface Diffusion of Amorphous O-Terphenyl and Its Competition with Viscous Flow in Surface Evolution. *J. Phys. Chem. B* **2015**, *119* (15), 5071–5078. https://doi.org/10.1021/jp5127464.

6. CONCLUSIONS

6.1 Overview of Results

Considered holistically, there are some interesting observations one can make based on the data presented herein. One consistent theme throughout each of the studies is the important role of surface energy. Surface energy has long been known to be an important factor during crystallization, as crystal habit and morphology during solution growth is largely determined by the specific surface energy of each crystal face. However, the role of the surface energy of the homogenous melt has not been previously studied when considering the evolution of crystals from glass or subcooled liquid. Additionally, surface energy has been known to be an important term in the physical chemistry of adsorption. This investigation extends that understanding and considers the dual impact of surface energy on crystallization driving force, surface transport, and adsorption propensity. The critical role of surface energy highlights the need to more carefully study surface properties in physical systems as well as more carefully engineer our pharmaceutical products with surface energy in mind.

Another recurring theme was molecular mobility and surface transport. Given the metastability of amorphous pharmaceuticals, thermodynamics will always tend towards crystallization if an enhanced solution driving force for adsorption is desired. In other words, as long as supersaturating formulations are needed, there is no way around the thermodynamic driving force to crystallize. Thus, crystallization inhibition is a question of kinetics, and, in the context of this work, transport phenomena. Surface transport is in fact not divorced from surface energy, as chemical potential gradients along the surface will give rise to the transport of surface molecules. If we wish to inhibit crystallization without reducing the activity of drug molecules and their ability to permeate into the blood stream, greater focus needs to be placed on designing additives and formulations based on their ability to regulate the transport phenomena of drug molecules.

6.2 Critique of the Work

Crystallization of amorphous pharmaceutical products is quite clearly challenging to understand, with many complex and interacting factors governing the fate of API molecules.

This dissertation has only touched on one pathway among many, *viz.*, liquid-liquid phase separation and subsequent solid-state crystallization. As such, these studies are limited in scope and other complicating factors may prove to be more significant during the manufacture, storage, or dosing of real amorphous pharmaceutical formulations.

Perhaps the greatest challenge to studying amorphous materials, regardless of the analytical techniques employed, is the inherent instability and unpredictability of high energy materials. These systems can be thought of much like a boulder placed atop a hill, gravity working to drive the rock down the hill along the path of least resistance, such that even subtle differences in the initial position of the boulder or slope of the hill can lead to markedly different trajectories. Furthermore, once the boulder begins to roll it is nearly impossible to direct its course. Conditions in these studies were carefully controlled to ensure the phenomenon of interest was being studied with the greatest degree of reproducibility possible, though invariably these experiments proved troublesome to perform and replicate.

One significant limitation of this study is the reliance on often qualitative data in the form of AFM and SEM micrographs. Studies of surface evolution lend themselves well to such imaging techniques, though this makes drawing strong conclusions somewhat troublesome. More quantitative analytical techniques, such as X-ray diffraction, infrared spectroscopy, Raman spectroscopy, and solid-state nuclear magnetic resonance could lend helpful orthogonal validation of the surface composition and properties which were often inferred from topographical maps. Regrettably, the limit of resolution and detection for such techniques can render them ineffective at studying the sometimes trace crystallinity observed in these studies, which precluded their use in this project.

6.3 Future Directions

Insofar as these investigations have lent significant insight into the inner workings of solid-state crystallization and additive regulation of such phase transformations, myriad questions remain unanswered, and indeed, many more puzzles have been unearthed. The first objective is of course to complete the surface decay study outlined in Chapter 5, as the method is fully developed and the preliminary results are promising. Even the types of experiments conducted in this dissertation should be replicated with additional systems containing more varied additives and especially biorelevant media. Beyond a simple reproduction of an established method, it

would be particularly interesting to investigate the behavior of real nanodroplets generated during LLPS. It would be of great benefit to develop a method to observe the amorphous-to-crystal transition of these nanodroplets *in situ*, though this is expected to be very challenging. A final level of complexity to consider is a ternary or even more complex formulation containing multiple additives. Real formulations will contain many additive species, and even trace amounts of some materials can have profound implications on formulation performance. Thus, a long term investigatory aim should be the systematic study and understanding multi-additive species and the effect of additive-additive interactions.

APPENDIX A. DERIVATION OF FILM DECAY EQUATIONS

The transport phenomena underlying rearrangement of an amorphous film can be elucidated through the analysis of the decay of a nearly planar sinusoidal surface. Mathematical determination of the flattening for a 2D sinusoidal surface has been presented previously in the literature[26,27]. A full derivation of the model equations from first principles is presented herein.

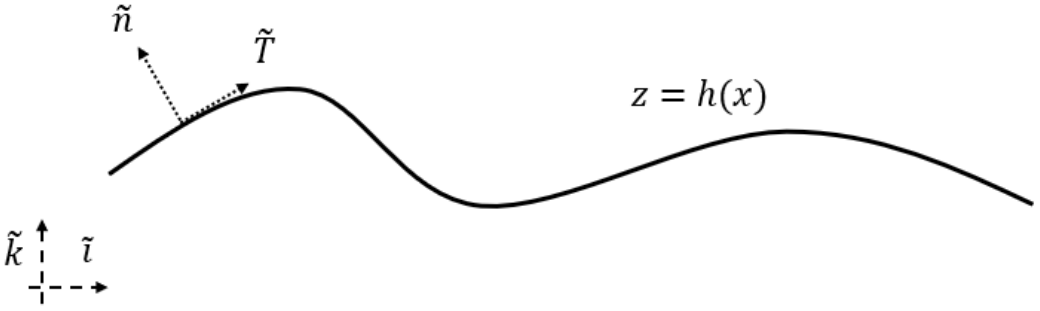

Figure A1. Schematic depicting arbitrary curved surface in space.

Consider an arbitrary 2D interface described by a height function $h = h(x, t)$. A simple visual representation is provided in Figure . Using the Ostwald-Freundlich equation, the pressure across the interface relative to a flat surface can be related to the curvature of the surface, given by:

$$\log\frac{P}{P_0} = \frac{R_{crit}}{R} = \frac{{}^{2\gamma\Omega}/_{kT}}{R} \qquad (3)$$

Here, P is the interfacial pressure for the real surface with radius of curvature R, P_0 is the interfacial pressure for the flat reference surface, $R_{crit} = 2\gamma\Omega/kT$ is the critical radius, γ is the surface tension/energy, Ω is the molecular volume, k is Boltzmann's constant, and T is the temperature of the system. Alternatively, the Gibbs-Thompson relation allows the pressure difference to be related to a chemical potential difference, which proves to be more useful for capturing a thermodynamic driving force for rearrangement. Thus, the chemical potential across the interface is given in terms of the radius of curvature as:

$$\frac{\mu}{\mu_0} = kT\log\frac{P}{P_0} = \frac{2\gamma\Omega}{R} \qquad (4)$$

Here, μ is the chemical potential of the curved interface and μ_0 is the chemical potential of the reference. For a general 2D interface, the curvature κ can of course be expressed as:

$$\kappa = \frac{2}{R} \qquad (5)$$

Substituting Equation *(5)* into Equation *(4)* results in an expression relating chemical potential to the local surface curvature, written as:

$$\frac{\mu}{\mu_0} = \Omega\gamma\kappa \qquad (6)$$

Given that the reference chemical potential is arbitrary, it can be assigned to be unity, such that Equation *(6)* can compactly be written as:

$$\mu(\kappa) = \Omega\gamma\kappa \qquad (7)$$

While it is mathematically elegant to write this expression in a generalized curvilinear coordinate, it is far more convenient to rewrite the curvature in Cartesian coordinates. As is known from any elementary text covering vector calculus, curvature is defined as an arc length derivative of the tangent vector:

$$\kappa \equiv \left|\frac{d\tilde{T}}{ds}\right| \qquad (8)$$

Here, $\tilde{T}$ is the unit vector tangent to the surface and *s* is the arc length. Neglecting any time dependence of the surface height function, the differential arc length can be written as:

$$ds^2 = dx^2 + dh^2 \rightarrow ds = \sqrt{dx^2 + dh^2} = \sqrt{1 + \left(\frac{dh}{dx}\right)^2} = \sqrt{1 + (h')^2} \qquad (9)$$

To determine the differential tangent, the unit vector normal to the surface $\tilde{n}$ must first be defined:

$$\tilde{n} \equiv \frac{\nabla\big(z - h(x)\big)}{\left|\nabla\big(z - h(x)\big)\right|} \qquad (10)$$

Evaluating the gradient operator from Equation *(10)* in Cartesian coordinates ultimately results in:

$$\tilde{n} = \frac{\tilde{k} - h'\tilde{\imath}}{\sqrt{1 + (h')^2}} \qquad (11)$$

Here, $\tilde{k}$ and $\tilde{\imath}$ are the usual unit vectors defining the Cartesian axes. Now, the unit tangent vector can be defined given the conditions of orthogonality and fixed magnitude of unity:

$$\tilde{n} \cdot \tilde{T} = 0, \qquad \tilde{T} \cdot \tilde{T} = 1 \qquad (12)$$

The constraints from Equation *(12)* imply that the unit tangent is given by:

$$\tilde{T} = \frac{\tilde{\imath} + h'\tilde{k}}{\sqrt{1 + (h')^2}} \quad (13)$$

In differential form, Equation *(13)* then yields:

$$d\tilde{T} = d\left(\frac{\tilde{\imath} + h'\tilde{k}}{\sqrt{1 + (h')^2}}\right) = -\frac{h'h''}{(1 + (h')^2)^{3/2}}\tilde{\imath} + \frac{h''}{(1 + (h')^2)^{3/2}}\tilde{k} \quad (14)$$

The curvature expression utilizes the magnitude of this differential vector:

$$\left|d\tilde{T}\right| = d\tilde{T} \cdot d\tilde{T} = \sqrt{\frac{(h'h'')^2}{(1 + (h')^2)^3} + \frac{(h'')^2}{(1 + (h')^2)^3}} = \frac{h''}{1 + (h')^2} \quad (15)$$

Combining Equation *(9)* and Equation *(15)*:

$$\kappa = \left|\frac{d\tilde{T}}{ds}\right| = \frac{h''}{(1 + (h')^2)^{3/2}} \quad (16)$$

To obtain an analytic solution to the governing differential equations, it is necessary to consider the limiting linearized behavior when the surface is nearly planar. Thus, assuming *h'* is small compared to unity, such that $1 + (h')^2 \sim 1$, the simplified curvature becomes the familiar form:

$$\kappa \sim h'' \quad (17)$$

The simplified curvature allows for the final form of the chemical potential across the curved interface in Cartesian coordinates by substituting Equation *(17)* into Equation *(7)*:

$$\mu(x) = \Omega\gamma h''(x) \quad (18)$$

Now that the thermodynamics have been evaluated, Equation *(18)* can be utilized in the various governing transport equations to assess the kinetics of surface relaxation. Moving forward from this point, the surface function will no longer be arbitrary but instead is treated to be a sinusoidal interface described by:

$$h(x,t) = \alpha \sin(\omega x) = \alpha \sin\left(\frac{2\pi}{\lambda}x\right), \alpha = \alpha(t) \quad (19)$$

Here, α is the amplitude, ω is the frequency, and λ is the wavelength of the sine wave. This implies that Equation *(18)* becomes:

$$\mu(x) = \Omega\gamma h''(x) = -\Omega\gamma\omega^2 h(x) = -\Omega\gamma\omega^2\alpha \sin(\omega x) \quad (20)$$

A.1 Viscous Flow

Assuming the amorphous film is an incompressible, Newtonian system, flow will be described by the Navier-Stokes and the continuity equation:

$$\nabla \cdot \tilde{v} = 0 \quad (21)$$

$$\rho\left(\frac{\partial\tilde{v}}{\partial t}+\tilde{v}\cdot\nabla\tilde{v}\right)=-\nabla P+\eta\nabla^2\tilde{v} \quad (22)$$

Here, $\tilde{v}$ is the velocity vector with z- and x-components u and w, respectively, ρ is the density, and η is the viscosity. Applying the Stokes' flow assumption, whereby in the dominant balance the inertial terms are negligible relative to the viscous and pressure terms:

$$0=-\nabla P+\eta\nabla^2\tilde{v} \quad (23)$$

Now Equation *(21)* and Equation *(23)* can be written in component form:

$$\frac{\partial u}{\partial x}+\frac{\partial w}{\partial z}=0 \quad (24)$$

$$\frac{\partial P}{\partial x}=\eta\left(\frac{\partial^2 u}{\partial x^2}+\frac{\partial^2 u}{\partial z^2}\right) \quad (25)$$

$$\frac{\partial P}{\partial z}=\eta\left(\frac{\partial^2 w}{\partial x^2}+\frac{\partial^2 w}{\partial z^2}\right) \quad (26)$$

At this point, it becomes convenient to follow the normal convention for incompressible, bidirectional flow problems and define the kinematic stream function ψ:

$$\nabla\times\psi\equiv\tilde{v}\rightarrow u\equiv\frac{\partial\psi}{\partial z},w\equiv-\frac{\partial\psi}{\partial x} \quad (27)$$

Such a definition will ultimately transform the system of PDEs (Equations *(24)*, *(25)*, and *(26)*) into a single PDE only in terms of ψ and the independent variables. Introducing the stream function into Equations *(24)*, *(25)*, and *(26)*:

$$\nabla\cdot(\nabla\times\psi)=0 \quad (28)$$

$$\frac{\partial P}{\partial x}=\eta\left(\frac{\partial^2\psi}{\partial x^2\partial z}+\frac{\partial^3\psi}{\partial z^3}\right) \quad (29)$$

$$\frac{\partial P}{\partial z}=-\eta\left(\frac{\partial^3\psi}{\partial x^3}+\frac{\partial^3\psi}{\partial z^2\partial x}\right) \quad (30)$$

The clever reader will recognize the path forward by recalling Schwarz's theorem which establishes the equality of mixed partial 2nd derivatives:

$$\frac{\partial^2 P}{\partial x\partial z}=\frac{\partial^2 P}{\partial z\partial x}\rightarrow\frac{\partial^2 P}{\partial x\partial z}-\frac{\partial^2 P}{\partial z\partial x}=0 \quad (31)$$

Given this useful relation, taking the mixed partial derivative of both Equations *(29)* and *(30)* followed by substitution into Equation *(31)* leads to the governing PDE:

$$\eta\left(\frac{\partial^4\psi}{\partial x^4}+2\frac{\partial^4\psi}{\partial z^2\partial^2 x}+\frac{\partial^4\psi}{\partial z^4}\right)=\eta\nabla^4\psi=\eta\nabla^2\nabla^2\psi=0 \quad (32)$$

Equation *(32)* is of course the biharmonic equation, classically seen in many Stokes' flow problems. To develop the solution to Equation *(32)*, the boundary conditions must be determined. For edge effects to be negligible, the film will be treated as infinitely long and deep,

such that the only interface of interest is the free surface boundary. The infinite depth condition implies that both velocity components must vanish in the bulk far from the interface:

$$u(x, z \to -\infty) = 0 \quad (33)$$
$$w(x, z \to -\infty) = 0 \quad (34)$$

The free interface provides several boundary conditions. First, assuming the fluid phase above the film is inviscid relative to the amorphous material (which is expected to hold for an aqueous solution), the shear stress τ_{xz} and τ_{zx} on the interface will vanish:

$$\tau_{xz}|_{z=h} = \tau_{zx}|_{z=h} = \eta\left(\frac{\partial u}{\partial z} + \frac{\partial w}{\partial x}\right)\Big|_{z=h} = 0 \quad (35)$$

Furthermore, the simplified form of the Young-Laplace equation relates the curvature to the normal pressure at the interface:

$$P|_{z=h} = -\gamma\kappa = -\gamma h''(x) = \gamma\alpha\omega^2 \sin(\omega x) \quad (36)$$

Returning to Equation *(32)*, this biharmonic equation is well studied and a general solution in Cartesian coordinates is known:

$$\psi(x,z) = [c_0\cosh(\beta z) + c_1\sinh(\beta z) + c_2 z\cosh(\beta z) + c_3 z\sinh(\beta z)](c_4\cos(\beta x) + c_5\sin(\beta x)) \quad (37)$$

Here, β and each c_i are constants determined by the boundary conditions. All that remains is the trivial, albeit somewhat tedious task, of returning the stream function to velocity components and applying the boundary conditions to determine each unknown. Utilizing the definitions given in Equation *(27)* gives:

$$u \equiv \frac{\partial\psi}{\partial z} = [(c_2 + \beta c_1)\cosh(\beta z) + (c_3 + c_0\beta)\sinh(\beta z) + c_3\beta z\cosh(\beta z) + c_2\beta z\sinh(\beta z)](c_4\cos(\beta x) + c_5\sin(\beta x)) \quad (38)$$

$$w \equiv -\frac{\partial\psi}{\partial x} = -\beta[c_0\cosh(\beta z) + c_1\sinh(\beta z) + c_2 z\cosh(\beta z) + c_3 z\sinh(\beta z)](-c_4\sin(\beta x) + c_5\cos(\beta x)) \quad (39)$$

First, the velocity conditions in the bulk, from Equations *(33)* and *(34)* must be satisfied. Given that both *cosh(z)* and *sinh(z)* diverge to positive and negative infinity, respectively, as *z* approaches negative infinity, this will require that like powers of *cosh(z)* and *sinh(z)* have the same coefficient to prevent the trivial solution (or $c_4 = c_5 = 0$, which would lead to $u = w = 0$).

$$c_0\cosh(\beta z) + c_1\sinh(\beta z) = 0 \to c_0 = c_1 \quad (40)$$

$$c_2 z\cosh(\beta z) + c_3 z\sinh(\beta z) = 0 \to c_2 = c_3 \quad (41)$$

Substituting Equations *(38)* and *(39)* into the zero-shear boundary condition from Equation*(35)* along with the results from Equations (40) and *(41)*:

$$\left(\frac{\partial u}{\partial z}+\frac{\partial w}{\partial x}\right)=[2\beta(c_3+c_0\beta)\cosh(\beta z)+2\beta(c_2+\beta c_1)\sinh(\beta z) + 2\beta^2 c_2 z\cosh(\beta z)+2\beta^2 c_3 z\cosh(\beta z)](c_4\cos(\beta x)+c_5\sin(\beta x)) \quad (42)$$

$$\left(\frac{\partial u}{\partial z}+\frac{\partial w}{\partial x}\right)\Big|_{z=0}=(c_4\cos(\beta x)+c_5\sin(\beta x))*2\beta(c_3+c_0\beta)=0\rightarrow c_3=-c_0\beta \quad (43)$$

$$c_0\equiv c\rightarrow c_1=\mathrm{c}, c_2=-\beta c, c_3=-\mathrm{c}\beta \quad (44)$$

This leaves only the determination of β, c_4, and c_5. To proceed, we must assume our expression for pressure is separable, such that Equation *(36)* implies:

$$P(x,z)=\gamma\alpha\omega^2\sin(\omega x)*f(z) \quad (45)$$

Now, evaluating Equations *(25)* and *(26)* with the Equations *(38)* and *(39)* and the results from Equation *(44)*:

$$\frac{\partial P}{\partial x}=\gamma\alpha\omega^3\cos(\omega x)*f(z)=\eta\left(\frac{\partial^2 u}{\partial x^2}+\frac{\partial^2 u}{\partial z^2}\right) =\eta\left(-2c\beta^3 e^{\beta z}\right)(c_4\cos(\beta x)+c_5\sin(\beta x)) \quad (46)$$

$$\frac{\partial P}{\partial z}=\gamma\alpha\omega^2\sin(\omega x)*f'(z)=\eta\left(\frac{\partial^2 w}{\partial x^2}+\frac{\partial^2 w}{\partial z^2}\right) =\eta\left(-2c\beta^3 e^{\beta z}\right)(c_4\sin(\beta x)-c_5\cos(\beta x)) \quad (47)$$

Comparing the left hand side and right hand side of each expression, it is clear that for these to hold in general:

$$f(z)=e^{\beta z} \quad (48)$$

$$\mathrm{c}_5=0 \quad (49)$$

$$\beta=\omega \quad (50)$$

$$\mathrm{c}*\mathrm{c}_4=\frac{\gamma\alpha}{2\eta} \quad (51)$$

The component forms of the velocity can now be written in their final forms:

$$u(x,z)=\frac{\gamma\alpha\omega}{2\eta}\cos(\omega x)\,e^{\omega z}\,\omega z \quad (52)$$

$$w(x,z)=\frac{\gamma\alpha\omega}{2\eta}\sin(\omega x)\,e^{\omega z}\,(\omega z-1) \quad (53)$$

Recognizing that the vertical velocity at the surface (*w(x, 0)*) is simply the rate of change of the surface height function (since *u(x,0)=0*), the time derivative of the surface height function is given as:

$$\frac{\partial h}{\partial t}=w(x,0)=-\frac{\gamma\alpha\omega}{2\eta}\sin(\omega x)=-\frac{\gamma\omega}{2\eta}h=-Fh \quad (54)$$

A.2 Bulk Diffusion

For a pure component material, bulk diffusion will be governed by Fick's First Law, which relates the flux *J* to the chemical potential gradient:

$$J = -\frac{D_B \rho}{kT} \nabla \mu \qquad (55)$$

Here, D_B is the self/bulk diffusion coefficient. From Equations *(18)* and *(20)* it is apparent that the chemical potential depends only on the x-coordinate, so that the gradient simply becomes a spatial derivative in x:

$$J = -\frac{D_B \rho}{kT} \frac{d\mu}{dx} \qquad (56)$$

Substituting Equation *(20)* into Equation *(56)*:

$$J = -\frac{D_B \rho \Omega \gamma}{kT} h'''(x) = \frac{\alpha D_B \rho \Omega \gamma \omega^3}{kT} \cos(\omega x) \qquad (57)$$

Note that the units of Equation *(57)* will be in molecules per unit area per time. Dividing Equation *(57)* by the density will yield an expression in units of distance per time, or equivalently the time rate of change in surface height:

$$r_n = \frac{\partial h}{\partial t} = -\frac{D_B \Omega \gamma \omega^3}{kT} h = -D\omega^3 h \qquad (58)$$

A.3 Dissolution and Deposition

Under the assumption of a dilute, ideal solution, the driving force for dissolution and deposition due to curvature is established by the Gibbs-Thompson relation from Equation *(4)* in the form given in Equation *(20)*. Diffusion through solution can be assumed to be quasi-steady state, such that we have Laplace's equation:

$$\nabla^2 \mu = 0 \qquad (59)$$

For this to hold when Euquation *(20)* serves as a boundary condition along *z=h(x)* and for the gradient to vanish at *z*→-∞, the expression for chemical potential must be given by:

$$\mu(x, z) = -\Omega \gamma \omega^2 e^{-\omega z} \alpha \sin(\omega x) \qquad (60)$$

Again applying Fick's First Law (except now with the diffusivity through solution) and performing the operations of 0:

$$\frac{\partial h}{\partial t} = -\frac{D_l \Omega^2 \gamma \omega^3}{kT} h = -A\omega^3 h \qquad (61)$$

A.4 Surface Diffusion

Surface diffusion is governed by the Nernst-Einstein equation, to relate the velocity of surface atoms *V* to the chemical potential surface gradient:

$$V = -\frac{D_s}{kt}\nabla_s \mu = -\frac{D_s}{kt}\frac{\partial \mu}{\partial s} = -\frac{D_s}{kt}\Omega\gamma\frac{\partial'' h(x)}{\partial s} \qquad (62)$$

Recalling Equation *(9)*, this can be converted from arc length coordinates to Cartesian coordinates:

$$V = -\frac{D_s}{kt}\Omega\gamma h'''(x) \qquad (63)$$

Velocity is converted to flux by multiplying by the area density, and then to rate of surface decay by applying the surface-divergence theorem:

$$r_n = \frac{\partial h}{\partial t} = -\frac{D_s\Omega^2\gamma\nu}{kt}h''''(x) = -\frac{D_s\Omega^2\gamma\nu}{kt}\omega^4 h = -B\omega^4 h \qquad (64)$$

APPENDIX B. COMPUTER CODE FOR CHAPTER 3 SIMULATIONS

```
## ============== MC Crystallization Simulation - Version 4.0 ============== ##
# ================================================================================
#  Version 1.0 is a 0th order random crystallization simulation, applying
#  arbitrary probabilities to the relevant phenomenological events of
#  nucleation, growth, and branching. Probabilities are adjusted empirically to
#  track trends of observed experimental data.
#
#  Version 2.0 is a more sophisticated Monte Carlo style simulation, applying a
#  pseudo-Metropolis method to evaluate trial MC moves. Energy benefits given
#  for forming "bonds", and energy penalties for forming "interfaces" are
#  assigned empirically to reproduce observations.
#
#  Version 2.1 enhances simulation by only selecting vacant sites for MC step
#  consideration, to account for limitation of Version 2.0 that showed
#  rate of crystallization "slowing" as more sites became occupied.
#
#  Version 3.0 also incorporates a distribution of surface energies across the
#  surface, which controls sites of nucleation and the balance between
#  nucleation and growth rates throughout course of the simulation.
#
#  Version 4.0 incorporates branching by allowing for 90-degree rotation
#  of a new unit as it is added, which favors the attaching of new adjacent
#  units in this orientation.
# ================================================================================
import numpy as np
import matplotlib.pyplot as plt
from matplotlib.colors import Normalize

## ======================== Initialize Parameters ======================== ##
MC_samples = 40000000 # Number of trial MC steps
Accepted = 0 # Tracks number of accepted MC moves
Rejected = 0 # Tracks number of rejected MC moves
```

```
Branches = 0 # Tracks number of times a rotated unit is added
Seed = np.random.randint(2147483646) # Generate seed
MC_seed = np.random.seed(Seed) # Seed random number generator
branching_probability = 0.25 # Probability of rotating new trial unit

cmap = 'afmhot'
norm = Normalize(-0.5, 1.8)

## ============================ Generate Grids ============================ ##
# ======================================================================
#  Variable 'grid' stores if a given "lattice" location
#  contains a crystallite unit (1 for yes, 0 for no)
# ======================================================================
dimensionality = 500
total_lattice_sites = int((dimensionality - 2)**2)
grid = np.zeros((dimensionality, dimensionality), dtype='int')
indices = np.indices((dimensionality, dimensionality))

# Orientation default is 1, value of 0 corresponds to 90 degree rotation
orientation = np.ones((dimensionality, dimensionality), dtype='int')

## ============================== Energetics ============================== ##
# ======================================================================
#  Assign energy benefits and penalties associated with forming "bonds"
#  and "interfaces". The base energy (surface energy) for each site is set at
#  zero initially and adjusted to provide desired configuration. "1" corresponds
#  to uniform (trivial) configuration. "2" corresponds to a distribution where
#  each site is randomly selected from the Gaussian distribution centered
#  around zero. "3" corresponds to a single, large 2D Gaussian function in the
#  center of the lattice. "4" corresponds to many randomly distributed small 2D
#  Gaussian functions. "5" corresponds to a single long and narrow diagonal
#  strip of high energy across the middle of the lattice.
# ======================================================================
bond = -5 # Energy benefit from adding an adjacent unit
vert_interface = 1.25 # Energy penalty from forming vertical interface
```

```
horz_interface = 5.25 # Energy penalty from forming horizontal interface

# Surface Energy Distribution
configuration = 1 # Determines which energy configuration to implement

if configuration == 1: # Uniform Distribution
surface_energy_distribution = np.zeros((dimensionality, dimensionality), \
dtype='int')

elif configuration == 2: # Random Distribution
surface_energy_mean = 0.0 # Mean of surface energy distribution
surface_energy_stdev = 1.0 # Standard deviation of surface energy distribution
surface_energy_distribution = np.random.normal( \
surface_energy_mean, surface_energy_stdev, \
                                  (dimensionality, dimensionality))

elif configuration == 3: # Large 2D Gaussian
    spread = dimensionality * 4 # Spread of effect of defect
    amp = 5 # Max surface energy at peak of defect
    center = dimensionality / 2 # Define the center coordinate of the lattice
x_diff = np.power(center - indices[1], 2) # X differences squared
y_diff = np.power(center - indices[0], 2) # Y differences squared
surface_energy_distribution = amp*np.exp(-((x_diff+y_diff)/spread))

elif configuration == 4: # Random Small 2D Gaussians
    defects = 40 # Number of defect sites in surface
    spread = dimensionality/10 # Spread of effect of defect
    amp = 5 # Max surface energy at peak of defect
surface_energy_distribution = np.zeros((dimensionality, dimensionality))
    for counter in range(0, defects):
        [x_center, y_center] = np.random.randint(1, dimensionality - 1, size=2)
x_diff = np.power(x_center - indices[1], 2)
y_diff = np.power(y_center - indices[0], 2)
surface_energy_distribution += amp*np.exp(-((x_diff+y_diff)/spread))
```

```
else: # Diagonal line
    width = 11 # Odd number giving the width of the line
    amp = 5 # Max surface energy at peak of defect
    base = amp*np.ones((dimensionality, dimensionality))
    upper = np.triu(base, (width-1)/2)
    lower = np.tril(base, -(width-1)/2)
surface_energy_distribution = np.subtract(np.subtract(base, upper), lower)

## ====================== Crystallization Simulation ====================== ##
for counter in range(MC_samples):
    # End simulation if entire surface crystallizes
    if Accepted == total_lattice_sites:
print('Surface completely crystallized')
        break

    # Save surface plot every specified number of steps
    if (counter + 1) % 5000000 == 0:
        fig = plt.figure()
        power = np.int(np.floor(np.log10(counter + 1)))
        value = (counter + 1) / pow(10, power)
file_name = 'E{:d}_{:.1f}_steps.png'.format(power, value)
plt.pcolormesh(grid, cmap=cmap, norm=norm)
plt.colorbar()
plt.title(format('%d Trial Monte Carlo Steps' % (counter + 1)))
fig.savefig(file_name)
plt.close(fig)

    # Pick an uncrystallized spot at random
    [trial_x_index, trial_y_index] = np.random.randint(
                                    1, dimensionality - 1, size=2)
    while grid[trial_y_index, trial_x_index] == 1:
        [trial_x_index, trial_y_index] = np.random.randint(
                                        1, dimensionality - 1, size=2)

    # Determine neighboring sites and corresponding orientation
```

```
up_neighbor = grid[trial_y_index - 1, trial_x_index]
up_neighbor_orient = orientation[trial_y_index - 1, trial_x_index]

down_neighbor = grid[trial_y_index + 1, trial_x_index]
down_neighbor_orient = orientation[trial_y_index + 1, trial_x_index]

left_neighbor = grid[trial_y_index, trial_x_index - 1]
left_neighbor_orient = orientation[trial_y_index, trial_x_index - 1]

right_neighbor = grid[trial_y_index, trial_x_index + 1]
right_neighbor_orient = orientation[trial_y_index, trial_x_index + 1]

all_neighbors = np.array([up_neighbor, down_neighbor,
left_neighbor, right_neighbor])
    [filled_neighbors] = np.nonzero(all_neighbors)

## ======================== Evalutate Orientation ======================== ##
# ======================================================================
#  Determine the average orientation to use for determining the definition
#  of rotate versus non-rotated unit
# ======================================================================
    # If site has no neighbors, use default value of left/right as preferred
    if len(filled_neighbors) == 0:
avg_orient = orientation[trial_y_index, trial_x_index]
    # If site has neighbors, use the average of their orientations for the
    # preferred direction. If they are equal, use left/right as preferrred
    else:
all_orient = np.array([up_neighbor_orient, down_neighbor_orient,
left_neighbor_orient, right_neighbor_orient])
avg_orient = np.round(np.average(all_orient[filled_neighbors]))

    # Determine branching or continuation
    # If the random number is less than the probability, 90 degree rotation
    # occurs relative to preferred orientation
orient_rand = np.random.random()
```

```
prob_check = int(orient_rand<branching_probability)
trial_orient = int((avg_orient and not(prob_check)) or
                   (not(avg_orient) and prob_check)) # XOR logic gate

    # Determine energy benefit/penalty to adding crystal unit in this location
delta_E = -surface_energy_distribution[trial_y_index, trial_x_index]

    # Evaluate energetics for standard orientation
    if trial_orient == 1:
        # If down site is unoccupied, penalize for new vertical interface
        if down_neighbor == 0:
delta_E += vert_interface
        # If down site is occupied and orientation matches down site,
        # benefit for removing vertical interface and forming a new bond.
        # If orientation does not match, treats site as unoccupied
        else:
delta_E += int(trial_orient == down_neighbor_orient) * \
            (bond - vert_interface) + \
int(not(trial_orient == down_neighbor_orient)) * vert_interface

        # If up site is unoccupied, penalize for new vertical interface
        if up_neighbor == 0:
delta_E += vert_interface
        # If up site is occupied and orientation matches up site,
        # benefit for removing vertical interface and forming a new bond.
        # If orientation does not match, treats site as unoccupied
        else:
delta_E += int(trial_orient == up_neighbor_orient) * \
            (bond - vert_interface) + \
int(not(trial_orient == up_neighbor_orient)) * vert_interface

        # If right site is unoccupied, penalize for new horizontal interface
        if right_neighbor == 0:
delta_E += horz_interface
        # If right site is occupied and orientation matches right site,
```

```
        # benefit for removing horizontal interface and forming a new bond.
        # If orientation does not match, treats site as unoccupied
        else:
delta_E += int(trial_orient == right_neighbor_orient) * \
            (bond - horz_interface) + \
int(not(trial_orient == right_neighbor_orient)) * horz_interface

        # If left site is unoccupied, penalize for new horizontal interface
        if left_neighbor == 0:
delta_E += horz_interface
        # If left site is occupied and orientation matches left site,
        # benefit for removing horizontal interface and forming a new bond.
        # If orientation does not match, treats site as unoccupied
        else:
delta_E += int(trial_orient == left_neighbor_orient) * \
            (bond - horz_interface) + \
int(not(trial_orient == left_neighbor_orient)) * horz_interface

    # Evaluate energetics for rotated orientation
    else:
        # If down site is unoccupied, penalize for new horizontal interface
        if down_neighbor == 0:
delta_E += horz_interface
        # If down site is occupied and orientation matches down site,
        # benefit for removing horizontal interface and forming a new bond.
        # If orientation does not match, treats site as unoccupied
        else:
delta_E += int(trial_orient == down_neighbor_orient) * \
            (bond - horz_interface) + \
int(not(trial_orient == down_neighbor_orient)) * horz_interface

        # If up site is unoccupied, penalize for new horizontal interface
        if up_neighbor == 0:
delta_E += horz_interface
        # If up site is occupied and orientation matches up site,
```

```
        # benefit for removing horizontal interface and forming a new bond.
        # If orientation does not match, treats site as unoccupied
        else:
delta_E += int(trial_orient == up_neighbor_orient) * \
            (bond - horz_interface) + \
int(not(trial_orient == up_neighbor_orient)) * horz_interface

        # If right site is unoccupied, penalize for new vertical interface
        if right_neighbor == 0:
delta_E += vert_interface
        # If right site is occupied and orientation matches right site,
        # benefit for removing vertical interface and forming a new bond.
        # If orientation does not match, treats site as unoccupied
        else:
delta_E += int(trial_orient == right_neighbor_orient) * \
            (bond - vert_interface) + \
int(not(trial_orient == right_neighbor_orient)) * vert_interface

        # If left site is unoccupied, penalize for new vertical interface
        if left_neighbor == 0:
delta_E += vert_interface
        # If left site is occupied and orientation matches right site,
        # benefit for removing vertical interface and forming a new bond.
        # If orientation does not match, treats site as unoccupied
        else:
delta_E += int(trial_orient == left_neighbor_orient) * \
            (bond - vert_interface) + \
int(not(trial_orient == left_neighbor_orient)) * vert_interface

    # Calculate probability of adding growth unit then compare against random
    # number between 0.0 and 1.0, accepting move if probability exceeds it
exp_E = np.exp(-delta_E)
    if exp_E>= 1.0:
grid[trial_y_index, trial_x_index] = 1
orientation[trial_y_index, trial_x_index] = trial_orient
```

```
        Accepted += 1
        Branches += prob_check
    else:
        test = np.random.random()
        if exp_E> test:
grid[trial_y_index, trial_x_index] = 1
orientation[trial_y_index, trial_x_index] = trial_orient
            Accepted += 1
            Branches += prob_check
        else:
            Rejected += 1

# Surface Energy Distribution Plot
plt.figure()
lower = 0 # Lower bound of data scale
upper = 5 # Upper bound of data scale
plt.pcolormesh(surface_energy_distribution)
plt.colorbar()
plt.clim(lower, upper)
plt.title('Surface Energy Distribution')
```

APPENDIX C. COMPUTER CODE FOR CHAPTER 4 SIMULATIONS

```
## ==================== MC Crystallization Simulation ==================== ##
## ====================  Polymer Model - Version 5.1  ==================== ##
# ============================================================================
#  Version 1.0 is a 0th order random crystallization simulation, applying
#  arbitrary probabilities to the relevent phenomenological events of
#  nucleation, growth, and branching. Probabilities are adjusted empirically to
#  track trends of observed experimental data.
#
#  Version 2.0 is a more sophisticaed Monte Carlo style simulation, applying a
#  pseduo-Metropolis method to evaluate trial MC moves. Energy benefits given
#  for forming "bonds", and energy penalties for forming "interfaces" are
#  assigned empirically to reproduce observations.
#
#  Version 2.1 enhances simulation by only selecting vacent sites for MC step
#  consideration, to account for limitation of Version 2.0 that showed
#  rate of crystallization "slowing" as more sites became occupied.
#
#  Version 3.0 also incorporates a distribution of surface energies across the
#  surface, which controls sites of nucleation and the balance between
#  nucleation and growth rates throughout course of the simulation.
#
#  Version 4.0 incorporates branching by allowing for 90 degree rotation
#  of a new unit as it is added, which favors the attaching of new adjacent
#  units in this orientation.
#
#  Version 5.0 incorporates polymer inhibition of crystallization via physical
#  blocking of sites. For version 5.0, a given number of polymers will adsorb
#  before the simulation begins, with adsoprtion probability based on site
#  surface energy, and physically prevent crystallization at that site.
#
#  Version 5.1 sophisticates adsorption via a modified Langmuir isotherm such
#  that dynamic equilibration is possible. Polymers no long pre-equilibrate,
```

```
#  and new trial moves of adsorbing and desorbing are allowed. Driving force
#  is described through the Langmuir isotherm, while energetic heterogeneities
#  are captured by the Gibbs Free Energy equilibrium relation.
# ============================================================================
#%%
import numpy as np
import matplotlib.pyplot as plt
from matplotlib.colors import Normalize
import time
#%%
start = time.time()
## ======================== Initialize Parameters ======================== ##
MC_samples = 500000 # Number of trial MC steps
Accepted = 0 # Tracks number of accepted MC moves
Rejected = 0 # Tracks number of rejected MC moves
Rotated = 0 # Tracks number of times a rotated unit is added
Seed = np.random.randint(2147483646) # Generate seed
counter = 0
#Seed = 1696456340
MC_seed = np.random.seed(Seed) # Seed random number generator
branching_probability = 0.25 # Probability of rotating new trial unit

cmap = 'afmhot'
norm = Normalize(-0.5, 1.8)

#%%
## ============================ Generate Grids ============================ ##
# ============================================================================
#  Variable 'grid' stores if a given "lattice" location
#  contains a crystallite unit (1 for yes, 0 for no)
# ============================================================================
dimensionality = 500
total_lattice_sites = int((dimensionality - 2)**2)
grid = np.zeros((dimensionality, dimensionality), dtype = 'int')
indices = np.indices((dimensionality, dimensionality))
```

```
# Orientation default is 1, value of 0 corresponds to 90 degree rotation
orientation = np.ones((dimensionality, dimensionality), dtype = 'int')

# Interfaces holds the labeled interfaces on each of the lattice sites, where
# an empty or polymer has zeros, a vertical interface is +1, and a horizontal
# interface is -1. The order is up, right, down, left
interface = np.zeros((dimensionality, dimensionality, 4), dtype = 'int')

#%%
## ============================== Energetics ============================== ##
# ======================================================================
#  Assign energy benefits and penalties associated with forming "bonds"
#  and "interfaces". The base energy (surface energy) for each site is set at
#  0 initially and adjusted to provide desired configuration. "1" corresponds
#  to uniform (trivial) configuration. "2" corresponds to a distribution where
#  each site is randomly selected from the Gaussian distribution centered
#  around zero. "3" corresponds to a single, large 2D Gaussian function in the
#  center of the lattice. "4" corresponds to many randomly distributed small 2D
#  Gaussian functions. "5" corresponds to a single long and narrow diagonal
#  strip of high energy across the middle of the lattice.
# ======================================================================
bond = -5 # Energy benefit from adding an adjacent unit
Ratio = 4.2
Nuc_Bar = 2 * (5.25 + 1.25)
vert_interface = 0.5 * Nuc_Bar / (1 + Ratio) # Penalty from verical interface
horz_interface = vert_interface * Ratio # Penalty from horizontal interface
interface_penalties = np.array([vert_interface, horz_interface])
Aspect_Theory = np.square(Ratio)

# Surface Energy Distribution
configuration = 1 # Determines which energy configuration to implement

if configuration == 1: # Uniform Distribution
    surface_energy_distribution = np.zeros((dimensionality, dimensionality), \
```

```
                                    dtype = 'int')

elif configuration == 2: # Random Distribution
    surface_energy_mean = 0.0 # Mean of surface energy distribution
    surface_energy_stdev = 1.0 # StDev of surface energy distribution
    surface_energy_distribution = np.random.normal( \
                                    surface_energy_mean, surface_energy_stdev, \
                                    (dimensionality, dimensionality))

elif configuration == 3: # Large 2D Gaussian
    spread = dimensionality * 4 # Spread of effect of defect
    amp = 5 # Max surface energy at peak of defect
    center = dimensionality / 2 # Define the center coordinate of the lattice
    x_diff = np.power(center - indices[1], 2) # X differences squared
    y_diff = np.power(center - indices[0], 2) # Y differences squared
    surface_energy_distribution = amp*np.exp(-((x_diff + y_diff) / spread))

elif configuration == 4: # Random Small 2D Gaussians
    defects = 40 # Number of defect sites in surface
    spread = dimensionality/10 # Spread of effect of defect
    amp = 5 # Max surface energy at peak of defect
    surface_energy_distribution = np.zeros((dimensionality, dimensionality))
    for counter in range(0, defects):
        [x_center, y_center] = np.random.randint(
                                1, dimensionality - 1, size = 2)
        x_diff = np.power(x_center - indices[1], 2)
        y_diff = np.power(y_center - indices[0], 2)
        surface_energy_distribution += amp * np.exp(
                                        -((x_diff + y_diff) / spread))

elif configuration == 5: # Diagonal line
    width = 11 # Odd number giving the width of the line
    amp = 5 # Max surface energy at peak of defect
    base = amp*np.ones((dimensionality, dimensionality))
    upper = np.triu(base, (width - 1) / 2)
```

```
    lower = np.tril(base, -(width - 1) / 2)
    surface_energy_distribution = np.subtract(np.subtract(base, upper), lower)

else: # Custom configuration
    QNM_file                =                open('20191124_ASP_SCANASYST-AIR_QNM-
AIR_ATZ#121_500nm_1_001_Flattened2.txt')
    full_data = np.loadtxt(QNM_file, skiprows = 1)
    QNM_file.close()

    height_data = np.reshape(full_data[:, 0], \
                  (dimensionality, dimensionality)) # Height, in nm
    adhesion_data = np.reshape(full_data[:, 1], \
                    (dimensionality, dimensionality)) # Force, in nN
    deformation_data = np.reshape(full_data[:, 2], \
                       (dimensionality, dimensionality)) # Deformation, in nm

    check = np.block([[adhesion_data, adhesion_data], \
            [adhesion_data, adhesion_data]])

    gamma1 = 51.2; # Surface energy of cantilever, in mJ*m^-2
    R = 80.0; # Cantilever radius, in nm
    kb = 1.38E-20 # Boltzmanns constant, in mJ*K^-1
    area = np.square(1E-9 * (5000 / 256)) # Area of pixel, in m^2
    T = 300 # Temperature, in K
    surface_energy = 1E6 * np.square(
                     adhesion_data / (R * np.pi * 3)) / (gamma1) # mJ*m^-2
#    surface_energy_distribution1 = surface_energy*area/(kb*T)
    surface_energy_distribution1 = surface_energy
#    avg = np.average(surface_energy_distribution1)
    avg = 0
    surface_energy_distribution = 0.8 * (surface_energy_distribution1 - avg)

#%%
## ====================== Polymer Pre-Equilibration ====================== ##
# ==========================================================================
```

```
#  Establishes rules for polymer adsorption. Version 5.1 fixes the solution
#  phase driving force, the energetic terms for adsorption onto the 3 possible
#  interfaces, and polymer globule size
# ============================================================================
Solution_phase = .1 # Solution phase thermodynamic driving force for adsorption
Polymer_size = 8
Polymer_amorphous = .05 # Multiplying factor when interacting with amorphous
sites
Polymer_vert = 1.25 # Multiplying factor when interacting with vert interface
Polymer_horz = 5.25 # Multiplying factor when interacting with horz interface
Polymer_filled = 0
# Globule counter and checker number and hold the lattice position of each
# polymer globule to make for easy tracking and removal
Globule_counter = 1
Globule_checker = np.zeros((dimensionality, dimensionality), dtype = 'int')

Keq = np.exp(Polymer_amorphous*np.square(Polymer_size))
Theta_eq = Keq*Solution_phase/(1 + Keq*Solution_phase)
Count_eq = Theta_eq*total_lattice_sites/(Polymer_size**2)

#Coverage = 0.25 # Fractional coverage of polymer onto film
#Polymer_size = 8
#Polymer_count = Coverage * total_lattice_sites/(Polymer_size**2)
#Polymer_energy = 2
#Polymer_filled = 0
#fail = 0
#while Globule_counter < Count_eq:
#    [trial_x_index, trial_y_index] = np.random.randint(
#                                          1, dimensionality - Polymer_size - 1,
size=2)
#       overlap = grid[trial_y_index, trial_x_index] + grid[trial_y_index +
Polymer_size - 1, trial_x_index] + grid[trial_y_index, trial_x_index +
Polymer_size - 1] + grid[trial_y_index + Polymer_size - 1, trial_x_index +
Polymer_size - 1]
#    while overlap != 0:
```

```
#        [trial_x_index, trial_y_index] = np.random.randint(
#                                             1, dimensionality - Polymer_size - 1,
size=2)
#           overlap = grid[trial_y_index, trial_x_index] + grid[trial_y_index +
Polymer_size  -  1,  trial_x_index]  +  grid[trial_y_index,  trial_x_index  +
Polymer_size  -  1]  +  grid[trial_y_index  +  Polymer_size  -  1,  trial_x_index  +
Polymer_size - 1]
#    polymer_x = np.zeros((Polymer_size, Polymer_size), dtype = 'int')
#    polymer_y = np.zeros((Polymer_size, Polymer_size), dtype = 'int')
#    for i in range(Polymer_size):
#        for j in range(Polymer_size):
#            polymer_x[j, i] = trial_x_index + i
#            polymer_y[j, i] = trial_y_index + j
#       delta_E  =  np.sum(-surface_energy_distribution[polymer_y,  polymer_x])  *
Polymer_amorphous
#    energy = np.exp(-delta_E)
#    prob = np.random.random()
#    if energy > prob:
#        grid[polymer_y, polymer_x] = -1
#        Globule_checker[polymer_y, polymer_x] = Globule_counter
#        Polymer_filled += Polymer_size**2
#        Globule_counter += 1
#    else:
#        fail += 1

Real_time_coverage = Polymer_filled / (dimensionality-2)**2
RTCov = np.array([Real_time_coverage])
step_count = np.array([0])

#%%
## ============================  Simulation ============================== ##
for counter in range(MC_samples):
    # End simulation if entire surface crystallizes
    if Accepted >= 0.9 * (total_lattice_sites - Polymer_filled):
        print('Surface 90% crystallized')
```

```
        break

    Real_time_coverage = Polymer_filled / (dimensionality-2)**2
    Qr = Real_time_coverage/(Solution_phase*(1-Real_time_coverage))
    RTCov = np.append(RTCov, Real_time_coverage)
    # Save real time polymer coverage throughout simulation
    if (counter + 1) % 100000 == 0:
        RTCov = np.append(RTCov, Real_time_coverage)
        step_count = np.append(step_count, counter + 1)

#    # Save surface plot every specified number of steps
    if (counter + 1) % 5000000 == 0:
        fig = plt.figure()
        power = np.int(np.floor(np.log10(counter + 1)))
        value = (counter + 1) / pow(10, power)
        file_name    =    'E{:d}_{:.1f}_steps_polymertest008_v2.png'.format(power,
value)
        plt.pcolormesh(grid, cmap=cmap, norm=norm)
        plt.colorbar()
        plt.title(format('%d Trial Monte Carlo Steps' % (counter + 1)))
        fig.savefig(file_name)
        plt.close(fig)
        print((Accepted/(total_lattice_sites - Polymer_filled)))

    # Pick an uncrystallized spot at random
    [trial_x_index, trial_y_index] = np.random.randint(
                                     1, dimensionality - 1, size = 2)
    while grid[trial_y_index, trial_x_index] == 1:
        [trial_x_index, trial_y_index] = np.random.randint(
                                         1, dimensionality - 1, size = 2)

    # Determines if site is film or covered in polymer
    site = grid[trial_y_index, trial_x_index]

    # Determine trial move; if a site contains a polymer the only trial move is
```

```
    # to remove the polymer (0), while if the site is amorphous the site can
    # either crystallize (1) or a polymer can adsorb onto it (2)
    trial_move = (site + 1) * np.random.random()
#    trial_move = 0.8

#    trial_move = 0
    ## ======================== Polymer Desorption ======================== ##
    # ==================================================================
    #  If a polymer desorption (trial_move == 0) is selected, all adjacent
    #  sites which constitute the given polymer globule are selected and the
    #  energetic change due to removing these sites is determined and used to
    #  determine probability of trial move
    # ==================================================================
    if trial_move == 0:

        ## ==================== Determine Polymer Sites ==================== ##
        # ==================================================================
        #  Determine sites constituting the given polymer
        # ==================================================================
        globule_number = Globule_checker[trial_y_index, trial_x_index]
        polymer = np.nonzero(Globule_checker == globule_number)
        polymer_y = np.reshape(polymer[0], (Polymer_size, Polymer_size))
        polymer_x = np.reshape(polymer[1], (Polymer_size, Polymer_size))


        ## ================= Determine Crystal Neighbors ================= ##
        # ==================================================================
        #  Determine contents of adjacent sites and interfaces
        # ==================================================================
        polymer_adjacent = np.zeros((Polymer_size, 4), dtype = 'int')
        for i in range(2):
            polymer_adjacent[:, 2 * i] = interface[polymer_y[(Polymer_size - 1) *
i, :] + np.power(-1, i + 1), polymer_x[(Polymer_size - 1) * i, :], 2 * (1 - i)]
```

```
            polymer_adjacent[:,  (2  *  i)  +  1]  =  interface[polymer_y[:,
(Polymer_size - 1) * (1 - i)], polymer_x[:, (Polymer_size - 1) * (1 - i)] +
np.power(-1, i), 3 - (2 * i)]


        ## ========================= Energetics ========================== ##
        # ==============================================================
        # ==============================================================
        delta_E = Polymer_amorphous * np.sum(surface_energy_distribution[
                  polymer_y, polymer_x]) + Polymer_vert * np.count_nonzero(
                  polymer_adjacent == 1) + Polymer_horz * np.count_nonzero(
                  polymer_adjacent == -1) - np.log(Qr/Keq)

        ## ======================= Probability Check ====================== ##
        # ==============================================================
        # ==============================================================

        # Calculate probability of trial move then compare against a random
        # number between 0.0 and 1.0, accepting move if probability exceeds it
        exp_E = np.exp(-delta_E)
        if (exp_E >= 1.0) or (exp_E > np.random.random()):
            grid[polymer_y, polymer_x] = 0
            Globule_checker[polymer_y, polymer_x] = 0
            for i in range(4):
                interface[polymer_y, polymer_x, i] = 0
            Polymer_filled -= Polymer_size**2
        else:
            Rejected += 1

    ## ======================== Crystallization ========================== ##
    # ==============================================================
    #  If crystallization is selected,
    # ==============================================================
    elif trial_move <= 0.75:
```

```
## ====================== Determine Neighbors ====================== ##
# ========================================================================
#  Determine contents of adjacent sites and interfaces
# ========================================================================
adjacent = np.zeros((4, 1), dtype='int')

for i in range(4):
    adjacent[i] = interface[trial_y_index + ((i + 1) % 2)* (i - 1), \
                  trial_x_index + (i % 2) * (2 - i), \
                  2 + i - 4 * int(i / 2)]

## ===================== Evalutate Orientation ===================== ##
# ========================================================================
#  Determine the average orientation to use for determining the
#  definition of rotate versus non-rotated unit
# ========================================================================
orient_check = np.zeros((4, 1), dtype = 'int')
for i in range(4):
    orient_check[i] = adjacent[i] * np.power(-1, i)

avg_orient = int(np.greater_equal(np.average(orient_check), 0)) * 2 - 1
orient_rand = np.random.random()
prob_check = int(orient_rand >= branching_probability) * 2 - 1
trial_interface = np.array([1, -1, 1, -1]) * avg_orient * prob_check

## ========================== Energetics ========================== ##
# ========================================================================
# ========================================================================

# Determine energy benefit/penalty to adding crystal unit
delta_E = -surface_energy_distribution[trial_y_index, trial_x_index]

for i in range(4):
    delta_E += int(trial_interface[i] == adjacent[i]) * \
```

```
                    (bond-interface_penalties[int(-(trial_interface[i]-1)/2)])
+ \
                    (trial_interface[i] != adjacent[i]) * \
                    interface_penalties[int(-(trial_interface[i]-1)/2)]

        ## ====================== Probability Check ====================== ##
        # ================================================================
        # ================================================================

        # Calculate probability of adding unit then compare against a random
        # number between 0.0 and 1.0, accepting move if probability exceeds it
        exp_E = np.exp(-delta_E)
        if (exp_E >= 1.0) or (exp_E > np.random.random()):
            grid[trial_y_index, trial_x_index] = 1
            for i in range(4):
                interface[trial_y_index, trial_x_index, i] = trial_interface[i]
            Accepted += 1
            Rotated += -(avg_orient * prob_check - 1) / 2
        else:
            Rejected += 1


    ## ======================== Polymer Adsorption ======================== ##
    # ================================================================
    #  If polymer adsorption is selected,
    # ================================================================
    else:


        if (trial_x_index > dimensionality - Polymer_size - 1) or (trial_y_index
> dimensionality - Polymer_size - 1):
            continue

        polymer_x = np.zeros((Polymer_size, Polymer_size), dtype = 'int')
        polymer_y = np.zeros((Polymer_size, Polymer_size), dtype = 'int')
```

```
        for i in range(Polymer_size):
            for j in range(Polymer_size):
                polymer_x[j, i] = trial_x_index + i
                polymer_y[j, i] = trial_y_index + j

        overlap = grid[polymer_y, polymer_x]
        if np.count_nonzero(overlap):
            continue

        polymer_adjacent = np.zeros((Polymer_size, 4), dtype = 'int')
        for i in range(2):
            polymer_adjacent[:, 2 * i] = interface[polymer_y[(Polymer_size - 1) *
i, :] + np.power(-1, i + 1), polymer_x[(Polymer_size - 1) * i, :], 2 * (1 - i)]
            polymer_adjacent[:,  (2  *  i)  +  1]  =  interface[polymer_y[:,
(Polymer_size - 1) * (1 - i)], polymer_x[:, (Polymer_size - 1) * (1 - i)] +
np.power(-1, i), 3 - (2 * i)]


        ## ========================== Energetics ========================== ##
        # ================================================================
        # ================================================================
        delta_E = Polymer_amorphous * np.sum(-surface_energy_distribution[
                  polymer_y, polymer_x]) - Polymer_vert * np.count_nonzero(
                  polymer_adjacent == 1) - Polymer_horz * np.count_nonzero(
                  polymer_adjacent == -1) + np.log(Qr/Keq)

        ## ====================== Probability Check ====================== ##
        # ================================================================
        # ================================================================

        # Calculate probability of trial move then compare against a random
        # number between 0.0 and 1.0, accepting move if probability exceeds it
        exp_E = np.exp(-delta_E)
        if (exp_E >= 1.0) or (exp_E > np.random.random()):
            grid[polymer_y, polymer_x] = -1
```

```
            Globule_checker[polymer_y, polymer_x] = Globule_counter
            Globule_counter += 1
            for i in range(4):
                interface[polymer_y, polymer_x, i] = 0
            Polymer_filled += Polymer_size**2
        else:
            Rejected += 1

#%%
#ending = time.time()
#print(ending-start)

## Real Time Coverage Data
#file_name = 'Eq_{:.2f}_test008_v2.txt'.format(Theta_eq)
#Cov_file = open(file_name, 'w')
#
#for i in range(len(RTCov)):
#    Cov_file.write(str(step_count[i]))
#    Cov_file.write('\t')
#    Cov_file.write(str(RTCov[i]))
#    Cov_file.write('\n')
#
#Cov_file.close()

## Surface Energy Distribution Plot
#plt.figure()
#lower = 0 # Lower bound of data scale
#upper = 5 # Upper bound of data scale
#plt.pcolormesh(surface_energy_distribution)
#plt.colorbar()
#plt.clim(lower, upper)
#plt.title('Surface Energy Distribution')

## Histogram of Surface Energy of Sites
#plt.figure()
```

```
#plt.hist(np.ravel(surface_energy_distribution), bins=10)

# Final Surface State
plt.figure()
plt.pcolormesh(grid, cmap=cmap, norm=norm)
#plt.pcolormesh(grid, cmap=cmap)
plt.colorbar()
plt.title(format('%d Trial Monte Carlo Steps' % (MC_samples)))
plt.figure()
plt.plot(RTCov)
```

APPENDIX D. COMPUTER CODE FOR CHAPTER 5 DATA ANALYSIS

```
close all
clear
clc
%% Establish file path parameters for data import
file_count = 12; % Number of files in batch to process
initial_time = [2020, 2, 27, 13, 36, 04]; % Year, month, day, hour, minute, second
fileID_base = 'Control_T2_XZdata'; % Base name of files
Rzcross_sections = zeros(file_count, 1); % Holds Rz for each section
FFTcross_sections = zeros(file_count, 3); % Holds height, freq, offset, from FFT
LSNRcross_sections = zeros(file_count, 3); % Holds height, freq, offset, from least-squares non-linear regression
elapsed_time = zeros(file_count, 1);

%% Import cross-section data and fit
for i = 1:1:file_count
    % Data Import
    filename = sprintf('%s%d.txt', fileID_base, i);
    delimiterIn1 = '\t';
    headerlinesIn1 = 1;
    XZ = importdata(filename, delimiterIn1, headerlinesIn1);
    X = XZ.data(1:1:end-1, 1);
    Z = XZ.data(1:1:end-1, 2);
    fID = fopen(filename);
    header = textscan(fID, '%s %s', 1);
    XZ2 = textscan(fID, '%f %f', length(X));
    extract_timestamp = textscan(fID, '%s %s %s %s %s %s', 1);
    updated_hour = datestr(sprintf('%s %s',extract_timestamp{1}{1}, extract_timestamp{2}{1}), 'HH:MM:SS');
    fclose(fID);
    timestamp = sprintf('%s %s, %s %s', extract_timestamp{4}{1}, extract_timestamp{5}{1}, extract_timestamp{6}{1}, updated_hour);
```

```
final = datetime(timestamp);
final_time = datevec(final);
elapsed_time(i) = etime(final_time, initial_time);
Rzcross_sections(i, 1) = mean(maxk(Z, 5)) - mean (mink(Z, 5));

% FFT Fit
L = length(X);
Y = fft(Z);
P2 = abs(Y/L);
P1 = P2(1:L/2+1);
P1(2:end-1) = 2*P1(2:end-1);
D = X(end)/L;
Fs = 1/D;
freq = Fs*(0:(L/2))/L;
lambda = 1./freq;
[peakwave, index] = max(P1);
peakfreq = freq(index);
j = 0:0.0001:1/peakfreq;
sqerr = sum((Z - peakwave*sin(2*pi*peakfreq*(X-j))).^2, 1);
sse_fft = sum(sqerr);
[minimum, j_index] = min(sqerr);
offset = j(j_index);
FFTcross_sections(i,1) = peakwave;
FFTcross_sections(i,2) = peakfreq;
FFTcross_sections(i,3) = offset;

 % FFT Plot
 figure()
 plot(freq', P1)
 figure()
 plot(X, Z)
 hold on
 plot(X, peakwave*sin(2*pi*peakfreq*(X-offset)))
 title('FFT Fit')
 hold off
```

```
    % LSNR Fit
    J = Z > 0;
    k = 1:1:length(J)-1;
    K = (J(k+1) > J(k));
    check = X(K);
    h = 1:1:length(check)-1;
    est_wave = mean(check(h+1)-check(h));
     est_freq = 1/est_wave;
    est_freq = peakfreq;
    est_amp = max(abs(Z));
    est_off = check(1);
    g = fittype('amp*sin(2*pi*freq*(X-offset))', 'independent', 'X', 'dependent',
'Z', 'coefficients', {'amp', 'freq', 'offset'});
    [f, gof] = fit(X, Z, g, 'Lower', [0.1, 0.1, 0], 'Upper', [2*est_amp,
est_freq*2, est_off*2], 'StartPoint', [est_amp, est_freq, est_off]);
    LSNRcross_sections(i,1) = f.amp;
    LSNRcross_sections(i,2) = f.freq;
    LSNRcross_sections(i,3) = f.offset;

     % LSNR Plot
     figure()
     plot(f, X, Z, '-')
     title('Regression Fit')
end


%% Rz Model
range = elapsed_time(end);
g_new0 = fittype('h0*exp(-K*t)', 'independent', 't', 'dependent', 'h',
'coefficients', {'h0', 'K'});
[f_new0, gof_new0] = fit(elapsed_time, Rzcross_sections(:,1), g_new0, 'Lower', [0,
0], 'Upper', [2*Rzcross_sections(1, 1), 5], 'StartPoint', [Rzcross_sections(1),
1E-6]);
domainRz = max(f_new0(0), max(Rzcross_sections(:,1)));
```

```
display(f_new0)
display(gof_new0)
figure()
plot(f_new0, elapsed_time, Rzcross_sections(:,1), 'x')
title('Height vs Time for Rz Model', 'FontSize', 20)
xlabel('Time (s)', 'FontSize', 16)
ylabel('Height (nm)', 'FontSize', 16)
legend({'Data', 'Fit'}, 'FontSize', 16)
text(5000, 40, sprintf('h(t) = %.1fe^{-%.2et}', f_new0.h0, f_new0.K), 'FontSize',
16)
text(5500, 35, sprintf('r^2 = %.2f', gof_new0.rsquare), 'FontSize', 16)
axis([-0.03*range, 1.03*range, -0.03*domainRz, 1.03*domainRz])
ax = gca;
ax.FontSize = 16;
fig = gcf;
fig.Color = [1 1 1];

%% FFT Model
[f_new1, gof_new1] = fit(elapsed_time, 2*FFTcross_sections(:,1), g_new, 'Lower',
[0,    0],    'Upper',    [4*FFTcross_sections(1,    1),    5],    'StartPoint',
[2*FFTcross_sections(1), 1E-6]);
domainFFT = max(f_new1(0), max(2*FFTcross_sections(:,1)));
display(f_new1)
display(gof_new1)
figure()
plot(f_new1, elapsed_time, 2*FFTcross_sections(:,1), 'x')
title('Height vs Time for FFT Model', 'FontSize', 20)
xlabel('Time (s)', 'FontSize', 16)
ylabel('Height (nm)', 'FontSize', 16)
legend({'Data', 'Fit'}, 'FontSize', 16)
text(5000, 40, sprintf('h(t) = %.1fe^{-%.2et}', f_new1.h0, f_new1.K), 'FontSize',
16)
text(5500, 35, sprintf('r^2 = %.2f', gof_new1.rsquare), 'FontSize', 16)
axis([-0.03*range, 1.03*range, -0.03*domainFFT, 1.03*domainFFT])
ax = gca;
```

```
ax.FontSize = 16;
fig = gcf;
fig.Color = [1 1 1];

%% LSNR Model
[f_new2, gof_new2] = fit(elapsed_time, 2*LSNRcross_sections(:,1), g_new, 'Lower',
[0,    0],    'Upper',    [4*LSNRcross_sections(1,    1),    5],    'StartPoint',
[2*LSNRcross_sections(1), 1E-6]);
domainLSNR = max(f_new2(0), max(2*LSNRcross_sections(:,1)));
display(f_new2)
display(gof_new2)
figure()
plot(f_new2, elapsed_time, 2*LSNRcross_sections(:,1), 'x')
title('Height vs Time for Regression Model', 'FontSize', 20)
xlabel('Time (s)', 'FontSize', 16)
ylabel('Height (nm)', 'FontSize', 16)
legend({'Data', 'Fit'}, 'FontSize', 16)
text(5000, 40, sprintf('h(t) = %.1fe^{-%.2et}', f_new2.h0, f_new2.K), 'FontSize',
16)
text(5500, 35, sprintf('r^2 = %.2f', gof_new2.rsquare), 'FontSize', 16)
axis([-0.03*range, 1.03*range, -0.03*domainLSNR, 1.03*domainLSNR])
ax = gca;
ax.FontSize = 16;
fig = gcf;
fig.Color = [1 1 1];

%% Assess surface feature accuracy/reproducability in model
K_est = [f_new1.K, f_new2.K, mean([f_new1.K, f_new2.K])];
rsq = [gof_new1.rsquare, gof_new2.rsquare];
figure()
plot(1:1:file_count,   1000./FFTcross_sections(:,   2),   'x',   1:1:file_count,
1000./LSNRcross_sections(:, 2), 'o')
legend('FFT Wavelength', 'Regression Wavelength', 'FontSize', 16)
title('Wavelength of Sinewave Fit to Surface', 'FontSize', 20)
xlabel('Scan #', 'FontSize', 16)
```

```
ylabel('Wavelength (nm)', 'FontSize', 16)
ax = gca;
ax.FontSize = 16;
fig = gcf;
fig.Color = [1 1 1];
```

APPENDIX E. SUPPLEMENTAL INFORMATION FOR DATA AND FIGURES

To facilitate reproduction and critique of data presented herein, cross-references are provided to any computer files and pages from laboratory notebooks which contain data or information on experiments used to generate figures. All computer files will be available on a thumb drive provided with the laboratory notebooks.

E.1 Chapter 3

All files for Figure 3.1 are found at \Beaudoin Group\Dissertation\Chapter3 – Surf E\Figures\

Figure 3.1	Notebook Reference	File path
Figure 3.1A	Notebook 1; page 57, 72-73	20170831_ASP_NPG-C_ATZ#10_fresh_ pH7buffer_50uguLdrug_nopolymer_5um_4.001
Figure 3.1B	Notebook 1; page 155, 169	20180130_ASP_NPG-C_ATZ#27_6hours_40C_ pH7buffer_25ugmLdrug_nopolymer_5um_2.001
Figure 3.1C	Notebook 1; page 155, 176	20180206_ASP_NPG-C_ATZ#27_14hours_40C_ pH7buffer_25ugmLdrug_nopolymer_5um_1.001
Figure 3.1D	Notebook 1; page 155, 179	20180208_ASP_NPG-C_ATZ#27_16hours_40C_ pH7buffer_25ugmLdrug_nopolymer_5um_1.001
Figure 3.1E	Notebook 1; page 155, 182	20180215_ASP_NPG-C_ATZ#27_20hours_40C_ pH7buffer_25ugmLdrug_nopolymer_5um_1.001
Figure 3.1F	Notebook 1; page 77, 90	20170921_ASP_NPG-C_ATZ#12_1day40C_ pH7buffer_75ugmLdrug_nopolymer_5um_5.002

All files for Figure 3.2 are found at \Beaudoin Group\Dissertation\Chapter3 – Surf E\Figures\

Figure 3.2	Notebook Reference	File path
Figure 3.2A	Notebook 2, page 101	20190507_ASP_SCANASYST-AIR_ATZ#S7_10um_1.001
Figure 3.2B	Notebook 2, page 101	20190507_ASP_SCANASYST-AIR_ATZ#S8_10um_1.001
Figure 3.3C	Notebook 2, page 102	20190508_ASP_SCANASYST-AIR_ATZ#S9_10um_1.001
Figure 3.4D	Notebook 2, page 102	20190508_ASP_SCANASYST-AIR_ATZ#S10_10um_1.001

All files for Figure 3.3 are found at \Beaudoin Group\Dissertation\Chapter3 – Surf E\Figures\

Figure 3.3	Notebook Reference	File path
Figure 3.2A	Notebook 2, page 73, 86	20181105_ASP_SEM_ATZ#114_015.TIF
Figure 3.2B	Notebook 2, page 2, 6, 7, 85	20181031_ASP_SEM_ATZ#41_005.TIF

All files for Figure 3.4 are found at \Beaudoin Group\Computation\Changing Surface Energy\Uniform Energy\

Figure 3.4	File path
Ratio 1.0	Aspect Ratio\AR1.00_E7_1.5.PNG
Ratio 1.5	Aspect Ratio\AR1.50_E7_1.5.PNG
Ratio 2.0	Aspect Ratio\AR2.00_E7_1.5.PNG
Ratio 2.5	Aspect Ratio\AR2.50_E7_1.5.PNG
Ratio 3.0	Aspect Ratio\AR3.00_E7_1.5.PNG
Ratio 4.2	E7_1.5.PNG
Ratio 5.0	Aspect Ratio\AR1.00_E7_1.5.PNG
Ratio 10.0	Aspect Ratio\AR10.0_E7_1.5.PNG

All files for Figure 3.5 are found at \Beaudoin Group\Computation\Changing Surface Energy\Uniform Energy\Nucleation Rate

Figure 3.5	File path
Barrier 0.1	Nucleation0.10_E5_1.3.PNG
Barrier 1.0	Nucleation1.00_E5_2.0.PNG
Barrier 4.0	Nucleation4.00_E5_6.5.PNG
Barrier 6.0	Nucleation6.00_E6_1.3.PNG
Barrier 8.0	Nucleation8.00_E6_3.5.PNG
Barrier 10.0	Nucleation10.0_E6_9.4.PNG
Barrier 13.0	Nucleation13.0_E7_4.4.PNG
Barrier 15.0	Nucleation15.0_E8_1.4.PNG

All files for Figure 3.6 are found at \Beaudoin Group\Computation\Changing Surface Energy\Uniform Energy\Lattice Energy

Figure 3.6	File path
Lattice 0	Lattice0.0_E8_2.2.PNG
Lattice -2	Lattice2.0_E7_8.1.PNG
Lattice -4	Lattice4.0_E7_4.8.PNG
Lattice -6	Lattice6.0_E7_2.8.PNG
Lattice -8	Lattice8.0_E7_1.7.PNG
Lattice -10	Lattice10.0_E7_1.0.PNG
Lattice -15	Lattice15.0_E6_.9.0PNG
Lattice -20	Lattice20.0_E6_9.6.PNG

Data for Figure 3.7 is found at Beaudoin Group\Computation\Changing Surface Energy\Uniform Energy\sensitivity_results_updatedlattice3 and Beaudoin Group\Computation\Changing Surface Energy\Uniform Energy\sensitivity_results_added-ratios

Figure 3.7A	Replicate Number									
Ratio	1	2	3	4	5	6	7	8	9	10
1	2.0E7	1.9E7	2.0E7	2.1E7	2.0E7	2.0E7	2.0E7	2.1E7	2.0E7	1.9E7
1.5	1.7E7	2.0E7	2.0E7	2.0E7	1.9E7	1.9E7	2.2E7	2.0E7	2.0E7	2.1E7
2	2.2E7	2.3E7	2.3E7	2.3E7	2.5E7	2.3E7	2.2E7	2.5E7	2.3E7	2.5E7
2.5	2.8E7	2.7E7	2.9E7	2.7E7	2.8E7	2.7E7	2.7E7	2.9E7	2.7E7	2.8E7
3	3.0E7	3.1E7	3.0E7	2.9E7	2.8E7	3.0E7	3.0E7	3.1E7	3.1E7	2.8E7
3.5	3.2E7	3.2E7	3.0E7	2.9E7	3.4E7	2.9E7	3.3E7	3.6E7	3.6E7	3.2E7
4	3.4E7	3.4E7	3.1E7	3.5E7	3.5E7	3.2E7	3.3E7	3.5E7	3.3E7	3.7E7
4.5	3.8E7	3.5E7	3.8E7	3.9E7	3.8E7	3.6E7	3.3E7	3.5E7	3.9E7	3.7E7
5	3.8E7	3.9E7	4.0E7	3.5E7	3.6E7	3.9E7	3.9E7	4.0E7	3.8E7	3.9E7
5.5	3.9E7	3.8E7	4.0E7	4.2E7	3.8E7	3.8E7	3.9E7	4.2E7	4.2E7	3.6E7
6	4.1E7	4.0E7	4.3E7	3.9E7	4.3E7	3.8E7	3.8E7	3.9E7	4.0E7	3.8E7
6.5	4.3E7	4.0E7	4.2E7	4.0E7	4.0E7	4.1E7	4.1E7	4.2E7	4.1E7	4.0E7
7	4.4E7	4.4E7	4.2E7	4.3E7	4.4E7	4.7E7	4.6E7	4.3E7	4.6E7	4.4E7
7.5	4.3E7	4.4E7	4.3E7	4.0E7	4.2E7	4.3E7	4.5E7	4.3E7	4.3E7	4.4E7
8	4.6E7	4.5E7	4.5E7	5.0E7	4.1E7	4.3E7	4.3E7	4.1E7	4.1E7	4.5E7
8.5	4.4E7	4.8E7	4.0E7	4.3E7						

Figure 3.7B	Replicate Number									
ln(E)	1	2	3	4	5	6	7	8	9	10
-20	9.8E6	9.5E6	1.0E7	1.1E7	1.0E7	9.0E6	9.6E6	8.3E6	8.0E6	1.1E7
-19	8.5E6	1.2E7	8.7E6	8.7E6	9.4E6	9.8E6	9.9E6	8.7E6	9.3E6	9.5E6
-18	9.8E6	9.5E6	8.2E6	9.6E6	9.2E6	9.5E6	1.0E7	1.0E7	8.2E6	1.2E7
-17	1.0E7	9.7E6	8.6E6	1.0E7	9.2E6	1.2E7	8.6E6	9.2E6	9.9E6	1.1E7
-16	9.5E6	9.9E6	9.4E6	9.6E6	9.5E6	8.4E6	7.7E6	8.9E6	9.0E6	7.6E6
-15	8.7E6	8.7E6	9.9E6	9.4E6	1.0E7	1.1E7	8.4E6	9.0E6	1.0E7	1.1E7
-14	9.4E6	8.5E6	9.6E6	1.1E7	9.4E6	1.0E7	1.1E7	1.1E7	8.7E6	1.0E7
-13	9.4E6	9.1E6	9.7E6	1.0E7	1.0E7	9.7E6	1.1E7	9.7E6	1.0E7	1.0E7
-12	8.5E6	8.3E6	1.1E7	9.1E6	8.8E6	1.0E7	1.0E7	9.2E6	8.7E6	9.1E6
-11	8.2E6	9.7E6	9.3E6	1.0E7	9.7E6	9.4E6	1.0E7	9.8E6	9.3E6	8.2E6
-10	1.2E7	1.1E7	1.0E7	1.3E7	1.1E7	1.3E7	1.1E7	1.1E7	1.0E7	1.1E7
-9	1.6E7	1.5E7	1.4E7	1.3E7	1.6E7	1.3E7	1.5E7	1.5E7	1.3E7	1.5E7
-8	1.7E7	1.7E7	1.7E7	1.7E7	1.7E7	1.7E7	2.0E7	1.7E7	1.8E7	2.3E7
-7	2.3E7	2.2E7	2.4E7	2.0E7	2.1E7	2.1E7	2.2E7	2.1E7	2.2E7	2.1E7
-6	3.0E7	2.8E7	2.9E7	2.8E7	2.9E7	2.7E7	2.9E7	2.6E7	2.7E7	2.8E7
-5	3.4E7	3.9E7	3.5E7	3.7E7	3.5E7	3.5E7	3.6E7	3.3E7	3.2E7	3.5E7
-4	4.6E7	4.3E7	4.4E7	4.1E7	4.0E7	4.6E7	4.5E7	4.2E7	4.4E7	4.4E7
-3	5.2E7	5.3E7	5.7E7	5.3E7	5.5E7	5.7E7	5.9E7	5.7E7	5.6E7	5.9E7
-2	7.8E7	8.7E7	7.9E7	7.9E7	7.1E7	8.2E7	8.1E7	7.2E7	7.8E7	7.3E7
-1	1.3E8	1.3E8	1.3E8	1.2E8	1.3E8	1.3E8	1.3E8	1.2E8	1.3E8	1.3E8

0	2.3E8	2.2E8	2.2E8	2.3E8						

Figure 3.7C	Replicate Number									
ln(N)	1	2	3	4	5	6	7	8	9	10
0	1.2E5	1.2E5	1.2E5	1.2E5	1.2E5	1.2E5	1.2E5	1.2E5	1.2E5	1.2E5
0.1	1.3E5	1.3E5	1.3E5	1.3E5	1.3E5	1.3E5	1.3E5	1.3E5	1.3E5	1.3E5
0.2	1.4E5	1.4E5	1.4E5	1.4E5	1.4E5	1.4E5	1.4E5	1.4E5	1.4E5	1.4E5
0.3	1.4E5	1.4E5	1.4E5	1.4E5	1.4E5	1.4E5	1.4E5	1.4E5	1.4E5	1.4E5
0.4	1.5E5	1.5E5	1.5E5	1.5E5	1.5E5	1.5E5	1.5E5	1.5E5	1.5E5	1.5E5
0.5	1.6E5	1.6E5	1.6E5	1.6E5	1.6E5	1.6E5	1.6E5	1.6E5	1.6E5	1.6E5
0.6	1.7E5	1.7E5	1.7E5	1.7E5	1.7E5	1.7E5	1.7E5	1.7E5	1.7E5	1.7E5
0.7	1.7E5	1.7E5	1.7E5	1.7E5	1.7E5	1.7E5	1.7E5	1.7E5	1.7E5	1.7E5
0.8	1.8E5	1.8E5	1.8E5	1.8E5	1.8E5	1.8E5	1.8E5	1.8E5	1.8E5	1.8E5
0.9	1.9E5	1.9E5	1.9E5	1.9E5	1.9E5	1.9E5	1.9E5	1.9E5	1.9E5	1.9E5
1	2.0E5	2.0E5	2.0E5	2.0E5	2.0E5	2.0E5	2.0E5	2.0E5	2.0E5	2.0E5
1.1	2.1E5	2.1E5	2.1E5	2.1E5	2.1E5	2.1E5	2.1E5	2.1E5	2.1E5	2.1E5
1.2	2.2E5	2.2E5	2.2E5	2.2E5	2.2E5	2.2E5	2.2E5	2.2E5	2.2E5	2.2E5
1.3	2.3E5	2.3E5	2.3E5	2.3E5	2.3E5	2.3E5	2.3E5	2.3E5	2.3E5	2.3E5
1.4	2.4E5	2.4E5	2.4E5	2.4E5	2.4E5	2.4E5	2.4E5	2.4E5	2.4E5	2.4E5
1.5	2.5E5	2.5E5	2.5E5	2.5E5	2.5E5	2.5E5	2.5E5	2.5E5	2.5E5	2.5E5
1.6	2.6E5	2.6E5	2.6E5	2.6E5	2.6E5	2.6E5	2.6E5	2.6E5	2.6E5	2.6E5
1.7	2.7E5	2.7E5	2.7E5	2.7E5	2.7E5	2.7E5	2.7E5	2.7E5	2.7E5	2.7E5
1.8	2.8E5	2.8E5	2.8E5	2.8E5	2.8E5	2.8E5	2.8E5	2.8E5	2.8E5	2.8E5
1.9	2.9E5	2.9E5	2.9E5	2.9E5	2.9E5	2.9E5	2.9E5	2.9E5	2.9E5	2.9E5
2	3.1E5	3.1E5	3.1E5	3.1E5	3.1E5	3.1E5	3.1E5	3.1E5	3.1E5	3.1E5
3	4.5E5	4.5E5	4.5E5	4.5E5	4.5E5	4.5E5	4.5E5	4.5E5	4.5E5	4.5E5
4	6.5E5	6.6E5	6.5E5	6.5E5	6.5E5	6.6E5	6.6E5	6.6E5	6.5E5	6.5E5
5	9.2E5	9.3E5	9.2E5	9.3E5	9.3E5	9.2E5	9.2E5	9.3E5	9.3E5	9.2E5
6	1.3E6	1.3E6	1.3E6	1.3E6	1.3E6	1.3E6	1.3E6	1.3E6	1.3E6	1.3E6
7	2.1E6	2.1E6	2.1E6	2.1E6	2.1E6	2.1E6	2.1E6	2.1E6	2.1E6	2.1E6
8	3.5E6	3.5E6	3.5E6	3.5E6	3.4E6	3.5E6	3.5E6	3.5E6	3.5E6	3.5E6
9	5.9E6	5.8E6	5.8E6	5.9E6	5.9E6	5.9E6	5.8E6	5.8E6	5.9E6	5.8E6
10	9.6E6	9.6E6	9.7E6	9.5E6	9.2E6	9.7E6	9.7E6	9.9E6	9.4E6	1.0E7
11	1.6E7	1.6E7	1.6E7	1.7E7	1.7E7	1.6E7	1.6E7	1.6E7	1.6E7	1.6E7
12	2.8E7	2.6E7	2.6E7	2.6E7	2.5E7	2.6E7	2.5E7	2.6E7	2.6E7	2.7E7
13	4.5E7	4.6E7	4.8E7	4.3E7	4.3E7	4.4E7	4.3E7	4.5E7	4.5E7	5.0E7
14	7.0E7	7.5E7	8.1E7	7.2E7	7.6E7	7.8E7	7.0E7	7.4E7	8.0E7	7.9E7
15	1.4E8	1.3E8	1.5E8	1.1E8	1.3E8	1.3E8	1.4E8	1.3E8	1.4E8	1.8E8

All files for Figure 3.8 are found at \Beaudoin Group\Computation\Changing Surface Energy\Random Distribution\

Figure 3.4	File path
Figure 3.4A	E6_5.0.PNG
Figure 3.4B	E7_1.0.PNG

Figure 3.4C	E7_1.5.PNG
Figure 3.4D	E7_2.0.PNG
Figure 3.4E	E7_2.5.PNG
Figure 3.4F	E7_3.0.PNG
Figure 3.4G	E7_3.5.PNG
Figure 3.4H	E7_4.0.PNG

Numeric data for Figure 3.9 is found at \Beaudoin Group\Computation\Percent_Crystallized\ Composite Data. Files used to generate numeric data from experiments found at \Beaudoin Group\Computation\Experiments\Raw Images and \Beaudoin Group\Computation\Experiments\ Binary Images which were processed and analyzed through ImageJ

Experimental			Simulation			
Time (h)	Avg	Std Dev	MC Steps	500,000*MC	Avg	Std Dev
0	0	0	0	0	0	0
2	0.061001	0.049425	1000000	1.666667	0.000535	5.93E-05
4	0.254762	0.085747	2000000	3.333333	0.002662	0.000237
6	0.220584	0.044451	3000000	5	0.007851	0.000731
8	0.230038	0.079526	4000000	6.666667	0.017534	0.001308
10	0.246563	0.052244	5000000	8.333333	0.034271	0.002149
12	0.288875	0.09091	6000000	10	0.059598	0.003082
14	0.383372	0.050972	7000000	11.66667	0.097034	0.003782
16	0.506021	0.04274	8000000	13.33333	0.148781	0.004696
18	0.469513	0.090869	9000000	15	0.218383	0.006016
20	0.475077	0.063842	10000000	16.66667	0.310094	0.008322
22			11000000	18.33333	0.429636	0.011587
24	1		12000000	20	0.584531	0.017311
			13000000	21.66667	0.797393	0.028944
			14000000	23.33333	1	0

All files for Figure 3.10 are found at \Beaudoin Group\Computation\Changing Surface Energy\Uniform Energy\

Figure 3.10	File path
Figure 3.10A	Surface_Energy_Distribution.PNG
Figure 3.10B	E6_5.0.PNG
Figure 3.10C	E7_1.0.PNG
Figure 3.10D	E7_1.5.PNG
Figure 3.10E	E7_2.0.PNG
Figure 3.10F	E7_2.5.PNG
Figure 3.10G	E7_3.0.PNG
Figure 3.10H	E7_3.5.PNG

Figure 3.10I	E7_4.0.PNG

All files for Figure 3.11 are found at \Beaudoin Group\Computation\Changing Surface Energy\Single Large 2D Gaussian\

Figure 3.11	File path
Figure 3.11A	Surface_Energy_Distribution.PNG
Figure 3.11B	E6_5.0.PNG
Figure 3.11C	E7_1.0.PNG
Figure 3.11D	E7_1.5.PNG
Figure 3.11E	E7_2.0.PNG
Figure 3.11F	E7_2.5.PNG
Figure 3.11G	E7_3.0.PNG
Figure 3.11H	E7_3.5.PNG
Figure 3.11I	E7_4.0.PNG

All files for Figure 3.12 are found at \Beaudoin Group\Computation\Changing Surface Energy\Multiple Small Defects\

Figure 3.12	File path
Figure 3.12A	Surface_Energy_Distribution.PNG
Figure 3.12B	E6_5.0.PNG
Figure 3.12C	E7_1.0.PNG
Figure 3.12D	E7_1.5.PNG
Figure 3.12E	E7_2.0.PNG
Figure 3.12F	E7_2.5.PNG
Figure 3.12G	E7_3.0.PNG
Figure 3.12H	E7_3.5.PNG

All files for Figure 3.13 are found at \Beaudoin Group\Computation\Changing Surface Energy\Diagonal Fracture\

Figure 3.13	File path
Figure 3.13A	Surface_Energy_Distribution.PNG
Figure 3.13B	E6_4.0.PNG
Figure 3.13C	E6_8.0.PNG
Figure 3.13D	E7_1.2.PNG
Figure 3.13E	E7_1.6.PNG
Figure 3.13F	E7_2.0.PNG
Figure 3.13G	E7_2.4.PNG
Figure 3.13H	E7_2.8.PNG
Figure 3.13I	E7_3.2.PNG

All files for Figure 3.13 are found at \Beaudoin Group\Computation\Surface_Energy_QNM

Figure 3.14	Notebook Reference	File path
Figure 3.14A	Notebook 2; page 141-142	20191124_ASP_SCANASYST-AIR_QNM_ATZ#121_500nm_Flattened2.001
Figure 3.14B		Surface_Energy3.PNG
Figure 3.14C		500nm-test3_E6_2.0_steps.PNG
Figure 3.14D		500nm-test3_E6_4.0_steps.PNG
Figure 3.14E		500nm-test3_E6_6.0_steps.PNG
Figure 3.14F		500nm-test3_E6_8.0_steps.PNG
Figure 3.14G		500nm-test3_E7_1.0_steps.PNG
Figure 3.14H		500nm-test3_E6_1.2_steps.PNG

E.2 Chapter 4

Files for Figure 4.2 are found at \Beaudoin Group\Manuscript 2 Polymer & Surfactant\ Figures\

Figure 4.2	Notebook Reference	File path
Figure 4.2A,F	Notebook 1; page 57, 72-73	20170831_ASP_NPG-C_ATZ#10_fresh_ pH7buffer_50uguLdrug_nopolymer_5um_4.001
Figure 4.2B,G	Notebook 1; page 68-69, 73	20170831_ASP_NPG-C_ATZ#11_fresh_pH7 buffer_50uguLdrug_10uguLPVAc_5um_7.001
Figure 4.2C,H	Notebook 2; page 2, 9-11	20180306_ASP_NPG-C_ATZ#44_fresh_pH6-8buffer_25ugmLdrug_10ugmLHPMCAS-HF_5um_1.001
Figure 4.2D,I	Notebook 2; page 2, 9-11	20180306_ASP_NPG-C_ATZ#45_fresh_pH6-8buffer_25ugmLdrug_10ugmLHPMCAS-MF_5um_3.001
Figure 4.2E,J	Notebook 1; page 37-42	20170720_ASP_NPG-C_Atazanavir#3_ pH7buffer_10ugmLPVP_5um.001

Files for Figure 4.3 are found at \Beaudoin Group\Manuscript 2 Polymer & Surfactant\ Figures\

Figure 4.3	Notebook Reference	File path
Figure 4.3A,C	Notebook 1; page 57, 72-73	20170831_ASP_NPG-C_ATZ#10_fresh_ pH7buffer_50uguLdrug_nopolymer_5um_4.001
Figure 4.3B,D	Notebook 1; page 151-154	20180109_ASP_NPG-C_ATZ#25_3hour_40C_ pH7buffer_25ugmLdrug_nopolymer_5um_3.002

Files for Figure 4.4 are found at \Beaudoin Group\Manuscript 2 Polymer & Surfactant\ Figures\

Figure 4.4	Notebook Reference	File path
Figure 4.4A,D	Notebook 2; page 2-3	20180226_ASP_NPG-C_ATZ#35_fresh_pH7 buffer_25ugmLdrug_10ugmLHPMCAS_5um_3.001
Figure 4.4B,E	Notebook 2; page 16-17	20180328_ASP_NPG-C_ATZ#51_1day_40C_ ph6-8buffer_25ugmLdrug_10ugmLHPMCAS-HF_5um_3.001
Figure 4.4C,F	Notebook 2; page 18	20180402_ASP_NPG-C_ATZ#51_6days_40C_ ph6-8buffer_25ugmLdrug_10ugmLHPMCAS-HF_5um_2.001

Files for Figure 4.5 are found at \Beaudoin Group\Manuscript 2 Polymer & Surfactant\ Figures\

Figure 4.5	Notebook Reference	File path
Figure 4.5A,D	Notebook 2; page 2, 9-11	20180306_ASP_NPG-C_ATZ#45_fresh_pH6-8buffer_25ugmLdrug_10ugmLHPMCAS-MF_5um_3.001
Figure 4.5B,E	Notebook 2; page 16-17	20180328_ASP_NPG-C_ATZ#50_1day_40C_ ph6-8buffer_25ugmLdrug_10ugmLHPMCAS-MF_5um_2.001
Figure 4.5C,F	Notebook 2; page 36, 51	20180619_ASP_NPG-C_ATZ#77_6days_40C_ ph6-8buffer_25ugmLdrug_10ugmLHPMCAS-MF_5um_1.001

Files for Figure 4.6 are found at \Beaudoin Group\Manuscript 2 Polymer & Surfactant\ Figures\

Figure 4.6	Notebook Reference	File path
Figure 4.6A,D	Notebook 1; page 110-113	20171024_ASP_NPG-C_ATZ#19_fresh_pH7 buffer_75ugmLdrug_100ugmLHPCMAS_2um_1.001
Figure 4.6B,E	Notebook 1; page 80,89-90	20170921_ASP_NPG-C_ATZ#14_1day_pH7 buffer_75ugmLdrug_100ugmLHPMCAS_2um_2.002
Figure 4.6C,F	Notebook 1; page 110-111, 116	20171026_ASP_NPG-C_ATZ#19_48hours_40C _pH7buffer_75upmLdrug_100ugmLHPMCAS_2um_1.001

Files for Figure 4.7 are found at \Beaudoin Group\Manuscript 2 Polymer & Surfactant\ Figures\

Figure 4.7	Notebook Reference	File path
Figure 4.7A		Fresh Film Picture Scalebar.TIF

Figure 4.7B		Fresh Film Scalebar.TIF
Figure 4.7C		24 Hour Crystallized Picture Scalebar.TIF
Figure 4.7D		24 Hour Crystallized Film Scalebar.TIF
Figure 4.7E	Notebook 2; page 50, 52-53, 83-84	ATZ#79_008.TIF
Figure 4.7F	Notebook 2; page 50, 52-53, 83-84	ATZ#79_006.TIF
Figure 4.7G	Notebook 2; page 50, 52-53, 83-84	ATZ#79_002.TIF
Figure 4.7H	Notebook 2; page 50, 52-53, 83-84	ATZ#79_007.TIF

Files for Figure 4.8 are found at \Beaudoin Group\Computation\Polymer\v1

Figure 4.8	File path
Figure 4.8A	E7_1.0_steps_0%cov.PNG E7_2.0_steps_0%cov.PNG E7_3.0_steps_0%cov.PNG E7_4.0_steps_0%cov.PNG
Figure 4.8B	E7_1.0_steps_25%cov.PNG E7_2.0_steps_25%cov.PNG E7_3.0_steps_25%cov.PNG E7_4.0_steps_25%cov .PNG
Figure 4.8C	Coverage_Scaling.XLSX

Figure 4.8C	Replicate									
Coverage	1	2	3	4	5	6	7	8	9	10
0	4.2E7	4.6E7	4.5E7	4.2E7	4.2E7	4.8E7	4.4E7	4.6E7	4.3E7	4.8E7
0.01	4.6E7	4.5E7	4.3E7	4.5E7	4.4E7	4.7E7	4.5E7	4.4E7	4.4E7	4.6E7
0.05	4.3E7	4.9E7	4.4E7	4.2E7	4.4E7	5.2E7	4.9E7	5.0E7	4.9E7	4.1E7
0.1	4.9E7	4.4E7	4.7E7	4.7E7	5.4E7	5.2E7	5.3E7	4.8E7	4.7E7	4.9E7
0.25	5.7E7	6.1E7	5.9E7	5.8E7	5.5E7	6.0E7	5.8E7	6.1E7	5.6E7	6.3E7
0.5	1.0E8	9.6E7	1.0E8	9.3E7	9.8E7	9.3E7	9.9E7	9.8E7	9.7E7	9.2E7

Files for Figure 4.9 are found at \Beaudoin Group\Computation\Polymer\

Figure 4.9	File path
Figure 4.9A	v2_test003\E6_5.0_steps_polymertest003_v2.PNG v2_test003\E7_2.0_steps_polymertest003_v2.PNG v2_test003\E7_3.5_steps_polymertest003_v2.PNG v2_test003\E7_5.0_steps_polymertest003_v2.PNG
Figure 4.9B	v2_test005\E6_5.0_steps_polymertest005_v2.PNG v2_test005\E7_2.0_steps_polymertest005_v2.PNG v2_test005\E7_3.5_steps_polymertest005_v2.PNG

	v2_test005\E7_5.0_steps_polymertest005_v2.PNG
Figure 4.9C	v2_Scaling.XLSX

Figure 4.9C	Conversion		
Steps	No Polymer	Symmetric	Asymmetric
0	0	0	0
5000000	0.00154836	0.000585	0.00032
10000000	0.00665312	0.002795	0.002783
15000000	0.01881421	0.007508	0.006659
20000000	0.04395897	0.015317	0.012714
25000000	0.08549459	0.027778	0.020659
30000000	0.14521137	0.045919	0.032437
35000000	0.22303673	0.069235	0.047966
40000000	0.32310366	0.097014	0.066452
45000000	0.44617829	0.130237	0.089834
50000000	0.60063951	0.166281	0.116804

Figure 4.9C	Polymer Coverage	
Steps	Symmetric	Asymmetric
0	0	0
500000	0.041548	0.042322
1000000	0.039741	0.040774
1500000	0.038193	0.039483
2000000	0.040774	0.037677
2500000	0.04129	0.037677
3000000	0.039741	0.039225
3500000	0.042838	0.040774
4000000	0.041548	0.040515
4500000	0.045677	0.042064
5000000	0.045935	0.042322
5500000	0.046451	0.04129
6000000	0.045935	0.040515
6500000	0.044386	0.041806
7000000	0.047741	0.046451
7500000	0.045935	0.047225
8000000	0.048257	0.045677
8500000	0.047483	0.044903
9000000	0.052386	0.04129
9500000	0.053677	0.045419
10000000	0.054967	0.048257
10500000	0.056773	0.046709
11000000	0.057031	0.045677
11500000	0.055741	0.047999
12000000	0.060902	0.051354
12500000	0.060128	0.052386

13000000	0.067096	0.052644
13500000	0.061676	0.05316
14000000	0.065805	0.057031
14500000	0.064257	0.060902
15000000	0.068644	0.062709
15500000	0.064773	0.059354
16000000	0.066322	0.064515
16500000	0.074321	0.065547
17000000	0.075096	0.061418
17500000	0.077676	0.068644
18000000	0.080773	0.068902
18500000	0.083353	0.070192
19000000	0.085934	0.072773
19500000	0.088515	0.076644
20000000	0.092644	0.078708
20500000	0.094966	0.081031
21000000	0.092902	0.079483
21500000	0.095224	0.083612
22000000	0.101418	0.077676
22500000	0.106063	0.089031
23000000	0.107095	0.090837
23500000	0.114321	0.094192
24000000	0.113805	0.096515
24500000	0.117676	0.096515
25000000	0.119998	0.102192
25500000	0.126708	0.099353
26000000	0.128772	0.106579
26500000	0.128256	0.105547
27000000	0.13832	0.108385
27500000	0.139353	0.112514
28000000	0.144514	0.116127
28500000	0.148901	0.115611
29000000	0.152256	0.121288
29500000	0.156901	0.123611
30000000	0.16232	0.12774
30500000	0.164643	0.133417
31000000	0.170836	0.137546
31500000	0.177546	0.137288
32000000	0.1809	0.142965
32500000	0.182965	0.143223
33000000	0.18761	0.147094
33500000	0.190965	0.149933
34000000	0.195868	0.156901
34500000	0.200771	0.160255
35000000	0.205932	0.161804
35500000	0.210319	0.165933

36000000	0.211351	0.170578
36500000	0.217029	0.172126
37000000	0.2209	0.173933
37500000	0.224513	0.178836
38000000	0.230706	0.179094
38500000	0.236383	0.183997
39000000	0.23948	0.185029
39500000	0.244899	0.189416
40000000	0.24748	0.192255
40500000	0.252125	0.194578
41000000	0.25548	0.202061
41500000	0.260641	0.202319
42000000	0.267867	0.205416
42500000	0.273802	0.206706
43000000	0.275867	0.207997
43500000	0.277415	0.215997
44000000	0.281286	0.219093
44500000	0.283608	0.223996
45000000	0.289802	0.23148
45500000	0.292382	0.230964
46000000	0.296511	0.231996
46500000	0.300382	0.235867
47000000	0.305027	0.237416
47500000	0.308898	0.241028
48000000	0.310189	0.244899
48500000	0.316124	0.246448
49000000	0.318446	0.248512
49500000	0.321285	0.252641
50000000	0.323866	0.253931

Files for Figure 4.10 are found at \Beaudoin Group\Computation\Polymer\

Figure 4.10	File path
Figure 4.10A	v2_test006\E7_1.0_steps_polymertest006_v2.PNG v2_test006\E7_3.0_steps_polymertest006_v2.PNG v2_test006\E7_5.0_steps_polymertest006_v2.PNG
Figure 4.10B	v2_test007\E7_1.0_steps_polymertest007_v2.PNG v2_test007\E7_3.0_steps_polymertest007_v2.PNG v2_test007\E7_5.0_steps_polymertest007_v2.PNG
Figure 4.10C	E7_1.0_steps_polymertest001_v3.PNG E7_2.5_steps_polymertest001_v3.PNG E7_4.0_steps_polymertest001_v3.PNG
Figure 4.10D	v2_Scaling.XLSX

Figure 4.10D	Conversion			Polymer Coverage
Steps	30% Slow	30% Fast	60% Fast	60% Fast
0	0	0	0	0
5000000	0.001323	0.000263	0.000442	0.58012
10000000	0.00425	0.00074	0.001758	0.578055
15000000	0.008951	0.001357	0.002611	0.582958
20000000	0.015752	0.002165	0.003308	0.580636
25000000	0.024601	0.002927	0.003834	0.579345
30000000	0.036081	0.003963	0.004552	0.58012
35000000	0.050074	0.005859	0.005457	0.578829
40000000	0.066689	0.007465	0.006772	0.58141
45000000	0.087655	0.009108		
50000000	0.109922	0.010777		

Figure 4.10D	Polymer Coverage	
Steps	30% Slow	30% Fast
0	0	0
500000	0.072515	0.236899
1000000	0.074063	0.241286
1500000	0.073547	0.242577
2000000	0.072257	0.238706
2500000	0.075612	0.236641
3000000	0.072515	0.242061
3500000	0.078708	0.249286
4000000	0.074579	0.244641
4500000	0.075612	0.240512
5000000	0.073805	0.234577
5500000	0.07845	0.236899
6000000	0.077418	0.24619
6500000	0.073289	0.238448
7000000	0.077934	0.238964
7500000	0.074838	0.249802
8000000	0.077676	0.247996
8500000	0.074321	0.246964
9000000	0.084902	0.242835
9500000	0.084644	0.239222
10000000	0.08645	0.237416
10500000	0.084128	0.237416
11000000	0.090063	0.240254
11500000	0.089031	0.24877
12000000	0.088257	0.247738
12500000	0.091095	0.245157
13000000	0.094708	0.241803
13500000	0.091869	0.241028
14000000	0.093418	0.249028

14500000	0.099611	0.243867
15000000	0.098579	0.251351
15500000	0.095482	0.248254
16000000	0.10116	0.252641
16500000	0.101418	0.255738
17000000	0.102708	0.247738
17500000	0.111482	0.251609
18000000	0.111998	0.251093
18500000	0.108901	0.243867
19000000	0.11303	0.248512
19500000	0.113288	0.258576
20000000	0.112772	0.24748
20500000	0.115095	0.243609
21000000	0.116643	0.242835
21500000	0.117159	0.24748
22000000	0.125159	0.250835
22500000	0.122579	0.253415
23000000	0.124385	0.253931
23500000	0.126708	0.245673
24000000	0.133417	0.249286
24500000	0.131353	0.242835
25000000	0.137546	0.255996
25500000	0.133933	0.25548
26000000	0.137546	0.259351
26500000	0.142191	0.249028
27000000	0.140643	0.259093
27500000	0.14503	0.254964
28000000	0.144514	0.254189
28500000	0.150191	0.253157
29000000	0.149675	0.247738
29500000	0.150449	0.256254
30000000	0.157159	0.255222
30500000	0.160255	0.253415
31000000	0.161546	0.254448
31500000	0.16103	0.254448
32000000	0.16361	0.256512
32500000	0.170062	0.25806
33000000	0.177287	0.258576
33500000	0.174449	0.261415
34000000	0.17832	0.259093
34500000	0.179868	0.263996
35000000	0.17832	0.264254
35500000	0.181158	0.269673
36000000	0.186836	0.251093
36500000	0.189932	0.261931
37000000	0.189674	0.263996

37500000	0.187352	0.27277
38000000	0.195352	0.272512
38500000	0.201029	0.267867
39000000	0.20361	0.268125
39500000	0.203868	0.26477
40000000	0.20619	0.262189
40500000	0.210319	0.271738
41000000	0.213158	0.273802
41500000	0.217029	0.268641
42000000	0.216255	0.262447
42500000	0.215738	0.27277
43000000	0.224254	0.281544
43500000	0.227609	0.271479
44000000	0.23148	0.277415
44500000	0.235609	0.278705
45000000	0.242319	0.276641
45500000	0.242319	0.278189
46000000	0.242835	0.273544
46500000	0.249544	0.269415
47000000	0.252125	0.277673
47500000	0.257802	0.27535
48000000	0.256254	0.282576
48500000	0.257028	0.275608
49000000	0.26348	0.277157
49500000	0.262705	0.276641
50000000	0.266576	0.277157

E.3 Chapter 5

Files for Figure 5.1 are found at \Beaudoin Group\AFM\

Figure 5.1	Notebook Reference	File path
Figure 5.1A	Notebook 2; page 102-104	20190508\20190508_ASP_SCANASYST-AIR_ATZ#S14_10um_1.001
Figure 5.1B		20200128_NCB\Sample14_120minutes_25C_ph 6-8buffer_25ugmLATZ_location2_1.002
Figure 5.1C	Notebook 2; page 110,114	20190523\20190523_ASP_SCANASYST-AIR_ATZ#S24_10um_1.005

Files for Figure 5.2 are found at \Beaudoin Group\AFM\20190726

Figure 5.2	Notebook Reference	File path
Figure 5.2A	Notebook 2; page 132-133	20190726_ASP_RTESPA-300_ATZ#S35_10um_2.001
Figure 5.2B	Notebook 2; page 132-133	20190726_ASP_RTESPA-300_ATZ#S35_10um_2_001_Cross.JPG

		20190726_ASP_RTESPA-300_ATZ#S35_10um_2_001_XZ.TXT

Table of Data for Figure 5.2B

X (μm)	Z (nm)
0.000000e+00	8.982019e+00
3.910217e-02	8.976221e+00
7.820434e-02	1.023433e+01
1.173065e-01	1.040339e+01
1.564087e-01	9.505490e+00
1.955109e-01	7.602683e+00
2.346130e-01	4.826278e+00
2.737152e-01	1.379945e+00
3.128174e-01	-2.500967e+00
3.519195e-01	-6.502195e+00
3.910217e-01	-1.028124e+01
4.301239e-01	-1.346186e+01
4.692261e-01	-1.570437e+01
5.083282e-01	-1.675155e+01
5.474304e-01	-1.645994e+01
5.865326e-01	-1.484025e+01
6.256348e-01	-1.204177e+01
6.647369e-01	-8.341400e+00
7.038391e-01	-4.070887e+00
7.429413e-01	4.121520e-01
7.820435e-01	4.765577e+00
8.211456e-01	8.691351e+00
8.602478e-01	1.194381e+01
8.993500e-01	1.441541e+01
9.384521e-01	1.582684e+01
9.775544e-01	1.618997e+01
1.016656e+00	1.547082e+01
1.055759e+00	1.374245e+01
X (μm)	Z (nm)
1.094861e+00	1.108210e+01
1.133963e+00	7.640079e+00
1.173065e+00	3.628377e+00
1.212167e+00	-6.903523e-01
1.251270e+00	-4.984869e+00
1.290372e+00	-8.899470e+00
1.329474e+00	-1.206090e+01
1.368576e+00	-1.417004e+01
1.407678e+00	-1.500190e+01
1.446780e+00	-1.449114e+01
1.485883e+00	-1.270307e+01
1.524985e+00	-9.854035e+00
1.564087e+00	-6.236581e+00
1.603189e+00	-2.192215e+00
1.642291e+00	1.932370e+00
1.681393e+00	5.822181e+00
1.720496e+00	9.219788e+00
1.759598e+00	1.193325e+01
1.798700e+00	1.372721e+01
1.837802e+00	1.453857e+01
1.876904e+00	1.433751e+01
1.916006e+00	1.306253e+01
1.955109e+00	1.088359e+01
1.994211e+00	7.873544e+00
2.033313e+00	4.224444e+00
2.072415e+00	1.555687e-01
2.111517e+00	-4.049687e+00
2.150619e+00	-8.044844e+00
X (μm)	Z (nm)
2.189722e+00	-1.148860e+01
2.228824e+00	-1.405588e+01
2.267926e+00	-1.548952e+01
2.307028e+00	-1.563578e+01
2.346130e+00	-1.448916e+01
2.385232e+00	-1.218484e+01
2.424335e+00	-8.955207e+00
2.463437e+00	-5.122292e+00
2.502539e+00	-1.022606e+00
2.541641e+00	3.013890e+00
2.580743e+00	6.699289e+00
2.619846e+00	9.813047e+00
2.658948e+00	1.211359e+01
2.698050e+00	1.350920e+01
2.737152e+00	1.393530e+01
2.776254e+00	1.334962e+01
2.815356e+00	1.179570e+01
2.854459e+00	9.254503e+00
2.893561e+00	6.025544e+00
2.932663e+00	2.230633e+00
2.971765e+00	-1.872746e+00

3.010867e+00	-5.986081e+00
3.049969e+00	-9.764324e+00
3.089072e+00	-1.285932e+01
3.128174e+00	-1.495427e+01
3.167276e+00	-1.583823e+01
3.206378e+00	-1.541436e+01
3.245480e+00	-1.374370e+01
3.284582e+00	-1.100727e+01
X (μm)	Z (nm)
3.323685e+00	-7.487093e+00
3.362787e+00	-3.503804e+00
3.401889e+00	5.895627e-01
3.440991e+00	4.492033e+00
3.480093e+00	8.023639e+00
3.519195e+00	1.078397e+01
3.558298e+00	1.271424e+01
3.597400e+00	1.371457e+01
3.636502e+00	1.373003e+01
3.675604e+00	1.277540e+01
3.714706e+00	1.089981e+01
3.753808e+00	8.215538e+00
3.792911e+00	4.874367e+00
3.832013e+00	9.828683e-01
3.871115e+00	-2.985532e+00
3.910217e+00	-6.837737e+00
3.949319e+00	-1.024928e+01
3.988422e+00	-1.289914e+01
4.027524e+00	-1.451558e+01
4.066626e+00	-1.492409e+01
4.105728e+00	-1.408598e+01
4.144830e+00	-1.208733e+01
4.183933e+00	-9.125605e+00
4.223034e+00	-5.499595e+00
4.262137e+00	-1.530843e+00
4.301239e+00	2.464629e+00
4.340341e+00	6.269757e+00
4.379443e+00	9.451166e+00
4.418545e+00	1.192143e+01
X (μm)	Z (nm)
4.457648e+00	1.353685e+01
4.496750e+00	1.421379e+01
4.535852e+00	1.393251e+01
4.574954e+00	1.270963e+01
4.614056e+00	1.062359e+01
4.653159e+00	7.789917e+00

4.692261e+00	4.390040e+00
4.731363e+00	6.328704e-01
4.770465e+00	-3.244824e+00
4.809567e+00	-6.842004e+00
4.848670e+00	-9.898279e+00
4.887771e+00	-1.211765e+01
4.926874e+00	-1.327099e+01
4.965976e+00	-1.323881e+01
5.005078e+00	-1.201192e+01
5.044180e+00	-9.712134e+00
5.083282e+00	-6.566413e+00
5.122385e+00	-2.858938e+00
5.161487e+00	1.093709e+00
5.200589e+00	4.997015e+00
5.239691e+00	8.624752e+00
5.278793e+00	1.161088e+01
5.317896e+00	1.384486e+01
5.356997e+00	1.518827e+01
5.396100e+00	1.557959e+01
5.435202e+00	1.497581e+01
5.474304e+00	1.340641e+01
5.513406e+00	1.094855e+01
5.552508e+00	7.730900e+00
X (μm)	Z (nm)
5.591611e+00	3.926774e+00
5.630713e+00	-2.132855e-01
5.669815e+00	-4.406455e+00
5.708917e+00	-8.429005e+00
5.748019e+00	-1.173805e+01
5.787122e+00	-1.413463e+01
5.826224e+00	-1.538542e+01
5.865326e+00	-1.538153e+01
5.904428e+00	-1.412817e+01
5.943530e+00	-1.179813e+01
5.982633e+00	-8.624165e+00
6.021734e+00	-4.931075e+00
6.060837e+00	-1.046084e+00
6.099939e+00	2.778522e+00
6.139041e+00	6.140814e+00
6.178143e+00	8.873917e+00
6.217245e+00	1.080681e+01
6.256348e+00	1.183952e+01
6.295450e+00	1.190539e+01
6.334552e+00	1.099816e+01
6.373654e+00	9.176128e+00

6.412756e+00	6.518857e+00
6.451859e+00	3.187616e+00
6.490960e+00	-6.141079e-01
6.530063e+00	-4.601470e+00
6.569165e+00	-8.476928e+00
6.608267e+00	-1.187223e+01
6.647369e+00	-1.444624e+01
6.686471e+00	-1.591567e+01
X (μm)	Z (nm)
6.725574e+00	-1.609650e+01
6.764676e+00	-1.498108e+01
6.803778e+00	-1.268989e+01
6.842880e+00	-9.470246e+00
6.881982e+00	-5.637088e+00
6.921085e+00	-1.540504e+00
6.960187e+00	2.568566e+00
6.999289e+00	6.216882e+00
7.038391e+00	9.244684e+00
7.077493e+00	1.146362e+01
7.116595e+00	1.274919e+01
7.155697e+00	1.303522e+01
7.194800e+00	1.229158e+01
7.233902e+00	1.056916e+01
7.273004e+00	7.968928e+00
7.312106e+00	4.644720e+00
7.351208e+00	8.317146e-01
7.390311e+00	-3.162832e+00
7.429413e+00	-6.992547e+00
7.468515e+00	-1.029151e+01
7.507617e+00	-1.269003e+01
7.546719e+00	-1.391733e+01
7.585822e+00	-1.380252e+01
7.624923e+00	-1.226392e+01
7.664025e+00	-9.567075e+00
7.703128e+00	-5.932874e+00
7.742230e+00	-1.714521e+00
7.781332e+00	2.728899e+00
7.820435e+00	7.134286e+00
X (μm)	Z (nm)
7.859537e+00	1.096939e+01
7.898639e+00	1.408860e+01
7.937741e+00	1.629559e+01
7.976843e+00	1.745682e+01
8.015945e+00	1.748816e+01
8.055047e+00	1.638271e+01
8.094150e+00	1.418571e+01
8.133252e+00	1.100108e+01
8.172354e+00	7.009243e+00
8.211457e+00	2.460311e+00
8.250558e+00	-2.337290e+00
8.289660e+00	-7.013029e+00
8.328762e+00	-1.117032e+01
8.367865e+00	-1.442942e+01
8.406967e+00	-1.647828e+01
8.446069e+00	-1.712431e+01
8.485172e+00	-1.631131e+01
8.524274e+00	-1.416122e+01
8.563376e+00	-1.082254e+01
8.602477e+00	-6.832207e+00
8.641580e+00	-2.470582e+00
8.680682e+00	1.979932e+00
8.719784e+00	6.022408e+00
8.758887e+00	9.485076e+00
8.797989e+00	1.215092e+01
8.837091e+00	1.388149e+01
8.876194e+00	1.459151e+01
8.915295e+00	1.425917e+01
8.954397e+00	1.290688e+01
X (μm)	Z (nm)
8.993499e+00	1.061572e+01
9.032602e+00	7.522339e+00
9.071704e+00	3.828893e+00
9.110806e+00	-1.996801e-01
9.149909e+00	-4.248375e+00
9.189011e+00	-7.953494e+00
9.228113e+00	-1.095757e+01
9.267214e+00	-1.294541e+01
X (μm)	Z (nm)
9.306317e+00	-1.371209e+01
9.345419e+00	-1.319144e+01
9.384521e+00	-1.148450e+01
9.423624e+00	-8.830422e+00
9.462726e+00	-5.576182e+00
9.501828e+00	-2.113457e+00
9.540930e+00	1.229005e+00

Files for Figure 5.3 are found at \Beaudoin Group\AFM\20190726

Figure 5.3	Notebook Reference	File path
Figure 5.3A	Notebook 2; page 132-133	20190726_ASP_RTESPA-300_ATZ#S35_10um_2_001_Cross.JPG 20190726_ASP_RTESPA-300_ATZ#S35_10um_2_001_XZ.TXT
Figure 5.3B	Notebook 2; page 132-133	FFT.TIF FFT_fit.TIF
Figure 5.3C	Notebook 2; page 132-133	Regression_fit.TIF

Files for Figure 5.4 are found at \Beaudoin Group\AFM\

Figure 5.4	Notebook Reference	File path
Figure 5.4A	Notebook 2; page 150-153	20200629\Control_T3_Replicate1\TIFF\20200629_ASP_NPG-C_contact-air_T3_GM#3_10um_1_001.TIF 20200629\Control_T3_Replicate1\TIFF\20200629_ASP_NPG-C_contact-fluid_T3_GM#3_control_30C_pH6-8buffer_25ugmLATZ_10um_1_002.TIF 20200623\Template2_Control_Replicate3\TIFF\20200623_ASP_NPG-C_contact-air_T2_GM#12_10um_2_001.TIF 20200623\Template2_Control_Replicate3\TIFF\20200623_ASP_NPG-C_contact-fluid_T2_GM#12_control_30C_pH6-8buffer_25ugmLATZ_10um_2_002.TIF
Figure 5.4B	Notebook 2; page 152-153	20200629\Control_T3_Replicate2\TIFF\20200629_ASP_NPG-C_contact-air_T3_GM#4_10um_3_001.TIF 20200629\Control_T3_Replicate2\TIFF\20200629_ASP_NPG-C_contact-fluid_T3_GM#4_control_30C_pH6-8buffer_50ugmLATZ_10um_3_002 20200629\Control_T3_Replicate2\TIFF\20200629_ASP_NPG-C_contact-fluid_T3_GM#4_control_30C_pH6-8buffer_50ugmLATZ_10um_3_003.TIF 20200629\Control_T3_Replicate2\TIFF\20200629_ASP_NPG-C_contact-fluid_T3_GM#4_control_30C_pH6-8buffer_50ugmLATZ_10um_3_004.TIF

File for Figure 5.5 found at \Beaudoin Group\AFM\20200217\XZdata\TempAnalysis and Notebook 2; page 147

Files for Figure 5.6 found at \Beaudoin Group\AFM\20200210\Crops and \ Beaudoin Group\AFM\20200210\XZdata

Data for Figure 5.7 found at \Beaudoin Group\Dissertation\Chapter5 – Surf Decay\Sine Decay Data